UNIVERSITÀ DEGLI STUDI DI BARI ALDO MORO

Dipartimento Interateneo di Fisica "M.Merlin"

DOTTORATO DI RICERCA IN FISICA

Ciclo XXXI

Settore scientifico-disciplinare FIS/01

D-meson correlations with charged particles in small systems with the ALICE experiment at the LHC

Supervisore:
Prof. Domenico Di Bari

Coordinatore:
Prof. Giuseppe Iaselli

Dottoranda:
Marianna Mazzilli

ESAME FINALE 2018

Abstract

The primary goal of the ALICE experiment at the LHC is to investigate the properties of the Quark-Gluon Plasma (QGP), the hot and dense state of strongly-interacting matter produced in high-energy heavy-ion collisions. Charm and beauty quarks are excellent probes to study the QGP properties: they are produced in hard parton scattering processes occurring in the early stages of the collision, traverse the QCD medium and interact with its constituents experiencing its whole evolution. In particular, they are subject to several modifications during the QGP phase, such as a progressive energy loss while traversing the hot nuclear medium. Their hadronization products, therefore, keep traces of the QGP effects. A fundamental challenge is to characterize the heavy-flavour production, propagation and fragmentation mechanism. Measurements of this kind would provide, from one side, a reliable test of perturbative QCD calculations which describe heavy quark production (in pp collisions) and, from the other side, would highlight the QGP properties (in Pb-Pb collisions) or the cold nuclear matter effects (in p-Pb collisions) affecting the heavy-quark propagation and hadronization process.
Two-particle azimuthal correlations, where at least one is a charmed hadron, are an important tool to study in better details the charm production. Their study is complementary with respect to the jet study, since the correlation distributions allow to characterize the behavior of all the associated particles related to the trigger particle (coming from the charm fragmentation) looking for example at the distributions of the initial parton momentum to the associated particles in which the charm fragments.
In detail, in pp collisions, the study of azimuthal correlations between charmed hadrons or with charged particles produced in the same event, allow us to gain further insight into the underlying heavy-quark production mechanism as well as the fragmentation and hadronization of heavy quarks into jets. Heavy-flavour correlation studies in more complex collisional systems, like Pb–Pb, play a crucial role in studying the modification of the charmed jets fragmentation due to in-medium (or cold nuclear matter, in case of p-Pb collisions) effects. For instance, in Pb–Pb collisions the azimuthal correlation distributions can provide information on the energy loss mechanism of heavy quarks in the QGP. Additionally, azimuthal correlations are sensitive to possible modifications of the heavy quark parton shower and hadronization in presence of the medium. Similar results to the double-ridge long-range di-hadron correlation for the light quark sector, can be investigate for heavier quarks via the correlation studies.
The best possibilities are obtained by studying $D\overline{D}$ or D-hadron angular correlations. Measuring the inclusive D-meson angular correlations with a generic charged hadron, and with another charmed meson, is not an easy task, due to the low cross section for charm production and to small branching ratios in the hadronic decay channels that allow D mesons to be experimentally reconstructed. In addition, excellent capabilities for the D meson reconstruction (high efficiencies) and selection (good background D rejection) are required by the detectors, in order to reduce the influence of the background for the

misidentified D mesons. The focus of this thesis is the description of the azimuthal correlations between D mesons and charged hadrons. Such measurements, experimentally easier to perform, are also more loosely related to the heavy quark separation angle. Anyway, information on the underlying quark pair is extracted by studying the shape and the height of the correlation peaks at $\Delta\phi = 0$ and $\Delta\phi = \pi$ and by comparing the peaks features with the expectations from Monte-Carlo simulations.
Moreover, the recent observation of long-range correlations in p-Pb for light flavour hadrons and for heavy-flavour decay electrons points towards the presence of collective effects or to effects originating from gluon saturation in the initial state. Additional information could be extracted by the eventual observation of the same effect with D mesons.
Therefore, the main goal of this research work is to study the azimuthal correlations between D^{*+} mesons and charged particles in small collision systems (pp and p–Pb). The analysis was computed at the same collision energy in order to a valid comparison among the two collision systems. Moreover, the results of this analysis are extracted averaging the independent results gained on three species of D mesons: D^0, D^{*+} and D^+. In particular, this thesis deals with the azimuthal correlations of D^{*+} and charged primary hadrons. Hence, specific results about the D^{*+} correlations with hadrons will be shown in this thesis; the final results are common for the three D-meson species and, therefore, take into account also the analysis work carried out independently from the other two D-mesons.

This thesis is organized in five chapters. The first chapter deals with the heavy-flavour production in hadronic collisions. Each section is devoted to a different collision system: pp, p–A and A–A. Here, the basic aspects of the QCD theory, which describes the interaction of hadrons and their constituents, and enounces the conditions to perform perturbative calculations of the cross sections, will be addressed. In the section focused on the A–A collision system, a description of the QGP phase transition and on the observables sensitive to the medium properties will also be provided. The second chapter describes the role of two-particle correlations in understanding the QCD processes (fragmentation, hadronization or different heavy quark production mechanism) which are still not well known. A selection of the experimental results on two-particle correlations and the comparison with theoretical models in the various collision systems will be discussed as well. The sections of the second chapter are organized following the collision system scheme. The third chapter is devoted to the description of the ALICE experiment. After a general overview of the apparatus, the focus is given to the detectors used for the analyses presented in this thesis: the Inner Tracking System, the Time Projection Chamber and the Time-Of-Flight detector, for particle identification. The algorithms used for tracking and vertexing are then discussed. Finally the model employed for the centrality determination will be described.
The fourth and the fifth chapters are focused on the analysis work. In particular, in

the fourth chapter the D-hadron correlation analysis in pp collisions at $\sqrt{s} = 5.02$ TeV will be presented. In the related sections, all the analysis steps will be treated in detail: starting from the analysis strategy, going through the corrections performed and to the evalution of the systematic uncertainties. Finally, the results will be presented and the comparison with model predictions will be discussed as well.
The fifth chapter is focused on the p–Pb collision system at $\sqrt{s_{\rm NN}} = 5.02$ TeV and, here, both the centrality integrated analysis and the multiplicity dependent analysis will be described. Since the analysis strategy is the same presented in the fourth chapter, I will focus especially on the differences between the two collision systems. In the end, the results will be discussed. A comparison with the proton proton measurements will be reported as well.
All the result presented in this thesis have been approved from the ALICE Collaboration as preliminary results and, currently, we are going toward a long paper publication.

Riassunto

Obiettivo principale dell'esperimento ALICE al Large Hadron Collider del CERN di Ginevra, è investigare le proprietà del Quark-Gluon Plasma (QGP): uno stato di materia fortemente interagente e caratterizzato da alte temperature e densità, prodotto nelle collisioni tra ioni pesanti. I quark pesanti, charm e beauty, sono ottimi strumenti di indagine per la caratterizzazione del QGP: prodotti nei primissimi istanti immediatamente successivi alla collisione, attraversano il mezzo e interagiscono con i suoi costituenti, partecipando a tutti gli stadi della sua evoluzione. In particolare, interagendo con il QGP, i quark pesanti perdono progressivamente energia mentre attraversano il mezzo. Pertanto, i prodotti finali dell'adronizzazione dei quark charm e beauty, conservano informazioni sugli effetti del QGP. Una delle più ardue sfide è dunque caratterizzare la produzione dei quark pesanti così come il meccanismo di frammentazione e adronizzazione. Misure sui quark charm e beauty consentono da un lato di testare la teoria Cromodinamica Quantistica (QCD) in regime perturbativo, che descrive la produzione dei quark pesanti e, dall'altro, sono un ottimo strumento per indagare gli effetti del QGP (in collisioni Pb–Pb) e della materia nucleare fredda (in collisioni p–Pb) sui processi di adronizzazione e propagazione.

Le correlazioni angolari tra coppie di particelle, di cui almeno una contenente un quark pesante, rappresentano un importante strumento per studiare la produzione di quark pesanti. Lo studio delle correlazioni è complementare allo studio dei jets; infatti, consente di caratterizzare il comportamento delle particelle associate alla particella trigger (prodotta dalla frammentazione del quark charm), studiando ad esempio come l'impulso iniziale del partone si distribuisce tra le particelle associate nelle quali il quark pesante frammenta.

In particolare, nelle collisioni pp, lo studio delle correlazioni angolari tra adroni contenenti il quark charm o tra un adrone contenente un quark charm e particelle cariche primarie prodotte nel medesimo evento consente di approfondire la nostra attuale conoscenza sui meccanismi di produzione dei quark pesanti, sulla loro frammentazione e sull'adronizzazione di questi in jets.

Lo studio delle correlazioni angolari di quark pesanti in sistemi di collisione più complessi, come in Pb–Pb, svolge un ruolo cruciale nell'investigare possibili modifiche nella frammentazione dei jet prodotti da quark charm dovuti all'interazione con il mezzo (o alla presenza di effetti di materia nucleare fredda, nel caso di collisioni p–Pb). Infatti, in collisioni Pb–Pb la distribuzione di correlazioni angolari fornisce informazioni sul meccanismo di perdita dell'energia dei quark pesanti nel Quark-Gluon-Plasma. Inoltre, le correlazioni angolari sono sensibili a possibili modifiche sia nel parton shower del charm, sia al processo di adronizzazione in presenza del mezzo. Analoghi risultati, rispetto a quelli osservati per le correlazioni nel settore dei quark leggeri, sono oggetto di indagine. Vi sono due principali strategie di analisi: studiare le correlazioni angolari $\mathrm{D\overline{D}}$ oppure le correlazioni tra un mesone D e le particelle cariche. Entrambe le strategie soffrono del

basso branching ratio dei mesoni D ricostruiti nei loro canali di decadimento adronici e della bassa sezione d'urto del charm. Inoltre, esse richiedono elevate efficienze del detector nel ricostruire e selezionare sperimentalmente i mesoni D.
Questo lavoro di tesi è incentrato sullo studio delle correlazioni angolari tra i mesoni e gli adroni carichi. Questa misura, sperimentalmente caratterizzata da maggiore statistica rispetto all'analisi di correlazioni $D\overline{\mathrm{D}}$, è correlata in modo più indiretto alla separazione angolare della coppia di quark pesanti originaria. Ad ogni modo, le proprietà sulla coppia di quark pesanti iniziali si ripercuotono sull'ampiezza e sull'altezza dei picchi delle distribuzioni di correlazioni angolari in $\Delta\phi = 0$ e in $\Delta\phi = \pi$ estratti dall'analisi sperimentale dei dati e confrontati con le simulazioni Monte Carlo. Inoltre, le recenti osservazioni di strutture a lungo raggio nelle correlazioni tra adroni leggeri e di elettroni provenienti dal decadimento di adroni contenenti quark pesanti, in collisioni p–Pb, puntano verso la presenza di effetti collettivi o di effetti dovuti alla saturazione gluonica negli stati iniziali. L'osservazione di simili strutture anche per i mesoni D potrebbero aiutare a comprendere meglio l'origine di tali strutture. Obiettivo principale del presente lavoro di ricerca è lo studio delle correlazioni angolari tra i mesoni D^{*+} e gli adroni carichi in collisioni pp e in collisioni p–Pb. L'analisi è stata eseguita alla stessa energia nel sistema del centro di massa al fine da avere un valido confronto tra i due sistemi di collisione. Successivamente, i risultati dell'analisi sono stati confrontati e mediati con i risultati delle correlazioni dei mesoni D^0 e D^+ con adroni carichi. Pertanto, in questa tesi sono presentati numerosi risultati specifici relativi al mesone D^{*+}; i risultati finali sono estratti dalle tre specie di mesoni D.

La tesi è organizzata in cinque capitoli. Il primo capitolo descrive la produzione di quark pesanti nelle collisioni adroniche. Ciascuna sezione del capitolo è dedicata ad un diverso sistema di collisione: pp, p–A e A–A. In questo capitolo, si affrontano i principali aspetti della teoria QCD: dalla descrizione dell'interazione tra adroni ed i loro costituenti, sino al calcolo delle sezioni d'urto entro i limiti di validità del regime perturbativo. In particolare, nella sezione incentrata sulle collisioni A–A, è riportata una descrizione della transizione di fase del QGP e delle osservabili sensibili alle proprietà del mezzo.
Il secondo capitolo descrive nella prima parte il ruolo dello studio delle correlazioni tra particelle nella comprensione dei processi QCD (meccanismi di produzione dei quark pesanti, frammentazione, adronizzazione), ancora oggetto di studio e di ricerca. La seconda parte del capitolo riporta una rassegna dei risultati sperimentali nelle correlazioni angolari tra due particelle e il relativo confronto con i modelli teorici nei diversi sistemi di collisione.
Il terzo capitolo è dedicato alla descrizione dell'apparato sperimentale di ALICE, con particolare attenzione ai rivelatori impiegati nell'analisi presentata in questa tesi (Inner Tracking System, Time Projection Chamber and Time-Of-Flight). Gli algoritmi adottati per il tracciamento e la ricostruzione dei vertici sono discussi insieme ai modelli impiegati per la determinazione della centralità.

Il quarto ed il quinto capitolo sono focalizzati sul lavoro di analisi. In particolare, nel quarto capitolo è presentata l'analisi delle correlazioni di mesoni D con adroni carichi in collisioni pp a $\sqrt{s}$ = 5.02 TeV. Le sezioni del capitolo descrivono dettagliatamente i vari step dell'analisi: dalla strategia di analisi alle correzioni applicate ed alla valutazione delle incertezze sistematiche. Nell'ultima sezione sono presentati i risultati ed il confronto con i modelli teorici. Il quinto capitolo è incentrato sull'analisi in collisioni p–Pb a $\sqrt{s_{\rm NN}}$ = 5.02 TeV, eseguita sia a centralità integrata sia in funzione delle classi di centralità. Infine, i risultati sono stati confrontati con la misura eseguita in collisioni pp e con i modelli teorici.
Tutti i risultati finali presentati in questa tesi sono stati approvati come risultati preliminari della Collaborazione ALICE e, attualmente, stiamo lavorando per la pubblicazione del presente lavoro di ricerca.

Contents

1

Heavy flavours

1.1 Introduction

Heavy-flavour hadrons, containing open or hidden charm and beauty quark, are effective tools for the study of Quantum Chromodynamics (QCD) in high-energy hadronic collisions. They allow studying the heavy-quarks production mechanism in proton-proton collisions, probing our understanding if the QCD in perturbative regime. In addition, Due to their large masses, heavy quarks are produced in the very initial stages of the hard parton-scattering process in nucleon-nucleon collisions and on short time scales ($\sim$0.1 fm/c and 0.02 fm/c for charm and beauty quark, respectively) compared to the Quark-Gluon Plasma (QGP) thermalisation time at Large Hadron Collider (LHC) energies. Moreover, in contrast to what happens for light quarks and gluons, heavy quarks have negligible annihilation rate within the QGP as well as a negligible secondary "thermal" charm and beauty production (from processes like $gg \to c\bar{c}$) for QGP temperature currently reached at the collider. Therefore, heavy quarks witness the full evolution of the hot medium produced in the heavy-ion collisions and, for this reason, are a powerful tool for study the interactions with the medium itself. To better understand and interprete nucleus-nucleus results, measurements in p–Pb collisions are essential as they provide an ideal tool to disentangle hot and cold nuclear matter effects in heavy-flavour production.
Experimentally, since we cannot access directly the heavy-quark behavior, we focus on their study after the hadronization stage. The main experimental strategies of investigation in the heavy-flavour field involve the study of D- and B-mesons in their exclusive hadronic decay channels (e.g. $D^0 \to K^-\pi^+$ or $D^0 \to J/\psi K^0_s$), the detection of leptons coming from their inclusive semi-leptonic decay channels as well as the selection of semi-inclusive decays (e.g. J/ψ mesons, Λ_c and Ξ_c) and the reconstruction on $b-$ and $c-$ jets.

The production of open heavy-flavour in different colliding systems will be treated in

this chapter. The formation process and the main models employed to describe the production of heavy-flavour mesons in elementary systems will be introduced in Section 1.1, whereas the modifications predicted for more complex collision system will be described in Sections 1.2 (p-A) and 1.3 (A-A). In particular, the section 1.2 will be focused on the cold nuclear matter modifications of the heavy-flavour production, and to their study through p-Pb collisions, while in the section 1.3 the modifications predicted for heavy-ion collisions will be described. Throughout these sections, highlight will be provided to the observables employed for these studies.

1.2 Heavy- quark production in pp collisions

The measurement of charm and beauty production in proton-proton represents the mandatory benchmark for the study of medium effects in nucleus-nucleus collisions, and it is of great interest to strengthen our understanding of strong interactions and to test both the perturbative and the non-perturbative sectors of QCD.
In the simplest picture, due to flavour conservation, heavy-quark pair $q\bar{q}$ are produced during a hard scattering process between two quarks or gluons ("partons") carrying a fraction of the colliding nucleon momenta x, as sketched Fig.1.1.

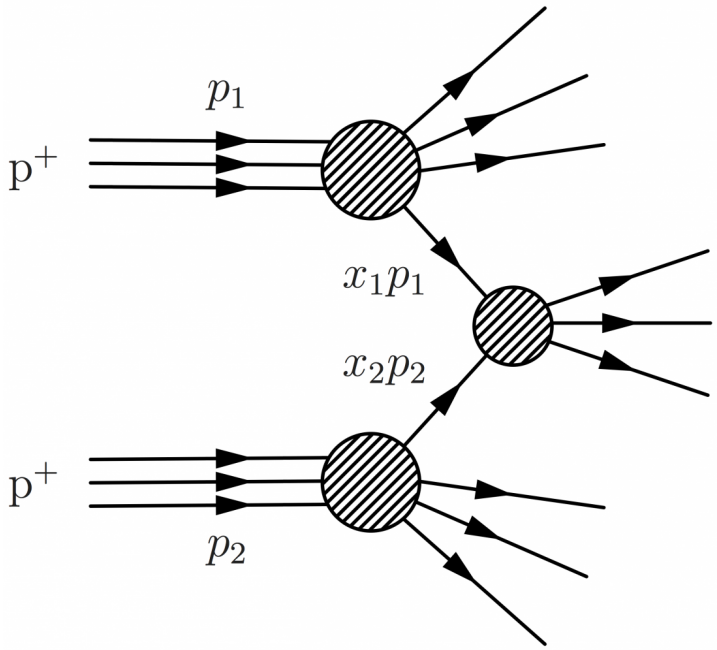

Figure 1.1 *– Schematic picture of a hard scattering process between two colliding particles leading to the formation of a heavy-quark pair.*

This fraction of the nucleon momentum, carried by the parton, is known as Bjorken-x

and its definition is the following:

$$x = \frac{M_{q\bar{q}}}{\sqrt{s_{NN}}} e^{(y_{q\bar{q}})} \tag{1.1}$$

where $M_{q\bar{q}}$ and $y_{q\bar{q}}$ are, respectively, the invariant mass and the rapidity of the $q\bar{q}$ pair in the nucleon-nucleon center-of-mass frame.

At the large center-of-mass energy provided by the modern colliders (such as LHC), the production of heavy quark pairs is strongly sensitive to the low Bjorken-x content of the incoming nucleons.

In particular, within the ALICE acceptance windows, at central rapidities $y \sim 0$, where the Bjorken-x values of the partons are approximately equal, the Bjorken-x value is expected to be equal to $6.4 \cdot 10^{-4}$ for a $b\bar{b}$ pair and $1.7 \cdot 10^{-4}$ for a $c\bar{c}$ pair at top LHC energies (14 TeV). At forward rapidities, values of x even 2 orders of magnitude lower are approachable. In Fig. 1.2 the accessible Bjorken-x intervals probed at the LHC in Pb–Pb collisions (left) panel and in pp collisions (right panel) with the ALICE detector are shown.

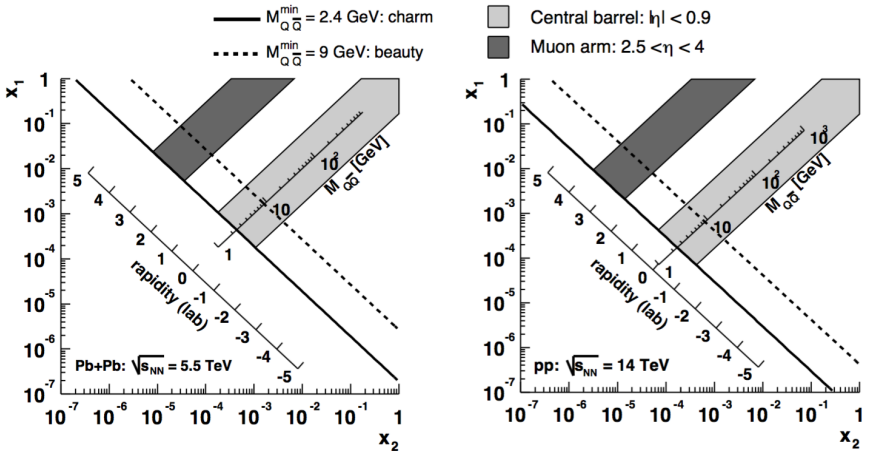

Figure 1.2 *– ALICE acceptances in the Bjorken (x_1; x_2) plane for Pb–Pb (left) and pp (right) collisions at $\sqrt{s_{\rm NN}} = 5.5 TeV$ and 14 TeV respectively. Charm- and beauty- quark pairs threshold production are reported. Figure from [2]*

The momentum distribution of the partons inside a free nucleon, in the collinear approach, is expressed in terms of the Parton Distribution Functions (PDFs) $f_i(x, Q^2)$, which describes the probability for each parton specie i (quark or gluon) to carry a fraction x of the nucleon longitudinal momentum. Such distributions can only be extracted from experimental measurements fitting the Deep Inelastic Scattering results since, for a large class of applications, they depend only on the energy scale Q^2 at which the pro-

cess occurs and not on the scattering process itself. Significant results on our current knowledge of PDFs were obtained from Deep Inelastic Scattering (DIS) performed at the HERA electon-proton collider. Indeed, even if the PDFs have been measured at a given energy scale and the momenta repartition among the constituent partons inside a nucleon has a non-perturbative nature, the PDFs can be evolved to a different Q^2 with a perturbative approach by means of the Dokshitzer-Gribov-Lipatov-Altarelli-Parisi (DGLAP) evolution equation, that is expected to work reasonably well in the kinematic region of high Q^2 and/or large Bjorken-x. The evaluation of PDFs is currently carried on either experimentally either developing new model parametrizations. An example of PDF parametrization derived from fits on H1 and ZEUS data at HERA is reported in Fig. 1.3.

Although very small values of Bjorken x ($\sim 10^{-5}$), have been already reached in DIS experiments at HERA, it should be noticed that these are typically constrained to small values of the transferred momentum scale Q^2, (about $Q^2 < 1$ GeV$^2/c^2$ for $x < 10^{-4}$) which are only marginally under control in perturbation theory. At LHC energies instead, most of the produced particles is controlled by partons with $x \sim 10^{-3}$, and it is experimentally possible to probe value down to x$\sim 10^{-6}$ with momentum transfers as high as $Q^2 = 10\ GeV^2/c^2$ [3]. In such a way, heavy-flavour measurements at the LHC should be considered as a useful input both for constraining the partonic content of nucleons, and for investigating several physical effects which are expected to strongly influence the nature of parton distribution functions inside nuclei at low Bjorken-x, such as gluon saturation and nuclear shadowing described in the next section.

Given the large momentum transfer that characterizes parton scattering processes for a heavy $q\bar{q}$ pair production, the calculation of its cross-section can be computed in the framework of the perturbative QCD. The large mass of heavy-flavour quarks $M_{q\bar{q}}$ acts as an effective short-distance cut-off on the strong coupling α_s preventing indeed from divergencies in the calculation (that could be generated from collinear gluon radiation and that are suppressed in case of massive quarks due to the so-called dead-cone effects [5]). As a result, the production cross section can be reasonably approximated with a finite number of terms, whose corresponding diagrams at leading order are shown in Fig. 1.4. The two processes expected to be dominant (leading order, LO) for the heavy-quark production in the perturbation theory are $q\bar{q} \rightarrow Q\bar{Q}$ and $gg \rightarrow Q\bar{Q}$. At Next-to-Leading-Order (NLO) additional mechanisms contribute to the total production cross section, as reported in the Figure 1.5. Among them, a clear trend as a function of multiplicity is predicted by models: pair production dominates at low energies, flavour excitation is the main contribution at intermediate energies while gluon splitting becomes the dominant process at very-high energies.

Following the collinear factorization approach, valid under the hypothesis that the probabilities of extracting a parton from the incoming nucleons are independent from the scattering process, the heavy-flavour hadron production in proton-proton collisions is calculated from the convolution of three terms: the parton distribution functions ($f_i(x_1, \mu_F^2)$,

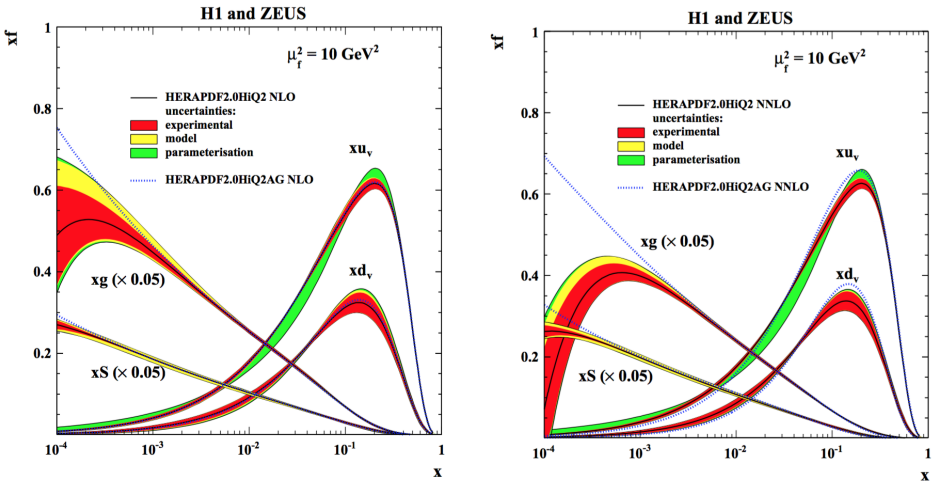

Figure 1.3 – *Left (right): parton distribution functions xu_v, xd_v, $xS = 2x(\bar{U} + \bar{D})$ and xg of HERAPDF2.0NLO (NNLO) at μ_f^2 =10 GeV^2 with Q^2_{min} = 3.5 GeV^2 (top) and of HERAPDF2.0HiQ2 NLO (NNLO) with Q^2_{min} = 10 GeV^2 (bottom). The gluon and sea distributions are scaled down by a factor of 20. The experimental, model and parametrisation uncertainties are shown. The dotted lines represent HERAPDF2.0AG NLO (NNLO) and HERAPDF2.0AG HiQ2 NLO (NNLO). Plots are taken from [4]*

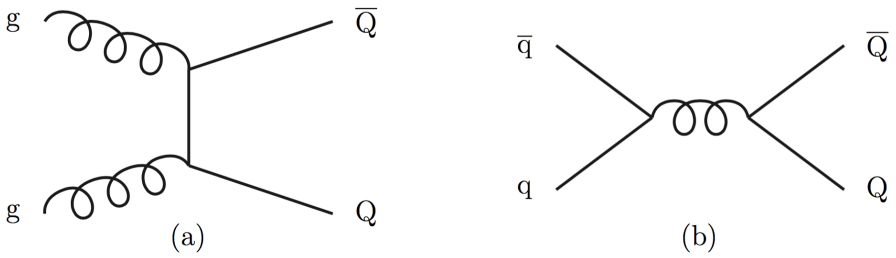

Figure 1.4 – *Leading-order diagrams for heavy-quark production mechanism.*

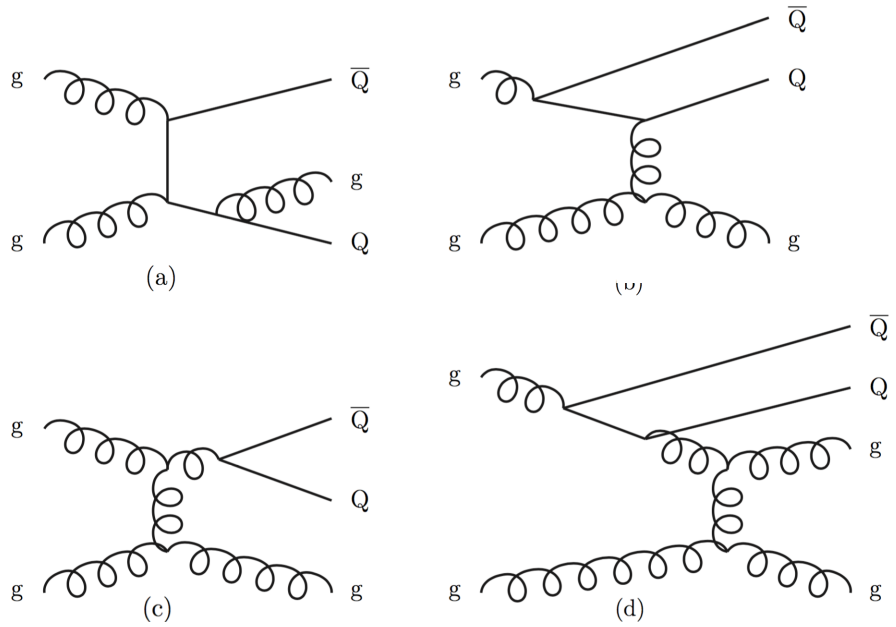

Figure 1.5 *– Examples of pair creation with gluon emission (a), flavour excitation (b), gluon splitting (c) and event classified as gluon splitting but of flavour-excitation character (d).*

$f_j(x_1, \mu_F^2)$), the hard partonic scattering cross section ($d\hat{\sigma}^{i,j\to Q(\bar{Q})\{k\}}$) and the fragmentation function ($D_Q^{H_Q}$). Therefore, the inclusive differential cross section for the production of a heavy-flavour hadron H_Q can be expressed as:

$$\begin{aligned} d\sigma^{pp\to H_Q X}(\sqrt{s}, m_Q, \mu_F^2, \mu_R^2) = & \\ & \sum_{i,j=q,\bar{q},g} f_i(x_1, \mu_F^2) \otimes f_j(x_2, \mu_F^2) \\ & \otimes d\hat{\sigma}^{i,j\to Q(\bar{Q})\{k\}}(\alpha_s(\mu_R^2), \mu_F^2, m_Q, x_1 x_2 s) \\ & \otimes D_Q^{H_Q}(z, \mu_F^2) \end{aligned} \tag{1.2}$$

The partonic cross section $d\hat{\sigma}^{i,j\to Q(\bar{Q})\{k\}}$ is calculated as a perturbative series in the strong coupling α_s, which depends on the energy scale of the process, indicated here as renormalization scale, μ_R. The Parton Distribution Function (PDF) $f_i(x_1, \mu_F^2)$ as already explained, can be interpreted as the probability to find a parton i inside the proton with fraction of momentum $x_1 = p_i/p_{\mathrm{p}}$ (Bjorken x). The fragmentation function $D_Q^{H_Q}(z, \mu_F^2)$ expresses the probability for the heavy quark Q to fragment into a hadron H_Q with a momentum fraction $z = p_{\mathrm{H_Q}}/p_{\mathrm{Q}}$. Either the PDFs and the fragmentation functions in the cross section calculations are evaluated at a given scale called factorization scale μ_F. The dependence of the final cross section from two QCD scale parameters, μ_F and μ_R,

can be viewed as a remnant of the non-perturbative process absorption in the finite order of perturbative calculations. More in detail, the renormalization scale μ_R is introduced by redefining the strong coupling constant at the value of $\alpha_s(R)$ so that the contributions from ultraviolet singularities in virtual loops are canceled, while the factorization scale μ_F can be viewed as the scale which separates the long- and short- distance dynamics calculable in pQCD, and is usually taken at the same order of the momentum transfer of the hard process $\mu_R \sim \mu_F \sim \sqrt{m_Q^2 + p_{\mathrm{T,Q}}^2}$.

The collinear-factorization framework is highly-successful in the description of high-Q^2 processes either in deep-inelastic scatterings experiments, or for jets, weak-gauge bosons, and Higgs production processes at hadron colliders. However, deviations can occur when the underlying assumption of the nucleons as dilute and collinear partonic systems breaks down, i.e. especially in the regimes of very low Bjorken-x and not large Q^2. Other kind of factorization schemes, such as the k_T-factorization or the Color Glass Condensate (CGC), that will be mentioned in this thesis, may prove to be valid alternatives for the study of the physical observables involved in these regimes, as for example the correlations of heavy-flavour quark pairs or the production of charmonia at low p_{T}.

Figure 1.6 reports, as an example, the charm and beauty production cross sections in pp collisions computed with a collinear-factorization approach, by means of PYTHIA program with the CTEQ5L set for the nucleon PDFs [6]. The previously discussed energy-dependence of the different NLO process contributions on the total cross section are also shown.

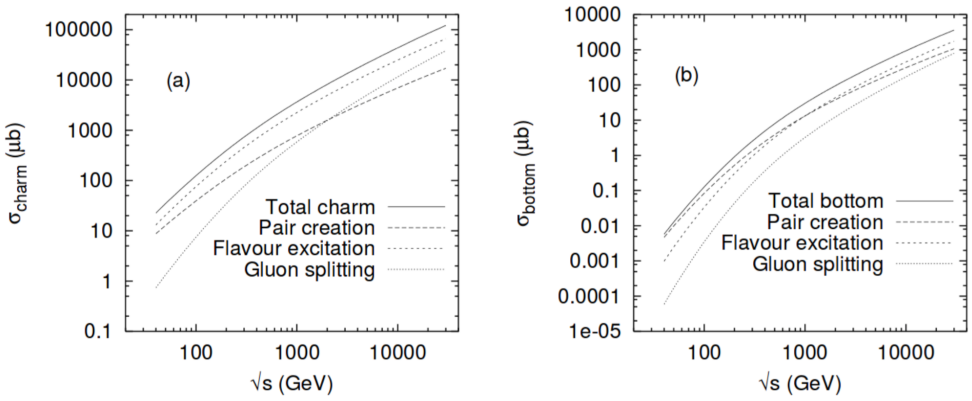

Figure 1.6 *– Energy dependence of the total charm (a) and beauty (b) cross sections in pp collisions computed via PYTHIA calculations described in [6]. The pair creation, flavour excitation and gluon-splitting are also shown separately.*

Analytic calculations that provide a description for inclusive heavy-hadron production or their decay products in pp collisions based on the collinear factorization approach are FONLL [7] [8] and GM-VFNS [9]. The Fixed-Order calculation with Next-to-Leading-

Logarithms (FONLL) consists in the matching of fixed order pQCD cross sections computations, typically at NLO, with a resummation (RS) of the logarithmic terms up to NLL, recovering in such a way the convergence of the series expansion. It provides calculations in the full kinematic range ($p_{\mathrm{T}} \ll m_q$, $p_{\mathrm{T}} \sim m_q$, $p_{\mathrm{T}} \gg m_q$) describing the beauty and charm production at Tevatron, RHIC and LHC. In Figure 1.7 the c and b production FONLL predictions [10] [11] at the LHC with $\sqrt{s} = 7$ TeV as a function of the transverse momentum at mid-rapidity ($|y| < 0.5$) and its comparison with the LHC measurements [12] [13] [14] are reported.

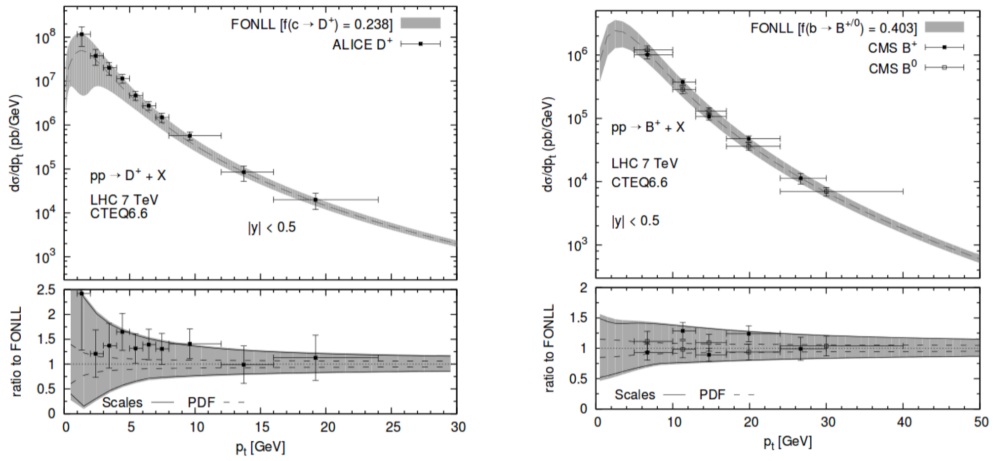

Figure 1.7 *– FONLL calculations and systematic uncertainty band for the p_{T} differential cross-section of D^+ (left) and B^+ (right) meson productions, rescaled to the —y—< 0.5 region. Predictions are compared to CMS [13] [14] and ALICE [12] data.*

Similarly to FONLL, the General-Mass-Variable-Flavour-Number-Scheme (GM-VFNS) [16] convolutes a perturbative cross section $d\sigma$ at the partonic level with a parton distribution function $f(x, Q^2)$ with a non-perturbative fragmentation function $D^{NP}_{q \to H_Q}$. Predictions based on GM-VFNS have been worked out for different colliding systems and proved fairly successful in describing experimental data from HERA, Tevatron as well as LHC. In Figure 1.8 the p_{T} differential cross section of prompt D^0 mesons in pp collisions at $\sqrt{s}$= 5 TeV compared to FONLL (right) and at $\sqrt{s}$= 7 TeV compared to GM-VFNS predictions is shown.

In addition to FONLL and GM-VFNS, that are based on NLO pQCD calculations and provide an accurate description of the inclusively produced heavy-hadrons, general-purpose numerical Monte Carlo (MC) computations represent an essential tool to produce more complete descriptions of the final state, including decay kinematics and detector response. Such generators simulate, as general scheme, the collision event basing on the

partonic cross sections computed at fixed-order with pQCD. The higher-order calculations are then included in an approximate perturbative treatment by means of a parton-shower algorithm. Therefore, the final state is described in full detail, including hard and soft interactions, parton distributions, initial- and final-state parton showers, multiple parton interactions, fragmentation and decay. Example of general purpose event generators are PYTHIA [17] and HERWIG [18]. In these frameworks, the final state hadrons are described up to LO+LL level of accuracy in pQCD. More recent implementation, such as MC@NLO [19], managed to match parton showers to NLO calculations with LL resummation.

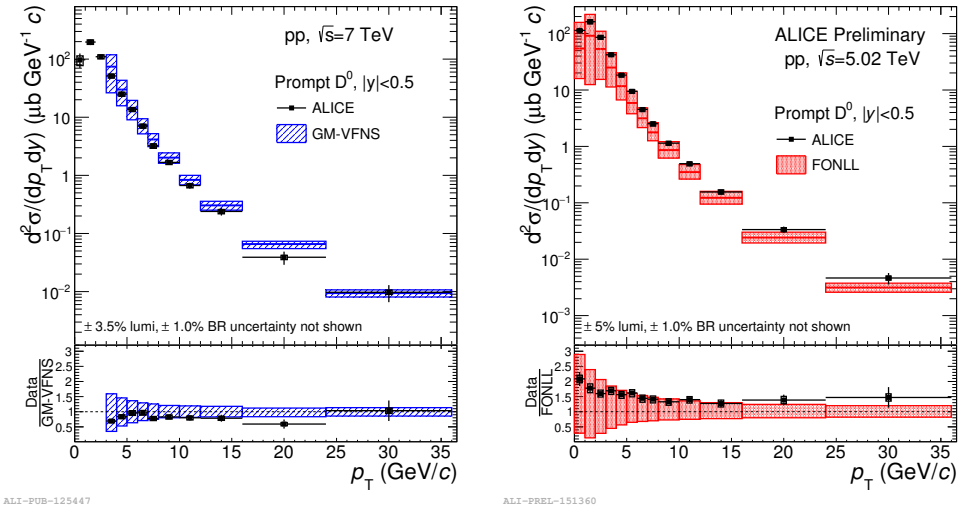

Figure 1.8 *– p_{T}-differential cross section of prompt D^0 mesons with $|y| < 0.5$ in the interval $0 < p_{\mathrm{T}} < 36$ GeV/c, in pp collisions at $\sqrt{s} = 5$ TeV compared with FONLL [7] [8] predictions.*

1.3 Heavy- quark production in p-A collisions

In more complex collision systems (p-A and A-A), a certain number of additional effects can occur in the heavy-quark production with respect to proton-proton system. Indeed, a nucleus-nucleus collision cannot be simply reduced to an incoherent superimposition of nucleon-nucleon collisions not only for the deconfinement effects. For this reason, it is of high interest the study of the "hybrid" collision system, i.e. p-A. Studying the heavy-flavour production in p-A collisions, in fact, allows us to discriminate phenomena that are direct consequence of the presence of deconfined matter in A-A collisions from the ones related to the presence of nuclei in the initial state. These effects, known as Cold-Nuclear Matter (CNM) effects, can involve the partons that undergo the hard-scattering process (initial-state effects) as well as the produced hadrons (final-state effects) and arise

mainly from the modification of the PDFs for nucleons bound in nuclei and multiple soft scatterings of the partons in the nuclei prior to the hard interaction energy loss in cold nuclear matter.
In this section, I will present the main cold-nuclear matter effects: the nuclear modification of the parton distribution and the broadening of the k_T parton distribution.

1.3.1 Nuclear modification of the parton distribution function

The nuclear modification of the parton distribution function can be quantified via the ratio:

$$R_i^A(x, Q^2) = F_{i/A}(x, Q^2)/F_{i/p}(x, Q^2) \tag{1.3}$$

where $F_{i/A}(x, Q^2)$ and $F_{i/p}(x, Q^2)$ are the parton distribution functions in the nucleus and in the proton, respectively. In colliding nuclei, a modification of the effective partonic luminosity with respect to colliding protons is observed. This effect is due to the different dynamics of partons within free protons with respect to those in nucleons, mainly as a consequence of the larger resulting density of partons. These effects depend on Bjorken-x and on the scale of the parton–parton interaction Q^2 (the square of the four-momentum transfer). In collinearly-factorised pQCD calculations the nuclear effects on the parton dynamics are described in terms of nuclear-modified PDFs (indicated as nPDF).

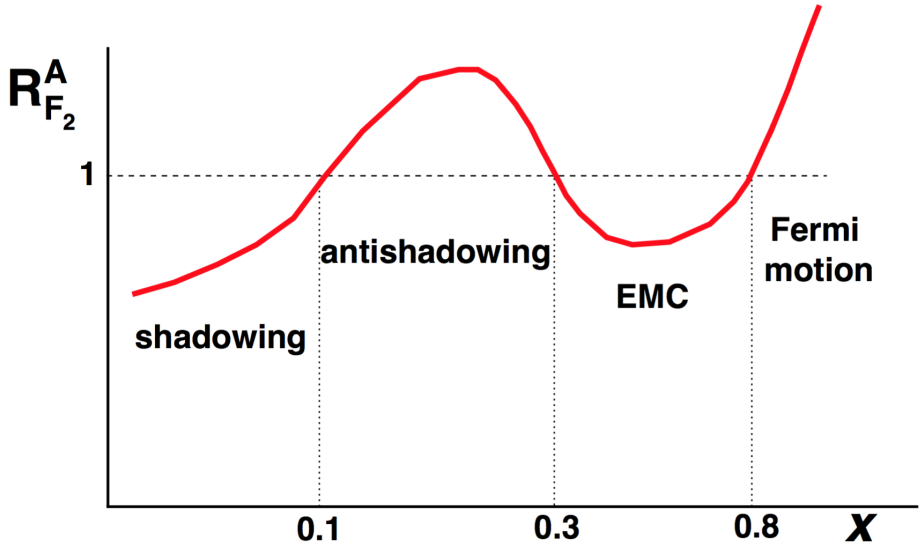

Figure 1.9 – *Different regimes of nuclear modification of the parton distribution function expressed by the ratio between the structure functions in the nucleon and in the nucleus with atomic mass number A. The figure is taken from [21]*

The behaviour of $R_i^A(x, Q^2)$ as a function of x for a given fixed Q^2 is shown schematically

in Fig. 1.9. Four different regions are visible in the trend of $R_i^A(x, Q^2)$, depending on the values of x. Starting from the higher value of x:

- *Fermi motion*: this effect is dominant for $x > 0.8$. It is basically due to the thermal momentum that nucleons have inside the nucleus. Thus the structure function $F_2^A(x)$ of the bound nucleons is the convolution of the structure function of the free nucleon $F_2^N(x/z)$ (where z is the momentum fraction of the nucleons times the atomic number of the nucleus) with the momentum distribution of nucleons $f_N(z)$ inside the nucleus: $F_A^2(x) = \int_x^A dz f_N(z) F_2^N(x/z)$

- *European Muon Collaboration (EMC) effect*: R_i shows a depletion in the region of valence quarks $0.3 < x < 0.8$. There exist several explanations: nuclear binding, pion exchange, a possible change in the nucleon radius,... Experimental observations shows that this effect is almost independent from the squared momentum and increases with the nuclear mass number.

- *Shadowing and anti-shadowing*: a second depletion region is observed in the ratio of parton distribution functions at very low $x < 0.01$ (where the partonic distributions are dominated by sea quarks and gluons) and it is commonly referred to as shadowing region. It is followed by an anti-shadowing region at $0.01 < x < 0.2$ in which the ratio $R_i^A(x, Q^2)$ is above the unity. Several models have been proposed to explain this effect; some of them address its origin in the multiple scattering [42], others do not try to investigate the origin of nuclear shadowing (or of modifications of parton densities in nuclei in general) but they study the Q^2-evolution of nuclear ratios of parton densities through the Dokshitzer-Gribov-Lipatov-Altarelli-Parisi (DGLAP) evolution equations [22] [23]. Parametrizations from different groups such as HKN [24],Sarcevic [25], EKS98 [26], Frankfurt [27], Armesto [28] and new HIJING [153] have been adopted for hadron colliders and are reported in Fig 1.10. In a simplified picture, the depletion can be thought to originate from the superposition and fusion of low-momentum partons (mainly gluons) of different nucleons into a parton with higher momentum fraction, favouring the population of the anti-shadowing region. Thus, the charm and beauty production cross sections measured at the LHC are expected to be reduced by the nuclear shadowing effect in the phase-space region of small-x incoming partons, as a consequence of the heavy suppression of the gluon distribution at very low-x values. For this reason, heavy-flavour hadron measurements at the LHC open the possibility to explore a very low-x region (x $\simeq 10^{-4}$ at central rapidity and x $\simeq 3 \cdot 10^{-6}$ for rapidity y $\simeq$ 4), where the main contribution to heavy quark productions comes from the gluon fusion.

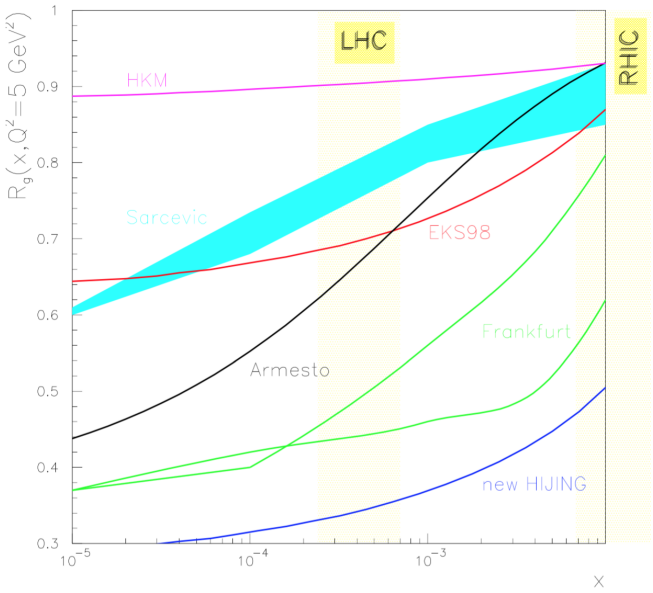

Figure 1.10 *– Ratios of gluon distribution functions for Pb versus x for different parametrizations at $Q^2 = 5\ GeV^2$: HKN [24], Sarcevic [25], EKS98 [26], Frankfurt [27], Armesto [28] and new HIJING [153]. Figure has been taken from [30]*

1.3.2 Broadening of parton k_T distribution

In order to correctly reproduce measurements for heavy-flavour production in pp collisions, it is necessary to introduce in pQCD calculations an intrinsic transverse momentum k_{T} for the interacting partons (it has been estimated to be $k_T \simeq$ 1 GeV/c [71]). In proton-nucleus and nucleus-nucleus collisions, partons can experience multiple interactions within the nucleus leading to a modification of the transverse momentum distribution which results to be broader. This effect is known as Cronin effect and it constitutes another initial state effect that we have to account for. It was first observed in 1987 as an enhancement of high-p_{T} hadron production in p-A collisions in the range of $p_{\mathrm{T}} < 2$ GeV/c [31]. The Cronin effect is caused by multiple scattering of the partons of each nucleus with partons in the other nucleus. As a results of such scatterings, the final average transverse momenta $\langle k_T^2 \rangle$ increases, causing the observed enhancement in the final-state hadron spectra. In particular, for c quarks, the broadening of the k_{T} distribution affects the shape in the p_{T} distribution of the charm hadrons at low-p_{T}, while the total cross section remains unmodified. Furthermore, this effect should reduce the back-to-back azimuthal correlation of the $c\bar{c}$ pair produced from the hard scattering, which reflects in the correlation distribution of the charmed hadrons.
Another proposed explanation for the modifications of the kinematic distributions observed in p-A collisions relies in the energy loss in cold nuclear matter. Even if its

contribution in the initial state is negligible with respect to the final state one in nucleus-nucleus collisions, a radiative energy loss takes place in nuclear matter via soft gluon emission in cold nuclear matter as a fully coherent process over the nuclear medium [32].

1.3.3 Experimental results in p-A collisions

The most relevant cold nuclear matter effect at LHC energies which modifies the nuclear modification of the parton distribution function (especially at low p_{T}) is the nuclear shadowing. As a consequence, hadron yields can be significantly affected by the shadowing, expecially at low-p_{T}. One can define a physical observable, the *nuclear modification factor* that can experimentally quantify this modification.
The nuclear modification factor in p-Pb collisions is defined in the following way:

$$R_{pPb} = \frac{1}{A} \frac{d^2\sigma_{pPb}/dp_{\mathrm{T}}dy}{d^2\sigma_{pp}/dp_{\mathrm{T}}dy} \tag{1.4}$$

where A is the Pb mass number A= 208. As an example, some results gained from the ALICE collaboration on the nuclear modification factor of the charm production in p-Pb collisions at $\sqrt{s_{\mathrm{NN}}}$=5.02 TeV will be reported below. ALICE measured the p_{T} differential nuclear modification factor $R^{\mu^{\pm}}_{pPb}$ at backward (-4.46 < y_{cms} < 2.96 in Pb-going direction) and forward (2.03 < y_{cms} < 3.53 in p-going direction) rapidity regions [33]. The Bjorken-x values of gluons in the Pb nucleus probed by measurements of muons from heavy-flavour hadron decays have been estimated with PYTHIA 8 (Tune 4C) [34] considering Leading Order (pair creation) and Next-to-Leading Order (flavour excitation and gluon splitting) processes. At forward rapidity, they are located in the range from about $5{\cdot}10^{-6}$ to 10^{-2} and the median of the distribution is about 10^{-4}. At backward rapidity, the Bjorken-x values are expected to vary from about 10^{-3} to 10^{-1} and the median is of the order of 10^{-2}.

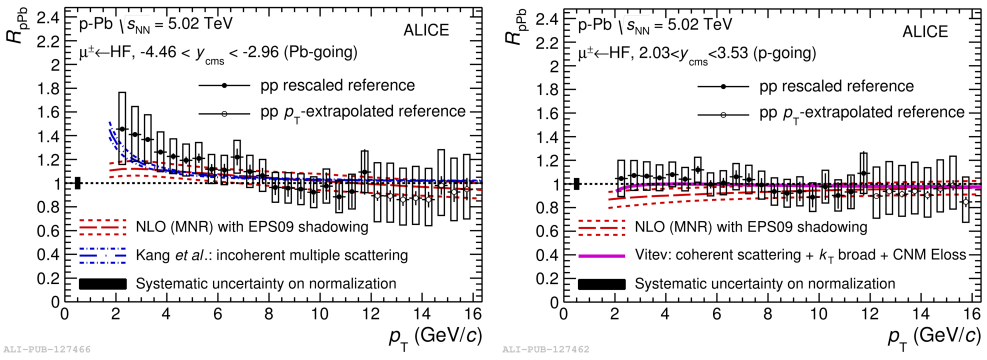

Figure 1.11 *– Nuclear modification factor of muons from heavy-flavour hadron decays as a function of transverse momentum p_{T} for p-Pb collisions at $\sqrt{s_{\mathrm{NN}}}$=5.02 TeV at backward rapidity (on the left) and forward rapidity (on the right) compared with models.*

The $p_{\rm T}$-differential $R_{pPb}^{\mu\leftarrow HF}$ at forward rapidity is compatible with unity within uncertainties over the whole p_T range. At backward rapidity, $R_{pPb}^{\mu\leftarrow HF}$ is larger than unity with a maximum significance of 2.2σ of the combined statistical and systematic uncertainties in the interval 2.5< $p_{\rm T}$ <3.5 GeV/c. At higher $p_{\rm T}$, it is compatible with unity.
The measurements indicate that CNM effects are small and that the strong suppression of the yields of muons from heavy-flavour hadron decays observed in the 10% most central Pb-Pb collisions [35] should result from final-state effects, e.g. the heavy-quark in-medium energy loss, as will be deeply discussed in the next section. The trends measured by ALICE in p–Pb collisions, including the hint for an enhancement at backward rapidity, are similar to those observed by the PHENIX Collaboration at RHIC for muons from heavy-flavour hadron decays measured in d–Au collisions at $\sqrt{s_{\rm NN}}$=200 GeV at forward ($1.4 < y_{cms} < 2.0$) and backward ($-2.0 < y_{cms} < -1.4$) rapidity [36].
As shown in Fig. 1.11, Next-to-Leading Order (NLO) perturbative QCD calculations by Mangano, Nason and Ridolfi (MNR) [37], which make use of the EPS09 [38] parameterization of nuclear PDFs (CTEQ6M [39]) and do not include any final-state effect, describe the measurements in the two rapidity regions reasonably well within experimental and theoretical uncertainties. The data at forward rapidity are also well described by calculations including nuclear shadowing, $k_{\rm T}$ broadening and energy loss in cold nuclear matter [40], which predict R_{pPb} very close to unity over the whole momentum range of the measurement. An agreement with these calculations has been also observed by ALICE for electrons coming from heavy-flavour hadron decays measured at mid-rapidity [41], as shown in Fig. 1.12.
The data are described within the uncertainties by pQCD calculations including initial-state effects (FONLL [7] + EPS09NLO [38] nuclear shadowing parametrisation). The results suggest that initial-state effects are small at high transverse momentum in p–Pb collisions. Predictions by Sharma et al., which include CNM energy loss, nuclear shadowing and coherent multiple scattering at the partonic level well describe the data [40]. Calculations based on incoherent multiple scatterings by Kang et al. predict an enhancement at low $p_{\rm T}$ [42]. The formation of a hydrodynamically expanding medium and consequently flow of charm and beauty quarks are expected to result in an enhancement in the nuclear modification factor R_{pPb} [43]. This possible effect on R_{pPb} has been quantified by extracting a blast wave calculation with parameters estimated from fits to the $p_{\rm T}$ spectra of light-flavour hadrons [44] measured in p–Pb collisions was employed. The model calculation and the data are in agreement. However, the present uncertainties of the measurement do not allow to discriminate among the aforementioned theoretical approaches.
ALICE also measured the R_{pPb} of the Λ_c as well as for prompt D mesons in p-Pb collisions at $\sqrt{s_{\rm NN}}$=5.02 TeV as a function of $p_{\rm T}$ and the results are shown in the left panel of the Fig. 1.13. The nuclear modification factor for the charmed baryon and for the prompt D results to be compatible with the unity.
Predictions for the R_{pPb} for Λ_c baryons from the POWHEG event generator with PYTHIA

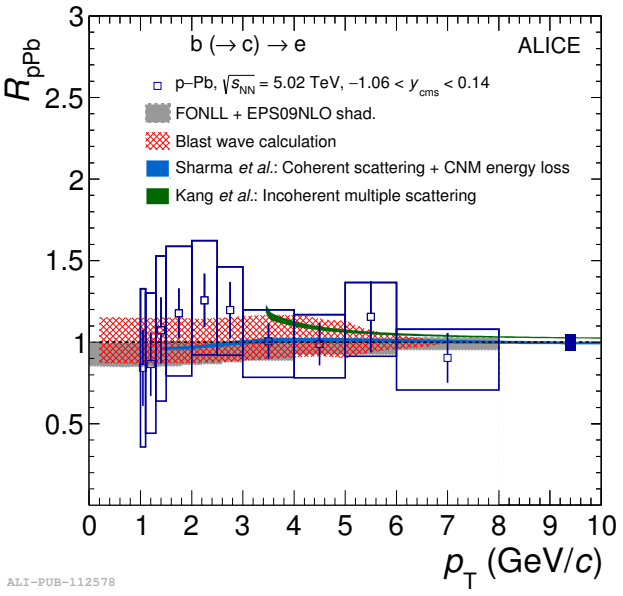

Figure 1.12 – *Nuclear modification factor of electrons from heavy-flavour hadron decays as a function of transverse momentum p_{T} for p-Pb collisions at $\sqrt{s_{\mathrm{NN}}}$=5.02 TeV, compared with theoretical models. The vertical bars represent the statistical uncertainties, and the boxes indicate the systematic uncertainties. The systematic uncertainty from the normalisation, common to all points, is shown as a filled box at high p_{T}.*

parton shower [34] and EPS09NLO parametrisation of nuclear modification of the PDFs [38] are presented in the right panel of Fig. 1.13. In the same panel, the calculations for the charmed-hadron nuclear modification factor from the POWLANG model [47], which assumes that also in p–Pb collisions at LHC energies a hot deconfined medium is formed, is superimposed. The POWLANG model utilises the Langevin approach to compute the transport of heavy quarks through an expanding QGP described by relativistic viscous hydrodynamics, but it does not include any specific mechanism to modify hadronisation, such as coalescence, that could lead to a baryon enhancement. This transport model predicts a deviation of $R_{\rm pPb}$ from unity which is about 20-40% at low and intermediate momentum ($p_T < 5$ GeV/c). The precision achieved with the current measurement does not allow us to distinguish between calculations with and without hot medium effects.

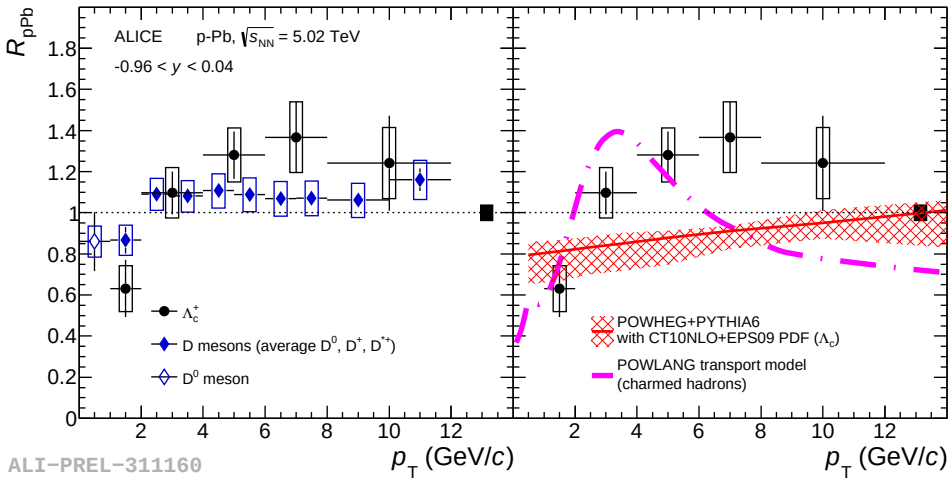

Figure 1.13 *– Nuclear modification factor R_{pPb} of prompt Λ_c baryons in p–Pb collisions at $\sqrt{s_{\rm NN}}$ = 5.02 TeV as a function of $p_{\rm T}$ compared to that of D mesons (average of D^0, D^+ and D^{*+} in the range $1 < p_{\rm T} < 12$ GeV/c, and D^0 in the range $0 < p_T < 1$ GeV/c) (left panel) and to model calculations (right panel). The predictions for the comparison are the Λ_c R_{pPb} from the POWHEG event generator [46] with EPS09NLO parametrisation of the nuclear modification of the PDFs [38] and the charm-hadron R_{pPb} from the POWLANG transport model [47] assuming a QGP is formed in p–Pb collisions*

In ALICE, the nuclear modification factor in p-Pb collisions has been also measured in given centrality classes. It is defined as:

$$Q_{pPb}^{mult} = \frac{(\mathrm{d}^2N/\mathrm{d}p_T\mathrm{d}y)_{pPb}^{mult}}{\langle T_{pPb}\rangle^{mult}(\mathrm{d}^2\sigma_{pp}/\mathrm{d}p_T\mathrm{d}y)} \tag{1.5}$$

where $(\mathrm{d}^2N/\mathrm{d}p_T\mathrm{d}y)_{pPb}^{mult}$ is the yield of a given species in p-Pb collisions for a specific centrality class, and $\langle T_{pPb}\rangle^{mult}$ is the average nuclear overlap function in the same centrality class. In order to describe with better precision the yields, the ratio of the nuclear

modification factor in central to peripheral events, $Q_{\rm CP}$, can be also defined as:

$$Q_{pPb}^{mult} = \frac{(\mathrm{d}^2N/\mathrm{d}p_T\mathrm{d}y)_{pPb}^{central}/\langle T_{pPb}\rangle^{central}}{(\mathrm{d}^2N/\mathrm{d}p_T\mathrm{d}y)_{pPb}^{peripheral}/\langle T_{pPb}\rangle^{peripheral}} \tag{1.6}$$

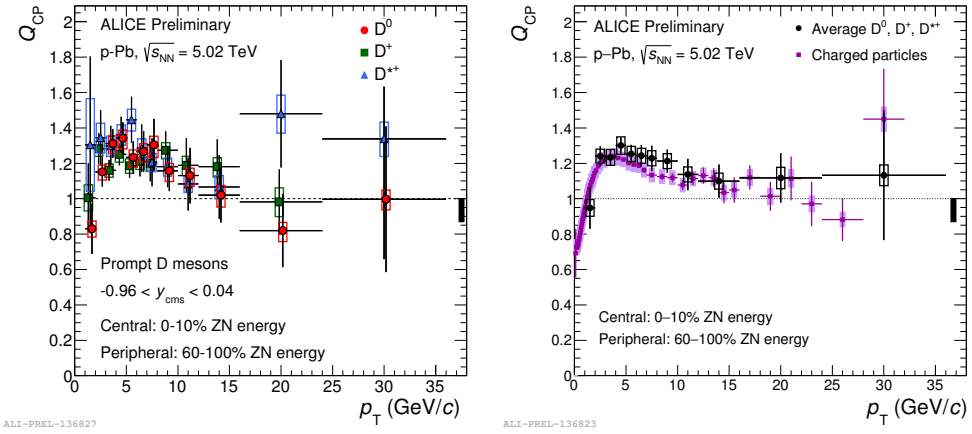

Figure 1.14 *– Left: D^0-D^+ and D^{*+} nuclear modification factor evaluated in 0-10% and 60-100% in 1< $p_{\rm T}$ < 36 GeV/C Right: D-meson (black) and charged-particle (magenta) central to-peripheral nuclear modification factor.*

The Q_{CP} of D mesons in the 0-10% as central class and 60-100% as peripheral class was measured by ALICE, as shown in the Fig. 1.14. An increasing trend is observed for both the measurements in the interval 1-5 GeV/c, up to values of about 1.3 and then tends to decrease in the interval 7-16 GeV/c. The average value of the D-meson Q_{CP} in the interval $3 < p_T < 8$ GeV/c is larger than unity by 1.5 standard deviations of the combined statistical and systematic uncertainty. It is an open question whether the observed bump of Q_{CP}, whose magnitude is similar for D mesons and charged particles, is related to initial state effects or to collectivity effects in the final state.

1.4 Heavy quark production in A–A collisions

In heavy-ion collisions, lattice QCD calculations predicts the formation of a peculiar state-of-matter, known as Quark-Gluon-Plasma. Its properties can be studied through several observables directly accessible through measurements on the particles produced in the collisions. The comparison of heavy ion measurements with pp collsion results at similar energy is mandatory to quantify and characterize the effects of the presence of a QGP on heavy hadrons. The analysis in p–Pb collisions allows us to disentagle the effects of the QGP formation from the ones due to the presence of many nucleons in addition to the interacting one (initial-state effects), which can modify the properties of the partons before the hard scattering occurs. Before discussing how heavy flavour measurements

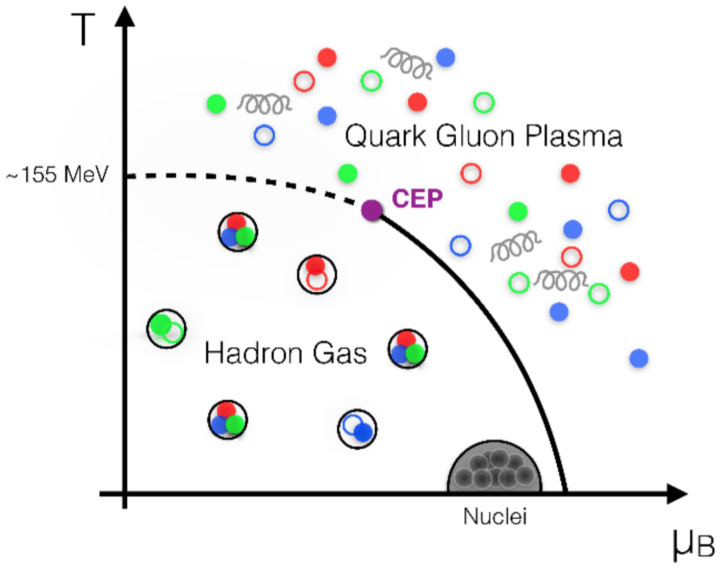

Figure 1.15 *– Phase diagram of QCD matter as a function of the temperature T and of the baryo-chemical potential μ_B.*

can be exploited to investigate the properties of the QGP, I will briefly describe the QCD phase diagram, the predicted phase transition of ordinary nuclear matter to the Quark-Gluon Plasma, and how this state can be produced in heavy ion collisions.

1.4.1 The Quark Gluon Plasma

The QCD phase diagram

From Quantum Chromodynamics (QCD) calculations on the lattice and thermodynamical considerations, it is expected that the features of strongly interacting matter can dramatically differ from the hadronic state, where quarks are bound into hadrons, and that different states can be formed if the values of the temperature T and of the baryo-chemical potential μ_B[1] are modified. Fig. 1.15 schematically reports the phase diagram of QCD matter as a function of T and μ_B along with the main transitions among the different states. At low temperatures and values of baryochemical potential of about $\mu_B \sim m_P \sim 938$ MeV, the strongly-interacting system is in its standard conditions, with quarks and gluons confined into hadrons and nuclear matter in the form of bound nuclei. By increasing the temperature of the system or varying its baryo-chemical potential

[1]The baryo-chemical potential μ_B can be defined as the minimum energy necessary to increase by one unity the total baryonic number (N_B= baryons - antibaryons) $\mu_B = \delta E/\delta B$, thus being directly related to the baryonic density.

different paths can be followed on the diagram, which correspond to different transformations of the system's thermodynamical state. If the energy density is increased by increasing the system's density and/or baryo-chemical potential, nucleons start interacting with each other producing excitations, pions and other hadrons, and form a hadron resonance gas (HRG). From this state, if the temperature is increased even further, the transition to a deconfined Quark-Gluon Plasma state is reached when the critical line at a corresponding energy density of about $\epsilon_c \sim$1 GeV/fm^3 is crossed. If this crossing is reached at small μ_B values, lattice QCD calculations predict the passage to the deconfined state to occur not as a proper phase transition but rather as a smooth cross-over, at approximately $T_c \sim$ 145 MeV. At ultra-high baryonic densities, a transition is expected to occur similar to the process of formation of neutron stars, where the gravitational field of the collapsing star produces a huge increase of the baryonic density at very low temperatures. Such a state is commonly known as CFL (Color-Flavour-Locked) and in this conditions the quarks of all the three colours and of all the three light flavours (u, d, s) form zero-momentum spinless Cooper pairs [48].
At extremely high values of temperature and energy density a transition to the Quark-Gluon Plasma is reached. In this state, quarks and gluons although still interacting, they are no longer bound into hadrons, but they become "deconfined" in a sort of plasma, in analogy to what happens to electrons and ions brought to very high temperatures. The degrees of freedom of the system become the flavour, spin, colour and charge states of quarks and gluons. These were the conditions of the primordial universe in the first micro-seconds after the Big Bang. In order to reach a complete understanding of the evolution of this state of matter, it is necessary to combine macroscopic initial conditions of the system temperature and energy density with the thermodynamics laws of the QCD. The understanding of the phase transition is still matter of study and it will allow us to understand whether the QCD thermodynamics rules the fireball creation and evolution in the heavy-ion collisions and whether the final products (hadrons) keep trace of these thermodynamics processes [49], [50]. The experimental research of this phase of matter started in the second half of the '80s, with the first fixed target experiments at the Super Proton Synchrotron (SPS) at CERN and at the Alternating Gradient Synchrotron (AGS) at Brookhaven National Laboratory (BNL). For the first time scientists tried to reproduce in the laboratory such a state of matter, initially through acceleration of light nuclei (Si and S respectively), then moving to heavier nuclei (Pb and Au). The Relativistic Heavy-Ion Collider (RHIC) at BNL, after the SPS, studied the creation of the QCD matter through Au-Au collisions at higher collision energy $\sqrt{s_{\mathrm{NN}}}$=200 GeV per nucleon-nucleon collision, that was one order of magnitude above the energy reached at the SPS. Currently, also the LHC is conducting this kind of experiments with the highest achievable center-of-mass energy of $\sqrt{s_{\mathrm{NN}}}$=5.02 TeV per nucleon-nucleon collision.

The QGP phase transition

Phase transitions between different states are generally characterized by breaking or restoring symmetries in the Lagrangian describing the system. In the case of QCD, strongly interacting systems exhibits global symmetries only in the limit situations of infinite or vanishing quark masses and undergoes explicitly break for finite mass values. Indeed, for massless quarks, the QCD Lagrangian shows an important symmetry: the *chiral symmetry*, associated to the $SU(N_f)_L \times SU(N_f)_R$ group (considering a N_f-flavoured system). Such symmetry exhibits an invariance under helicity transformations of the quark fields[2]. As a consequence of the chiral symmetry, the chiral condensate $\langle\psi\bar{\psi}\rangle$ expressed as:

$$\langle\bar{\psi}\psi\rangle = \langle\bar{\psi}_L\psi_R + \bar{\psi}_R\psi_L\rangle \tag{1.7}$$

shoud be zero for the ground state. Instead, its value is found to be about 235 MeV and it is confirmed by the existence of pions, which are therefore considered the pseudo-Goldstone bosons of this symmetry. The breakdown of the symmetry even in the QCD vacuum is interpreted as the origin of the dominant part of the light quark masses (*constituent mass*), which has to be summed to the mass value generated by the coupling of the quarks with Higgs boson (*bare mass*). The symmetry restoration or its breakdown is often related to the crossing of a critical temperature. The best non-perturbative approach to study the properties of the phase transition and quantify the critical values of T and μ_B is given by lattice QCD (lQCD) [51]. In the framework of the lattice QCD, it is predicted that the value of the chiral condensate $\langle\psi\bar{\psi}\rangle$ vanishes (as the quark constituent masses) in coincidence with the critical temperature T_c of the QGP phase transition, thus restoring the chiral simmetry in the QGP phase.
A typical behaviour of the chiral condensate parameter from recent lQCD calculations is reported in the red curve of the Fig. 1.16. The decrease of the chiral condensate parameter mean that at the critical temperature for QGP formation, a transition towards a chirally symmetric state is achieved.
Another important feature that characterizes the phase transition to the QGP is the deconfinement of quarks and gluons as a consequence of the modification of the $q\bar{q}$ bounding potential. This aspect can be explained in terms of the *Debye screening*, an effect already observed for electromagnetism and occurring when charged particles are placed inside a charged medium. In this situation, the presence of the medium reduces the strength of the mutual interaction between two charges by an exponential factor e^{-r/λ_D}, where λ_D is called *Debye length* and represents the distance over which the interaction among two charges becomes screened by the medium. In a simplified picture, above the critical temperature for the QGP transition, a large number of $q\bar{q}$ pairs is created inside the medium. These pairs screen the colour charge of the initial quark pair and reduce the

[2]For chiral symmetry we refer to the property for which two eigenstates of the chirality operator $\psi_{L,R} = \frac{1}{2}(1 \mp \gamma_5)\psi$ remain invariant under global transformations: $\psi_{L,R} = e^{-i\lambda^j\theta^j_{L,R}}\psi_{L,R}$.

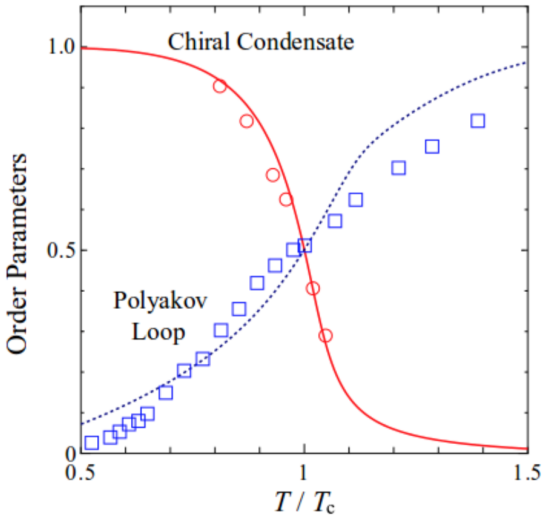

Figure 1.16 *– The red curve shows the temperature dependence of the chiral condensate* $\langle\psi\bar{\psi}\rangle$*, representing the order parameter for the chiral symmetry of a QCD system, as resulting from lQCD calculations [51]. An inflection point in coincidence of the cross-over temperature Tc = 145 MeV of QGP phase transition is shown. Figure from [15].*

bounding potential, which can be expressed as:

$$V_{q\bar{q}}(r) = -\frac{4}{3}\frac{\alpha_s}{r} \cdot e^{-r/\lambda_D}. \tag{1.8}$$

The long-range component of the potential which caused the confinement disappears, while the Coulombian component is strongly reduced. The quark cannot feel anymore the presence of the other quark at distances greater than few λ_D. Hence, hadronic bound states are no longer formed and the whole medium acts like a strongly interacting medium composed of deconfined quarks and gluons.

Going more in detail with the theoretical predictions on the QGP phase transition, the lattice QCD approach [51] describes the euclidean time-space in terms of a discretized lattice in which quarks occupy the lattice points (where the QCD Lagrangian can be numerically solved) while gauge fields occupy lattice links. In principle, the main uncertainty derives from the assumption on the finite spacing between consecutive points. In the framework of lattice QCD calculations, the results depend on the number of flavours and on the values of quark masses involved in the calculations and t. For massless quarks and $\mu_B = 0$, the lQCD calculations predict a phase transition at a critical temperature of T $\sim$ 155 MeV. To have a quantitative idea, this temperature is hundred thousand times the temperature of the Sun's core. The corresponding crical energy density is ϵ= 0.7 $\pm$ 0.3 $(GeV/fm)^3$; above the critical temperature, the energy density grows proportionally to T^4 (as ruled by Stefan-Boltzmann law) [52].

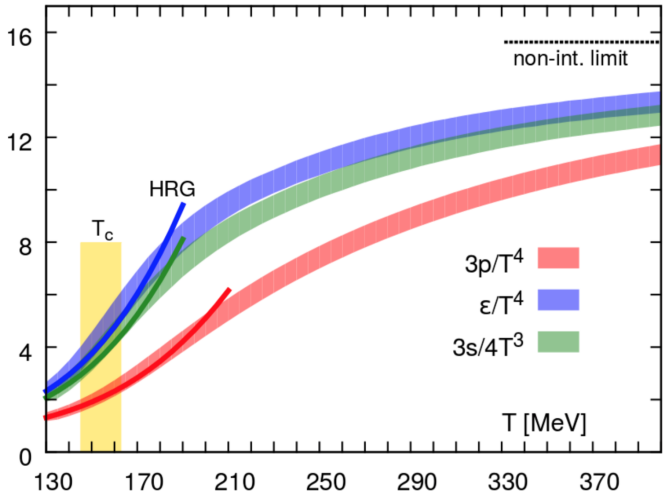

Figure 1.17 – *Temperature dependence of the energy density ϵ, pressure p and entropy density s, properly normalized by powers of temperature T, as resulting from recent lattice QCD calculations [53]. Solid lines at low temperatures correspond to results obtained from hadron resonance gas (HRG) model calculations.*

A remarkable deviation from the limit of a Stefan-Boltzmann ideal gas is observed, suggesting that strong interactions are still present in the deconfined phase. Furthermore, the increase above the critical temperature is not steep, as would be in the case of a first-order phase transition, but smooth, indicating that the phase transition at $\mu_B \sim 0$ occurs as continuous cross-over. The trend of the thermodynamic coordinates in the vicinity of the critical temperature still appears to be fairly well described by a Hadron Resonance Gas (HRG) model, but clear deviations set in at higher temperatures above the transition, indicating that the system can no longer be described in terms of hadronic degrees of freedom. This last point is evident if one recalls that, in the limit of an ideal Stefan-Boltzmann gas, the energy density ϵ of a system is related to the temperature through the number of elementary degrees of freedom n_{dof} as:

$$\epsilon = n_{dof} \frac{\pi^2}{30} T^4 \tag{1.9}$$

The increase in energy density at the cross-over temperature is hence a consequence of the increased number of effective degrees of freedom, from that of a typical pion gas, to that of a de-confined system in which the quark and gluon degrees of freedom become available, and start contributing to the system thermodynamics. The assumption of massive quarks modifies the expected value of the critical temperature as well as the order of the transition, as can be observed in Fig. 1.17.

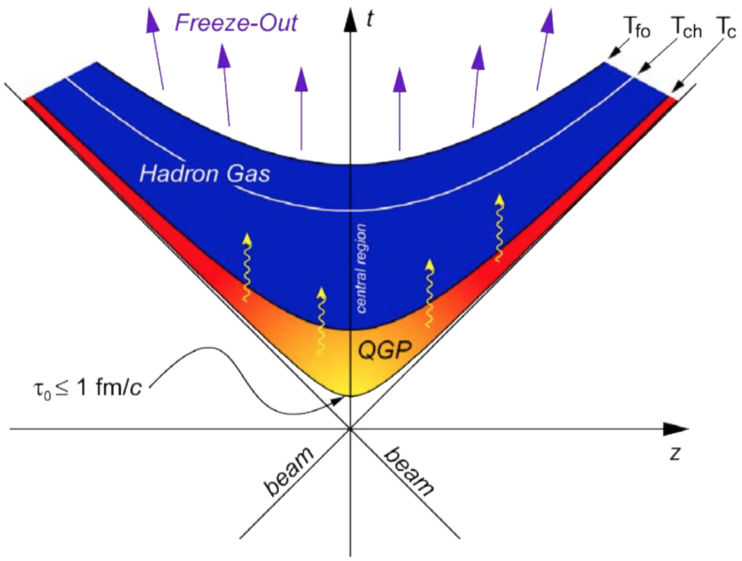

Figure 1.18 *– Evolution of a heavy ion collision between two nuclei at relativistic energies in the Minkowski plane (horizontal axis represents the spatial axis, vertical axis shows the time, starting from the instant of the collision). The QGP is produced in the collision and undergoes different stages, delimited by solid-line hyperbolas in the diagram.*

From the QGP to the hadronization

From the lattice QCD we learnt that if the energy density of the medium created in the early stages of the heavy-ion collisions is higher than a critical value, it allows for the formation of the Quark Gluon Plasma. The evolution of such a system created in the laboratory undergoes different phases:

- **Pre-equilibrium phase**: hard scatterings produce a large number of partons; they interact among each other leading the fireball to reach a local thermal equilibrium after a time of 0.6-1 fm/c. This is the stage at which hard particles (i.e. with either large masses or large transverse momenta) are produced. Their creation involves large transverse momentum.
- **QGP phase**: with high-energy collisions, if the temperature inside the fireball exceeds the critical temperature T_c, the system is in a deconfined phase with partonic degrees of freedom. Hence, the system is characterized by a strong thermal pressure which is not equilibrated by the surrounding vacuum, and therefore leads to a collective expansion of the fireball well described by several hydrodynamic-based models. As a consequence of the expansion of the system, the fireball cools down and its energy density decreases until it approaches the critical energy $\epsilon_c \sim 1$ GeV/c for confinement. During the transition toward hadronic matter, the entropy

density follows a steep decrease over a small time interval, during which the fireball keeps expanding until all partons are eventually combined into hadrons. The collision energy and centrality (defined in the Section 3.5) define the time τ_{had} at which hadronization occurs and hence, the life-time of the QGP phase.

- **Hadronisation phase**: this phase is typically further subdivided in two different steps. Immediately after the hadronization of the QCD medium, the hadrons still keep rescattering one another, both elastically and inelastically, for a certain amount of time, continuing the expansion. Inelastic processes can change the nature of the interacting hadrons and hence contribute modifying their relative abundances. However, the corresponding inelastic cross sections are small compared to the total interaction cross section, and the rate of inelastic interactions eventually stops at the time at which it cannot keep up with the expansion of the hadron gas. From this time τ_{ch}, which is identified as **chemical freeze-out** the chemical composition of the hadron spectra is fixed to that of the final detectable particles, apart from unstable resonance decays. The composition of the hadron spectra at this stage follows an approximately exponential trend as a function of the mass, which can be well explained in terms of thermal/statistical models [54] as shown in Fig. 1.19. The slope of the hadron mass distribution is related the temperature at the chemical freeze-out T_{ch}, which is still approximately close to the critical temperature T_c, and therefore provides a snapshot of the dynamical evolution of the collision near the phase boundary.

Heavy quarks as probes of the QGP

Heavy flavour quarks are unique probes of the Quark-Gluon Plasma (QGP) created in Pb-Pb collisions. Due to their large mass, the production of $c\bar{c}$ and $b\bar{b}$ pairs takes place in a very short time scale, of about $t_{c\bar{c}} = 2m_c^{-1} \simeq 0.1$ fm/c for charm and even less for beauty. Such a time interval is much lower compared with the peculiar time in which the QGP formation occurs ($\tau \sim$1fm/c) and, for this reason, allow the heavy quarks to experience all the stages of the QGP evolution and, interacting with the medium, they can witness all effects induced by it. One of the main medium-induced effect is, for example, the parton energy loss via collisions among quarks and gluon radiation, where a colour charge and a quark mass dependence is predicted from theoretical models [55] [59]. Perturbative QCD calculations can be used to predict the expected production cross section in pp collisions (since $m_{c,b} \ll \Lambda_{QCD}$) and to rescale measurements at different energies and collision systems. pQCD predicts a cross section for charm production 20 times larger than for beauty at LHC energies. Furthermore, charmed hadrons are also better detectable in their inclusive decay channels with respect to beauty hadrons.

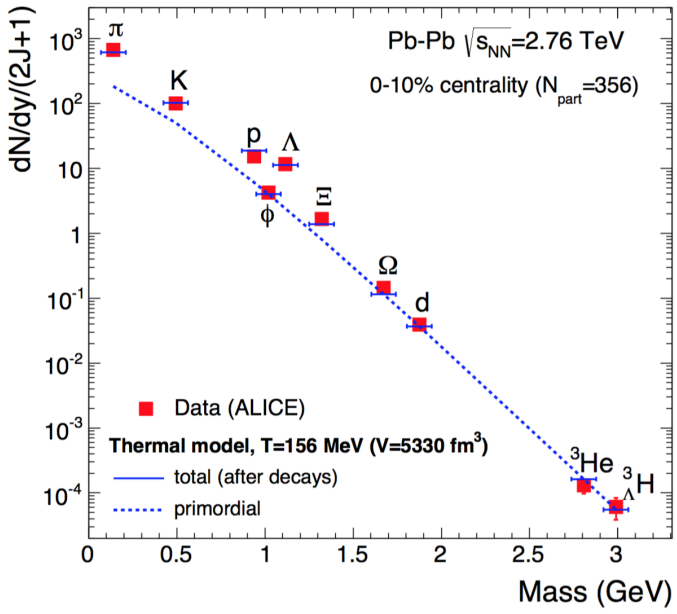

Figure 1.19 – *Measured hadron abundances divided by the spin degeneracy factor (2J + 1) in comparison with thermal model calculations in central Pb–Pb collisions at the LHC. The model plots the "total" yields, including all contributions from high-mass resonances (for the Λ hyperon, the contribution from the electromagnetic decay $\Sigma_0 \rightarrow \Lambda\gamma$, which cannot be resolved experimentally, is also included), and the yields prior to decays. The plot has been taken from [54].*

1.4.2 Heavy quark production cross section in A-A collisions

The production of heavy quarks in nucleus-nucleus collisions, as already explained in the introduction of this section, is affected not only by the presence of two nuclei before the collision (which modifies the parton distribution function into a nuclear distribution function) but also by the presence of the QGP after it. If we neglect for the latter effects, we can consider the nucleus-nucleus collision as a superimposition of a certain number of independent pp collisions (*binary scaling*). Within this simplified picture, the cross section for hard processes can be obtained assuming that it scales linearly (in the framework of the Glauber model [61]) with the number of inelastic nucleon-nucleon collisions which take place in the nuclei scattering. In this context, the inelastic cross section between two nuclei, containing respectively A and B nucleons, depends on the centrality, a quantity which reflects the impact parameter[3] of the collision. For example, to compute the inelastic cross section for the most central events in Pb–Pb collisions (5% or 10%), it is necessary to take only those collisions with impact parameter b inside the cut values b_l and b_h: $b_l < b < b_h$, with $b_l = 0$ and b_h depending on the centrality class chosen (b_h=3.5 fm for 5% case and $b_h = 5$ fm for the 10% case) [62]:

$$\sigma_{AB}^{inel}(b_l, b_h) = \int_{b_l}^{b_h} \mathrm{d}b \frac{\mathrm{d}\sigma_{AB}^{inel}}{\mathrm{d}b} = 2\pi \int_{b_l}^{b_h} b\,\mathrm{d}b \left\{1 - [1 - \sigma_{pp} T_{AB}]^{AB}\right\}$$

where σ_{pp} is the nucleon-nucleon inelastic cross section and T_{AB} is the overlapping function, defined as a function of the nuclear thickness functions T_A and T_B:

$$T_{AB} = \int \mathrm{d}^2 s T_A(\vec{s}) T_B(\vec{s} - \vec{b}) \tag{1.10}$$

where the meaning of the vectors $\vec{s}$ and $\vec{b}$ can be understood from the Fig. 1.20
The cross section for a hard process in a nucleus-nucleus collision can be obtained replacing the nucleon-nucleon inelastic cross section σ_{pp}^{inel} by the cross section for a given hard process σ_{pp}^{hard} (like the heavy-quark production). If there is no selection on the centrality, i.e. b_l=0 and $b_h = \infty$, the total cross section can be simply calculated as:

$$\sigma_{AB}^{hard} = A \cdot B \cdot \sigma_{PP}^{hard} \tag{1.11}$$

Such calculations hold only in the hypothesis that there is no effect which can modify the binary scaling. Actually, either the presence of nuclei either the formation of the QGP affect the value of the final cross sections for hard processes. As discussed in the section 1.3, in p-A collisions, the deviation of the heavy-quark production from the binary scaling derives from the presence of nuclei and it is usually referred to as "initial state effect" (in particular, the nuclear shadowing and the k_T distribution of the parton are the most relevant, as discussed in the previous section). While in nucleus-nucleus collisions, the presence of the QCD medium can modify the final kinematical variables of

[3]The impact parameter between two nuclei is defined as the length of the vector $\vec{b}$ conjugating the two colliding nuclei in the plane perpendicular to the beam axis, as shown in Fig. 1.20

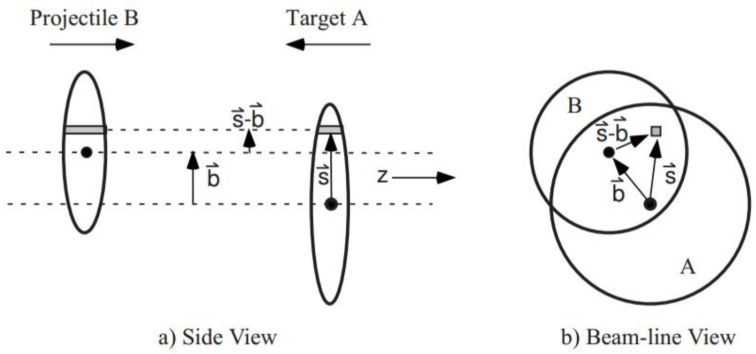

Figure 1.20 *– Geometry of a nucleus-nucleus collision, with transverse (a) and longitudinal (b) views.*

the heavy quarks produced in the collision, depending on the QGP properties. For this reason, we use to refer to these effects as "final state effects". They are a source of useful informations to study the medium itself. In the following paragraphs the most relevant final state effect that involve heavy quarks (parton energy loss in the medium and dead cone effect, thermal production of $c\bar{c}$ pairs, charmonium suppression and regeneration) will be discussed.

Parton energy loss in the medium

High-momentum partons traversing the QGP are expected to lose energy interacting with the medium constituents [56]. The magnitude of the energy lost in the medium is strictly related to the properties of the fireball, i.e. the transport coefficients encode the momentum transfers with the medium while the mean free path depends on the medium density ρ and on the cross section σ of the interaction between medium and partons. The energy loss takes place by two main mechanisms: elastic and inelastic interactions with the medium constituents and they are responsible for the collisional and radiative energy loss, respectively. One of the two contributions can dominate the other, depending on the in-medium path length and on the energy of the travelling parton. The total energy lost in the collisions increases linearly with the in-medium path-length and, according to some models, has only a logarithmical dependence on the initial parton energy [60].
In heavy ion collisions, at low energies collisional and radiative energy loss contribute almost equally to the energy loss, while the collisional contribution is expected to become negligible for higher parton energies. The theoretical approaches developed for the description of the heavy-quark energy loss in general can differ in the treatment of the interactions occurring between the heavy quark and the constituents of the QGP. As typical feature, it depends on two main observables: the *mean free path* $\lambda = 1/(\rho\sigma)$ and the *Debye radius* r_{D} (related to the colour-density and to the temperature T of the

medium). According to BDMPS [57] [58], the partons produced in the hard scattering, while traversing the medium, undergo a series of collisions in a Brownian-like motion, typically described by the Boltzmann equation, with mean free path decreasing with increasing medium density. This multiple scattering process allow the gluons to gain transverse momentum with respect to parton direction and can lead to a *gluonstrahlung* process, in analogy to the QED *bremstrahlung*, describing the emission of photons from the deceleration of electrically-charged particles in a medium. As in QED, the characteristic energy of the radiation ω_c, which determines the overall scale of the energy loss, is defined as:

$$\omega_c = \hat{q}L^2/2 \tag{1.12}$$

It depends on the path length inside the medium L and on the transport coefficient $\hat{q}$, which represents the average squared transverse momentum $\langle k_T^2 \rangle$ transferred to the emitted gluon over the free mean path of the traversing particle: $\hat{q} = \langle k_T^2 \rangle / \lambda$. For a static medium, the gluonstrahlung spectrum of the radiated gluons can be expressed in the form:

$$\omega \frac{\mathrm{d}I_{rad}}{\mathrm{d}\omega} \simeq \frac{2\alpha_s C_R}{\pi} \sqrt{\frac{\omega_c}{2\omega}} \tag{1.13}$$

for energies $\omega \ll \omega_c$. The average energy loss of the parton can be computed by integrating the previous equation up to ω_c:

$$\langle \Delta E_{rad} \rangle = \int_0^{\omega_c} \omega \frac{\mathrm{d}I_{rad}}{\mathrm{d}\omega} \propto \alpha_s C_R \hat{q} L^2 \tag{1.14}$$

Thus, the average energy loss results to be proportional to the strong coupling constant α_s, to the square of the path length L and to the Casimir factor C_R. and it does not explicitly depend on the initial energy (this is a peculiarity of the BDMPS model), but an intrinsic dependence comes from the impossibility to overcome its initial value: $\langle \Delta E \rangle \leq E$. The proportionality of the average radiated energy on the square of the path-length L^2 shed light on an important feature that differentiate the QCD with respect to the QED, where this dependence is linear ($\langle \Delta E_{brem} \rangle \propto L$). Indeed, such behavior derives from the non-Abelian nature of the QCD theory and it implies that the radiated gluons can also release energy by emitting other gluons. Finally, the dependence on the Casimir factor, which assumes the value of 3 in the case of gluon-gluon coupling and of 4/3 in the case of quark-gluon couplings, allow to conclude that gluons release an higher amount of energy compared to quarks. A comparison between radiative and collisional energy loss as a function of the initial energy of the quark, from different pQCD predictions for charm (left) and beauty (right) quarks in central Pb–Pb collisions at the LHC, has been reported to this purpose in Fig. 1.21 [63].
Here, elastic interactions dominate the low-p_{T} region, up to $\sim$ 6 GeV/c for charm and $\sim$16 GeV/c for beauty quarks. At higher p_{T}, the contribution from radiative processe become the dominant one and must be considered when performing calculations at LHC energies.

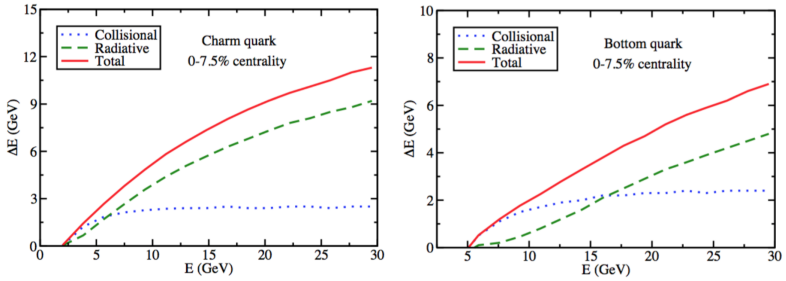

Figure 1.21 *– Comparison of radiative and collisional energy losses for charm (left) and for bottom (right) quarks as a function of the initial energy of the quark from theoretical predictions [63] in Pb–Pb collisions at* $\sqrt{s_{\rm NN}}$*=5.02 TeV.*

Another effect contributes to further suppress the gluon emission from heavy quarks, thus decreasing the medium-induced radiation with respect to lighter quarks and gluons. Indeed, the average gluon radiation in the vacuum is expected to depend on the mass and colour charge of the traversing parton, with a hierarchy: $\langle \Delta E_{heavyQ} \rangle < \langle \Delta E_{lightQ} \rangle < \langle \Delta E_{gluon} \rangle$. Heavy quarks travelling in the vacuum with moderate energy (m/E $\simeq$ 1) have a velocity significantly smaller than the light velocity c: $\beta = \sqrt{1-(m/E)^2} \ll 1$. Therefore, the emitted gluon radiation inside a front cone with opening angle $\Theta = m_q/E$ is suppressed due to destructive interference processes. Such a phenomenon is known as *dead cone effect* [64]. The higher the mass of the parton, the larger the angular opening of the "dead cone", and consequently the smaller the energy loss by gluonstrahlung. This effect is expected to hold also for partons travelling in the medium, with a suppression of the gluon radiation from heavy quarks with respect to light quarks. Energy-loss processes can be experimentally investigated by comparing the measurements of the nuclear modification factor R_{AA} of different high $p_{\rm T}$ particles.

In-medium charmonium suppression and regeneration

The suppression of charmonium states when traversing the medium was proposed as one of the most powerful signatures of the QGP formation. The first J/ψ suppression in heavy ion collisions had place at the SPS, by the NA38 and NA50 experiments [65]. Theoretical calculations explains this phenomenon as a consequence of the Debye screening of the colour force in a deconfined medium, due to the presence of free color charges, which becomes stronger as the temperature increases. When the screening radius becomes lower than the binding radius of the quark-antiquark system, the dissolution of the charmonium state occurs. In Fig. 1.22 a schematic cartoon of the quarkonium suppression is shown. The highest charmonium excitations, characterized by a lower binding energy and thus a larger binding radius, should dissolve for temperatures even lower than the critical temperature T_c at which the QGP phase transition occurs. While the more

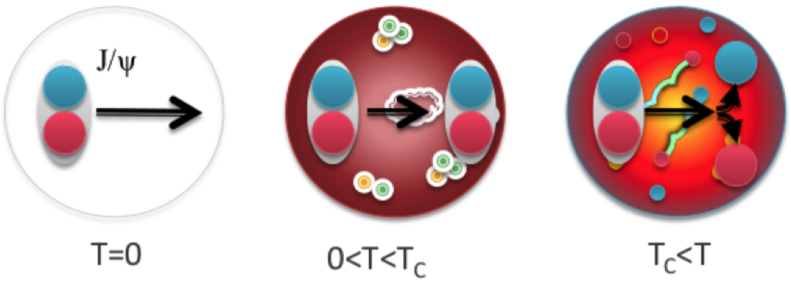

Figure 1.22 *– Cartoon showing quarkonium (from left to right) at vacuum temperature, remaining intact in a "cold" hadronic environment below the critical temperature T_c of the QGP phase transition, and dissociating in "hot" deconfined matter above T_c.*

strongly bound states as the Υ(1S) show less suppression compared to more weakly bound states, as sketched in the top panel of the Fig. 1.23. Increasing the system temperature, also the most bound bottomonium states should melt. In the bottom panel of the Fig. 1.23 the sequential suppression pattern for J/ψ, with thresholds predicted (in terms of temperature or energy density) by finite temperature QCD.
At the LHC energies, where the production cross section of $c\bar{c}$ is higher with respect to SPS and RHIC, a regeneration of the $c\bar{c}$ bound states is observed due to a recombination of the $\bar{c}$ and c quarks from the hot nuclear matter. For what concerns the bottomonium, the recombination process is negligible even at LHC energies.

1.4.3 Experimental results in A-A collisions

In order to study the QGP properties, i.e. looking at the medium signatures highlighted in the previous section, several experimental observables were introduced. In particular, in the heavy flavour domain, the nuclear modification factor is the main observable that allow us to study the parton energy loss due to multiple scatterings with other partons and gluon radiation, while measurements on the azimuthal distribution of the produced particles are addressed for the study of possible collective effects induced by a strongly interacting medium.

Nuclear modification factor

In section 1.3.3 we already introduced the *nuclear modification factor* for p-A collisions. For A-A collisions the same definition holds, provided that this time we scale the ratio for the estimated number of binary collisions taking place in the AA interaction, $\langle N_{coll} \rangle$. It is defined as:

$$R_{AA}(p_T) = \frac{\mathrm{d}N_{AA}/\mathrm{d}p_\mathrm{T}}{\langle N_{coll} \rangle \cdot \mathrm{d}N_{pp}/\mathrm{d}p_\mathrm{T}} \tag{1.15}$$

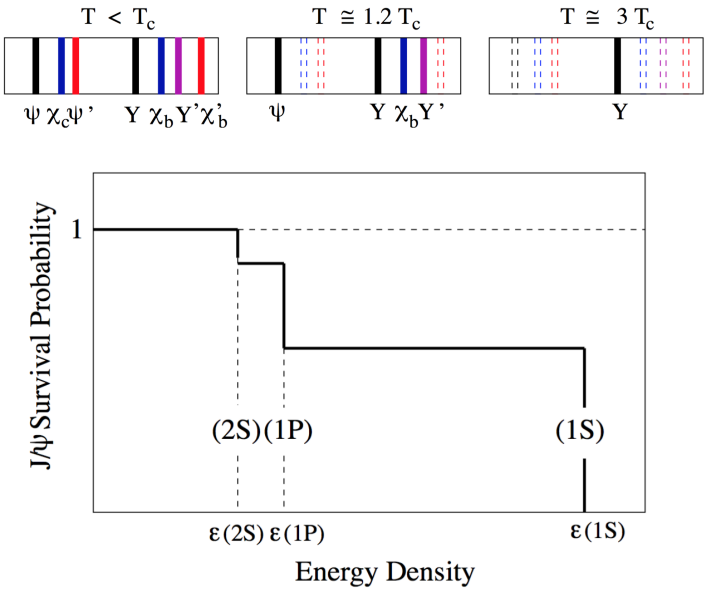

Figure 1.23 *– Top: quarkonium spectral lines as thermometer [66]. Bottom: Sequential melting pattern for the feed-down contributions to J/ψ production due to color screening [66].*

where $\mathrm{d}N_{AA}/\mathrm{d}p_{\mathrm{T}}$ and $\mathrm{d}N_{pp}/\mathrm{d}p_{\mathrm{T}}$ are the measured p_{T}-differential yields in AA collisions and pp collisions, respectively. The value of $\langle N_{coll} \rangle$ depends on the centrality of the collision and can be evaluated from the Glauber model.
In Fig. 1.24, the nuclear modification factor of D mesons at $\sqrt{s_{\mathrm{NN}}} = 5.02$ TeV in the 0-10% centrality class is compared with the ALICE measurement at lower energy ($\sqrt{s_{\mathrm{NN}}} = 2.76$ TeV). The R_{AA} suppression is compatible within uncertainties at the two energies. The close similarity of the R_{AA} measurements at the two energies was predicted by the Djordjevic model [75] (reported in the solid line of the plot), which includes both radiative and collisional energy loss processes. This results from the combination of a higher medium temperature at 5.02 TeV (estimated to be about 7% higher than at 2.76 TeV), which would decrease the R_{AA} by about 5% if the medium temperature were the same as at 2.76 TeV. This result was unexpected. Indeed, in the initial state, the modification of the parton distribution functions in a nuclear environment is predicted to lead to a stronger suppression of the heavy- quark production yields at low p_{T} with increasing center of mass energy [38], because of the smaller values of Bjorken-x probed. In addition, the momentum (k_T) broadening effect, which gives rise to an enhancement of the R_{AA} at intermediate p_{T} (Cronin peak), is known to be more pronounced at lower collision energies [71], as highlighted in the section 1.3. In the final state, in addition to energy loss, the collective expansion of the medium is also predicted to affect the momentum distribution of charmed hadrons in heavy-ion collisions. Indeed, the interactions with

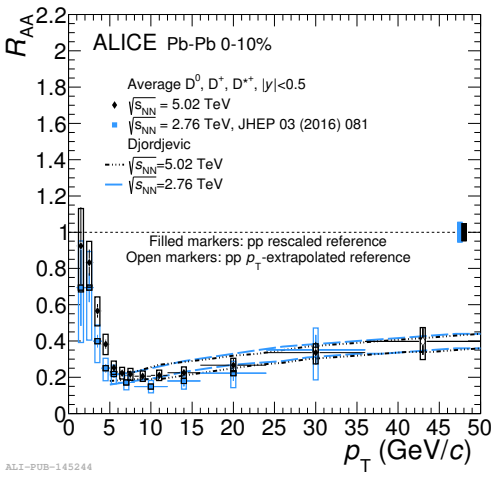

Figure 1.24 *– Average R_{AA} of D^0, D^+ and D^{*+} mesons compared with the Djordjevic model in the 0-10% centrality class at two collision energies. Statistical (bars), systematic (empty boxes), and normalisation (shaded box) uncertainties are shown.*

the medium constituents are expected to transfer momentum to low-$p_{\rm T}$ charm quarks, which could take part in the collective radial flow of the medium. This effect could be enhanced by hadronisation via recombination, which is predicted in some models to contribute significantly to hadron formation at low and intermediate $p_{\rm T}$ [72].
The R_{AA} of prompt D^0, D^+ and D^{*+} mesons is shown in Fig. 1.25, from central (top) to peripheral (bottom) collisions. The nuclear modification factors of the three D-meson species are compatible within statistical and systematic uncertainties, which are obtained by propagating those on the Pb–Pb yields and those of the pp reference.
In Fig. 1.26, the R_{AA} of prompt D mesons is compared with that of charged particles in the same p_T intervals, at the same energy and in the same centrality classes [67]. The ratio of their nuclear modification factors is displayed in the bottom panels, for the three centrality classes. The R_{AA} of D mesons and charged particles differ by more than 2σ of the combined statistical and systematic uncertainties in all the $p_{\rm T}$ intervals within $3< p_{\rm T} <8$ GeV/c in central collisions. The difference is less than 2σ in this range for semi-central collisions, while the two R_{AA} are the same within 1σ for $p_{\rm T} > 10$ GeV/c in both central and semi- central collisions. In the 60-80% class the measurements are compatible in the common $p_{\rm T}$ interval. The interpretation of the difference observed for $p_{\rm T} < 8$ GeV/c in central and semi-central collisions is not straightforward, because several factors can play a role in defining the shape of the R_{AA}. In presence of a colour-charge and quark-mass dependent energy loss, the harder $p_{\rm T}$ distribution and the harder fragmentation function of charm quarks compared to those of light quarks and gluons should lead to similar values of D-meson and pion R_{AA}. Since the pions are the dominant contribution in the inclusive charged-particle yields, this statement is expected to be still valid for the comparison of the D-meson and the charged particle R_{AA}. In addition, it should be

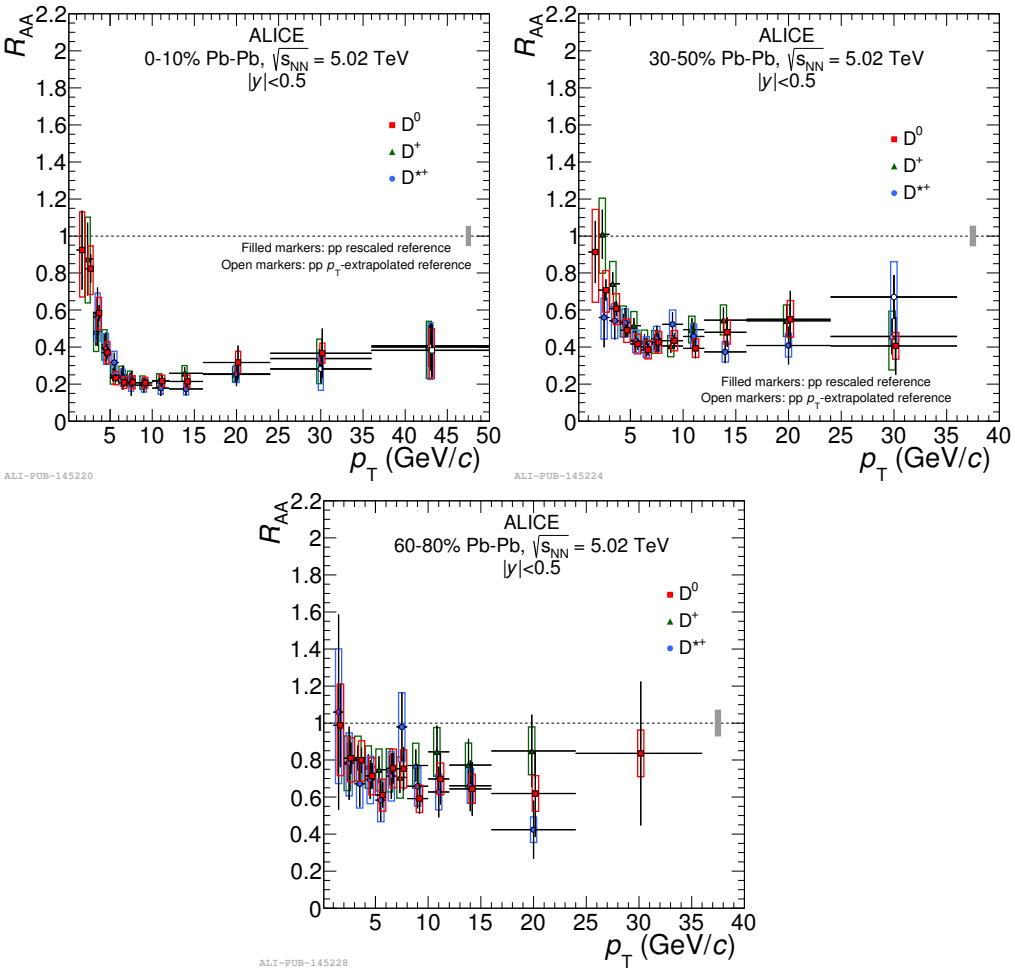

Figure 1.25 – *R_{AA} of prompt D^0, D^+ and D^{*+} mesons for the 0-10%, 30-50% and 60-80% centrality classes. Statistical (bars), systematic (empty boxes), and normalisation (shaded box around unity) uncertainties are shown. Filled markers are obtained with the pp rescaled reference, empty markers with the p_T-rescaled reference.*

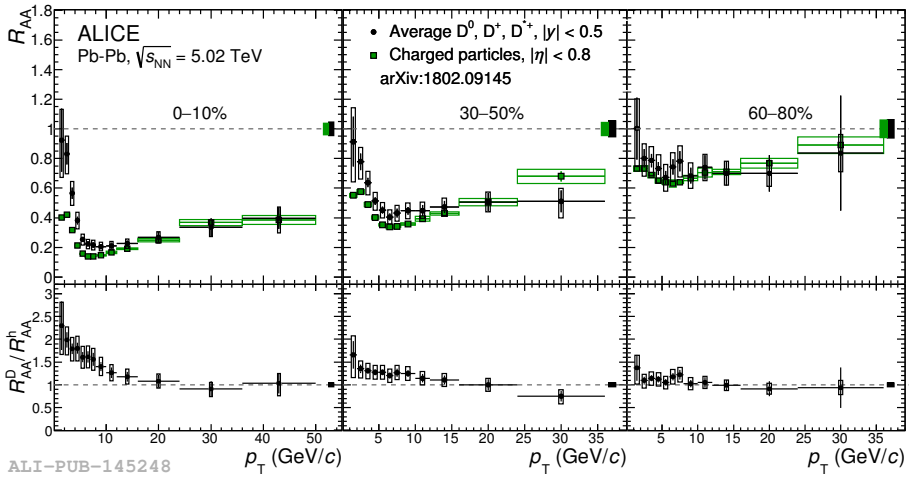

Figure 1.26 *– Average R_{AA} of prompt D^0, D^+ and D^{*+} mesons in the 0-10% (left), 30-50% (middle) and 60-80% (right) centrality classes at $\sqrt{s_{NN}}$ = 5.02 TeV compared to the R_{AA} of charged particles in the same centrality classes [67]. The ratios of the R_{AA} are shown in the bottom panels. Statistical (bars), systematic (empty boxes), and normalisation (shaded box around unity) uncertainties are shown.*

considered that the yield of light-flavour hadrons could have a substantial contribution up to transverse momenta of about 2-3 GeV/c from soft production processes, such as the break-down of participant nucleons into quarks and gluons that subsequently hadronise. This component scales with the number of participants rather than the number of binary collisions. Finally, the effects of radial flow and hadronisation via recombination, as well as initial-state effects, could affect D-meson and light-hadron yields differently at a given p_{T}.

Collective motion: flow

A strongly interacting system can be characterized by collective motions, commonly known as *flow*. In the framework of hydrodynamical models, it originates by particular conditions of the fireball in the early stages of its evolution and, for this reason, they can provide important informations about the properties of the system at that moment. It is possible to distinguish between different types of flow: the *radial flow* and the *anisotropic flow*. The former is caused by the fireball expansion and is isotropic, as the term "radial" may suggest; the latter derives from system asymmetries in the pressure gradients and can be measured by studying the azimuthal distribution of the final detectable particles. In order to account for the different flow contributions, the azimuthal distribution of the

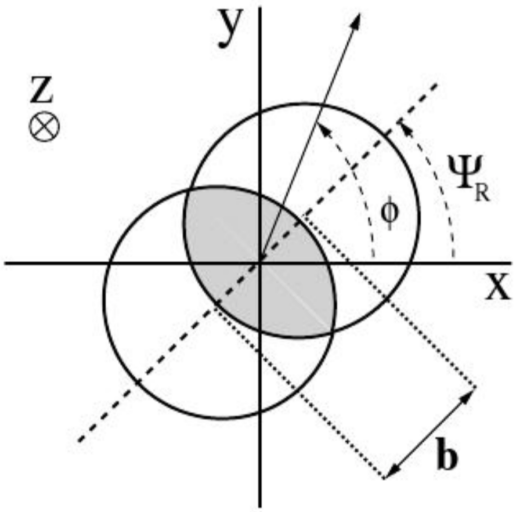

Figure 1.27 *– Schematic view of the geometry of a peripheral collision as seen in the plane transverse to the beam direction (z axis).*

particles in the transverse plane is usually described by means of a Fourier expansion:

$$E\frac{\mathrm{d}N}{\mathrm{d}^3p} = \frac{1}{2\pi}\frac{\mathrm{d}^2N}{p_{\mathrm{T}}dp_{\mathrm{T}}dy}(1+\sum_{n=1}^{\infty} v_n \cos[n(\phi-\Psi_R)] \tag{1.16}$$

where E is the particle energy, p is the momentum, ϕ the azimuthal angle, y the rapidity and Ψ_R indicates the reaction plane (which is the plane defined by the beam axis and the impact parameter) angle. Each of the v_n coefficients in the Equ. 1.16 identifies a certain component of the flow and has a physical interpretation. The dominant contribution is expected to come from the v_2 (*elliptic flow*), the second term of the Fourier expansion. It quantifies the asymmetries for the emission of particles inside or outside the reaction plane. In non-central heavy-ion collisions, an initially asymmetric overlap region (almond shaped) is created as shown in Fig. 1.27. Due to the pressure gradients, the almond shaped region tends to assume a more symmetric shape as the system expands and cools down. If the particles produced in the collision are subject to a large number of rescatterings in the overlap region, the spatial anisotropy is converted into a momentum anisotropy of the produced particles with respect to the reaction plane (Ψ_R). This particle anisotropy is experimentally quantified with anisotropic flow measurements, which provide information on the properties of the QGP and on the energy loss mechanism.
In non-central collisions, the largest contribution corresponds derives from the second order Fourier coefficient $v_2 = \langle\cos[2(\phi-\Psi_2)]\rangle$, called *elliptic flow*. The D-meson v_2 at low p_{T} provides insight into the possible collective flow imparted by the medium to charm quarks [76], while at high p_{T} it is more sensitive to the path-length dependence of parton energy loss [77]. At low and intermediate p_{T}, a fraction of charm quarks could

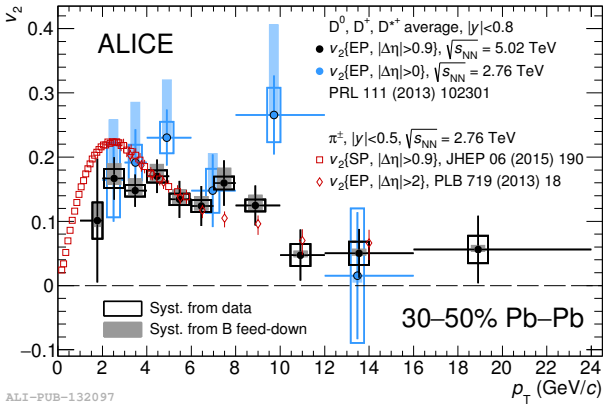

Figure 1.28 – *Average of D^0, D^+ and D^{*+} v_2 as a function of $p_{\rm T}$ at $\sqrt{s_{\rm NN}}$ = 5.02 TeV, compared with the same measurement at $\sqrt{s_{\rm NN}}$ = 2.76TeV [84] and to the $\pi^{\pm}$ v_2 measured with the Event Plane method [87] and with the scalar production (SP) method [88].*

hadronize via recombination with light quarks from the medium, leading to an increase of the D-meson v_2 with respect to that of charm quarks [78].

A positive v_2 was observed in Au–Au collisions by PHENIX [80] and STAR [82] at $\sqrt{s_{\rm NN}}$ = 200 GeV and in Pb–Pb collisions by ALICE [84] [85] and CMS [83] at $\sqrt{s_{\rm NN}}$ = 2.76 and 5.02 TeV. Calculations based on heavy-quark transport in a hydrodynamically-expanding medium well describe the measurements

Fig. 1.28 shows that the average v_2 of D^0, D^+ and D^{*+} at $\sqrt{s_{\rm NN}}$= 5.02 TeV is compatible with the same measurement at $\sqrt{s_{\rm NN}}$ = 2.76 TeV ($L_{int} \sim 6\ \mu b^{-1}$) [84], which has uncertainties larger by a factor of about two compared to the new result at 5.02 TeV. The average D-meson v_2 is also compared with the $\pi^{\pm}$ v_2 at $\sqrt{s_{\rm NN}}$ = 2.76 TeV measured with the Event Plane (EP) method [87], considering a pseudorapidity separation of 2 units between $\pi^{\pm}$ and the particles used to measure the EP angle, and the scalar-product method [88], also based on two-particle correlations. The comparison of the D-meson v_2 at $\sqrt{s_{\rm NN}}$ = 5.02 TeV and of the pion v_2 at $\sqrt{s_{\rm NN}}$ = 2.76 TeV is justified by the observation that the $p_{\rm T}$-differential v_2 of charged particles, which is dominated by the pion component, is compatible at these two energies [86]. The D-meson v_2 is similar to that of $\pi^{\pm}$ in the common $p_{\rm T}$ interval (1-16 GeV/c) and it is lower in the interval below 4 GeV/c, the difference reaching about 2 σ in 2-4 GeV/c, where a mass ordering of v_2 is observed for light-flavour hadrons and described by hydrodynamical calculations. In Fig. 1.29, the average v_2 of D^0, D^+ and D^{*+} mesons is compared with theoretical calculations that include a hydrodynamical model for the QGP expansion (models that lack this expansion underestimated the D-meson v_2 measurements at $\sqrt{s_{\rm NN}}$ = 2.76 TeV in 2< $p_{\rm T}$ < 6 GeV/c [84]). The BAMPS-el [89], POWLANG [47] and TAMU [90] calculations include only collisional (i.e. elastic) interaction processes, while the BAMPS-el+rad, LBT [91], MC@sHQ [92] and PHSD [93] calculations also include energy loss via gluon radiation. All calculations, with the exception of BAMPS, include hadronization

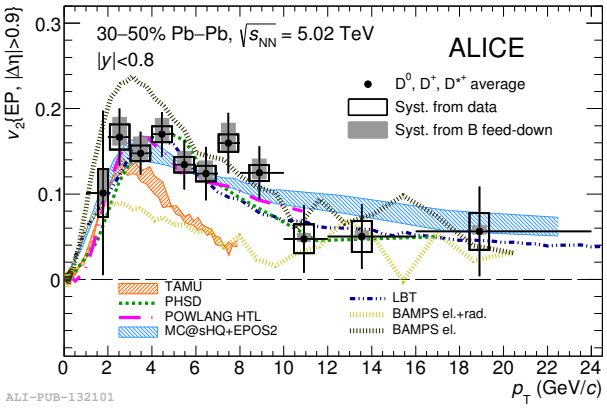

Figure 1.29 – *Average of D^0, D^+ and D^{*+} v_2 as a function of p_{T}, compared with model calculations.*

via quark recombination, in addition to independent fragmentation. The v_2 measurement at $\sqrt{s_{\mathrm{NN}}} = 5.02$ TeV is described by most of these calculations, in which the interactions with the hydrodynamically-expanding medium impart a positive v_2 to charm quarks. The comparison with model calculations indicates that low-momentum charm quarks take part in the collective motion of the QGP and that collisional interaction processes as well as recombination of charm and light quarks both contribute to the observed elliptic flow.

2

Two-particle correlations

2.1 Introduction

Two-particle angular correlations are a powerful tool to study the dynamical evolution of the system created in ultra-relativistic collisions of protons or nuclei. The differences in the azimuthal angle ($\Delta\phi$) and in pseudorapidity ($\Delta\eta$) between a reference ("trigger") particle and other particles produced in the event are considered. The typical shape of the correlation distribution features a near-side peak at ($\Delta\phi$, $\Delta\eta$) $\sim$ (0, 0), induced by the jet containing the trigger particle, and an away-side structure centered at $\Delta\phi \sim \pi$ and extending over a wide pseudorapidity range, due to the recoil jet [94]. In nucleus-nucleus collisions the correlation distribution also exhibits pronounced structures on the near- and away-side extending over a large $\Delta\eta$ region, commonly referred to as "ridges" [95]. The $\Delta\phi$ projection of the correlation distribution, after removal of the jet contribution, can be described by a Fourier decomposition, whose coefficients are denoted as Δv_n. These coefficients can be factorised into single-particle coefficients v_n related to the azimuthal distribution of the particles with respect to the reaction plane of the collision [96]. In non-central nucleus-nucleus collisions, the dominant coefficient is that of the second-order harmonic, referred to as elliptic flow (v_2), and its value is used to characterize the collective motion of the system. The measurements are well described in the framework of a hydrodynamic expansion of the hot and dense medium produced in the collision.

Surprisingly, the presence of similar long-range ridge like structures and a positive v_2 coefficient were also observed for light-flavour hadrons in high-multiplicity proton-lead (p–Pb) collisions by the ALICE [97], ATLAS [98] and CMS [99] collaborations at the LHC. The pattern of the v_2 coefficient as a function of the particle mass and transverse momentum is similar in p–Pb and Pb–Pb collisions [100]. The PHENIX and STAR collaborations at RHIC also measured a positive v_2 coefficient for charged hadrons in

high- multiplicity deuteron–gold collisions [101,102]. A near-side structure extended over a large $\Delta\eta$ range was also reported for high-multiplicity proton-proton (pp) collisions by the CMS [103] and ATLAS [98] collaborations. The interpretation of a positive v_2 in these small collision systems is currently highly debated. One possible interpretation is based on collective effects induced by a hydrodynamical evolution of the particles produced in the collision [104, 105]. Other approaches include mechanisms involving initial-state effects, such as gluon saturation within the Color-Glass Condensate effective field theory [106, 107], or final-state colour-charge exchanges.
In this chapter, the role of charmed hadron azimuthal correlations, both in pp and in Pb–Pb collisions, in understanding the QCD processes (heavy quark fragmentation and hadronization and their modification in heavy-ion collisions) as well as the study of the modification of the correlation pattern coming from different source of energy loss or to possible collective effects will be presented in the section 2.2. After that, the possible observables for studying two-particle correlation will be discussed in the section 2.3. In section 2.4 an overview of the experimental results related to correlation measurements in the various collision systems will be reported.

2.2 From the pQCD test to QGP probe

The analysis of angular correlations between heavy flavour hadrons and charged particles can provide further insight into the heavy quark production in proton-proton collisions. In fact, studies on angular correlation provide a way to characterize charm production and fragmentation, allowing us to probe our understanding of QCD in perturbative regimes accessible in a large kinematic range given the large mass of heavy quarks. Flavour conservation in QCD implies that charm is always produced as pairs of quarks and anti-quarks. In particular, prompt charm quark-antiquark pair production is back to back in azimuth at leading-order of perturbative-QCD (pQCD). If a hadron from the quark hadronization is taken as trigger particle, a near-side (at $\Delta\phi = 0$) and an away-side (at $\Delta\phi = \pi$) peak would appear in the azimuthal correlation distributions, coming from the fragmentation of the quark pair (*pair production*) [73]. At the next-to-leading order, the azimuthal correlation patterns are modified as a consequence of processes like *gluon splitting* and *flavour excitation* [73]. Heavy quarks produced from the splitting of a massless gluon can be rather collimated and may generate sprays of hadrons at small $\Delta\phi$. Finally, for hard-scattering topologies classified as "flavour-excitation", a charm quark undergoes hard interaction from an initial splitting ($g \rightarrow c\bar{c}$), leading to a big separation in rapidity of the hadrons originating from the antiquark (quark) with respect to the trigger particle and contribute to a rather flat term to the $\Delta\phi$-correlation distribution.
Therefore, one of the interesting physics goal that could be addressed through azimuthal correlation studies is the possibility to disentangle the various LO and NLO processes, responsible for the heavy quark production at the LHC energies. Indeed, these processes

are characterized by different distribution of the angle between the c and $\bar{c}$ quarks. In detail, one can compare the experimental observed angular correlation distributions of the heavy flavoured hadrons with Monte Carlo simulations. For example, using a PYTHIA tune as event generator, it is possible to reproduce the kinematical distribution of c and $\bar{c}$ quarks produced from pair production (LO process), gluon splitting and flavour excitation (NLO processes) and to estimate the weight of each contribution by comparing with data distributions. In Fig. 2.1 and 2.2 the results of this study for the production cross section of $c\bar{c}$ and $b\bar{b}$ pairs in proton-proton collisions at $\sqrt{s}$= 14 TeV against several kinematical variables (the invariant mass of the quark pair $M_{c\bar{c}}$ ($M_{b\bar{b}}$), the transverse momentum $p_{\mathrm{T}}(c\bar{c})$ ($p_{\mathrm{T}}(b\bar{b})$), the difference of the azimuthal angles $\Delta\phi(c\bar{c})$) ($\Delta\phi(b\bar{b})$)) is reported. For each variable, together with the total cross section (solid histogram), the single contributions from pair production (dashed line), flavour excitation (dotted line) and gluon splitting (dot-dashed line) are shown. It can be observed that the cross section as a function of the azimuthal correlations of the heavy quark pairs have completely different shapes with respect to the three processes. As expected, the LO process reflects the back-to-back production in the azimuthal correlations, while NLO processes do not show any preferential $\Delta\phi$ distribution, giving an almost flat contribution to the total cross section. However, the NLO contribution is expected to generate harder p_{T} distribution with respect to pair production (both for charm and beauty cross sections) and it dominates for the charm total cross section while the LO process gives the highest contribution to the the bottom one. Both PYTHIA (solid histogram) and MNR (triangles) simulations are in agreement in describing the total charm and bottom cross section as a function of the invariant mass and of the transverse momentum, while some tension arises in the $\Delta\phi$-dependent description.

In pp collisions, the hadronization of two energetic partons produced via hard scattering results in a back-to-back jet production provided that there is not any gluon radiation that manifests the presence of a third jet. In nucleus-nucleus collision, the back-to-back correlation pattern is broken by the interaction of partons with the QGP medium. Indeed, when the energetic partons are produced in the medium, they lose energy while traveling through it and, if their path length in the medium is long enough, they do not have sufficient residual energy to give rise to a jet. For this reason the study of two-particle correlations in heavy ion collisions can provide additional information about the parton energy loss in a QGP medium by investigating the jet quenching effect. In Fig.2.3, a sketch describing the jet production in heavy ion collision, for a hard scattering occurring near the surface of the fireball is shown. The parton produced in the outward direction fragments in a jet, while the other one is quenched by the medium. As a general feature, the jet quenching results in the suppression of the away side peak (for $\Delta\phi = \pi$) in the azimuthal correlation distribution of the particle produced in the event, if the track with the highest p_{T} is chosen as trigger particle. Indeed, within this choice, the correlations of the trigger with the other particles composing its jet give rise to a near side peak (at $\Delta\phi = 0$). If the other parton produced in the hard scattering loses enough energy while

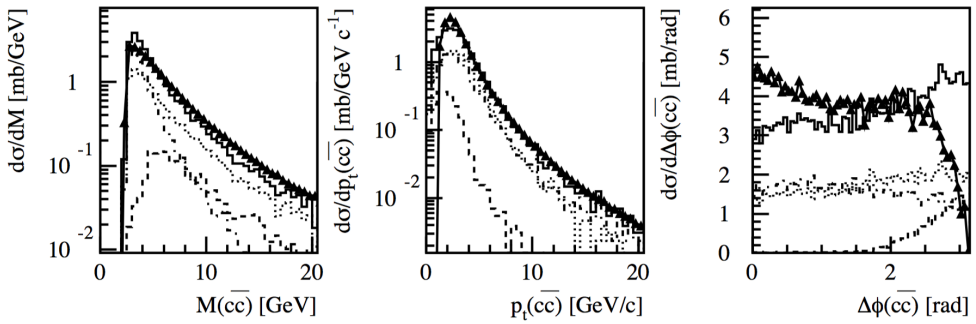

Figure 2.1 – *Comparison between charm production in the NLO calculation by Mangano, Nason and Ridolfi (MNR) and in PYTHIA in proton-proton collisions at $\sqrt{s}$= 14 TeV. The triangles show the MNR calculation while the solid histogram corresponds to the PYTHIA total production. Cross sections are shown as a function of some kinematical variables: $M_{c\bar{c}}$ (left), $p_{\mathrm{T}}(c\bar{c})$ (middle) and $\Delta\phi(c\bar{c})$) (right). For PYTHIA simulations, the total cross section is split into the contributions coming from pair production (dashed), flavour excitation (dotted) and gluon splitting (dot-dashed). Figure taken from [108].*

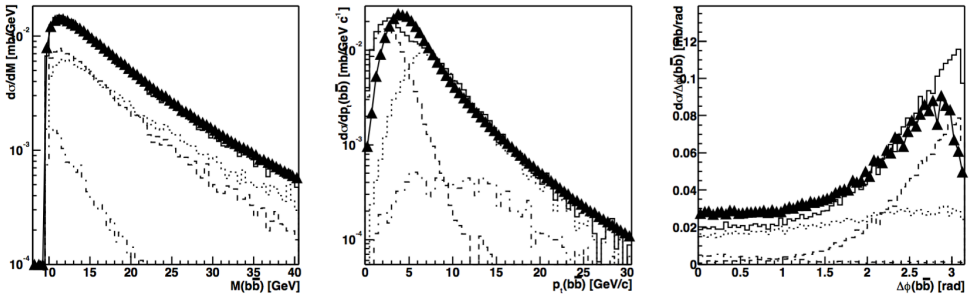

Figure 2.2 – *Comparison between beauty production in the NLO calculation by Mangano, Nason and Ridolfi (MNR) and in PYTHIA in proton-proton collisions at $\sqrt{s}$= 14 TeV. The triangles show the MNR calculation while the solid histogram corresponds to the PYTHIA total production. Cross sections are shown as a function of some kinematical variables: $M_{b\bar{b}}$ (left), $p_{\mathrm{T}}(b\bar{b})$ (middle) and $\Delta\phi(b\bar{b})$) (right). For PYTHIA simulations, the total cross section is split into the contributions coming from pair production (dashed), flavour excitation (dotted) and gluon splitting (dot-dashed). Figure taken from [108].*

traversing the medium, no other jets will be reconstructed in the event. This is verified, for example, when the hard scattering occurs near the surface of the medium produced in the collision. On average, the absence of the other jets in heavy ion collisions results in the suppression of the typical away-side peak in the correlation distribution.

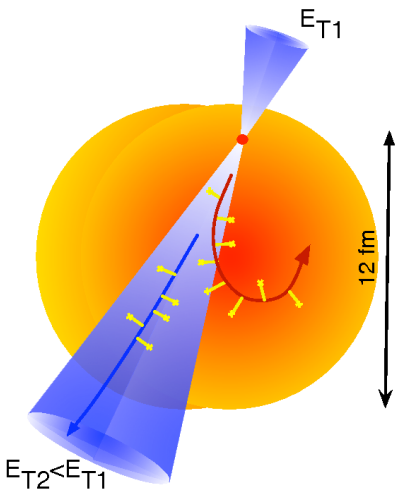

Figure 2.3 *– Sketch describing the jet production in heavy ion collision, for a hard scattering. The parton produced in the outward direction fragments in a jet, while the other one is quenched by the medium.*

A study by Nahrgang, Aichelin, Gossieau and Werner has suggested that the azimuthal correlation distribution between heavy flavour mesons in heavy ion collisions may give useful indications to discriminate the relative contributions of collisional and radiative mechanism in parton energy loss, induced by the QGP medium in heavy ion collisions [109]. In this model, a (3+1)-dimensional fluid dynamical description of the QGP medium evolution coming from the initial conditions of the EPOS model [156] is combined with a MC@sHQ interaction mechanism surrounded by the initial p_{T} distribution from FONLL calculations [7]. Then, the propagation through the medium is encoded by Boltzmann equation while the coalescence at low p_{T} and the fragmentation at high p_{T} rule the hadronization process. In addition, a global and temperature-independent K-factor was introduced as scaling factor for the pQCD cross sections for heavy quark production, in order to match the LHC data for the high p_{T} D meson R_{AA}.
In Fig. 2.4, the prediction of the model for the azimuthal correlation distribution of $D\bar{D}$ coming from $c\bar{c}$ quarks produced in the initial hard scattering for Pb–Pb collisions at $\sqrt{s_{\mathrm{NN}}} = 2.76$ TeV in three different centrality classes (0-20%, 20-40%, 40-60%) with the respective values of the K-factor is shown. The distribution of azimuthal correlations are reported for three different intervals of p_{T}. The lowest p_{T} class collects all $Q\bar{Q}$ pairs, where both the quark and the antiquark have a final p_{T} between 1 and 4 GeV. In the

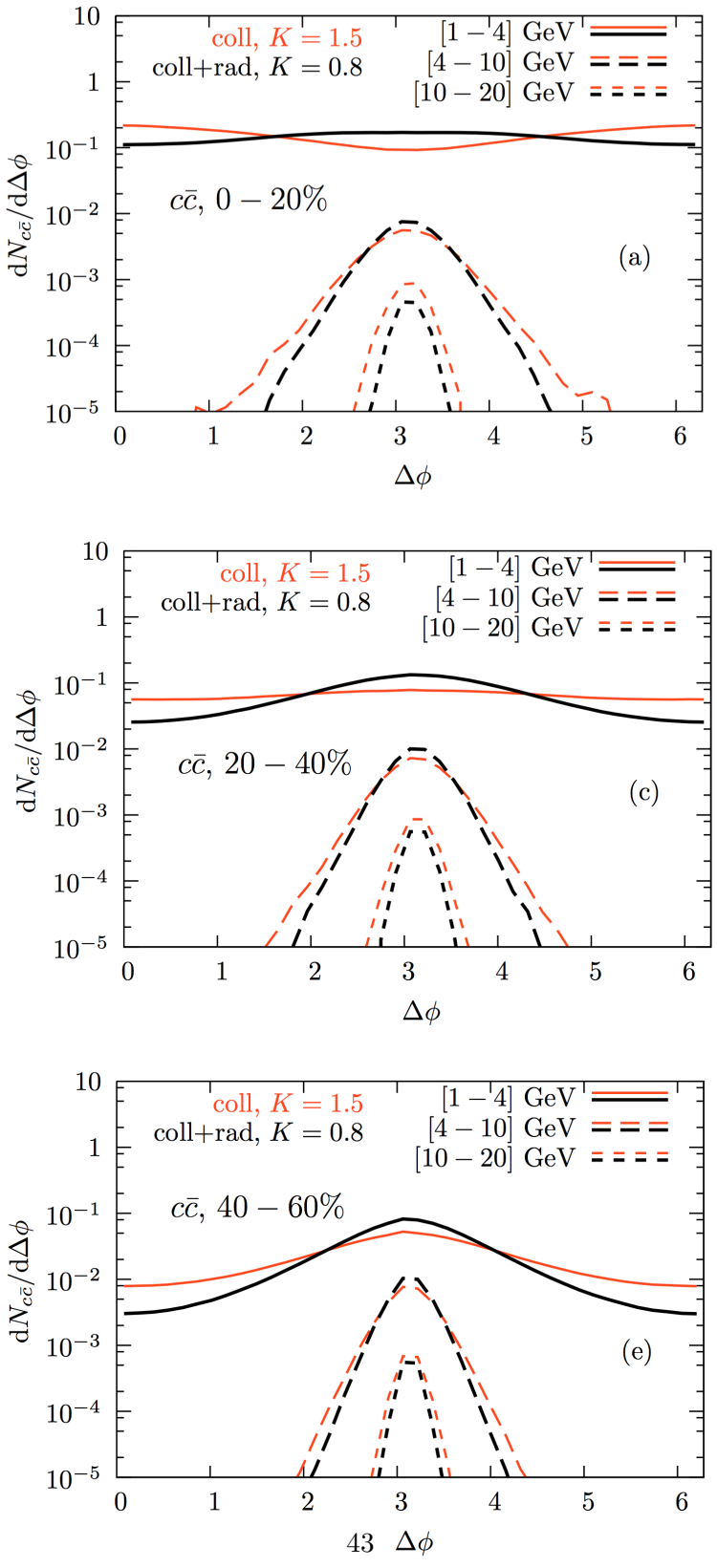

Figure 2.4 – *Azimuthal distributions of $c\bar{c}$ pairs at midrapidity in three centrality classes. The centralities are 0-20% (upper row), 20-40% (middle row) and 40-60% (lower row). In each plot, the purely collisional (orange/light), the collisional plus radiative (black/dark) interaction mechanism for different classes of final p_{T} are reported. Plots published in [110]*

intermediate-p_{T} class quark and anti-quark have a final p_{T} between 4 and 10 GeV and in the higher p_{T} -class the final p_{T} of the quark and antiquark is between 10 and 20 GeV. As a general feature, the purely collisional interaction mechanism is characterized by larger average values of p_{T}^2 per unit time than for the mechanism including radiative corrections, as can be observed in Fig. 2.5. This causes a stronger broadening of the initial correlations in all systems and kinematic classes for the purely collisional contribution.

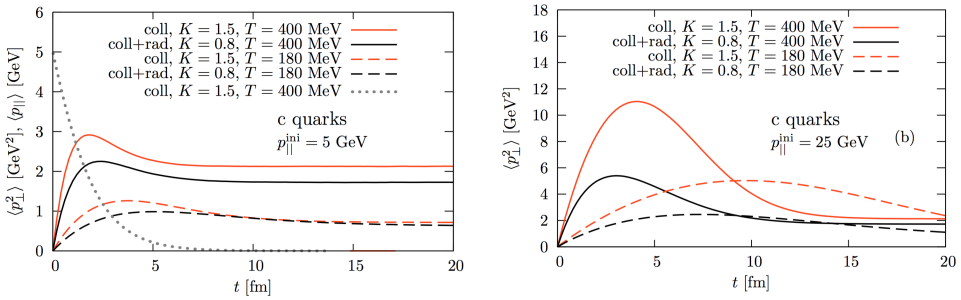

Figure 2.5 – *Time evolution of the p_{T}^2 of a charm quark with initial parallel momentum $p_{\parallel} = 5$ GeV (a) and $p_{//} = 25$ GeV (b) interacting with the QGP purely collisionally (orange/light) or including radiative corrections (black/dark) at medium temperature $T = 400$ MeV (solid) and $T = 180$ MeV (dashed). In (a) also the time evolution of the average $p_{\parallel}$ for one scenario is shown. Figure taken from [110].*

The systems created in the most central collisions (0-20%) are expected to be the largest and to reach the highest temperatures and densities. This is confirmed by most efficient broadening of the initial back-to-back pattern of the azimuthal correlations. Indeed, a substantial broadening of these correlations for all p_{T} classes in both interaction mechanisms for $c\bar{c}$ pairs is observed. For lowest p_{T}, the initial correlations are almost completely washed out as a consequence of the thermalization of the heavy quarks within the QGP. Furthermore, in the lowest p_{T} -class, the purely collisional interaction mechanism is also affected by the "partonic wind" effect [110]. It implies that the initially produced $c\bar{c}$ pairs are not completely washed out but, due to radial flow of the matter, they are pushed into the same direction toward smaller angular separation enhancing the azimuthal correlation in the region of $\Delta\phi \simeq 0$. In Fig. 2.6 a sketch of the partonic wind effect is shown. For the mechanism including the radiative processes, the broadening of the correlations is not affected by the radial flow in the same way, and the correlations around $\Delta\phi \simeq 0$ is flatter. Such an effect is much less significant for $b\bar{b}$ pairs because of their larger mass. It disappears also at higher p_{T} of $c\bar{c}$ pairs for both interaction mechanisms, where the $q\bar{q}$ pairs are too energetic to be strongly affected by the radial flow, and in peripheral collisions.

At higher p_{T}, the initial correlations are less affected by the medium since those particles leave the system more rapidly and the time that the heavy quarks spend in the medium is of the order of the radius R. Furthermore, comparing $c\bar{c}$ with $b\bar{b}$ pairs, the latter seem

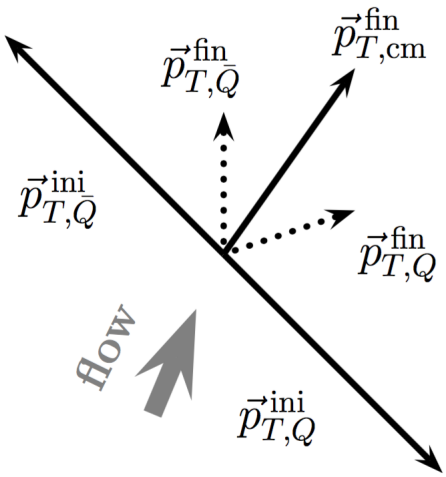

Figure 2.6 *– Sketch of the "partonic wind" effect on low-p_{T} heavy $q\bar{q}$ pairs. Figure from [110].*

to suffer from larger broadening in the higher p_{T} class, especially for the most central collisions. Such an effect results from the interplay of two features: $b\bar{b}$ pairs lose significantly less energy within the medium (it is unlike that they end up in a lower p_{T} interval) and, on average, high p_{T} of $b\bar{b}$ pairs spend more time in the QGP medium than charm quarks do. Thus, in the higher p_{T} classes, where thermalization does not play a role, $b\bar{b}$ pairs develop a broader correlation peak and are typically characterized by smaller initial p_{T} than the equivalent $c\bar{c}$.
A way to quantify the broadening of the correlation is to evaluate the variance of the peak around $\Delta\phi = \pi$ [110]. In an experimental situation it might not always be possible to identify a heavy quark and antiquark as having been initially produced in a pair. In particular, there are many $c\bar{c}$ pairs produced in one event. This inability of determining experimentally an initially correlated pair results in an uncorrelated background in addition to the distributions of Fig.2.4.

2.3 Experimental observables

Due to the quark confinement, it is not possible to access directly the quark kinematical distributions, but it is necessary to build observables involving their hadronic final states. In order to investigate the heavy flavour azimuthal correlations, the best choice that can be made is to detect hadrons that reflect the $q\bar{q}$ original distribution, preserving the possibility to study the hard scattering. Therefore, possible observables could be

the angular correlations of $D\bar{D}$, $B\bar{B}$, $bjet - bjet$, HFe-HFe or B/D-HFe/μ, as shown if Fig.2.7. Such observables are high demanding in term of statistics, especially in the case of $D\bar{D}$ or $B\bar{B}$ angular correlations, since D and B mesons have small branching ratios in their exclusive hadronic decay channels. Alternative choices of observables are the angular correlation between a meson carrying the heavy quark (i.e. D or B mesons) with charged hadrons or heavy flavour decay leptons (i.e. electron or muon) with charged hadrons. These measurements, though experimentally easier to perform thanks to the higher statistics, are more loosely related to the underlying $q\bar{q}$ distributions but they allow to study the quark pair (from which they belong) by investigating the shape and the height of the peaks at $\Delta\phi$=0 and $\Delta\phi = \pi$. Furthermore these angular distributions, even if more washed out, are still sensitive to the heavy-quark fragmentation and hadronization process. With the current cross section for charm production at the LHC energies and the available ALICE detector capabilities, the best option is to study the correlation of D mesons with charged particles. Indeed, D meson detection is easier also with respect to B mesons with the current ALICE detector performance. Therefore, the analysis presented in this thesis (in chapter 4 and 5) is performed exploiting the azimuthal correlation distributions of D mesons with charged particles.

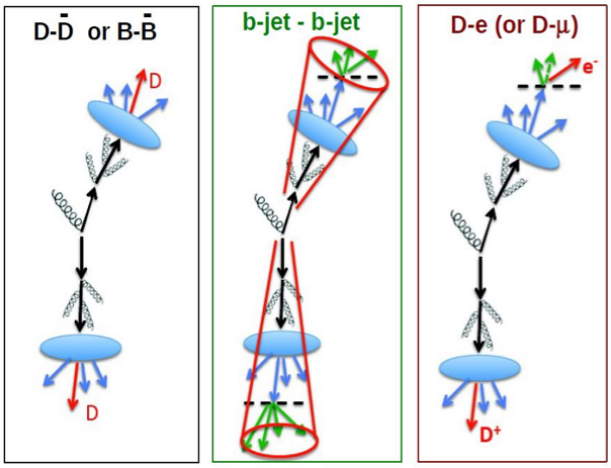

Figure 2.7 *– Possible observables of heavy flavour correlations ($c\bar{c}$, $b\bar{b}$).*

2.4 Overview of experimental results

In this section the major results on angular correlations will be discussed with particular focus on the experimental heavy flavour angular correlation results.

2.4.1 Results in pp collisions

Studying the angular correlations in pp collisions represents a way to probe our understanding of the QCD in perturbative regime. Indeed, it is expected that their angular distributions reflect the hadronization and fragmentation mechanism properties. In particular, since the hadronization of two energetic partons produced via hard scattering results in a back-to-back jet production, the near- and away- side are expected to show similar yields. In addition, what is found to be even more interesting is the experimental break of the expectations, i.e. the presence of structures in the near-side region observed from CMS and ATLAS for high-multiplicity proton-proton (pp) collisions, which will be discussed as well.

The first results on charm correlations in pp collisions were obtained by the STAR experiment at RHIC, from events at $\sqrt{s} = 200$ GeV. Due to the poor vertexing capabilities of the detector, it was not possible to perform any measurement of charm-charm correlations ($D^0 - \bar{D^0}$) by STAR [111]. In any case, it was possible to perform azimuthal correlation distribution studies between D^0 mesons and non-photonic electrons, which are mainly produced by semileptonic decays of heavy flavour mesons. In Fig.2.8 the azimuthal correlation distribution between non-photonic electrons (positrons) and D^0 ($\bar{D^0}$) is shown.

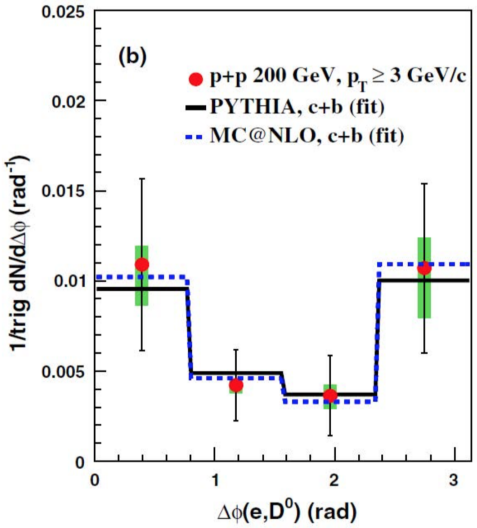

Figure 2.8 *– Azimuthal correlation distribution between non-photonic electrons and D^0 mesons (for like-sign e-K pairs) in proton-proton collisions at $\sqrt{s}$ = 200 GeV. Error bars represent statistical errors- The solid (dashed) line is a fit of the correlation function from PYTHIA (MC@NLO) simulations to the data points.*

Despite the very large uncertainties, near- and away- side are characterized by similar yields. The resulting distributions are also fitted with the correlation functions obtained

from PYTHIA and MC@NLO simulations for charm and beauty contributions, leaving the relative B contribution of the latter as a free parameter. This kind of measurements allow to weight the relative charm and beauty contribution to D meson production. In the reported analysis, the observed away-side correlation peak can be attributed to prompt charm pair production ($\sim 75\%$) and B decays ($\sim 25\%$), whereas the contributions to the near- side peak are mainly from B decays. The relative beauty contribution r_B[1] is determined by fitting the measured correlation with PYTHIA and MC@NLO and using the average of the two fits for the final value.
At Tevatron, thanks to the higher luminosity and center of mass energy, the CDF experiment was able to study the $c\bar{c}$ correlations through $D\bar{D}$ angular analysis with sufficient precision in $p\bar{p}$ collisions at $\sqrt{s}$=1.96 TeV [112]. In Fig. 2.9 the total cross section of D^0, D^{*-} and D^+, D^{*-} is shown as a function of the angular difference $\Delta\phi$. The D mesons are reconstructed at mid rapidity, in the high p_{T} region. The comparison of the experimental results of the total cross section with PYTHIA event generator (tune A configures the simulations to run with LO plus parton shower) are superimposed to the data and a good agreement between model and simulation is found. A prediction of the relative contribution of the three main production mechanisms (pair production, flavour excitation and gluon splitting) is also reported.
At LHC, the production of pairs of open charmed hadrons (i.e. $c\bar{c}$ with the following channels: $D^0\bar{D}^0$, D^0D^-, $D^0D_s^-$, $D^0\bar{\Lambda}_c^-$, D^+D^-, $D^+D_s^-$ and $D^+\overline{\Lambda_c^-}$ and cc for these modes: D^0D^0, D^0D^+, $D^0D_s^+$, $D^0\Lambda_c^+$,D^+D^+ and $D^+D_s^+$) and of open and hidden charmed hadrons (i.e. $J/\psi c$ through the channels: $J/\psi D^0$, $J/\psi D^+$, $J/\psi D_s^+$ and $J/\psi\Lambda_c^+$) has been measured in pp collisions at $\sqrt{s}$ = 7 TeV with the LHCb experiment [113]. The cross-sections and the properties of these events have been studied. In Fig. 2.10 the angular difference $\Delta\phi$ and the Δy distribution for D^0D^0 and D^0D^+ is reported. Since these pairs reflect the behavior of cc quark pairs, they are expected to be uncorrelated as a consequence of the fact that they derive from independent hard processes. The experimental shape of the angular distribution is found to be roughly flat while the Δy distribution shows a triangular trend. Both these behaviors confirm the uncorrelated origin.

On the opposite side, looking at the Fig.2.11, where the $D\bar{D}$ distribution is reported, a clear enhancement is present for small $\Delta\phi$ and Δy values. Such a trend is compatible with the production of charm pairs through gluon splitting mechanism, which is confirmed also by the enhancement of small invariant mass in the related spectra $m_{c\bar{c}}$ in Fig.2.12.
At the LHC, ALICE measured the angular correlation distribution of electrons from

[1]The fraction r_B is defined as:

$$r_B = \frac{N_B}{N_B + N_C} \tag{2.1}$$

where N_B represents the total number of electrons originating from beauty decays, while N_C is the total number of electrons originating from charm decays.

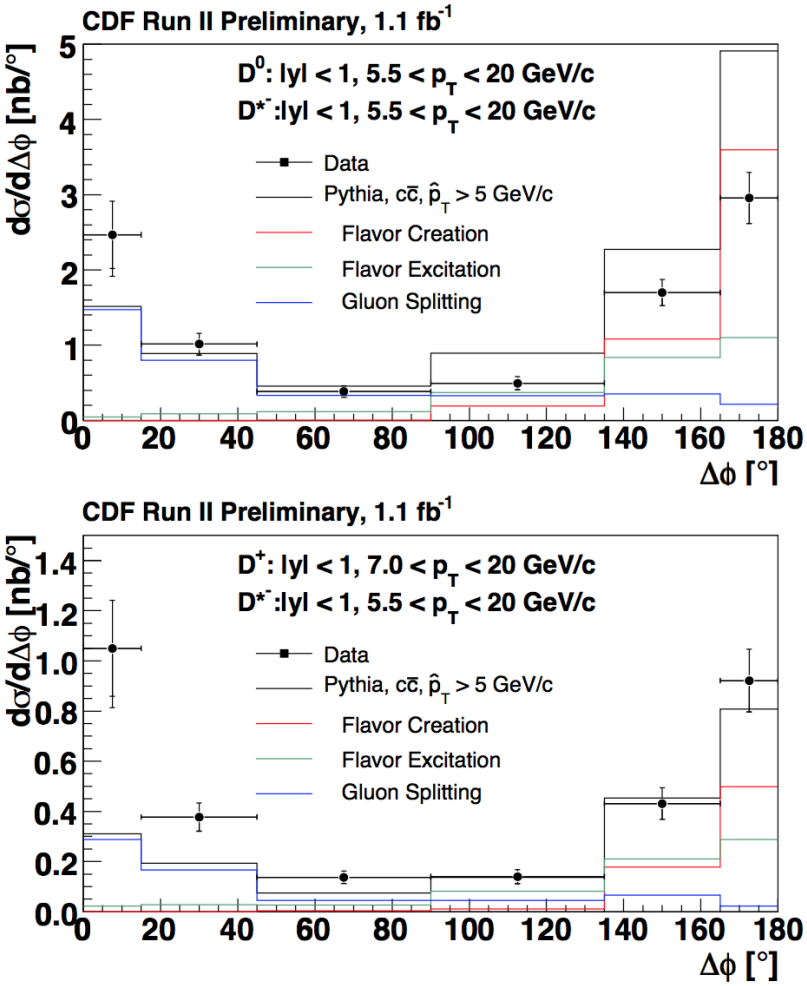

Figure 2.9 – *D^0, D^{*-} (top) and D^+, D^{*-} (bottom) cross section production as a function of the azimuthal angular difference $\Delta\phi$ in $p\bar{p}$ collisions at $\sqrt{s}$=1.96 TeV [112]. Comparison with PYTHIA predictions for the total cross section is reported with a black line. The coloured lines show the simulated relative contribution of pair production (red), flavour excitation (green) and gluon splitting (blue) to the total cross section.*

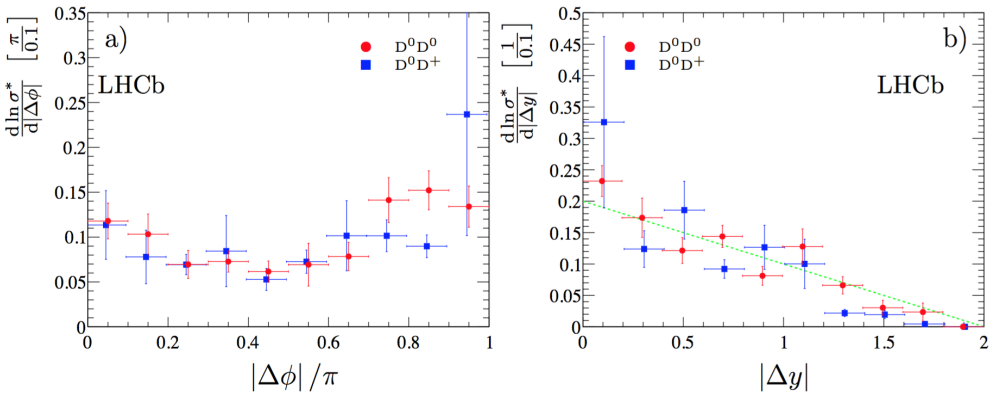

Figure 2.10 *– Distributions of azimuthal angle difference (left panel) and rapidity difference (right panel) for D^0D^0 (red) and D^0D^+ (blue) pairs, measured by LHCb in pp collisions at 7 TeV. The expected $|\Delta y|$ distribution for uncorrelated pairs is shown with a dashed line.*

heavy-flavour decays (from beauty hadrons and charm hadrons) and charged particles in pp, p–Pb and Pb–Pb collisions. In pp collisions, by exploiting the different decay kinematics (that is due to the fact that beauty hadrons are heavier than charm hadrons) the two contributions can be separated [74], and the fraction of electrons from beauty decays, r_B, can be extracted using PYTHIA Monte-Carlo templates [34]. The Fig. 2.13 shows the heavy-flavour decay electron (HFE)-charged particle $\Delta\varphi$ distribution from data and those then Monte-Carlo templates: $\Delta\varphi^C_{templ}$, the template of electrons from charm-hadron decays and, $\Delta\varphi^B_{templ}$, the template of electrons from beauty-hadron decays. These measured distributions are fitted following the parametrisation: $\Delta\varphi = const + r_B\Delta\varphi^B_{templ} + (1 - r_B)\Delta\varphi^c_{templ}$. From the fitting procedure it is possible to extract r_B.
Recent observations of two-particles angular correlations of charged hadrons revealed an unexpected long-range correlations in high-multiplicity proton-proton collisions at $\sqrt{s}$ = 0.9, 2.36, and 7 TeV. Such a result, previously found only in heavy-ion collisions, shed new interest in the understanding of non-perturbative particle production. Such measurements, reported by CMS [103] and ATLAS [98] experiment, were very surprisingly from the theoretical point of view, which describes the near-side ridge in heavy-ion collisions as a consequence of the hydrodynamical flow of the produced strongly interacting matter. Similar long-range correlation has been observed also in p-Pb collisions and will be discussed in the section 2.4.2.
Even if the general shape that can be found in the correlations are similar for colliding protons, heavy-ions or mixed systems of protons and ions, the physical explanation of the features may not be the same and are also not yet fully understood. In common notation, one distinguishes between short-range ($|\Delta\eta| \leq 2$) correlations and long-range ($|\Delta\eta| \geq 2$) correlations. In Fig. 2.14 the two-dimensional two-particle correlations is shown for minimum bias events with p_{T}-inclusive selection (left) and in the p_{T} interval

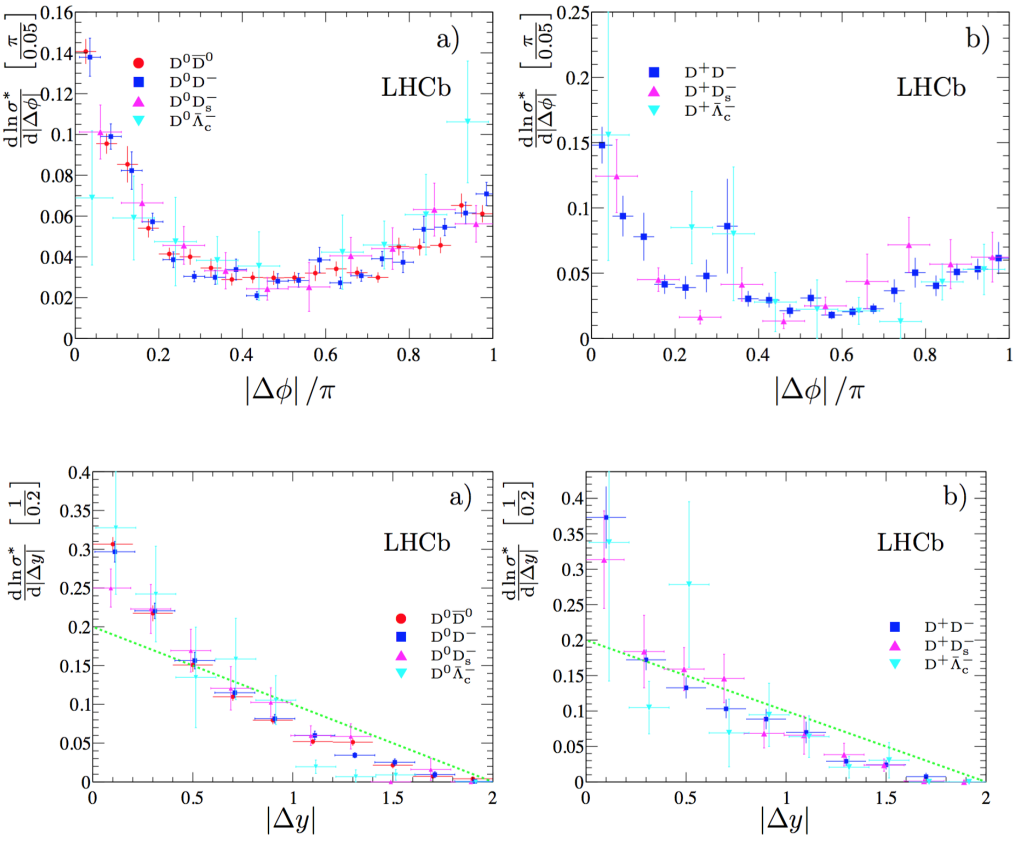

Figure 2.11 – *Distributions of the difference in azimuthal angle (top) and in rapidity (bottom) for $c\bar{c}$ events: a)$D^0\bar{D}^0$, D^0D^-, $D^0D_s^-$ and $D^0\bar{\Lambda}_c^-$; b) D^+D^-, $D^+D_s^-$ and $D^+\bar{\Lambda}_c^-$ [113].*

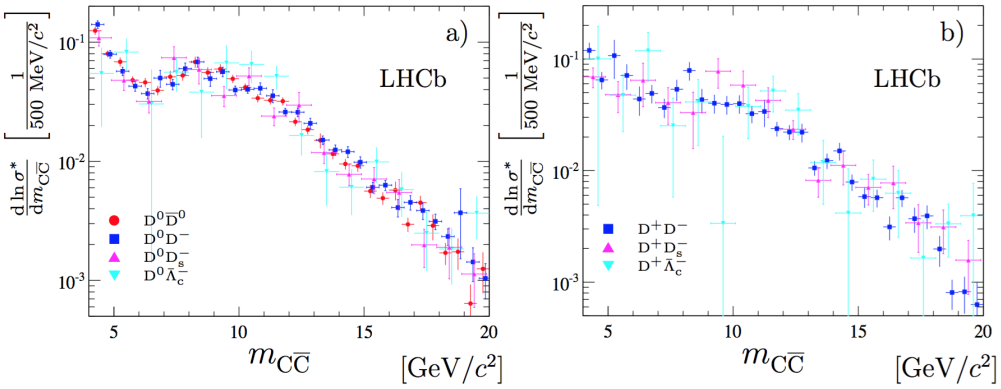

Figure 2.12 – *Invariant mass spectra for $c\bar{c}$ events: a)$D^0\bar{D}^0$, D^0D^-, $D^0D_s^-$ and $D^0\bar{\Lambda}_c^-$; b) D^+D^-, $D^+D_s^-$ and $D^+\bar{\Lambda}_c^-$.*

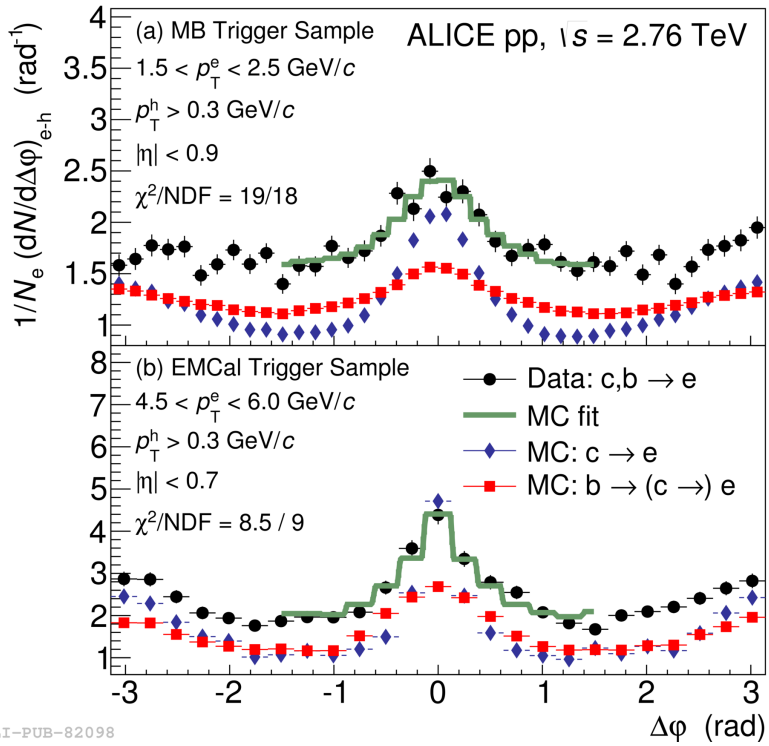

Figure 2.13 – *Azimuthal correlation of electrons from heavy-flavour decays and charged particles in pp collisions at* $\sqrt{s}$ = *2.76 TeV for* $1.5 < p_{\mathrm{T}}^{e} < 2.5$ *GeV/c (top),* $4.5 < p_{\mathrm{T}}^{e} < 6$ *GeV/c (bottom) and* $p_{\mathrm{T}}^{assoc} > 0.3$ *GeV/c [74].*

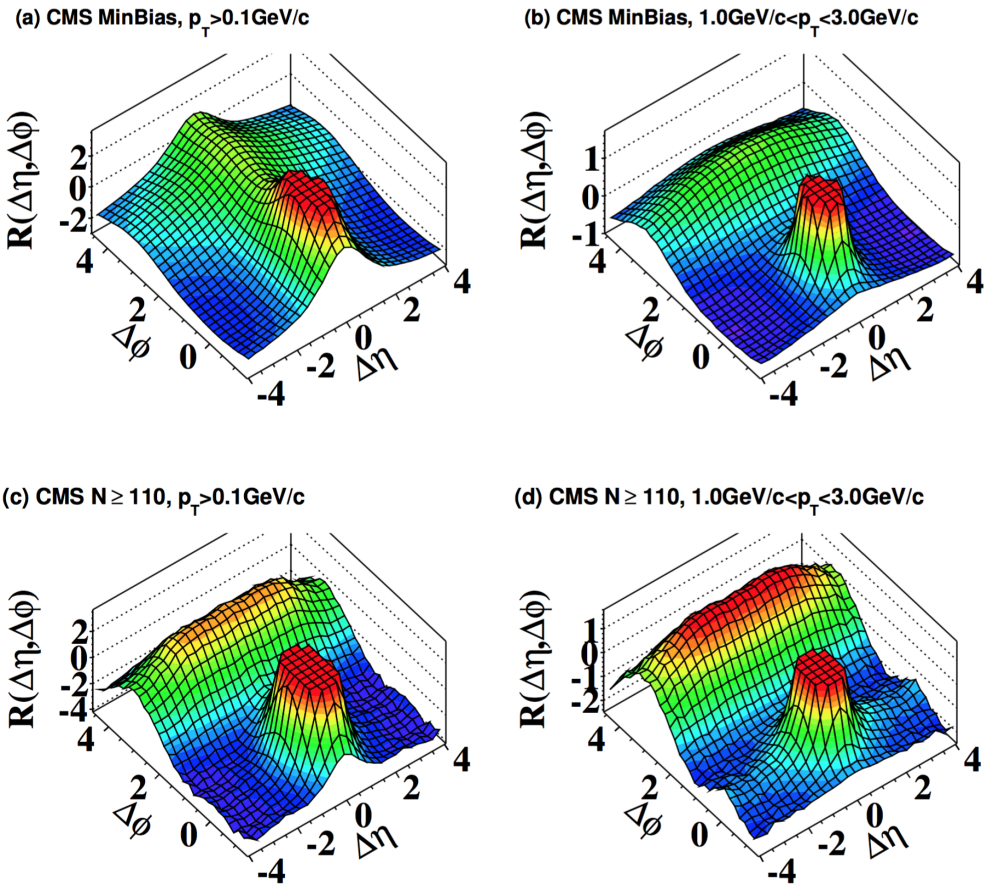

Figure 2.14 – *Two-particle correlation for pp at $\sqrt{s}$ = 7 TeV measured by CMS. In (a) minimum bias events with $p_T > 0.1$ GeV/c are considered; in (b) minimum bias events with $1 < p_T < 3$ GeV/c are selected, in (c) high multiplicity ($N_{trk}^{offline} \geq 110$) events with $p_T > 0.1$ GeV/c and in (d) high multiplicity ($N_{trk}^{offline} \geq 110$) events with $1 < p_T < 3$ GeV/c are considered. The sharp near-side peak from jet correlations is cut off in order to better visualize the structure outside that region. The figure is taken from [103].*

1< p_{T} < 3 GeV/c. A broad ridge structure centered at $\Delta\eta \sim 0$ but extending over the entire $\Delta\phi$-range emerges when including particles with lower p_{T} in the correlation function, as in the plot (a). This structure extends over the entire $\Delta\phi$-range and becomes broader in $\Delta\eta$ with increasing $\Delta\phi$. They are typically known as "short range" correlations. Simulation studies demonstrate that these correlations are qualitatively reproduced by low-mass resonances within the independent cluster model [114], or by isotropic cluster decays [115]. Another pronounced ridge is present on the away-side ($\Delta\phi \sim \pi$) and elongates over a broad range in $\Delta\eta$. This ridge is present over the entire p_{T}-range, but is more pronounced towards larger p_{T}.
An additional long-range correlation on the near-side can be seen in the bottom of the Fig. 2.14 for pp collisions with a very high particle multiplicity and for particles in a p_{T}-range of 1< p_{T} < 3 GeV. The observation of the near-side ridge in pp collisions was unexpected even though the structure is reminiscent of the ridge seen in nucleus-nucleus collision. Currently, no consistent explanation for this correlation comprising high multiplicity pp collisions and more complex systems of ultra-relativistic nuclei. In the heavy-ion community, the collective behaviour seen in nucleus-nucleus collisions is assumed to originate from the hydrodynamical flow of the created medium or from interactions between hard scattering processes and the medium. However, in pp collisions, the particle density is expected to be not high enough to create such a medium that could account for these long-range effects. Recent observations of this ridge structure also in proton-ion collisions at the LHC, as will be show in the next section, can help to understand the common origin of this correlation. Apparently, also in collisions where no hot nuclear medium is created but still a very large number of particles are produced, some common collective behavior is observed. In order to explain the presence of these structures, several phenomenological studies are carried on. A detailed comparison of long-range rapidity correlations have been performed in the color glass condensate framework [116] (CGC) to high multiplicity di-hadron data both in proton-proton and in p-Pb collisions from CMS, ALICE and ATLAS experiments at the LHC. In Fig.2.15 the results for the per-trigger yield as a function of the azimuthal angular difference $|\Delta\phi|$ from high multiplicty ($N_{trk}^{offline} \geq 110$) pp collisions are shown. A very good agreement is found with CMS proton proton data over a wide range of p_{T}^{trig} and p_{T}^{assoc}. This strongly supports that gluon saturation has a role in these systems and, therefore, this suggest that initial state effects must play an important role even if other QCD effects might contribute in the description of these striking experimental phenomena.

2.4.2 Results in p–Pb collisions

Several experiments performed the analysis of di-hadron correlations in pA collision systems. The main goal of this analysis was to disentangle the final state effects, due to the presence of the hot nuclear medium after the collisions, from the initial state effects, like the nuclear shadowing or the k_T broadening. Indeed, it was expected that the ini-

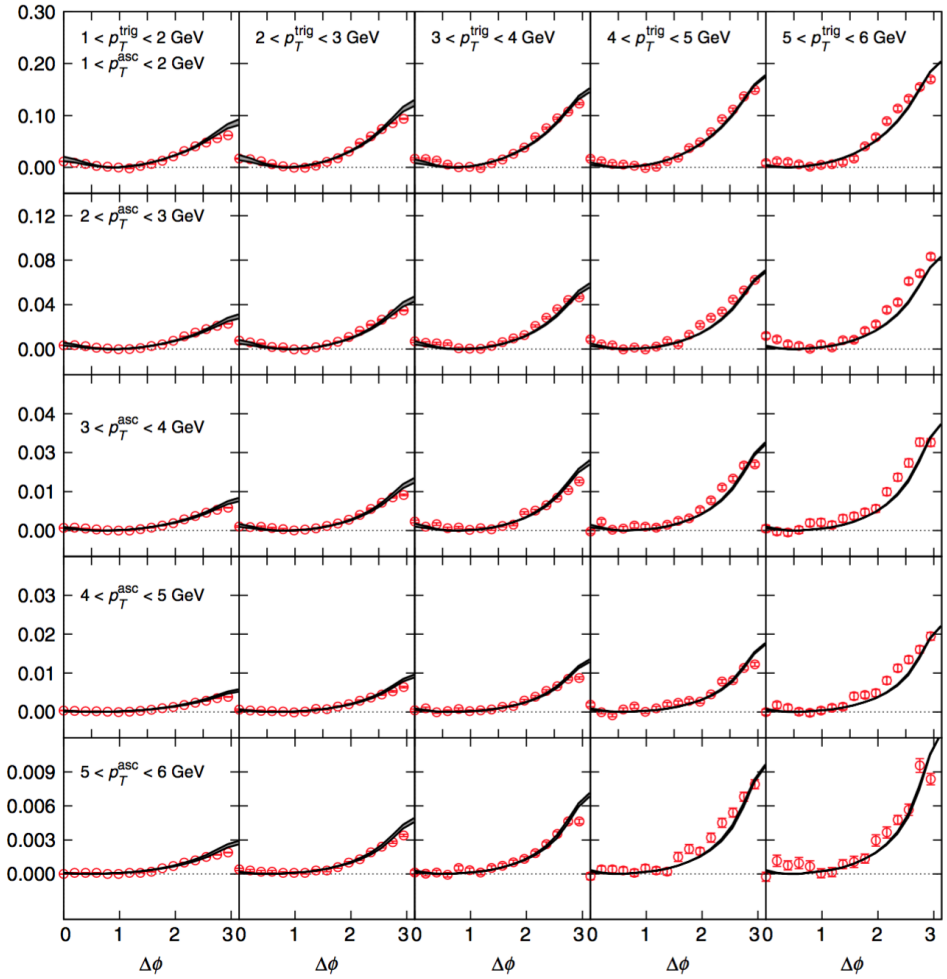

Figure 2.15 – *Long-range ($2 \leq |\eta| \leq 4$) per-trigger yields of charged particles as a function of the azimuthal angular difference $|\Delta\phi|$ from high multiplicty ($N_{trk}^{offline} \geq 110$) pp collisions. Data are from CMS Collaboration. The figure is taken from [116].*

tial state effect would cause an enhancement of the baseline of the azimuthal correlation distribution. Therefore, the interpretation of the away-side suppression in heavy-ion collisions was strictly related to the medium produced in the latter systems. In the top of the Fig. 2.16, the correlation distribution in d-Au collisions at STAR is compared to nucleon-nucleon collisions and, indeed, no suppression of the away-side is visible. The comparison with the Au-Au case, in the bottom of the figure, shows an unvaried near-side peak and a dramatic suppression for the away-side, where the peak is completely missing.

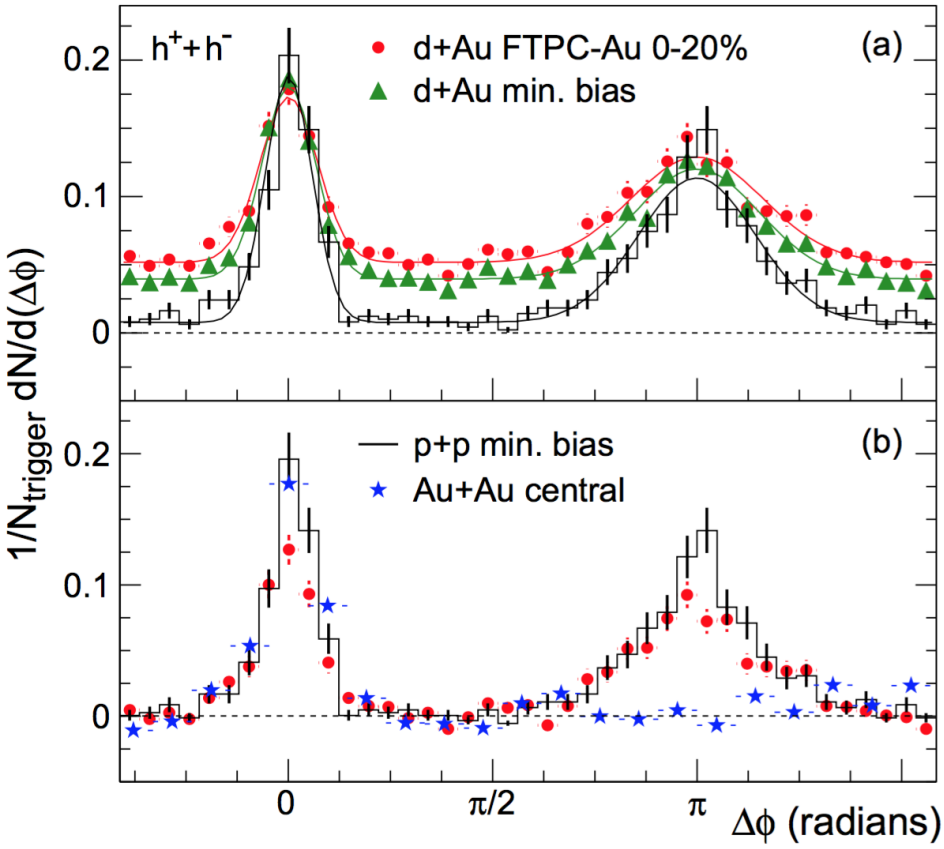

Figure 2.16 *– (a) Azimuthal distributions for minimum bias and central d+Au collisions, and for p+p collisions [117]. (b) Comparison of pedestal subtracted two-particle azimuthal distributions for central d+Au collisions to those seen in p+p and central Au+Au collisions. The figure is taken from [118]*

More recently, after the results obtained at high-multiplicity proton-proton collisions at the LHC, also measurements in proton-lead (p–Pb) collisions at a centre-of-mass energy of $\sqrt{s_{NN}} = 5.02$ TeV have revealed long-range ($2< |\Delta\eta| < 4$) near-side ($\Delta\phi \sim 0$)

correlations described by a positive v_2 coefficient in events with significantly higher-than-average particle multiplicity with ALICE [97], ATLAS [98] and CMS [99] collaborations at the LHC. Given the similar results gained by the experiments at the LHC, in the following only the ALICE measurements on the di-hadron correlations in p–Pb collisions, which reported for the first time also the excess in the away-side region, will be discussed. In Fig. 2.17 the associated yield per trigger particle in $\Delta\phi$ and $\Delta\eta$ is shown for pairs of charged particles with $2 < p_{T,trig} < 4$ GeV/c and $1 < p_{T,assoc} < 2$ GeV/c in p–Pb collisions at $\sqrt{s_{\rm NN}} = 5.02$ TeV in the 60-100% (left) and 0-20% (right) event classes. In 0-20% class, both the yields on the near-side and the away-side are higher with respect to 60-100% class (which, on the contrary, shows very similar features to those observed in pp collisions at $\sqrt{s} = 2.76$ TeV and 7 TeV). The per-trigger yields in $\Delta\phi$, all subtracted by the yield at $\Delta\phi = 1.3$, on the near side and on the away side are similar for low-multiplicity p–Pb collisions and for pp collisions at $\sqrt{s} = 7$ TeV, and increase with increasing multiplicity in p–Pb collisions as shown in Fig 2.18.

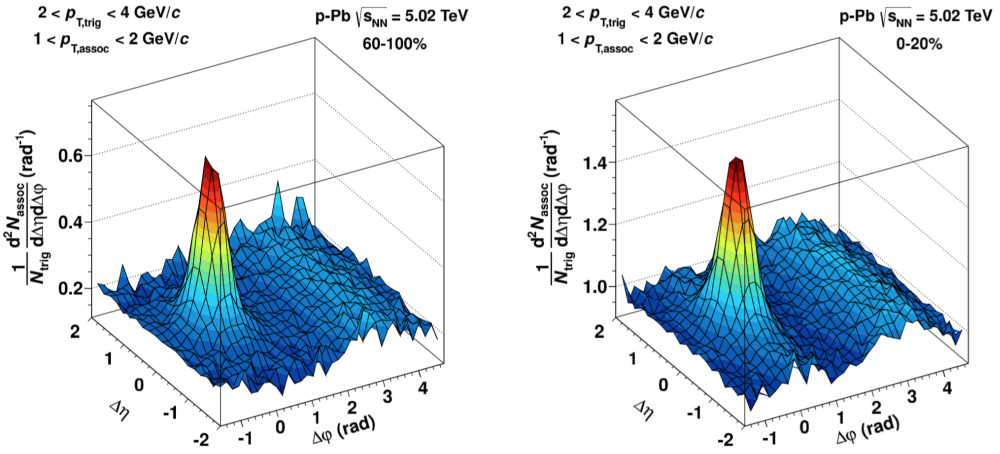

Figure 2.17 *– Associated yield per trigger particle in $\Delta\phi$ and $\Delta\eta$ for pairs of charged particles with $2 < p_{T,trig} < 4$ GeV/c and $1 < p_{T,assoc} < 2$ GeV/c in p–Pb collisions at $\sqrt{s_{\rm NN}} = 5.02$ TeV for the 60-100% (left) and 0-20% (right) event classes.*

In order to quantify the change from low to high multiplicity event classes, the per-trigger yield of the lowest (60-100%) has been subtracted from that of the higher multiplicity classes. The resulting distribution in $\Delta\phi$ and $\Delta\eta$ for the 0-20% event class is shown in Fig. 2.19. A distinct excess structure in the correlation is observed, which forms two ridges, one on the near side and one on the away side. The ridge on the near side is qualitatively similar to the those reported by the CMS and ATLAS collaboration.
On the top of the Fig. 2.20 the projection resulting from the low multiplicity subtracted distribution onto $\Delta\eta$ averaged over different $\Delta\phi$ intervals is shown. The near-side and away-side distributions are flat apart from the discussed small peak around $\Delta\eta = 0$.

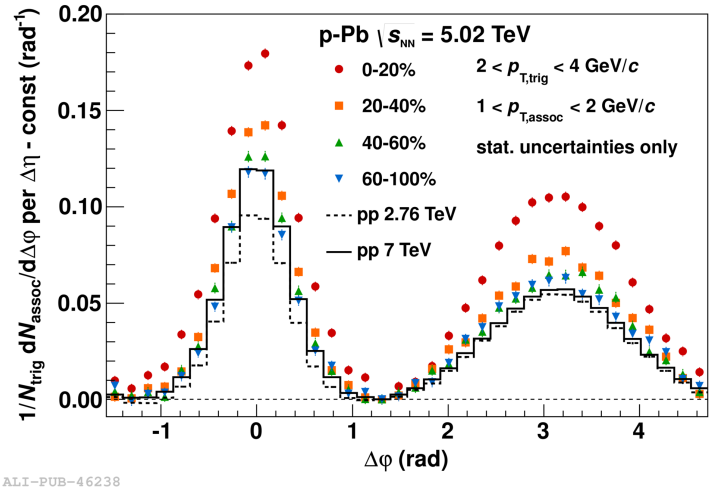

Figure 2.18 – *Associated yield per trigger particle as a function of $\Delta\phi$ averaged over $|\Delta\eta| < 1.8$ for pairs of charged particles with $2< p_{T,trig} < 4$ GeV/c and $1< p_{T,assoc} < 2$ GeV/c in p–Pb collisions at $\sqrt{s_{\rm NN}} = 5.02$ TeV for different event classes, and in pp collisions at 2.76 and 7 TeV. The yield between the peaks (determined at $\Delta\phi \approx 1.3$) has been subtracted in each case.*

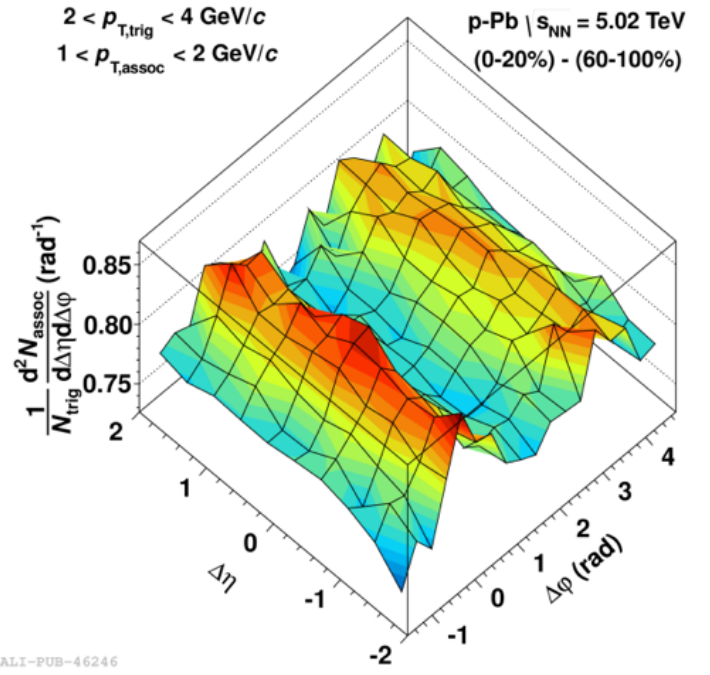

Figure 2.19 – *Associated yield per trigger particle in $\Delta\phi$ and $\Delta\eta$ for pairs of charged particles with $2 < p_{\rm T,trig} < 4$ GeV/c and $1 < p_{\rm T,assoc} < 2$ GeV/c in p–Pb collisions at $\sqrt{s_{\rm NN}} = 5.02$ TeV for the 0-20% multiplicity class, after subtraction of the associated yield obtained in the 60-100% event class.*

The bottom panel shows the projection to $\Delta\phi$, where a modulation is observed. The $\Delta\phi$ projection of the correlation distribution can be described by a Fourier decomposition up to third order, whose coefficients are denoted as Δv_n. A functional form, whose parameters are strictly related to the Fourier coefficients, is used to fit the data. An example for the fit with and without the third order of the Fourier decompositions (by means of $a_3 \cos(3\Delta\phi)$ term) is shown in the bottom panel of Fig. 2.20. The fit parameters a_2 and a_3 are a measure of the absolute modulation in the subtracted per-trigger yield and characterize a modulation relative to the baseline b in the higher multiplicity class assuming that such a modulation is not present in the 60 -100% event class. This assumption has been checked by subtracting the yields obtained in pp collisions at $\sqrt{s}$= 2.76 and 7 TeV from the yields obtained for the 60 -100% p–Pb event class and verifying that in both cases no significant signal remains. Therefore, the Fourier coefficients v_n of the corresponding single-particle distribution, commonly used in the analysis of particle correlations in nucleus-nucleus collisions, can be obtained in bins where the $p_{T,trig}$ and $p_{T,assoc}$ intervals are identical using:

$$v_n = \sqrt{a_n/b} \tag{2.2}$$

The coefficients v_2 and v_3 are shown in the left panel of Fig. 2.21 for different event classes. The coefficient v_2 increases with increasing p_{T}, and shows only a small dependence on multiplicity. In order to extract physical information on the excess distributions of the near and the away side in Fig. 2.20(bottom), the yield and the width are estimated after removing the contribution of a constant baseline from the distribution for different event classes and for different combinations of p_{T}^{trig} and p_{T}^{assoc}. The interesting result is that the near- and away-side yields always agree within uncertainties for a given sample (even if their absolute value is strongly dependent on the event class and on the p_{T} interval), leading to a common underlying physical origin for the observed ridges.
The observed compatibility of the near- and away-side ridge-like structures was also predicted with Colour Glass Condensate model calculations [130], as shown in Fig. 2.22. On the other side, the extracted v_2 and v_3 are found to be qualitatively consistent with a hydrodynamical model calculations [129] performed in the framework of event-by-event 3+1-dimensional viscous hydrodynamics [156] and reported in Fig. 2.23. Both models compared their results with the near-side ridge extracted with CMS data. Hence, there is not an exhaustive and unambiguous theoretical explanations of the origin of these long-range correlation structures. After subtracting the near-side ridge from the near side and away side symmetrically, the correlation shape in $\Delta\varphi$ becomes independent of multiplicity and similar to those of pp collisions at 7 TeV. There is no evidence in the present data for further significant structures in two-particle correlations at mid-rapidity in p–Pb collisions at $\sqrt{s_{\mathrm{NN}}} = 5.02$ TeV.
More recently, also the PHENIX and the STAR collaborations at Relativistic Heavy Ion Collider (RHIC) measured a positive v_2 coefficient for charged hadrons in high-multiplicity deuteron–gold collisions [101, 102].

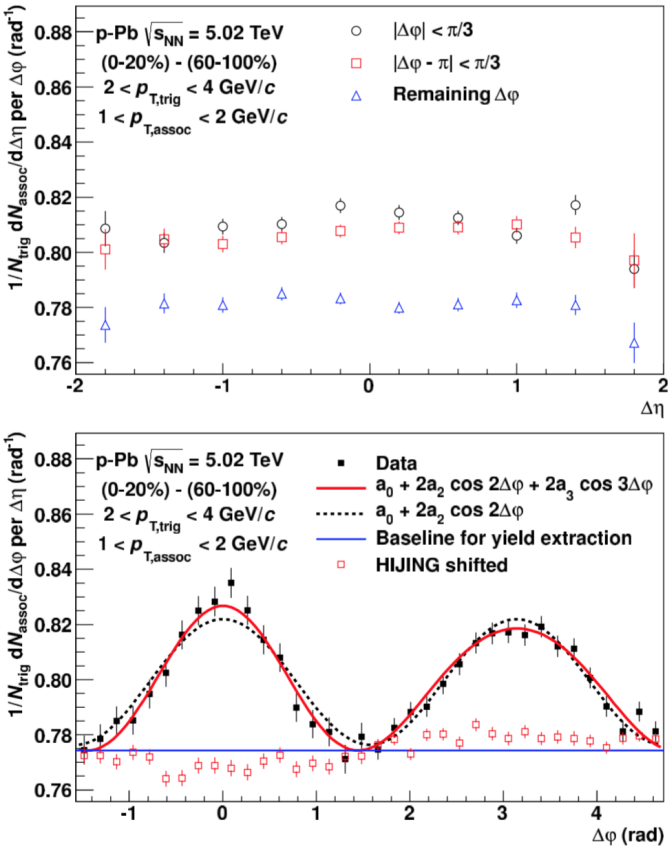

Figure 2.20 – *Top: projection of the associated per-trigger yield after subtraction onto $\Delta\eta$ averaged over $\Delta\phi < \pi/3$ (black circles), $|\Delta\phi - \pi| < \pi/3$ (red squares), and the remaining area (blue triangles). Bottom: projection onto $\Delta\phi$ averaged over $0.8 < |\Delta\eta| < 1.8$ on the near side and $|\Delta\eta| < 1.8$ on the away side. Superimposed fits containing a $\cos(2\Delta\phi)$ modulation (black dashed line) and a combination of $\cos(2\Delta\phi)$ and $\cos(3\Delta\phi)$ shapes (red solid line). The blue horizontal line shows the baseline obtained from the latter fit which is used for the yield calculation. Also shown for comparison is the subtracted associated yield when the same procedure is applied on HIJING shifted to the same baseline.*

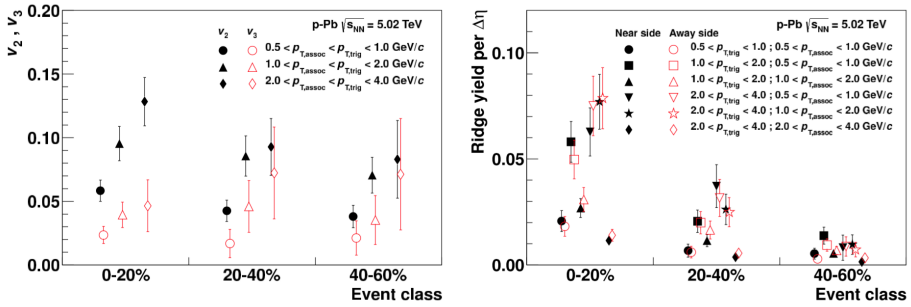

Figure 2.21 – *Left:* v_2 *(black closed symbols) and* v_3 *(red open symbols) for different multiplicity classes and overlapping* $p_{T,assoc}$ *and* $p_{T,trig}$ *intervals. Right: Near-side (black closed symbols) and away-side (red open symbols) ridge yields per unit of* $\Delta\eta$ *for different* $p_{T,trig}$ *and* $p_{T,assoc}$ *bins as a function of the multiplicity class. In both panels the points are slightly displaced horizontally for visibility.*

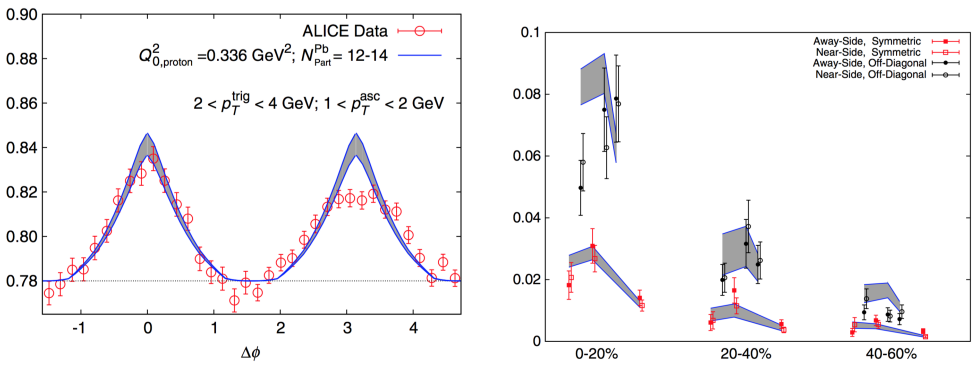

Figure 2.22 – *Left: Comparison of the 0-20% subtracted of the 60-100% azimuthal correlation distributions of ALICE data (red circles) with Color Glass Condensate predictions (grey band). Right: Comparison of near-side and away-side yield of the difference distributions along* $\Delta\phi$ *with Color Glass condensate calculations (grey bands) common* p_{T} *ranges for trigger and associated particles (black points) and for* $p_{\mathrm{T}}^{trig} > p_{\mathrm{T}}^{assoc}$ *(red points).*

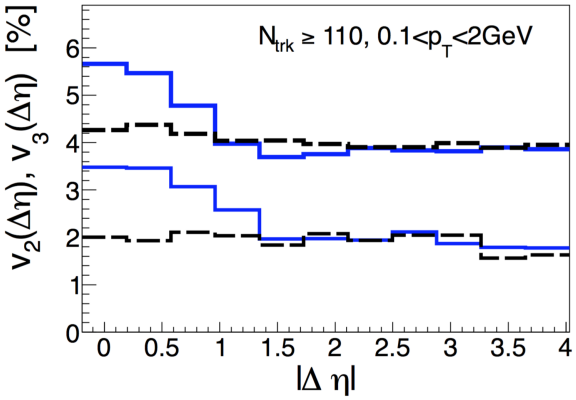

Figure 2.23 *– Hydrodynamical calculations (event-by-event 3+1-dimensional viscous hydrodynamics) for $v_2(\Delta\eta)$ (upper lines) and $v_3(\Delta\eta)$ (lower lines) from the two-particle correlations as function of the relative pseudorapidity of the particles in the pair in p–Pb collisions. The solid and dashed lines are for the unlike- and like-sign pairs, respectively.*

In the following, I will discuss only the PHENIX results.
The measurements of a the strong anisotropic long-range correlations in angular distributions of hadron pairs observed at the LHC in p–Pb collisions, have been complemented by similar but larger anisotropies arising from azimuthal di-hadron correlations near midrapidity in d+Au collisions at $\sqrt{s_{\rm NN}}$= 200 GeV [101]. Differently from previous analyses on two-particle correlations from d+Au collisions at RHIC, the observation of long-range features at small $\Delta\phi$ was possible thanks to a tight $p_{\rm T}$ selection that emphasize jet-like correlations with respect to the underlying events. In Fig. 2.24 the azimuthal correlation yields for central (0-5%) and peripheral (50-88%) events and their differences are shown. As observed for the ALICE measurement, this subtraction removes any centrality independent correlation as well as the jet component. The remaining excess structure is well described by a symmetric functional form with a dominant contribution coming from a second order sinusoidal modulation ($\cos(2\Delta\phi)$) for all the kinematic ranges analysed. From the fit parameters, the v_2 can be extracted under a factorization assumption [96, 131] and it is reported in the left panel of the Fig. 2.25. The comparison with ATLAS results [132] is also shown, revealing a qualitatively similar $p_{\rm T}$ dependence with a larger amplitude, and with two hydrodynamical calculations (both based on MC-Glauber model and with impact parameter glasma initial conditions), confirming a good agreement between the data and the model. To further investigate the origin of this effect, in the right panel of Fig. 2.25 the PHENIX measurements for both d+Au and Au+Au scaled by the eccentricity (ϵ_2), as calculated in a MC- Glauber model are reported as a function of the charged-particle multiplicity at midrapidity. The intriguing observation is that, scaling the results from RHIC and the LHC by the initial second-order participant eccentricity from a MC-Glauber model brings to a common trend as a function of

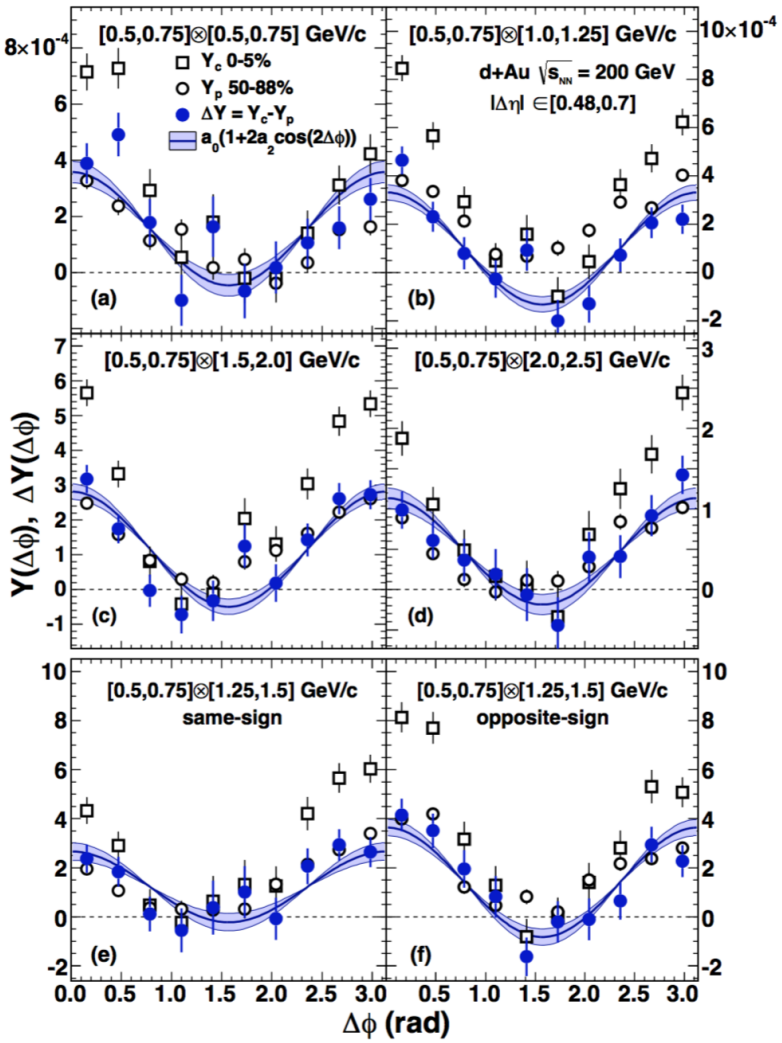

Figure 2.24 – *Azimuthal per-trigger yields for (open black squares) 0%-5% most central and (open black circles) peripheral (50%-88% least central) collisions with a minimum $\Delta\eta$ separation of 0.48 units. The difference distribution (filled blue circles), obtained subtracting the peripheral correlations, are shown. The fit function (blue curve) is also reported.*

$dN_{ch}/d\eta$.

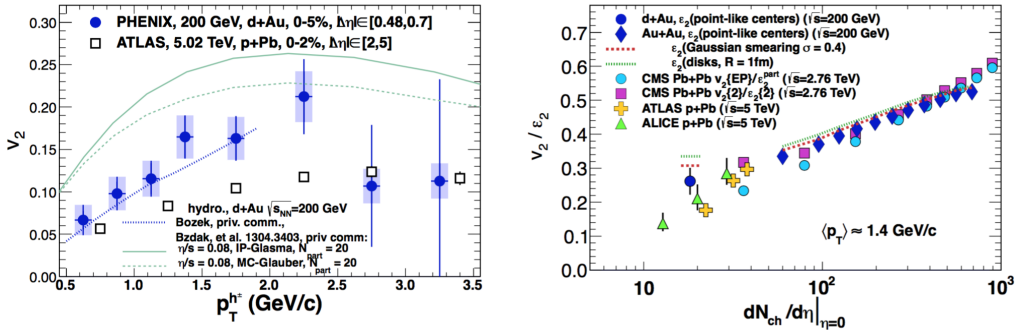

Figure 2.25 – *Left: charged hadron second-order anisotropy, v_2, as a function transverse momentum for (filled-blue circles) PHENIX and (open-black squares) ATLAS [132]. The comparison with hydrodynamic calculations from Bozek [133] (dotted-blue curve) and Bzdak et al. [134] and the MC-Glauber model initial conditions (dashed curve) is also shown. Right: d+Au and Au+Au scaled by the eccentricity (ϵ_2), as calculated in a MC- Glauber model, as a function of the charged-particle multiplicity at midrapidity.*

Interesting results about the collective behavior of small systems have been collected also in the heavy-flavour field at the LHC. Here, both CMS and ALICE, presented two independent measurements of the elliptic anisotropies of heavy-flavoured particles in p–Pb collisions via two particle-correlations. In particular CMS performed the measurement of a positive elliptic flow from the azimuthal correlations of prompt D^0 with charged hadrons, while ALICE gained a comparable result extracting the v_2 from the correlations of heavy flavour decay electrons with charged hadrons. In the following the observed v_2, published by the two LHC experiments, will be discussed.

The CMS experiment presented the first measurement of the elliptic flow anisotropies, i.e. v_2, of prompt D^0 mesons combined with strange hadrons (K^0_s, Λ, Ξ^- and Ω^-) in p–Pb collisions at a center-of-mass energy of $\sqrt{s_{\rm NN}} = 8.16$ TeV. The v_2 harmonic of all particle species in high-multiplicity p–Pb events is determined in different kinematic regions by means of the study of two-particle correlations with charged particles. The two-dimensional correlation function is constructed by pairing each D^0 candidate with primary charged particle tracks and applying several corrections such as the event mixing (in order to account for the limited acceptance and the detector inhomogeneities), the reconstruction efficiency (which is found to have a negligible effect), the subtraction of the non-prompt D^0 candidates.

Therefore, the $\Delta\phi$ correlation functions averaged on $|\Delta\eta| > 1$ (to remove short range correlations as jet fragmentation) is then obtained by projecting the 2D distributions and fitting the resulting one by the first three terms ($v_{n\Delta}$) of a Fourier series, where the residual contribution from back-to-back di-jets is removed by subtracting the low-multiplicity pPb events ($N^{offline}_{trk} < 35$) from the high-multiplicity ones ($185 < N^{offline}_{trk} < 250$).

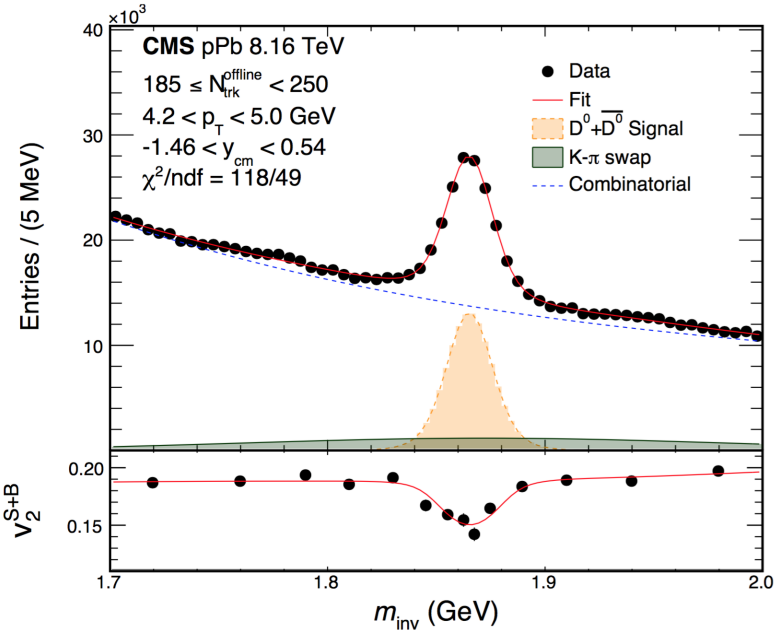

Figure 2.26 – *Simultaneous fit of the invariant mass spectrum and $v_2^{S+B}(m_{inv})$ in the $p_{\rm T}$ range: $4.2 < p_{\rm T} < 5.0$ GeV/c for high-multiplicity events ($185 \leq N_{trk}^{offline} < 250$)*

Assuming the factorization of the Fourier coefficients into the product of single-particle anisotropies, the v_n anisotropy harmonics for D^0 candidates have been extracted as a function of the D^0 invariant mass, by means of a simultaneous fit. An example of it in the $p_{\rm T}$ range of $4.2 < p_{\rm T} < 5.0$ GeV/c is reported in Fig. 2.26.
Then, the v_2 of the prompt D^0 is extracted after removing the background contribution (v_2^B) contained in the fit result. Fig. 2.27 shows the results of the v_2 measurement of the prompt D^0 meson with for -1.46 $< y_{cm} <$ 0.54 in high-multiplicity ($185 \leq N_{trk}^{offline} <$250) p–Pb collisions. The v_2 values for strange hadrons are also shown for comparison. A clear mass ordering trend in the elliptic flow is observed. Indeed, in the low-$p_{\rm T}$ region of $\leq$ 2.5 GeV, heavier particle species have a smaller v_2 signal at a given $p_{\rm T}$ value. For larger $p_{\rm T}$ ($p_{\rm T} >$ 2.5 GeV), v_2 values for Λ, Ξ^- and Ω^- baryons, which are similar to each other, all become higher than those of D^0 and K_S^0 mesons.
More recently, the ALICE collaboration presented the measurement of v_2 for open heavy-flavour particles at mid-rapidity in high- multiplicity p–Pb collisions at $\sqrt{s_{\rm NN}}$ = 5.02 TeV via azimuthal correlations of electrons from charm- and beauty-hadron decays, and charged particles. This result complements ALICE previous studies of hidden charm particles based on the measurement of the correlations between J/ψ mesons at forward rapidity and charged particles at mid-rapidity in high-multiplicity p–Pb collisions at $\sqrt{s_{\rm NN}}$= 5.02 TeV and 8.16 TeV, which found evidences for a positive v_2 for J/ψ mesons [136]. The ALICE collaboration also measured a positive v_2 for muons at forward and back-

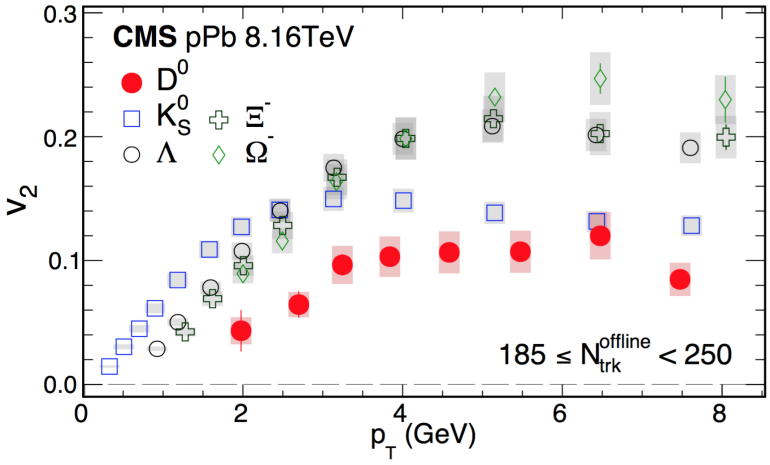

Figure 2.27 – *Elliptic flow (v_2) for D^0 mesons and for K^0_s, Λ, Ξ^- and Ω^- particles as functions of $p_{\rm T}$ for -1.46 < y_{cm} < 0.54 in high-multiplicity ($185 \leq N^{offline}_{trk} < 250$) p–Pb collisions at $\sqrt{s_{\rm NN}}$ = 8.16 TeV.*

ward rapidity, which are predominantly produced by heavy-flavour decays for transverse momentum ($p_{\rm T}$) greater than 2 GeV/c, in high-multiplicity p–Pb collisions at $\sqrt{s_{\rm NN}}$ = 5.02 TeV [141]. The two-particle correlation distributions between electrons (trigger) and

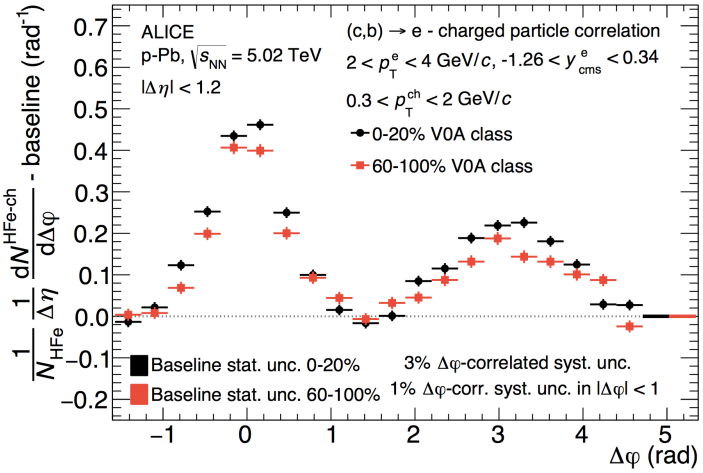

Figure 2.28 – *Azimuthal correlations between heavy-flavour decay electrons and charged particles, for high-multiplicity and low-multiplicity p–Pb collisions, after subtracting the baseline for $2 < p^e_{\rm T} < 4$ GeV/c and $0.3 < p^{ch}_{\rm T} < 2$ GeV/c. Statistical uncertainties are shown as error bars. The statistical uncertainties on the baseline subtraction are represented as boxes at $\Delta\varphi \sim 5$.*

charged (associated) particles were obtained for three different $p_{\rm T}$ intervals ($1.5 < p_{\rm T} <$

2 GeV/c, 2 $< p_{\rm T} <$4 GeV/c and 4$< p_{\rm T} <$ 6 GeV/c) in two centrality classes (0-20% and 60-100%). Associated charged particles with 0.3 $< p_{\rm T}^{ch} <$ 2 GeV/c and $|\eta| <$ 0.8 were selected with similar criteria as used for electrons: particle identifications by means of TPC and TOF. After applying several corrections on the two-correlation distribution (event-mixing, efficiency reconstructions, contamination of secondaries, hadron contamination on the electron sample), the azimuthal correlation distribution was projected onto $\Delta\phi$ for $|\Delta\eta| <$1.2 and divided by the width of the selected $\Delta\eta$ interval. In order to compare the jet-induced peaks from different multiplicity ranges, a "baseline" term, constant in $\Delta\phi$, was calculated from the weighted average of the three lowest points of the correlation distribution (following the zero yield at minimum, ZYAM, approach [138]) and was subtracted from it. The resulting correlation distributions in the two considered multiplicity classes (0-20% and 60-100%) are shown in Fig. 2.28 for the interval 2 $< p_{\rm T}^{e} <$ 4 GeV/c. An enhancement of the near- and away-side peaks is present in high-multiplicity collisions.

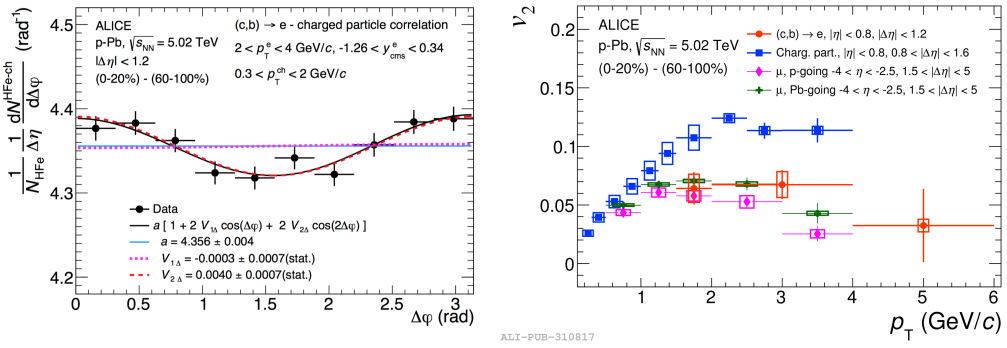

Figure 2.29 *– Left: azimuthal correlation distribution between heavy-flavour decay electrons and charged particles, for high-multiplicity p–Pb collisions after subtracting the jet contribution based on low-multiplicity collisions. The distribution is shown for 2 $< p_{\rm T}^{e} <$ 4 GeV/c and 0.3 $< p_{\rm T}^{ch} <$2 GeV/c. The fit to the data points and its Fourier decomposition are also shown. Right: heavy-flavour decay electron v_2 as a function of transverse momentum compared to the v_2 of unidentified charged particles [139] and inclusive muons [141]. Statistical and systematic uncertainties are shown as bars and boxes, respectively.*

To study this feature, the baseline-subtracted correlation distribution obtained in low-multiplicity events was subtracted from the correlation distribution measured in high-multiplicity events. This removes the jet-induced correlation peaks, under the assumption that they are the same in low- and high-multiplicity events. The correlation distribution was restricted to the (0,π) range by reflecting the symmetrical points. The resulting distribution shows an azimuthal anisotropy compatible with the presence of a dominant second-order ($V_{2\Delta}^{HFe-ch}$) modulation in its Fourier decomposition, as shown in the left panel of Fig. 2.29. The $V_{2\Delta}^{HFe-ch}$ coefficient was extracted by fitting the distribution in Fig. 2.29. The v_2^{HFe} values were obtained assuming the $V_{2\Delta}^{HFe-ch}$ factorization in single-

particle v_2 coefficients [131] and evaluating the v_2^{ch} values from the weighted average of the values measured in smaller $p_{\rm T}^{ch}$ ranges [139]. The v_2^{HFe} values are reported in the right panel of the Fig. 2.29 and compared to those measured for charged particles, dominated by light-flavour hadrons, and inclusive muons at large rapidity (in p-going and Pb-going directions), which are mostly coming from heavy-flavour hadron decays for $p_{\rm T}^{\mu} > 2$ GeV/c [141].

2.4.3 Results in A–A collisions

As discussed in the section 2.2, in nucleus-nucleus collisions the interaction of partons with the QGP medium results in the away-side peak suppression. It was observed for the first time by STAR [118,119] and PHENIX [81] experiments at RHIC, by comparing the correlation of charged particles with respect to a high-$p_{\rm T}$ trigger particle in Au-Au, d-Au and pp collisions, all at $\sqrt{s_{\rm NN}} = 200$ GeV. In Fig. 2.16, the two-particle azimuthal distribution normalized to the number of trigger particles, measured by STAR in d-Au collisions and Au–Au collisions, compared to results from pp collisions was reported. In the Au-Au case, the away side peak shows a dramatic suppression, leaving a flat distribution of azimuthal correlations in the $\Delta\varphi$ region. The shape of the near-side, instead, reveal a very similar trend to the pp one. An interesting study of dijets in central Au–Au collisions, in different kinematic regions has been published by STAR [119]. Here the behavior of the away-side peak reveals to be strongly dependent even on the $p_{\rm T}$ of the trigger particle. To this purpose, Fig. 2.30 shows di-hadron azimuthal distributions normalized per-trigger particle for central (0-5%) Au–Au collisions. The results are reported in three intervals of the trigger transverse momentum, increasing from left to right, and in two different ranges of the associated particle $p_{\rm T}$ (top and bottom panels in the figure). The height of the baseline, which is related to the inclusive yield, is strictly dependent to the $p_{\rm T}$ of the associated tracks, indeed it is similar for different $p_{\rm T}$ of the trigger particle in each $p_{\rm T}^{assoc}$ interval. Increasing the $p_{\rm T}^{assoc}$, the height of the baseline decreases dramatically. At the lowest $p_{\rm T}^{trig}$, the away-side peak is completely missing (it is consistent with the previous study of $\Delta\varphi$ correlation studies in central Au–Au events and in similar kinematic regions). An away-side peak emerges when going to larger $p_{\rm T}$ of the triggers. The narrow, back-to-back peaks reflect the azimuthally back-to-back nature of di-jets observed in elementary collisions. Near-side peaks are clearly visible in all the kinematic ranges shown and indicate larger yields for higher $p_{\rm T}^{trig}$ at fixed $p_{\rm T}^{assoc}$, as expected for correlations dominated by jet fragmentation.
In the same analysis, also a comparison with two-particle correlations in d-Au collisions and in two centrality class in Au–Au events is addressed by exploiting the behavior of the fragmentation function $D(z_T)$ (where z_T is defined as: $z_T = p_{\rm T}^{assoc}/p_{\rm T}^{trig}$) as a function of the z_T. Fig. 2.31 shows the per trigger-normalized fragment distribution $D(z_T)$ for both near- and away-side. The z_T range corresponds to the $p_{\rm T}^{assoc}$ range for which dijets are observed above background (see Fig.2.31). The near-side distributions are very

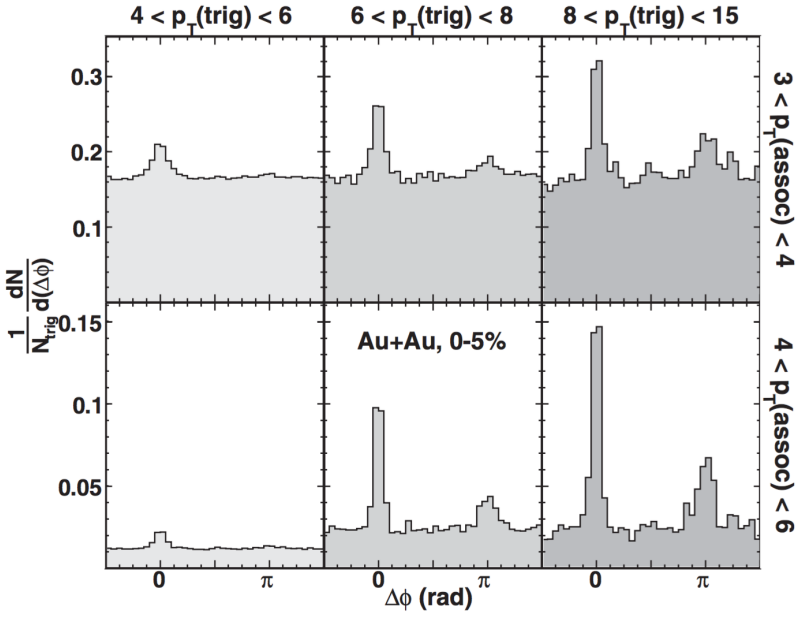

Figure 2.30 – *Azimuthal correlation histograms of high p_{T} charged hadron pairs for 0-5% Au-Au collisions, for various p_{T}^{trig} and p_{T}^{assoc}. In the lower left panel, the yield is suppressed due to the constraint $p_{\mathrm{T}}^{assoc} < p_{\mathrm{T}}^{trig}$.*

similar among the three systems (d-Au, Au–Au in 0-5% and Au–Au in 20-40%) and over a broad range of z_T. Such similarities in the three systems reveal a small near-side energy loss (arising from shorter in-medium path lengths). The away-side distributions are characterized by similar exponential trends (the exponential fit are reported with solid and dashed lines in the right panel of the figure), but different magnitude among the three systems denoting its suppression in high-multiplicity events. As one can also observe from Fig. 2.30, the width of the away-side azimuthal distribution for high p_{T} pairs is also independent on the centrality, revealing that the strong suppression of the away-side taking place at high-p_{T} is not combined with a significant modification of the momentum distribution. The bottom panel of the Fig. 2.31 shows the ratio of near-(left) and away-side(right) fragmentation function $D(z_T)$ for the two Au–Au centrality class with respect to the d-Au events. In all the analysed cases, the ratio is independent on z_T. For the away-side the suppression hierarchy is clearly visible in the plot.

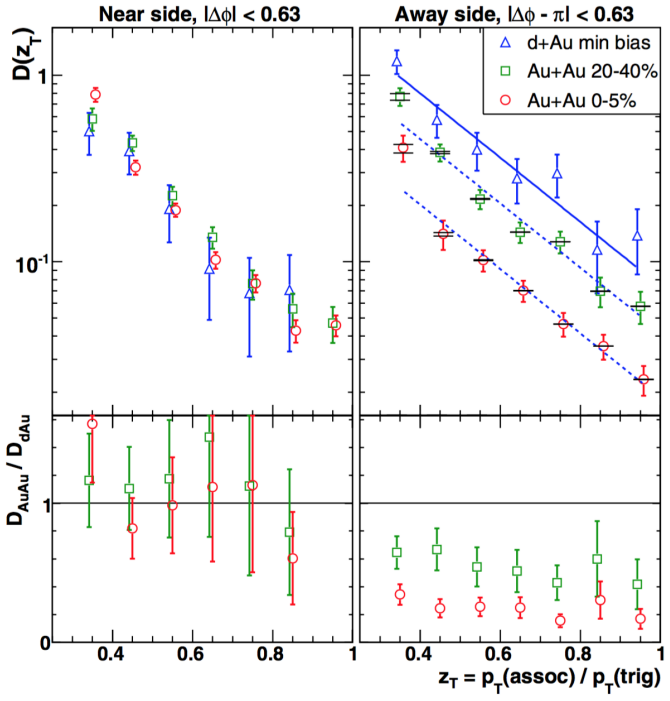

Figure 2.31 *– Top panels: $D(z_T)$ with $8 < p_{\mathrm{T}}^{trig} < 15$ GeV/c for near- (left) and away-side (right) correlations in d-Au and Au–Au collisions at $\sqrt{s_{\mathrm{NN}}} = 200$ GeV. The exponential fit are superimposed for the away-side distribution. Bottom: ratio of near-(left) and away-side(right) fragmentation function $D(z_T)$ for the two Au–Au centrality class with respect to the d-Au events.*

At the LHC, the much larger cross section for jet production opened a new kinematic regime for jet quenching studies in heavy ion collisions, increasing at the same time the accuracy of the measurements performed at RHIC. The suppression of charged hadrons

in central Pb–Pb collisions at $\sqrt{s_{\rm NN}}$ = 2.76 TeV has been observed with the ALICE experiment together with a strong di-jet energy asymmetry reported by the ATLAS and CMS collaborations. In the following, I will report the modification of the per-trigger yield of associated particles, extracted from di-hadron correlations in central and peripheral Pb–Pb collisions at $\sqrt{s_{\rm NN}}$ = 2.76 TeV with ALICE [140]. This measurement, combined with the R_{AA}, provides strong constraints on the quenching mechanism in the hot and dense matter produced in heavy ion collisions.

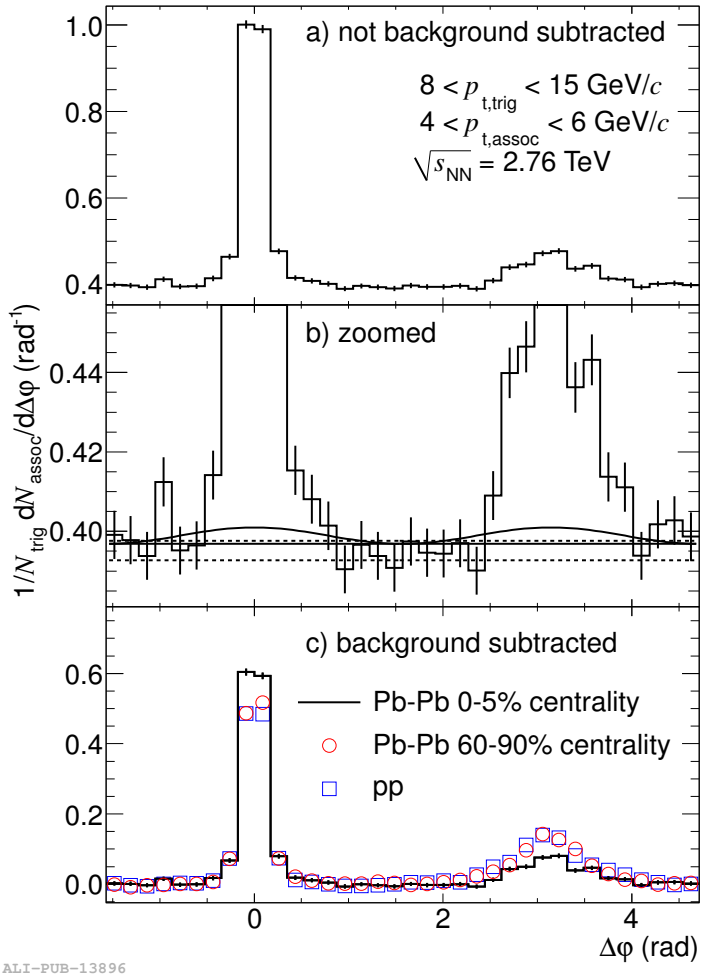

Figure 2.32 – *Corrected per-trigger pair yield for 4 < $p_{\rm T}^{assoc}$ < 6 GeV/c for central Pb–Pb events (histogram), peripheral Pb–Pb events (red circles) and pp events (blue squares). a) azimuthal correlation; b) zoom on the region where the pedestal values (horizontal lines) and the v_2 component ($\cos 2\Delta\varphi$) are indicated; c) background-subtracted distributions using the flat pedestal.*

Fig. 2.32 (a) shows a typical distribution of the corrected per-trigger pair yield before background subtraction. The integrated associated yield is identified as the signal over a

flat background. Fig. 2.32(b) illustrates the background determination. Also indicated is a background shape accounting for a non zero elliptic flow $v_{2\Delta}$. In Fig. 2.32(c) the flat-pedestal subtracted distributions of central and peripheral Pb–Pb collisions are compared to that of pp collisions. The integral over those distributions in the region where the signal is significantly above the background,

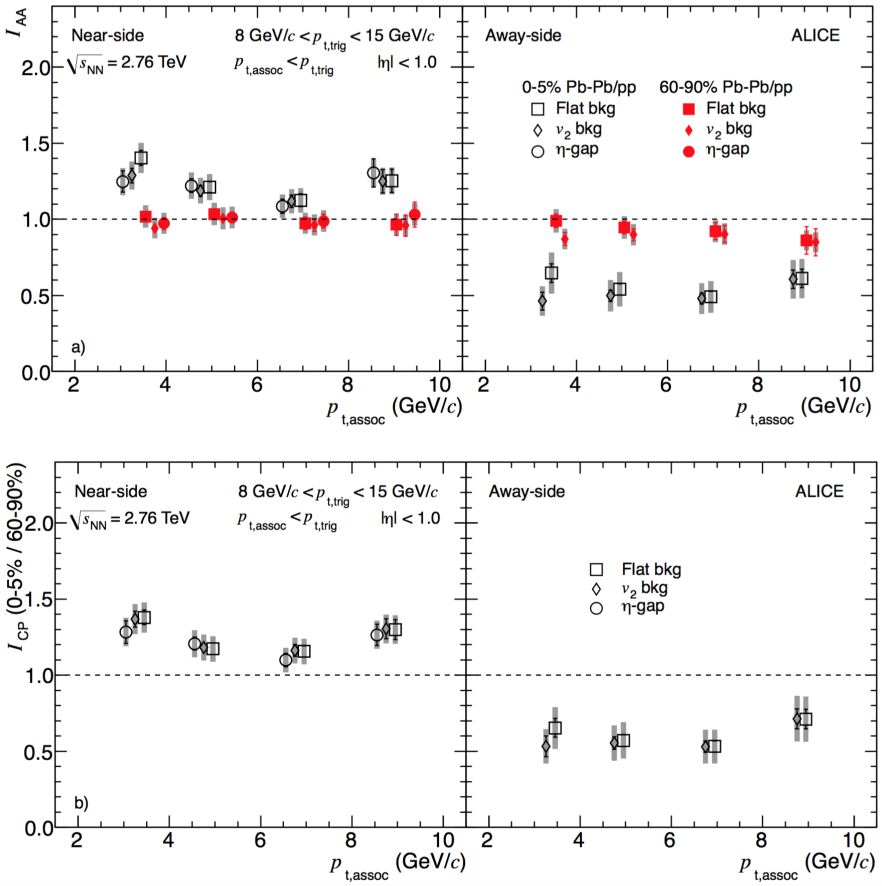

Figure 2.33 *– a) I_{AA} for central (0-5% Pb–Pb/pp, open black symbols) and peripheral (60-90% Pb–Pb/pp, filled red symbols) collisions and b) I_{CP}. Results using different background subtraction schemes are presented: using a flat pedestal (squares), using v_2 subtraction (diamonds) and subtracting the large $|\Delta\eta|$-region (circles, only on the near-side). In the plots, data points are slightly displaced on the p_{T}^{assoc}-axis.*

In order to quantitatively describe the two-particle correlation results in Pb–Pb collisions, two observables are introduced: I_{AA} and I_{CP}. I_{AA} is defined as the ratio of the particle yield in the near side (or away side) peak of the azimuthal correlation distribution in heavy ion collisions over the yield in pp collisions. In particular, on the near side, I_{AA} describes the features of the fragmenting jet escaping the medium, while on the away

side it quantifies the probability that the other parton from the hard scattering survives the passage through the fireball. In Fig. 2.33 measurements of the I_{AA} observable are shown, performed by ALICE in Pb–Pb collisions for different centralities at $\sqrt{s_{\rm NN}} = 2.76$ TeV. In the absence of effects originating from the nuclear medium on the jet production in heavy ion collisions, a value of $I_{AA} = 1$ is expected; while an $I_{AA} > (<) 1$ signals an enhancement (suppression) of the number of particles present in the jets in those collisions. According to ALICE measurements, no particular medium effects are present in peripheral collisions, for both near-side and away-side peaks (red points). Significant effects are instead visible for the most central collisions. Here a slight enhancement (20-30%) of the yield occurs in the near side peaks, never observed before in experiments at lower energies. Several effects could produce this enhancement, i.e. a softening of the fragmentation functions in the medium, a change of the quark/gluon jet ratio with respect to pp collisions or some bias in the parton $p_{\rm T}$ spectrum after the energy loss due to the trigger particle selection. In general, all the three effects are expected to contribute. By studying I_{AA} in the away side, instead, a decrease of the yield is evident, due to the parton in-medium energy loss. The suppression is weaker by about 50% with respect to measurements made at RHIC.
I_{CP} is defined as the ratio of the particle yield in the near side (or away side) peak of the azimuthal correlation distribution in central over the yield in peripheral heavy ion collisions. In the bottom panel of Fig. 2.33, I_{CP} is consistent with I_{AA} in central collisions with respect to the near-side enhancement and the away-side suppression. These measurements represent the first observation of a significant near-side enhancement of I_{AA} and I_{CP} in the $p_{\rm T}$ region studied. This enhancement suggests that the near-side parton is also subject to medium effects.

3

The ALICE experiment at the LHC

3.1 The Large Hadron Collider

The Large Hadron Collider (LHC), with a circumference of 27 km, is the world largest and most powerful hadron collider ever built. It has been constructed by the European Organisation of Nuclear Research (CERN) starting from 2001, after the Large Electron Positron (LEP) decomisioning, at a depth between 50 and 175 m underground. A schematic view of the whole LHC accelerator chain is shown in Fig. 3.1. Before reaching the LHC ring, particle beams (extracted from a tank of hydrogen gas) experience several steps of increasing acceleration. The first stage of the acceleration takes place on the Linac2, a linear accelerator with an output proton energy of 50 MeV. The beam is then injected into the Proton Synchrotron Booster (PSB), which increases the energy up to 1.4 GeV and then into the Proton Synchrotron (PS). This accelerates the beam to 26 GeV and injects it into the Super Proton Synchrotron (SPS), where the protons reach an energy of 450 GeV and are finally transferred to two LHC beam pipes for the start of the ramp up to the energy of 7 TeV. Thousands superconducting dipoles and hundreds of smaller magnets are used, respectively, to bend the beam along the circular path and to operate the beam focusing. The magnetic field (B $\sim$ 8.3 Tesla) necessary to provide the required bending power led to the construction of dipoles cooled using superfluid liquid helium down to a temperature of T = 1.9 K, which was one of the most technologically challenging part of the accelerator. At the nominal configuration, LHC accelerates protons grouped in 2808 bunches per beam and reaches a nominal instantaneous luminosity for pp collisions, with a bunch crossing every 25 ns, of 10^{34} $s^{-1}cm^{-2}$. The lead beams, for the heavy-ion program, follow a quite different path. Indeed, lead atoms (extracted from a small pure lead source) are accelerated in a linear accelerator (Linac3) up to 4.5 MeV per nucleon and are subsequentely injected in the Low Energy Ion Ring (LEIR),

where they become fully ionized. Finally, ions are injected into the PS where they follow the same proton route, reaching the LHC in bunches of 7×10^7 lead ions and a nominal luminosity of $10^{27}\mathrm{s}^{-1}\mathrm{cm}^{-2}$.

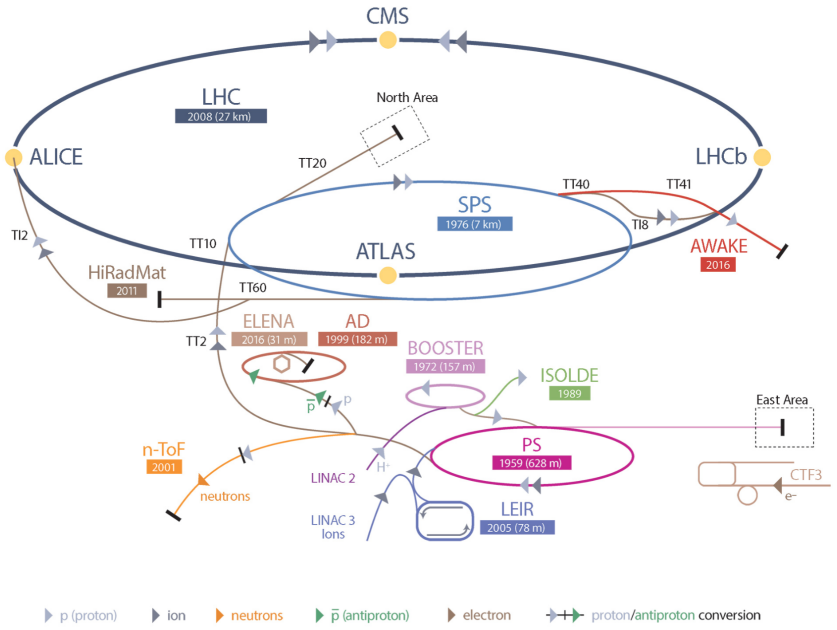

Figure 3.1 *– Layout of the CERN accelerator complex. The acceleration routes followed by the different particle species are depicted in different colors.*

3.2 The ALICE experiment

ALICE (*A Large Hadron Collider Experiment*) is the LHC experiment completely focused to the heavy-ion physics. The aim of ALICE is to study the matter behavior under the critical experimental conditions expected for the ultra-relativistic Pb–Pb collisions at the LHC energy scale. One of the major challenge faced during the ALICE design was to have a detector able to handle the huge amount of particles produced in heavy-ion collisions. Moreover, the study of the matter under high densities and temperatures required the capability to reconstruct tracks down to low momenta and to identify them on a wide momentum range. For these reasons, ALICE detectors were designed to have high granularity, a low transverse momentum (p_{T}) threshold, a precise vertexing of particle near the interaction point and a good performance in the particle identification. These requirements led to a very different design for the ALICE detector with respect to the other pp-devoted experiments al LHC.

A schematic view of the ALICE layout is shown in Fig.3.2. ALICE, with an overall dimensions of $16\times16\times26$ m^3 and a total weight of $\sim$10000 tons is one of the smallest

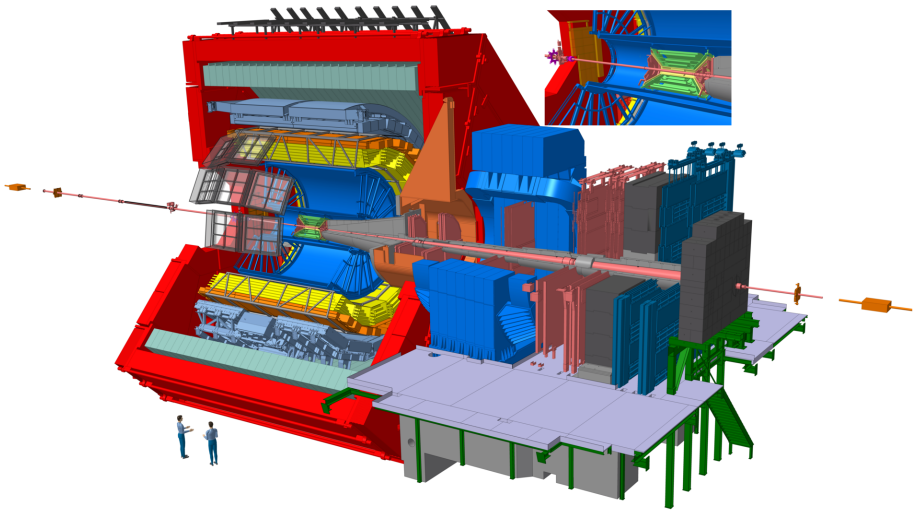

Figure 3.2 *– Layout of the ALICE detector at the LHC. The upper-right panel provides a detailed view of the Inner Tracking System (ITS) detectors.*

detectors at the LHC. The apparatus consists of three main parts:

- **central barrel**: embedded in a large solenoidal magnet which produces a moderate magnetic field of B = 0.5 T. It covers the full azimuth and the pseudorapidity interval $|\eta|<0.9$. It consists of an Inner Tracking System (ITS), with six layers of silicon vertex detectors, optimised for vertex reconstruction and tracking; a cylindrical Time Projection Chamber (TPC), surrounding the ITS, that is the main tracking detector; a Transition Radiation Detector (TRD), aimed to the electron identification; a barrel-shaped Time of Flight (TOF) detector, that provides pion, proton and kaon identification; a small-area ring imaging Cherenkov detector (High Momentum Particle IDentification); a Photon Spectrometer (PHOS); an electromagnetic calorimeters (EMCal) and a Di-Jet Calorimeter (DCal) and the ALICE Cosmic Ray Detector (ACORDE).
- **forward muon spectrometer**: devoted to the detection of muons in the pseudorapidity range $-4<\eta<-2.5$.
- **forward detectors**: ALICE set-up is completed by small detectors optimised for the event selection and for global-event features measurements in the forward rapidity region. It consists of a forward photon counting detector (Photon Multiplicity Detector, PMD), a multiplicity detector (Forward Multiplicity Detector, FMD), two arrays of segmented scintillator counters (VZERO detector) and quartz counters (T0 detectors) and two calorimeters (Zero Degree Calorimeters, ZDC) located on both side of the interaction region.

A more detailed description of the main detectors used for the analysis reported in

this thesis and their performance will be provided in the next sections. In [1] more informations about the other detectors can be found.

3.2.1 Magnet

ALICE magnet is the one already installed for the L3 experiment at LEP and it produces a fairly low solenoidal magnetic field (B $<$ 0.5 T). The field strength is the results of a compromise between a good track-momentum resolution and, at the same time, a reasonable acceptance at low momentum. For this reason, the momentum cut-off should be as low as possible: $p_{\mathrm{cut-off}}$=0.3 BR$\sim$ 0.2 GeV/c, where B is the magnetic field expressed in Tesla and R is the minimum radius for a particle to traverse the entire TPC. Tracks with lower momentum can be reconstructed with the Inner Tracking System.

3.2.2 Inner Tracking System (ITS)

The Inner Tracking System is the innermost detector of the ALICE central barrel. The main goals of the ITS are to reconstruct primary and secondary vertices with high resolution, to track and identify low transverse momentum particles (down to 100 MeV/c) that are not tracked in the TPC due to acceptance limitation and to improve the overall momentum and angular measurements of higher-p_{T} particles traversing the TPC. It is composed of six cylindrical layers of silicon detectors placed coaxially around the beam pipe, at a distance ranging from 3.9 cm to 44 cm and covering the pseudo-rapidity range $|\eta|<$ 0.9. The two innermost layers are Silicon Pixel Detectors (SPD), located at radii between 4 cm and 7 cm. The two middle layers are made of Silicon Drift Detectors (SDD) and are placed at r= 14 and 24 cm. The two outermost layers, located at r = 39 and 44 cm, are made of Silicon micro-Strip detectors (SSD). Furthermore, the SDD and SSD subsystems contribute to the PID by measuring the specific energy deposit in the $1/\beta^2$ region of Bethe-Bloch curve. All the ITS detectors were carefully optimized to minimize the material budget, achieving a record radiation length of 0.83-1.26% X_0 per layer, the lowest value among all the current LHC experiments. A schematic view of the ITS detector is shown in Fig.3.3.

Silicon Pixel Detector

The two innermost layers of the ITS, equipped with pixel detectors (SPD), have a crucial role in primary vertex reconstruction and secondary vertex tagging. Being very close to the beam pipe, this subsystem deals with high track density (up to 50 tracks/cm^2); hence, it was realized with high-granularity pixels of very small dimensions, with excellent resolution and two-track separation capabilities. Each pixel is made of a diode junction with reverse bias and has a dimension of 50 μm ($r\phi$) 425 μm (z), which grants an intrinsic spatial resolution of 12 ($r\phi$) $\times$100 (z) μm^2. The readout channels were connected to the pixels by bump-bonding the sensor to the readout chip.The output of each pixel is a

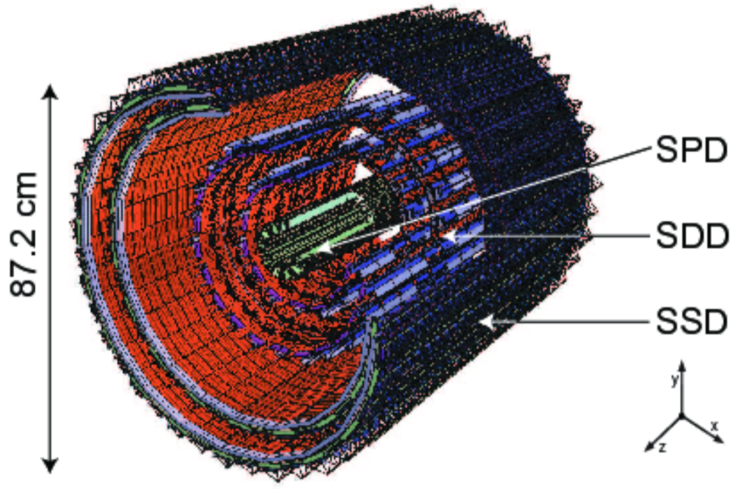

Figure 3.3 *– Schematic view of the Inner Tracking System.*

digital signal, without any information on the energy release of the crossing particle.

Five sets of pixel arrays are accommodated into a ladder, a silicon layer 200 μm thick with 12.8 mm ($r\phi$) 69.6 mm (z) sizes, while two ladders compose a half-stave, the basic detector element. The two SPD layers are composed of 60 staves (each is made of two half-staves and covers the full SPD length), for a total of about $9.8 \cdot 10^6$ pixels. The staves are slightly tilted and displaced, according to a turbo geometry, in order to ensure a coverage of the azimuthal angle without holes. In addition to tracking and vertexing, the SPD can provide a first level (L0) trigger signal and it is commonly used in the definition of the selection of minimum-bias events, in all collision systems. It can also be used to define rare triggers, e.g. the one selecting high multiplicity events in pp collision. When at least one of the pixels of a chip array is red, the chip generates a FAST-OR signal, which is able to reach the Central Trigger Preprocessor (CTP) with an overall time latency from the time of the interaction of about 800 ns [142].

Silicon Drift Detector

The two central layers of the ITS are composed of drift detectors (SDD). The SDD layers cover a range of pseudorapidity $|\eta| < 0.9$ range and the full azimuthal angle and grant a good performance in track separation and energy loss (via dE/dx) measurement capability. The SDD measure the drift time of the electrons created by a particle traversing the active region. Each SDD layer is composed of modules, 84 for the inner and 176 for outer layers; each module is split in two drift regions separated by a central cathode

strip. The cathode strips provide the electric field needed for charge drifting (intensity of approximately 500 V/cm). On each drift region, 256 anodes provide the charge collection.
Thus, when a particle crosses the active region of one module, generating e-h pairs, the electrons move from the generation points to the anodes, located at the edge of the modules. From the time needed to collect all the generated electrons, it is possible to get the $r\phi$ coordinate of the track crossing point. The z coordinate can be obtained from the centroid of the collected charge distribution. Moreover, since the collected charge is proportional to the energy release of the crossing particle, the SDD contributes also to the particle identification. The SDD subsystem has an intrinsic spatial resolution of 35 μm along $r\phi$, slightly worse than SPD, and 20 μm along z, the best of the ITS subsystems for this coordinate.

Silicon Strip Detector

The Silicon Strip Detector (SSD), composed of 1698 double-sided microstrip silicon sensors, comprises the two outermost layers of the ITS. It has the same azimuthal and pseudorapidity coverage as the SDD with a very good intrinsic spatial resolution in the $r\phi$ direction (20 μm). On the contrary, due to the strip length and the stereo angle it suffers of a poorer resolution along the z direction (about 830 μm). Since it is the outer ITS subsystem, the SSD plays a strategical role in combining tracks from the ITS to the TPC or vice-versa. Each microstrip sensor has a surface of 75×42 mm^2 and it is readable by two hybrid circuits. A microstrip with its two readout circuits constitutes the basic SDD structure, commonly referred to as "module". In the sensor area of each module 768 strips are implanted on each side; each strip is 40 mm long and there is a 95 μm pitch between two adjacent strips. The strips are not perpendicular to the sensor edges, but are slightly tilted, leading to a stereoscopic angle of 35 $mrad$ between the strips on the two sides. This particular configuration was chosen in order to remove the ambiguities that could arise in the event reconstruction ("ghost" hits). The working mechanism of the SSD relies on the collection at the edges of the strips of the e-h pairs created by the passage of a charged track trough the sensors, providing a two dimensional measurement of the position of the track crossing point. Also for this subsystem the quantity of charge collected is related to the energy deposited by the crossing particle, allowing particle identification via dE/dx measurement.

3.2.3 Time Projection Chamber

The TPC is the main tracking detector of the ALICE experiment. The choice of this kind of detector, notably slower compared to other tracking detectors, was based on the need of an efficient and robust device able to face the large amount of charged particles (designed to handle up to ∼8000 charged particles) within its geometrical acceptance, guaranteeing at the same time a good performance in track finding, momentum measurement, as well

as particle identification via specific energy loss ($\mathrm{d}E/\mathrm{d}x$) measurements. Moreover, the ALICE TPC represents the largest and the lightest detector of this specific kind ever built. In particular, the overall amount of material employed in the TPC is comparable to that of the ITS.A schematic view of the detector is shown in Fig. 3.4. As for other ALICE detectors, its design was aimed not only to gain the best performances but also to employ the lowest possible material budgets, realized through an appropriate choice of materials, gas and environmental controls.

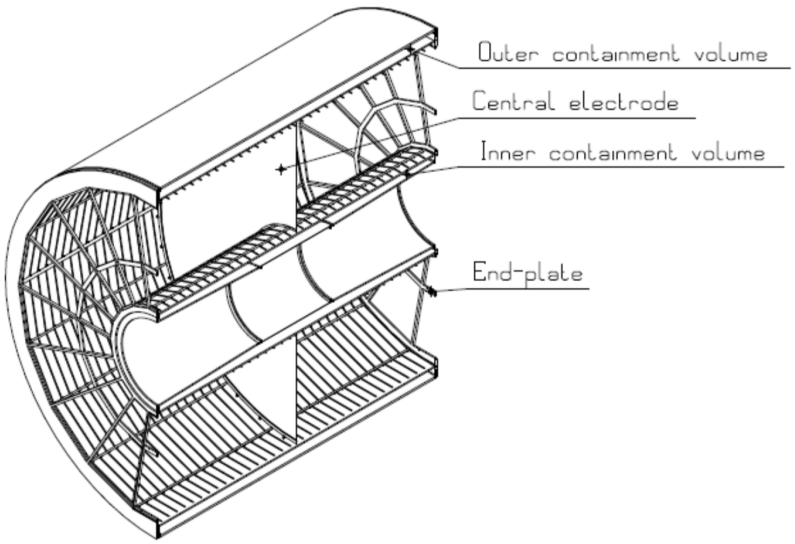

Figure 3.4 *– A view of the ALICE Time Projection Chamber.*

The TPC covers the whole azimuthal range of 2π, whereas in terms of measured p_{T} of the track, it can cover a range from $\simeq$150 MeV/c up to hundreds of GeV/c, with good effective resolution. It has a cylindrical shape with inner and outer radius of 80 and 250 cm, respectively, and an overall length in the beam direction of 500 cm. The minimum inner radius of the TPC was determined by the maximum acceptable hit density. The outer radius was defined by the minimum length required for a $\mathrm{d}E/\mathrm{d}x$ resolution better than 10%. At smaller radii (and larger track densities), tracking is performed by the ITS which grants a better resolution. The TPC covers an acceptance of $|\eta| < 0.9$. It is a chamber full of high-purity gas aimed to transport ionization electrons over long distances (2.5 m) towards the read-out end-plates. The current mixture of gas is composed by Ar/CO_2 (90%/10%); originally it was: $Ne/CO_2/N_2$ (90%/10%/5%). It is composed by a central high-voltage (HV) electrode which divides the gas volume into two symmetric drift regions, and two opposite axial potential degraders to create a highly uniform electrostatic field of up to 400 V/cm, as shown in Fig.3.4. Charged particles traversing the gas create a ionization trace that will move at constant velocity drift towards one of the two end-plates. The density of ionization depends on the velocity and on the particle mass. Once

on the end-plate, readout chambers amplify the signals of particle tracks. The end-plates are segmented into 18 trapezoidal sectors and equipped with multi-wire proportional chambers covering an overall active area of 32.5 m^2. Particle Identification (PID) with the

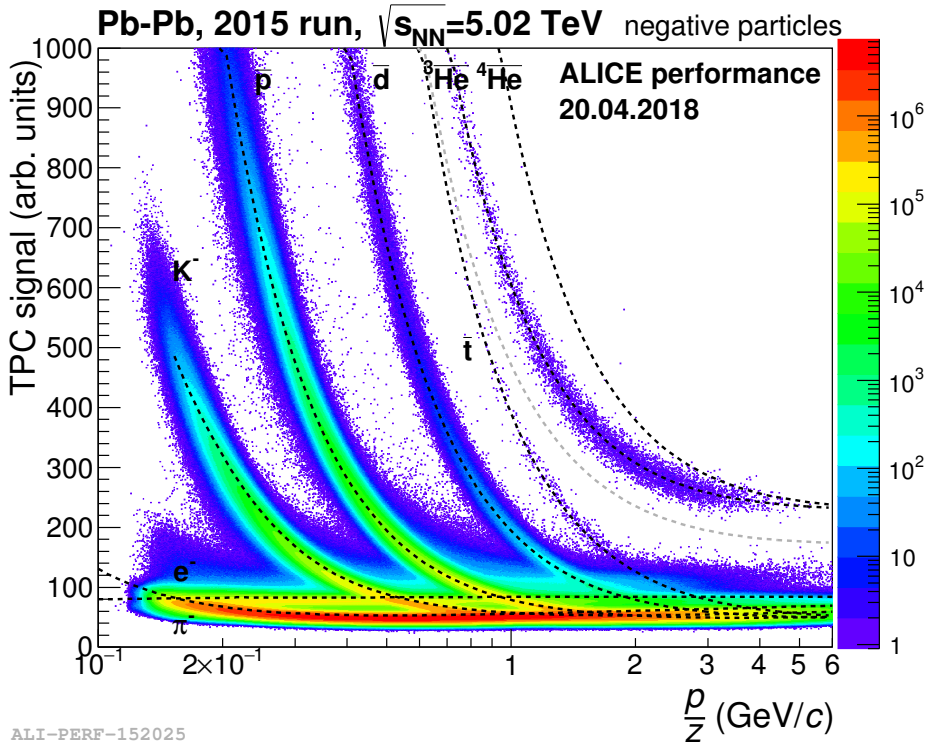

Figure 3.5 *– Distribution of the energy-loss signal in the TPC as a function of the momentum. The lines show the parameterizations of the expected mean energy loss.*

TPC is performed over a wide momentum range. It is made by simultaneously measuring the specific energy loss, the charge and the momentum of the particles traversing the detector gas. The maximum number of clusters associated to a track in the TPC is 159 and the dE/dx value of the track is determined using a truncated mean. The $\mathrm{d}E/\mathrm{d}x$, described by the Bethe Bloch formula, is parameterized by a function developed by ALEPH Collaboration:

$$f(\beta_\gamma) = \frac{P_1}{\beta^{P_4}}(P_2 - \beta^{P_4} - ln(P_3 + \frac{1}{(\beta_\gamma)^{P_5}})) \tag{3.1}$$

where β is the particle velocity, γ the Lorentz factor and P_{1-5} are fit parameters. The measured dE/dx as a function of the track momentum measured in TPC is shown in Fig. 3.5. The lines correspond to the parametrization. A clear separation among the different particle species is observed for p_{T} $\leq$1 GeV/c, which allows for a track-by-track PID. At higher p_{T} the separation of the species is still feasible on a statistical basis via multi-Gaussian fits. The PID resolution is about 5.2% in pp collisions and 6.5% in the

most central Pb-Pb collisions (0-5% centrality class). Thanks to the $\mathrm{d}E/\mathrm{d}x$ resolution, particle ratios can be measured in the relativistic rise region at p_{T} up to 20 GeV/c.

3.2.4 Time of Flight (TOF)

The TOF detector is a large area array of Multigap Resistive Plate Chambers (MRPC), positioned at radial distance of 370-399 cm from the beam axis. It has a cylindrical shape, covering polar angles between 45 and 135 degrees over the full azimuth. The TOF is organized in 18 sectors in ϕ (Fig. 3.6); each of these sectors is divided into 5 modules along the beam direction. This detector is completely devoted to particle identification. The ionization produced by any particle crossing the MRPCs starts a gas avalanche which generates the registered signal. The TOF identifies the particle species via the time of flight measurements (i.e. the time that a particle needs to reach the TOF's arrays) inside the chambers. The PID is obtained with the following relation:

$$m = p\sqrt{\frac{t_{TOF}^2}{L^2} - 1} \tag{3.2}$$

where m is the mass of the particle, p the momentum, t_{TOF} the time-of-flight and L the track length. The start time (t_0) of the time-of-flight measurement is the time in which the collision occurs and it is obtained on an event-by-event basis either using the particle arrival times at the TOF, or the signal from the T0 detector, or a combination of the two.

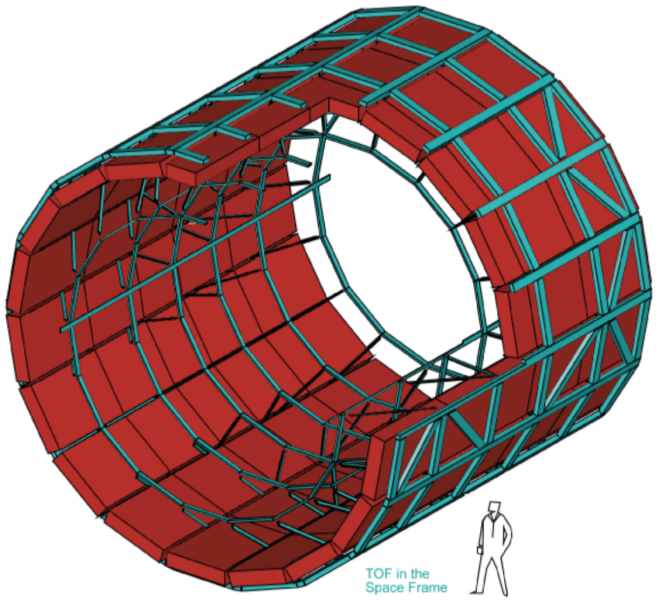

Figure 3.6 *– Layout of the ALICE Time-Of-Flight.*

The T0 detector is composed by two arrays of Cherenkov counters, T0A and T0C, located at apposite sides of the interaction point at -3.28< η <-2.97 and 4.61< η < 4.92. It has a time resolution of 20-25 *ps* in Pb–Pb collisions and ∼40 *ps* in pp collisions. The TOF resolution is 80 *ps* for pions with a momentum around 1 GeV/c, in 0-70% Pb–Pb collisions. This value includes the detector resolution, the contribution from electronics and the uncertainty on the start time of the event. It provides PID in the intermediate momentum range, allowing for pion/kaon separation at 3σ level up to $p_{\mathrm{T}} \approx 2.5$ GeV/c and kaon/pion separation up to $p_{\mathrm{T}} \approx 4$ GeV/c. Fig. 3.7 shows the distribution of the measured velocity as a function of momentum (measured by TPC). The background is due to tracks that are incorrectly matched to TOF hits in high-multiplicity Pb–Pb collisions.

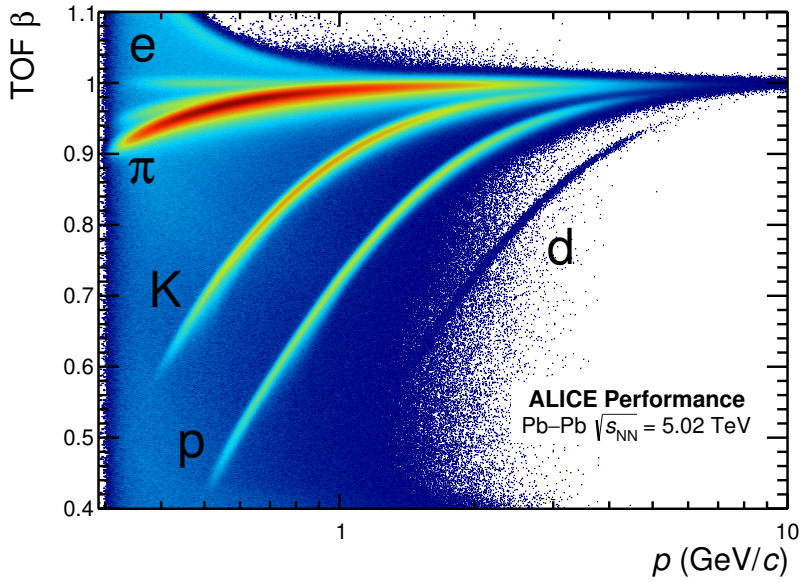

Figure 3.7 – *Layout of the ALICE Time-Of-Flight.*

3.2.5 V0 detector

The V0 detector is made of two arrays of scintillator counters, V0A and V0C, positioned on both sides of the interaction point. The V0A detector is located at 340 *cm* from the nominal interaction point position, along the beam axis, on the opposite side with respect to the muon spectrometer, whereas V0C is fixed to the front face of the hadronic absorber, 90 cm from the nominal interaction point. They cover the pseudo-rapidity ranges 2.8< η <5.1 (V0A) and -3.7 < η <-1.7 (V0C) and are segmented into 32 individual counters each distributed in four radial rings and 8 azimuthal sectors. The V0 provides a

minimum bias trigger as well as high-multiplicity triggers for the central barrel detectors and can be used to estimate the centrality of the collision based on the energy deposited in the V0 scintillator tiles. Furthermore, it is used for the beam-gas background rejection.

3.2.6 Zero Degree Calorimeter

The ZDC provides a measurement of the energy carried in the forward direction (at zero degree relative to the beam direction) by non-interacting nucleons (known as "spectators"). This quantity is useful to estimate the centrality of the event. Typically the beams are deflected by means of two separation dipoles located at about 65 m distance from the interaction point (IP). These magnets will also deflect the spectator protons, separating them from the spectator neutrons, which fly away at zero degree. Two sets of ZDCs are placed at about 115 m distance on both sides of the nominal interaction point. Each set is constituted by one calorimeter for neutron detection (ZN), positioned between the two beam vacuum tubes to intercept the spectator neutrons, and one for proton detection (ZP), placed externally to the outgoing beam, to collect the spectator protons. The hadronic ZDCs are quartz-fibre sampling calorimeters. The shower generated by crossing particles in a dense absorber (tungsten for ZN and brass for ZP) produces Cherenkov radiation in quartz fibers (the active material) interspersed in the absorber. The two sets of ZDCs are complemented by the information of two small electromagnetic calorimeters (ZEM), located at 7.5 m from the interaction point, to detect the energy of particles emitted at forward rapidity (mainly photons generated from decays collinear to the beam direction).

3.3 Tracking

Track reconstruction and vertex finding within the ALICE central barrel is performed on the basis of the information provided from the TPC and ITS detectors, which have been discussed above. The whole tracking procedure can be divided in different steps and it is based on a widely adopted in High-Energy Physics experiments: the Kalman filter algorithm [143], The main steps of the reconstruction are the following:

- **clusterisation**: an online procedure is separately performed for each detector, before any tracking. During this stage, the charge signals released in adjacent detector elements are converted into "clusters", with well-defined positions, signal amplitudes, signal times and associated errors.
- **First vertex reconstruction**: a first vertex candidate is also reconstructed at this stage, basing on the information from the SPD only. The vertex is reconstructed combining the so-called SPD tracklets, i.e. segments of tracks build by associating pairs of hits close in azimuthal angle ($\Delta\phi < 0.01$ rad) and pseudo-rapidity in the two SPD layer. The preliminary vertex is defined as a space point where

the maximum number of tracklets converge. In pp collisions, where interaction pileup is expected, the algorithm is repeated several times, discarding at each iteration those clusters which contributed to already-found vertices. In particular conditions, such as in low-multiplicity pp events or in Pb–Pb collisions, it can happen that no primary vertex is found. In these cases, the algorithm performes a one-dimensional search along the beam direction of the vertices exploiting the distribution of the points of closest approach of tracklets to the nominal beam axis.

- **TPC track finding**: the first step of the tracking procedure is then performed in the inward direction, starting from the clusters in the outer radii of the TPC where the track density is lower. Track seeds, i.e. initial outer track segments, are identified by trying different combinations of the TPC outer clusters and including the SPD vertex information, which constraints the inward propagation. Track reconstruction is then performed starting from the identified seeds in the inward-direction by means of the Kalman filter algorithm, which re-evaluates the best parameterization of the track after adding each candidate track cluster and increases at each step the quality of the fit. Afterwards, TPC tracks are prolongated inward to the ITS, starting from the higher p_{T} candidates. The TPC tracks from the previous step are used as seeds, and are matched to clusters in the ITS outer layers within a fiducial region.

- **Track inward propagation to the ITS**: for each cluster, track parameters are recalculated and the new candidate tracks are matched to clusters in the outermost ITS layers. They are then propagated inwards and updated at each ITS layer attaching all clusters that satisfy a proximity cut, until the innermost layer has been reached. Each TPC track is hence associated to a tree of tracks in the ITS. The track candidates in ITS are then selected with quality cuts (reduced χ^2 and number of shared clusters with other tracks). The tracks are then extrapolated to their point of closest approach to the interaction point reconstructed with SPD tracklets. The track prolongation efficiency from TPC to ITS, also called matching efficiency, in Pb–Pb collisions is shown in Fig. 3.8, as a function of p_{T} of the tracks for different requests on ITS points. The prolongation efficiencies from data and Monte Carlo (MC) simulations are shown by solid and open symbols, respectively.

- **Standalone ITS track finding**: the whole tracking procedure is also repeated inside the ITS only, where the algorithm tries to reconstruct tracks from the clusters which were not associated to any TPC track, allowing the reconstruction of either very low p_{T} tracks (down to $p_{\mathrm{T}} \sim 80$ MeV/c for pions), not reaching the TPC, or which did not release any cluster in the TPC due to the presence of dead TPC zones.

- **Track outward propagation**: the Kalman filter is used to propagate the tracks in the outward direction using the clusters found at the previous stage. The tracks

are matched to TRD tracklets in each of the six TRD layers, if possible, and to TOF clusters. The total track length and the time of flight expected for various particle species are updated for subsequent particle identification with TOF. The matching with outer detectors (EMCal, PHOS and HMPID) is also attempted. Only the TPC and the ITS points are used to update the measured track kinematics.

- **Final inward propagation (re-fit)**: a conclusive reconstruction step is finally performed by applying an inward Kalman filter refit starting from the outer radius of the TPC towards the primary vertex. The position, direction, curvature of the track (proportional to the inverse of transverse momentum) and its covariance matrix are then determined.

3.4 Vertexing

Once all possible global tracks have been reconstructed in TPC and ITS according to the Kalman filter procedure, the position of the primary interaction vertex can be determined with a higher precision than in the initial step where it was determined using only the information provided by the SPD tracklets. The final reconstruction of the interaction vertex is performed by extrapolating the global tracks to the point of closest approach to the nominal beam line position. The most far outliers are excluded, and a weighted vertex fit is subsequently performed with all the remaining validated tracks, suppressing the contribution of the most distant contributors. As one may expect, the resulting resolution on the final vertex position improves with increasing event multiplicity. Indeed, the resolution scales with the square root of the number of contributing tracks (tracklets). Hence, the resolution improves in heavier systems thanks to large multiplicities that allow a more precise determination of the primary vertex. The resolution on the transverse (x; y) position of the interaction vertices found with SPD and with global tracks are shown in the left panel of Fig. 3.9.
The resolution of the distance of closest approach to the primary vertex in the transverse plane for charged-particle ITS-TPC tracks in pp, p-Pb and Pb-Pb collisions is shown in the right panel of the Fig. 3.9. The relative transverse momentum resolution of the tracks is related to the resolution on the track curvature by the following relation:

$$\frac{\sigma(p_{\mathrm{T}})}{p_{\mathrm{T}}} = p_{\mathrm{T}}\sigma_{1/p_{\mathrm{T}}}. \tag{3.3}$$

At the end of the track finding procedure, the majority of the reconstructed global tracks come from the primary interaction vertex. The remaining secondary tracks, removed or suppressed in the primary vertex fitting, represent the component of particles with a displaced origin, either due to the weak decay of strange particles and heavy-flavour hadrons or to secondary interactions with the detector material. The most effective constraint for the selection of such particles is represented by the track impact parameter d_0, which evaluates the displacement of a track from the measurement of the Distance of

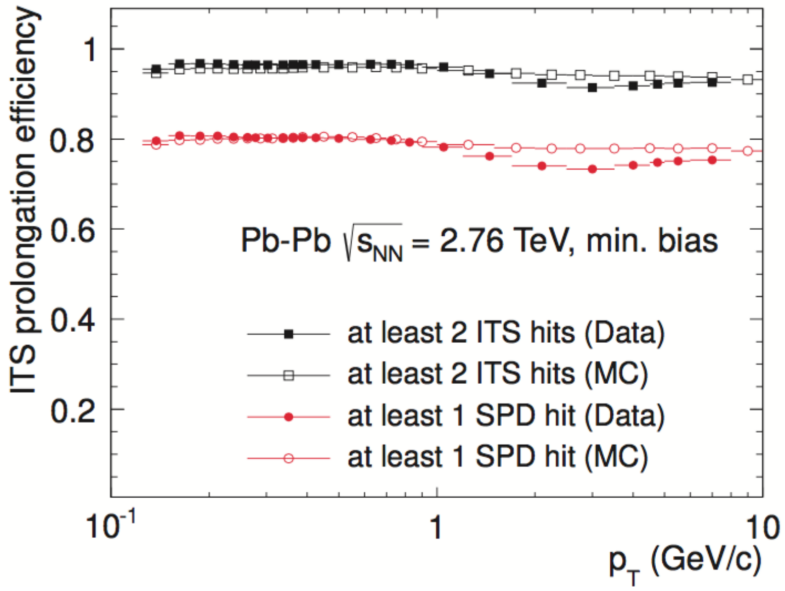

Figure 3.8 – *Track prolongation efficiency from TPC to ITS as a function of* p_{T} *for data and Monte Carlo in Pb–Pb collisions at* $\sqrt{s_{\mathrm{NN}}}$

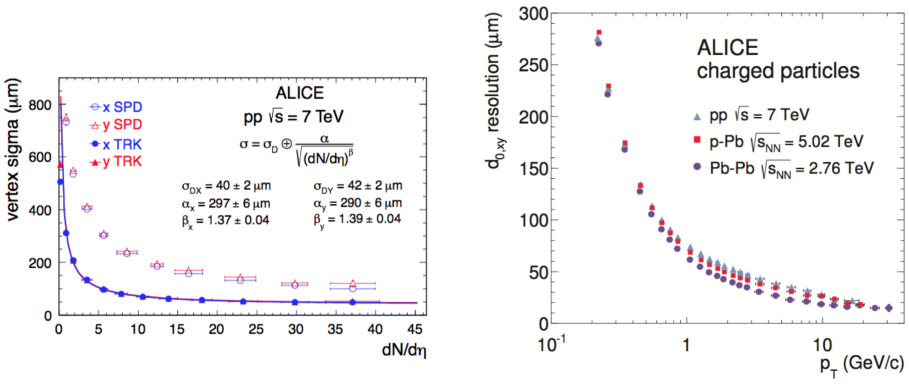

Figure 3.9 – *Left: resolution on the transverse coordinate of the vertex position from global tracks (solid points) and SPD tracklets (open points) as a function of multiplicity [144]. Right: resolution of the distance of closest approach to the primary vertex in the transverse plane for charged ITS-TPC tracks. The contribution from the vertex resolution is not subtracted [144].*

Closest Approach (DCA) of the corresponding trajectory to the primary vertex. In the transverse plane ($r\phi$) and along the beam direction (z), the projections of the impact parameter are defined as:

$$d_0(r\phi) = \rho - \sqrt{(x_V - x_0)^2 + (y_V - y_0)^2} \quad \text{and} \quad d_0(z) = z_{track} - z_V \tag{3.4}$$

where ρ and $(x_0,\ y_0)$ represent the radius and the centre of the track projection in the transverse plane, respectively. $(x_V,\ y_V,\ z_V)$ identifies the position of the primary vertex, and z_{track} is the z coordinate of the track after its propagation to the Point of Closest Approach (PCA) in the transverse plane. The capability of identifying secondary vertices from e.g. weak particle decays or photon conversions is strictly related to the resolution of the impact parameters provided by the tracking detectors. In this respect, one of the main purposes for the minimization of the ITS material thickness was to provide a good precision for the measurement of the track impact parameters, especially at low momenta, where track reconstruction is dominated by multiple scatterings in the detector material. If the d_0 resolution is sufficiently high to allow a good determination of displaced tracks, a series of topological selections can be applied to identify secondary particle decay vertices, as shown for example in Fig.3.10.

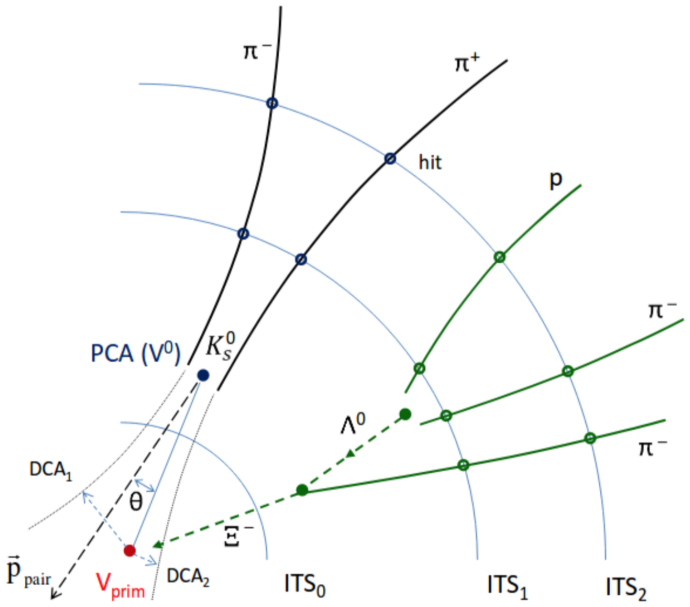

Figure 3.10 *– Principle of secondary vertex reconstruction in ALICE, with K_s^0 and Ξ^- decays shown as an example. The solid lines represent the reconstructed charged particle tracks, extrapolated to the secondary vertex candidates. Extrapolations to the primary vertex and auxiliary vectors are shown with dashed lines. The radii of the ITS layers are not to scale. Figure from [144].*

3.5 Centrality determination

For the description of nucleus-nucleus collisions, one must take into account the geometry of the process, since it determines in a large way the observed results. A peripheral collision implies that less nucleons are participating compared to the case of a central collision. A quantification of many relevant aspects can be done then by evaluating the value of the impact parameter of the colliding system, defined as the length of the vector $\vec{b}$ conjugating the two colliding nuclei. A schematic picture of the process is sketched in Fig.**??**. The underlying concept is that the impact parameter b can define the number of participants and spectator nucleons in the collision. Experimentally one could determine the centrality of a nuclear collision evaluating the fraction of energy carried by the spectators and deposited in the Zero Degree Calorimeters (ZDC) or by looking at the total multiplicity of the detected particles, which is expected to increase with the number of participants. Both quantities may in principle be used as centrality estimator to reconstruct the process impact parameter and thus select, for example, the class of very central collision events, which are namely those with $b \simeq 0$. This is fundamental in order to apply a rescaling of the observed results to the proton-proton collision case, (in which obviously only two participant nucleons are present), and also for a quantitative comparison of different heavy-ion collisions [158].
From an experimental point of view, one typically exploits the dependence of a measurable quantity n, such as the charged multiplicity or the energy in ZDC's, as a function of the number of participant or spectators nucleons (and hence, to the impact parameter) in order to estimate the centrality of the collision. In this way, the data sample can be subdivided in different centrality classes $c(N)$, each defined in terms of percentiles N of the corresponding distributions as a function of the estimator variable n. In the commonly adopted convention, one than identifies centrality classes $c(N)$, with the most central class defined by events with the highest n. Therefore, the centrality class C(0-10%) identifies the 10% most central collisions of the observed distributions, corresponding to the 10% highest multiplicity events and hence as well as to the 10% collisions with the smallest impact parameter. The Glauber model, described in the following, allows to compute the number of participant nucleons or of binary collisions at a given b, and hence to identify a centrality class to the corresponding interval of the impact parameter from the scaling of measurable quantities. A rather good approximation can however be achieved, for the case of two colliding nuclei with radii R_A and R_B and inelastic cross section σ_{in}^{AB} by means of the geometrical relation:

$$c(N) \simeq \frac{\pi b^2(N)}{\sigma_{in}^{AB}} \quad \text{with} \quad b < R_A + R_B \tag{3.5}$$

3.5.1 Centrality in p–Pb collisions

The evaluation of centrality for proton–nucleus collisions case is not as straight-forward. For instance, the number of participant nucleons N_{part} is more loosely correlated to both the impact parameter and the multiplicity of charged particle with respect to the nucleus-nucleus case. Provided some thoughtful choices of the categorizing variable, it is however still possible to divide data samples in reasonable centrality classes through the use of an appropriate centrality estimators. In the case of ALICE analyses as a function of centrality in p–Pb collisions, the slow nucleons energy deposited by the Pb nucleus remnants in the ZDC has been used as centrality estimator. Such observable was found to be less sensitive to the dynamical bias observed in centrality estimations based on charged-particle multiplicity (usually employed in Pb–Pb collisions), which is caused by the presence of large relative statistical fluctuations in particle multiplicity per nucleon-nucleon collision. An approach referred to as "hybrid method" in [157], was adopted to relate the average nuclear thickness function $\langle T_{pA} \rangle$ and the number of binary collisions $\langle N_{coll} \rangle$ to the corresponding energy deposited in the Pb-remnant side of ZN for each given centrality class. The method relies on the assumption that the charged-particle multiplicity measured at mid-rapidity is directly correlated to the number of participant nucleons N_{part}, as in the case of Pb–Pb collisions. The values of N_{part} for a given ZN-energy class, are then calculated by scaling the Minimum-Bias value of the number of participant nucleons $\langle N_{part}^{MB} \rangle$, by the ratio $\langle N_{ch}^{ZN} \rangle / \langle N_{ch}^{MB} \rangle$, where $\langle N_{ch}^{ZN} \rangle$ indicates the average charged-particle multiplicities measured at mid-rapidity for the considered ZN-energy event class, while $\langle N_{ch}^{MB} \rangle$ represents the corresponding value in MB collisions. The Glauber model is then applied to calculate $\langle T_{pA} \rangle$ and $\langle N_{coll} \rangle$ from the calculated number of participant nucleons. Alternative approaches for the derivation of $\langle N_{coll} \rangle$ relies on the proportionality of $\langle N_{coll} \rangle$ to the yield of high-p_{T} particles at mid-rapidity, or to the charged-particle multiplicity measured with the V0 detector in the Pb-going direction at forward rapidity. Variations in the order of a few percentage between the three different methods were found. An example of this procedure is shown in Fig. 3.12, for the case of energy deposited in the ZN calorimeters.

3.5.2 The Glauber model

The Glauber model [146] relates statistically the geometry of nuclear collisions with the number of participant nucleons and of binary nucleon-nucleon collisions. Taking as inputs the nuclear density distributions and the nucleon-nucleon cross sections, the Glauber model allows to estimate the average number of participant nucleons and of binary collisions, along-side with their statistical uncertainties, as a function of the impact parameter, which is the input parameter for theoretical calculations. The probabilistic approach at the basis of Glauber model is based on a set of underlying assumptions (the so-called "optical limit" hypothesis) which require that:

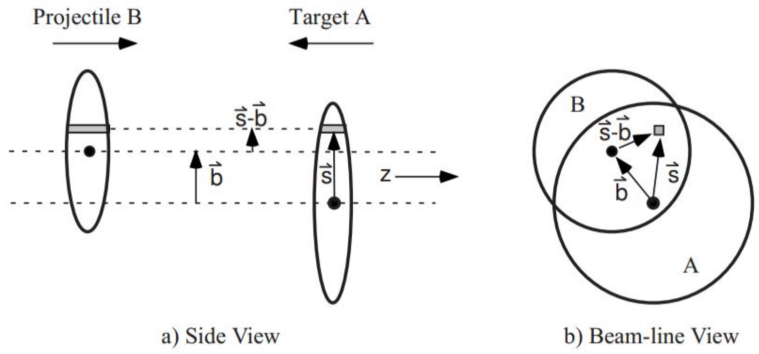

Figure 3.11 *– Geometry of a nucleus-nucleus collision, with transverse (a) and longitudinal (b) views.*

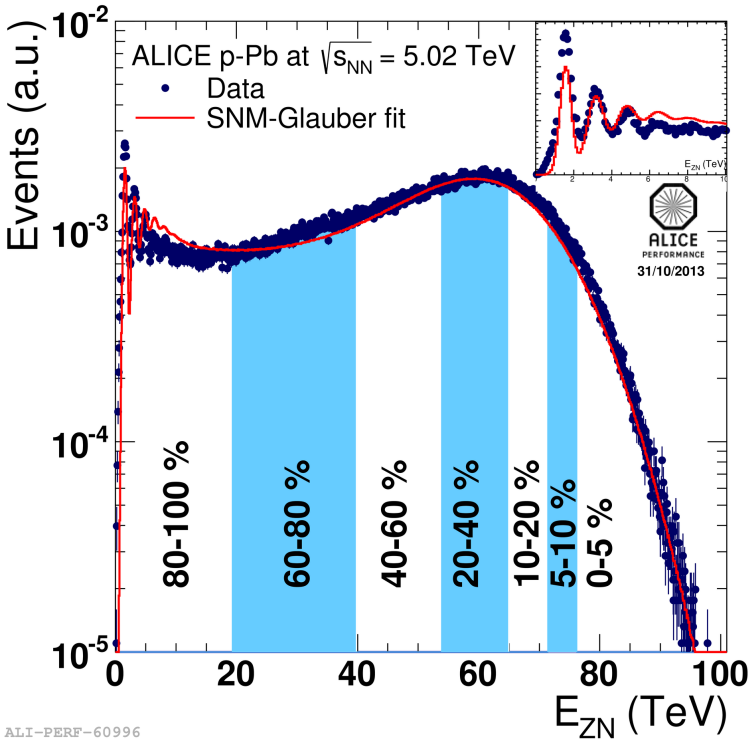

Figure 3.12 *– Distribution of the sum of amplitudes in the ZN calorimeters for events in p–Pb collisions at* $\sqrt{s_{\rm NN}}$ *= 5.02 TeV [145]. The distribution is fitted with the combined NBD-Glauber models; the fit is shown as a red line. The centrality classes used in the analysis are indicated in the figure. The inset shows a zoom of the most peripheral region.*

- nucleons travel within nuclei on straight lines;
- collisions do not alter the nucleons nature nor their trajectories;
- proton and neutrons in the colliding nuclei are indistinguishable;
- the interaction probability is given by a constant, elementary nucleon-nucleon cross section σ_{NN}^{inel}.

All these assumptions can be considered as reasonably satisfied in ultra-relativistic heavy-ion collisions, such as those at the LHC. Indeed, in these regimes the transferred transverse momenta are negligible compared to the longitudinal ones, and the time between two consecutive N–N collisions is smaller than that for its excitation or for the production of particles.
The geometry of two heavy ions colliding with impact parameter **b** can be represented as in Fig. 3.11. During the collision, the two tube-shaped regions (the gray areas) located at a displacement **s** with respect to the centre of the target nucleus and at a distance **s-b** from the centre of the projectile, overlap. By employing a realistic distribution for the description of the nucleon distributions ρ_A in nuclei such as, commonly, a Wood-Saxon potential, and having defined $\rho(\mathbf{s} - z_A)$ as the probability per unit volume for finding a given nucleon at the position $(\mathbf{s} - z_A)$, one can identify $T_A(s) = \int \rho_A \rho(\mathbf{s} - z_A) dz_A$ as the probability per unit transverse area for a nucleon to be located into the target flux-tube. The product $T_A(\mathbf{s} T_B(\mathbf{s} - \mathbf{b}))d^2s$ then gives the joint probability per unit area for the nucleons to be located in the respective overlapping target and projectile flux tubes of area $d^2\mathbf{s}$. The nuclear overlap function $T_{AB}(b)$ is then defined as the integral of the aforementioned probability over all values of **s**:

$$T_{AB}(b) = \int T_A(\mathbf{s}) T_B(\mathbf{s} - \mathbf{b}) d^2\mathbf{s} \tag{3.6}$$

and can be interpreted as the effective overlap area in which a nucleon from nucleus A interacts with a given nucleon in B. Provided the knowledge of the nucleon-nucleon inelastic cross section σ_{NN}^{inel}, all the relevant quantities which characterize the collision geometry can be determined starting from the nuclear overlap function. In particular, the probability for a nucleon-nucleon interaction to occur is given by $T_{AB}(b) \cdot \sigma_{NN}^{inel}$, whereas the probability of having n different interactions between the A and B nucleons of the projectile and target nuclei can be derived according to a binomial distribution $P_n(b)$:

$$P_n(b) = \binom{AB}{n} \cdot [T_{AB}(b) \cdot \sigma_{NN}^{inel}]^n \cdot [1 - T_{AB} \cdot \sigma_{NN}^{inel}]^{AB-n}. \tag{3.7}$$

where the binomial coefficient encodes the number of combinations for colliding n nucleons out of $A \cdot B$ possible nucleon–nucleon combinations, while the second and third terms represent the probabilities of having exactly n collisions and AB - n misses, respectively.

On the basis of such probability distribution, the number of binary nucleon-nucleon collisions for a collision with a given impact parameter are:

$$N_{coll}(b) = \sum_{n=1}^{AB} n \cdot P_n(b) = AB \cdot T_{AB}(b) \cdot \sigma_{NN}^{inel} \tag{3.8}$$

which can then be employed to infer the mean value of the impact parameter for a measured centrality class starting from the observed distributions of a given centrality estimator. A commonly adopted approach for the estimation is to extract the mean values of such quantities via a mapping procedure, in which the measured distributions are mapped to the corresponding Monte Carlo distributions based on Glauber calculations, as showed in Fig. 3.12.

4

D-h correlations in pp collisions at $\sqrt{s} = 5.02$ TeV

4.1 Introduction

The study of the azimuthal correlations of heavy-flavour particles and charged particles at the LHC energies, as widely discussed in the second chapter, provides a way to characterize charm production and fragmentation processes in pp collisions. The measurement also provide a way to probe our understanding of QCD in the perturbative regime, accessible in a large kinematic range given the large mass of heavy quarks.
Due to flavour conservation in QCD, charm quarks are always produced as pairs of quarks and anti-quarks. In particular, prompt charm quark-antiquark pair production is back to back in azimuth at first order in leading-order(LO) perturbative-QCD (pQCD). Hence, if a hadron from the quark hadronization is taken as "trigger" particle, the typical shape of the azimuthal correlation distribution features a near-side at $(\Delta\varphi, \Delta\eta) = (0, 0)$ and an away-side peak at $\Delta\varphi = \pi$. The former originates from the jet containing the"trigger" D meson, the latter is induced by the recoil jet, which can also include the decay products of the other charmed hadron produced in the collision. At the Next-to Leading-Order (NLO) additional effects can modify significantly the shape of the azimuthal correlation distributions. For example, the radiation of a hard gluon from a charm quark smears the back-to-back topology of LO production and broadens both the near- and the away-side peak. In addition, heavy quarks produced from the "splitting" of a massless gluon, can be rather collimated and, especially at high-p_{T}, may generate sprays of hadrons at small $\Delta\varphi$ contributing to broader near-side peak pattern. In such cases, the away-side peak is originated from the particles coming from the fragmentation of the recoil parton, which is not aligned with the trigger particle. Furthermore, for hard-scattering topologies classified as "flavour-excitation", a charm quark undergoes a hard interaction from an initial splitting $g \to c\bar{c}$, leading to a big separation in rapidity of the hadrons originating from

the antiquark (quark) with respect to the trigger D meson and contribute to a rather flat term to the $\Delta\varphi$-correlation distribution which tends to enhance the baseline height.
The best option to characterize the $q\bar{q}$ quark pair is to study the azimuthal correlations obtained using direct observables like $D\bar{D}$ or $B\bar{B}$ (see chapter 2). Due to the large statistics required for these kind of analysis, the more doable way is to correlate a meson carrying a heavy quark as trigger particle with the other charged particles in the same event. Anyway, it gives the possibility to study the underlying charm production mechanism in detail, though more indirectly with respect to $c\bar{c}$ (i.e. $D\bar{D}$) azimuthal correlations.
In this thesis, the D meson and charged particle correlations have been studied in small systems (i.e. pp and p–Pb collisions) within the ALICE experiment at the same collision energy of 5.02 TeV.

In this chapter, I will discuss the azimuthal correlations of D mesons with charged hadrons in pp collisions at $\sqrt{s}$ = 5.02 TeV, while the next chapter will be focused on the results carried out in p–Pb collisions. Therefore, in this chapter, I will introduce the analysis strategy for the correlations of D-mesons with charged particles in pp collisions at $\sqrt{s}$ = 5.02 TeV in all its steps in section 4.4. It will be followed by a section devoted to the systematic uncertainty estimation. Finally, the results of $\Delta\varphi$ correlations and quantitative observables extracted from fits to the averaged distributions, obtained for prompt D^{*+}, D^0 and D^+ in different ranges of transverse momentum for the D-meson (trigger particle) and of the associated particles, are presented.
The large statistics available for the pp at $\sqrt{s}$= 5.02 TeV, collected at the end of 2017 data taking, allowed us to extend the momentum ranges (both for D mesons and associated particles) with respect to the 2010 and 2016 pp datasets (at $\sqrt{s}$ = 7 TeV and $\sqrt{s}$ = 13 TeV, respectively). The improved precision in the common ranges allows a more detailed investigation of the charm quark fragmentation properties (multiplicity of tracks as a function of momentum, geometrical profile of charm jets, p_{T} distribution of the tracks inside the jet). This can also drive towards new constraints of charm fragmentation and charm jet properties provided by models.
Furthermore, 2017 pp data sample allows us a direct and more reasonable comparison with 2016 p–Pb data, since it has the same center-of-mass energy and, thanks to the higher precision and statistics, it was possible to exploit the azimuthal correlations in the same (extended and more differential) p_{T} ranges of both the trigger and the associated particle of the 2016 p–Pb data sample.
Finally, this new pp reference data, together with new p-Pb 2016 data will help to study cold nuclear matter effects affecting the charm fragmentation in p-Pb with better precision. In addition, this analysis on pp data represents a solid and precise reference in view of an analysis on a Pb-Pb sample at the same energy, which will be taken during the last weeks of 2018 data taking.
All the results that will be displayed in this manuscript have been approved from the

ALICE Collaboration. Specific results will be presented only for the D^{*+} meson for which I am the main author.

4.2 Event selection

The analysed data sample consists of about 990 million of minimum bias events, corresponding to an integrated luminosity $L_{int} = (19 \pm 1)$ nb^{-1} , collected during the 2017 proton proton run at $\sqrt{s}$=5.02 TeV. The minimum-bias (MB) trigger, used to collect the data sample, requires coincident signals in the two V0 counters. Events were selected offline by using the timing information from the V0 and the correlation between the number of hits and track segments in the SPD detector to remove background due to the interaction between one of the beams and the residual gas present in the beam vacuum tube. The pile-up events (less than 1%) were rejected by detecting multiple interaction vertices using track segments defined with the SPD layers. The remaining undetected pile-up is negligible in the present analysis. Only events with a primary vertex reconstructed within ±10 cm from the centre of the detector along the beam line were used for the analysis. This choice maximizes the detector coverage of the selected events, considering the longitudinal size of the interaction region, and the detector acceptances, without introducing sizable η dependencies for the reconstruction efficiencies in the considered pseudorapidity ranges. The events were collected within different data taking periods: LHC17p_FAST, LHC17p_CENT_woSDD, LHC17q_FAST and LHC17q_CENT_woSDD. Since 2017 pp datasets were distinguished into two categories - one including SDD detector (CENT_wSDD sample) and the second one without the SDD in the reconstruction, or in the acquisition (CENT_woSDD and FAST samples, respectively), a study of performance of the D-hadron correlation analysis with respect to the data samples employed has been carried out for D^{*+} (with the D^+, it is more sensitive to the presence of the SDD with respect to the D^0, due to their reconstruction from three decay tracks), very similar of what was done for the p–Pb 2016 data sample, also splitted in a similar fashion and reported in the subsection, reaching exactly the same conclusion. Therefore, this study confirmed that a more solid analysis would be obtained using more uniform samples (both datasets without the SDD information), at the price of a slight reduction of the statistical precision. Moreover, analogously as in the p–Pb 2016 data sample, it was verified, by looking at D-meson and associated charged track η and φ distributions, and at the mixed-event correlation distributions for each sub-samples, that no visible differences is present for the four periods (though the 17q samples suffer from very large statistical uncertainties), hence it was possible to perform the analysis directly on the merged samples without any bias. For more details on this topic, see the section 5.1.
Monte-Carlo simulations are used in this analysis to calculate the corrections for the azimuthal-correlation distributions evaluated from data. These simulations include a complete description of the ALICE detector, i.e. the distribution of the collision vertex

along the beam line, the conditions of all the detectors, and their evolution with time during the pp and p–Pb. The Monte Carlo productions adopted for this study were:

1. LHC18a4a2_fast: proton-proton collisions are simulated with PYTHIA6 [148] with Perugia-2011 tune event generator. The generated particles are transported through the ALICE apparatus using the GEANT3 [147] package. In this production, in each event it is required that a $c\bar{c}$ or $b\bar{b}$ pair is present (enrichment of heavy quarks) and with forced hadronic decays of the charmed hadrons.

2. LHC17l3b_fast, minimum-bias sample produced with DPMJET generator, used for the evaluation of the tracking efficiencies.

4.3 Monte-Carlo simulations

The measured angular-correlation distributions are compared to simulation results obtained with the event generators PYTHIA 6.4.25 [148] (tunes Perugia-0, Perugia-2010, and Perugia-2011sets [149]), PYTHIA 8.2 (tune 4C) [34], POWHEG [46] coupled to PYTHIA6 (Perugia-2011 tune). PYTHIA simulations employ LO-pQCD matrix elements for 2→2 processes, along with a leading-logarithmic p_{T}-ordered parton shower, the Lund string model for hadronisation, and an underlying-event simulation including Multiple-Parton Interactions (MPI). With respect to older tunes, the Perugia tunes use different initial-state radiation and final-state radiation models. One of the main differences is that the parton shower algorithm is based on a p_{T}-ordered evolution rather than a virtuality-ordered one. Significant differences in the treatment of colour reconnection, MPI, and the underlying event were also introduced. Perugia 0 is the first of the series. The Perugia-2010 tunes differ from those of Perugia-0 in the amount of final-state radiation and by a modification of the high-z fragmentation (inducing a slight hardening of the spectra). They are expected to better reproduce observables related to the jet shape. The first LHC data, mainly from multiplicity and underlying-event related measurements, were considered for the Perugia-2011 tunes. PYTHIA 8.1 also includes several improvements in the treatment of MPI and colour reconnection [34].
POWHEG is a NLO-pQCD generator [46] that, coupled to parton shower programs (e.g. from PYTHIA or HERWIG [155]), can provide exclusive final-state particles, maintaining the next-to- leading order accuracy for inclusive observables. The charm-production cross sections obtained with POWHEG+PYTHIA are consistent with FONLL [7]and GM-VFNS [9] calculations within the respective uncertainties, and are in agreement with measured D-meson production cross sections within the model and experimental uncertainties [120]. The POWHEG + PYTHIA simulations used in this analysis are obtained with the POWHEG BOX framework [150] and the tune Perugia 2011 of PYTHIA 6. For the comparison with the measured p–Pb collision data, parton distribution functions (PDFs) corrected for nuclear effects (CT10nlo [151] with EPS09 [38]) are used.

4.4 Analysis strategy

The correlation analysis is performed by associating D^{*+} mesons (and their antiparticles), identified as "trigger" particles, with charged primary particles in the same event, and excluding those coming from the decay of the trigger D^{*+} meson itsself. Such correlations are measured as a function of the azimuthal difference $\Delta\varphi$ (defined within $\pi/2$ and $3\pi/2$) and pseudorapidity difference $\Delta\eta$. The correlation is expressed in terms of the associated yield per trigger particle for different intervals of trigger and associated transverse momentum, p_{T}^{trig} and p_{T}^{assoc}, at central rapidity. In this study, the trigger particle is defined by the identification of D^{*+}-mesons, rather than by a cut on the momentum (like in jet analysis). This choice doesn't constrain the momentum of the associated particles and let us to explore larger kinematic regions, independently on the trigger particle momentum. The associated particles are defined as primary charged particles coming from the primary vertex, including also particles from strong and electromagnetic decays and particles deriving from the decay of heavy flavour hadrons. Particles coming from weak decays of strange hadrons and particles produced in interactions with the detector material are instead excluded from this criterion and are considered as secondaries. In particular, our definition of primary charged particles includes primary particles of the following species: pion, kaon, proton, electron, muon. The corresponding contribution to the azimuthal correlations, therefore, will be removed from the results.
The analysis is performed through the following steps:

- D^{*+} meson selection and signal extraction;
- correlation of D^{*+} candidates with associated tracks;
- correction for limited acceptance and detector inhomogeneities with Event Mixing;
- subtraction of background correlation from signal distribution;
- correction for D^{*+} meson efficiency and associated track efficiency;
- projection in $\Delta\varphi$;
- correction for the contamination of secondary particles;
- correction for bias on B to D^{*+} decay topologies;
- correction for feed-down of D^{*+} meson from b-hadron decay;
- study of correlation properties;

4.4.1 D meson selection and signal extraction

For each single event, "trigger" particles are defined as the selected D^{*+} meson candidates within a given $p_{\mathrm{T}}^{\mathrm{trig}}$ range. The detection strategy for D^{*+} mesons at central rapidity is the same performed for the analyses of the D-meson production at central rapidity [120].

It is based on the fully reconstruction of D^{*+} charmed hadron via its exclusive hadronic decay channel: $D^{*+} \to D^0\pi^+$ (BR of 67.7 ± 0.5% [152]) with $D^0 \to K^-\pi^+$ (BR of 3.87± 0.05% [152]), and its charge conjugates. As a general feature, the selection of all the D-mesons develops from the reconstruction and selection of secondary vertex topologies with significant separation from the primary vertex. This technique was applied also for the D^{*+} case, even if here the decay proceeds via the strong interaction and it is not possible to resolve the secondary D^{*+} vertex. In this case, the analysis exploited the topological selection criteria applied in the D^0 meson analysis. The D^{*+} signal was reconstructed calculating the invariant-mass difference $\Delta m = m_{D^{*+}} - m_{D^0}$ between the reconstructed D^{*+} and the decay D^0, as a narrow peak at $\Delta m \approx 145\ MeV/c^2$ close to the threshold and thus in a rather low combinatorial background region. Furthermore, the resolution in Δm is mostly defined by the pion momentum resolution.
In particular, D^{*+} candidates were reconstructed by applying kinematical selections on the final decay products and on the topology of the D^0 decay. The D^0 decay candidates were selected from pairs of tracks with similar criteria to that applied for the D^0 analysis. The selection values vary in the D^{*+} candidates p_T interval. For example, the angle between the D^0 reconstructed momentum and its flight line was kept to tigher values ($\cos\theta_{pointing} > 0.9$) for candidates with D^{*+} $p_T < 5$ GeV/c while it was released up to 0.6-0.7 for higher p_T thanks to the low combinatorial background. A typical value of the product of the track impact parameters was $d_0^\pi \times d_0^K <$ -(60 μm)^2. The topological selection criteria applied for the trigger mesons are p_T dependent and were adjusted to optimize the statistical significance ($S/\sqrt{S+B}$, where S represents the signal and B represents the background) of the signal and the S/B ratio, while keeping the selection efficiency increasing with p_T, in order to reduce fluctuations which are mainly induced by the sideband subtraction. Given that the cut values are dependent on the p_T of the D^{*+} candidate, the signal and background values are determined for each p_T bin and are extracted from the fitted invariant mass distribution. The identification of the charged kaons and pions in the TPC and TOF detectors allowed to further reduce the combinatorial background, especially at low p_T. A $\pm 3\sigma$ cut around the expected value for pions and kaons is applied on both TPC and TOF signals.

An invariant-mass analysis is then used to extract the D^{*+} raw signal yields for particles and the corresponding anti-particles in each p_T interval. They were obtained by fitting the invariant-mass distribution with a Gaussian distribution to describe the signal and a peculiar function for the background. For D^{*+} the convolution of the exponential with a threshold function was used ($a\sqrt{\Delta M - M_\pi}\cdot e^{b(\Delta M - M_\pi)}$[1]). The D^{*+} mesons were selected in the rapidity range varying from $|y| < 0.5$ at low p_T to $|y| < 0.8$ for $p_T > 5$ GeV/c.

[1]The parameters a and b in the background parametrisation are free parameters and are estimated in a first instance by fitting only the invariant mass entries that are in the side-bands of the distribution. Once those parameters are obtained, they are fixed in the overall fit function and then the full invariant mass spectrum is fitted.

The invariant mass distributions of $\Delta m = m_{\mathrm{D}^{*+}} - m_{\mathrm{D}^0}$ (for the D^{*+} reconstruction) in various p_{T} ranges are shown in Figs. 4.1 and 4.2 . The distributions are weighted by the D^{*+}-meson selection and reconstruction efficiency, to allow a correct normalization of the correlation distributions, which have also these weights.

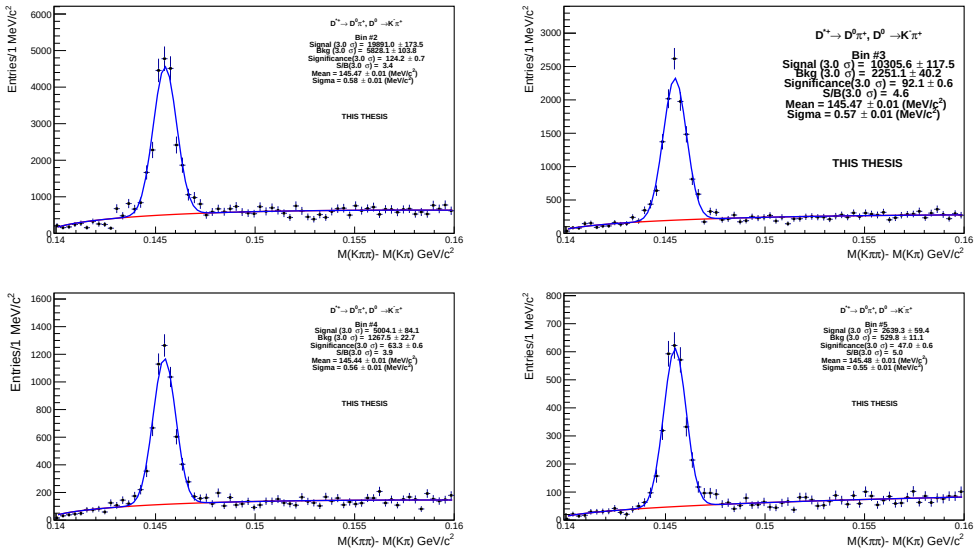

Figure 4.1 – *Invariant mass distributions of $M(K\pi\pi) - M(K\pi)$ corrected with efficiency in different p_T regions. Top: $3 < p_T^D < 4$ GeV/c (left), $4 < p_T^D < 5$ GeV/c right), Bottom: $5 < p_T^D < 6$ GeV/c (left) and $6 < p_T^D < 7$ GeV/c (right).*

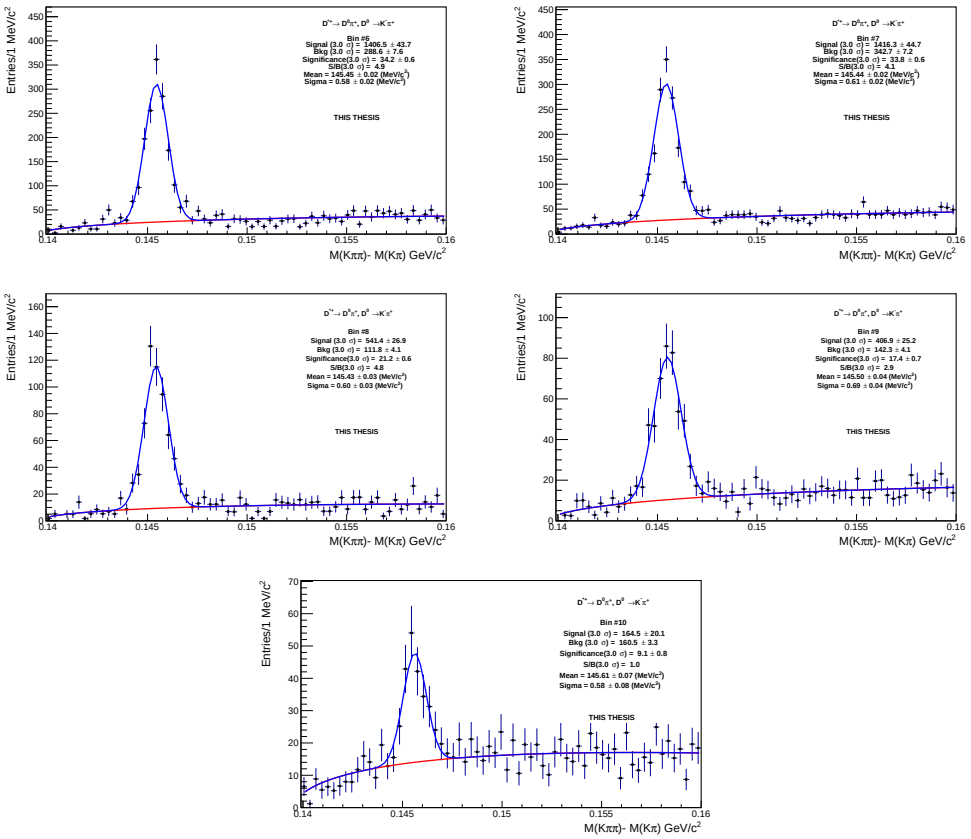

Figure 4.2 – *Invariant mass distributions of* $M(K\pi\pi)-M(K\pi)$ *corrected with efficiency in different* p_T *regions. Top: ,* $7 < p_T^D < 8$ GeV/c *(left),* $8 < p_T^D < 10$ GeV/c*(right),; Middle:* $10 < p_T^D < 12$ GeV/c *(left),* $12 < p_T^D < 16$ GeV/c *(right) and Bottom:* $16 < p_T^D < 24$ GeV/c .

Extension to vey-low p_{T} of D mesons

Thanks to the higher statistic of the 2017 pp data sample, an extension of the correlation studies to very-low p_{T} of the trigger particle was tried. Indeed, the Figure 4.3 shows the good performance on the invariant mass extraction for the D^{*+} with $2 < p_T^{\mathrm{D}} < 3$ GeV/c.

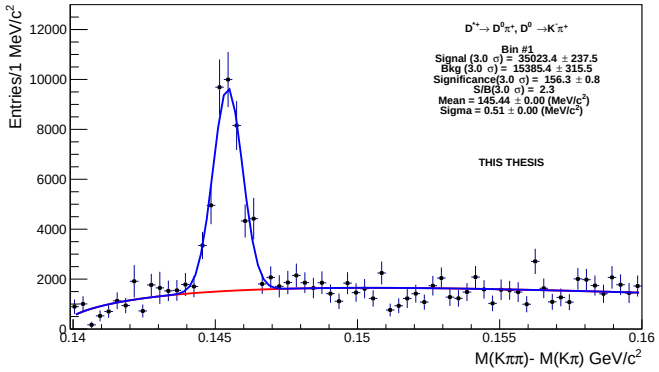

Figure 4.3 – *Invariant mass distribution of* D^{*+} *(bottom) corrected with efficiency for very low-*p_{T}*:* $2 < p_{\mathrm{T}}^{D} < 3$.

The extension of the analysis to this p_{T} interval is of high interest for the jet structure characterization. Indeed, this study allow us to investigate a kinematic region in which the trigger particle has compatible or even lower momentum with respect to the associated particles. This give us the possibility to better understand the production processes. In fact, for example, at the Leading Order (LO) for $p_{\mathrm{T}}(trig) \sim p_{\mathrm{T}}(ass)$ we don't expect any peak on the near-side region. A peak could arise only from Next-to-Leading-Order (NLO) production process.
Despite the good statistics, it wasn't enough to perform the correlation analysis. Indeed, the correlation distribution peaks are very small, due to the small energy of the parton, resulting in few tracks being produced in the fragmentation on top of the D meson. Hence, the correlation peaks were smoothened by the baseline fluctuations (of the same order of magnitude of the peak itself), especially on the away-side region, where indeed it was not possible to extract physical observables.

4.4.2 Associated particle selection

Associated particles are defined as all charged primary particles with $p_{\mathrm{T}}^{assoc} > 0.3$ GeV/c and with pseudorapidity $|\eta| < 0.8$, except for the decay products of the trigger D meson. Particles coming from other weak decays or originating from interactions with the detector material are defined as secondary particles and are, therefore, discarded. Reconstructed tracks with at least 70 points in the TPC and 3 in the ITS, and a χ^2/NDF of the momentum fit in the TPC smaller than 2 are associated to D-meson candidates. The

contamination of secondary particles is removed by requiring the DCA of the associated tracks to the primary vertex to be less than 2.5 mm in the transverse (x, y) plane and less than 1 cm along the beam line (z direction). This selection identifies primary particles with a purity (p_{prim}) of approximately 96% and an efficiency higher than 99%, also for particles originating from decays of charm or beauty hadrons, which can be displaced by several hundred micrometers from the primary vertex, as will be justified in the section 4.4.7.

4.4.3 Correlation of D^{*+} candidates with associated tracks

In each event, pairs were formed by combining each selected D^{*+} meson candidate with the other charged primary particles passing the track selection. For each particle pair, the pseudorapidity difference $\Delta\eta = \eta_{trig} - \eta_{track}$ and the corresponding azimuthal angle difference $\Delta\varphi = \varphi_{trig} - \varphi_{track}$ were evaluated and used to build a two-dimensional correlation distribution $C(\Delta\varphi, \Delta\eta)_{peak}$. Since the difference in the azimuthal angle is periodic, the $\Delta\phi$ range in these distributions was limited to the interval [$-\pi/2$, $3\pi/2$] which provides a good visibility of the correlation pattern, peaked around 0 and π. It includes also the angular correlation of combinatorial D^{*+}-meson candidates in the peak range, which is a source of background and needs to be subtracted. This contribution is estimated by means of the per-trigger correlation distribution of background candidates in the sideband invariant-mass range, $1/B_{sidebands} \times C(\Delta\varphi, \Delta\eta)_{peak}$, where $B_{sidebands}$ is the amount of background in the sideband region. The sidebands were defined $5\sigma < |M - \mu| < 10\sigma$ for D^{*+} on the right side of the Gaussian peak. An example of the signal region and the sidebands are shown in Fig. 4.4 superimposed to the D^{*+} invariant mass distribution.

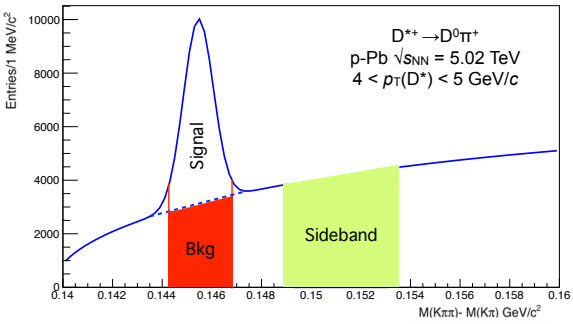

Figure 4.4 *– Example of signal, background (red) and sideband (green) regions, highlighted for a* D^{*+} *candidate invariant mass distribution.*

4.4.4 Correction for the detector inhomogeneities

The shape of the angular correlations of D^{*+} mesons and charged particles could be affected by the presence of unphysical structures in the $\Delta\varphi$ distribution due to detector inhomogeneities. In addition, the limited acceptance of the detector for the D^{*+} meson and charged particles reconstruction causes a triangular-shaped correlation in $\Delta\eta$. Therefore, the event-mixing technique is used for correcting the raw correlation distribution for these effects. The calculation of the Event Mixing correlation distribution is performed online. In this technique, an event pool is created. Therefore, events preceding the one containing a D^{*+} candidate are stored based on their properties (position of the vertex along the z axis and multiplicity) and the events are then splitted into bins of multiplicity and position of the vertex along the z-axis. Each time a D^{*+} meson candidate is found in an event, only the events contained in the same pool as the event under analysis is used to evaluate the correlations for the event mixing correction.
The multiplicity and z vertex position bins for the pools used in the pp analysis are the following:

- Multiplicity bins: $(0, 20)\,;(20, 35)\,;(35, +\infty)$
- Vertex z $(cm) = (-10, -2.5)\,;(-2.5, 2.5)\,;(2.5, 10)$

In an ideal case, the mixed event distribution is expected to have a constant flat distribution as function of $\Delta\varphi$ and a triangular shaped distribution in $\Delta\eta$ deriving from the limited η acceptance of the detector. Since the correlations built in this way are not influenced by correlations coming from physical processes, every modification to this pattern should be interpreted as a possible detector inefficient regions, or holes, in the same angular position for D meson and associated tracks. These structures produce an excess of correlations at $\Delta\varphi = 0$ in the $\Delta\varphi$ distribution, plus possibly other structures depending on the relative position of the inefficient regions and on their number.
The mixed-event distribution is used as a weight in each correlation bin, i.e, the corrected correlation distribution is calculated as follows:

$$\frac{dN^{corr}\left(\Delta\varphi\Delta\eta\right)}{d\Delta\varphi d\Delta\eta} = \frac{\frac{dN^{SE}(\Delta\varphi\Delta\eta)}{d\Delta\varphi d\Delta\eta}}{\frac{dN^{ME}(\Delta\varphi\Delta\eta)}{d\Delta\varphi d\Delta\eta}} \frac{dN^{ME}\left(0,0\right)}{d\Delta\varphi d\Delta\eta} \tag{4.1}$$

In Eq. 4.1, the last term stands for the average of the bins in the region $-0.2 < \Delta\eta < 0.2$, $-0.2 < \Delta\varphi < 0.2$ (multiple bins are used to minimize the effect of statistical fluctuations on the normalization of the mixed-event plots). This kind of normalization, adopted in the analysis of hadron-hadron correlations, relies on the fact that at $(\Delta\eta, \Delta\varphi) = (0, 0)$ the trigger and associated particle experience the same detector effects, therefore no correction is necessary. In the D meson case this is true only on average and not at very low p_{T}, since D mesons are reconstructed from particles that can go in different detector region. However, $(\Delta\eta, \Delta\varphi) = (0, 0)$ is in any case the region with maximum efficiency for the pairs (both correlated and uncorrelated). Thus the same convention was adopted.

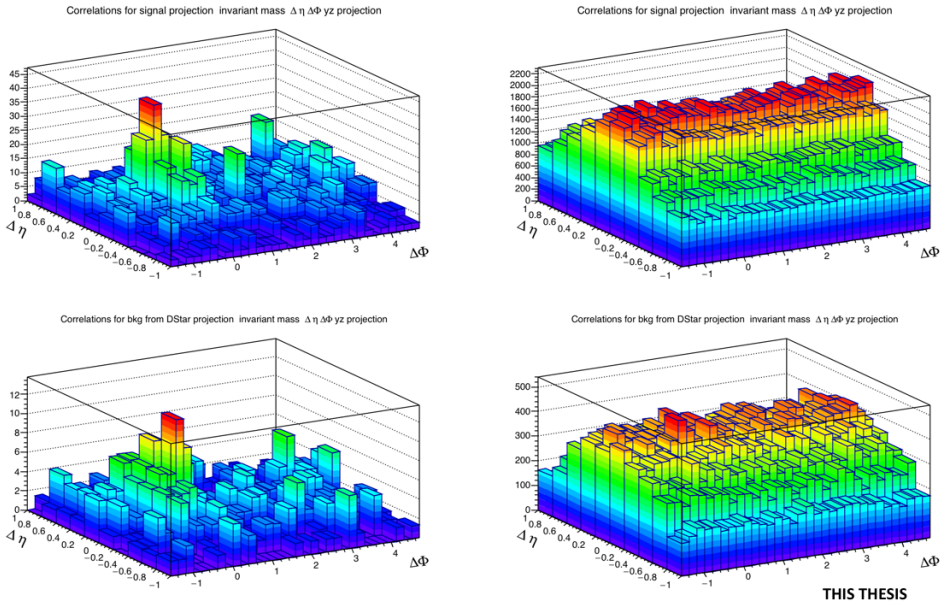

Figure 4.5 – D^{*+} *meson* $(\Delta\varphi, \Delta\eta)$ *correlation for in the signal region (top row) and sidebands (bottom row) from pool1, for Single Event (left) and Mixed Event analysis (right) for high* p_{T}*:* $3 < p_{\mathrm{T}} < 5$ *GeV/c with associated* $p_{\mathrm{T}} > 0.3$ *GeV/c.*

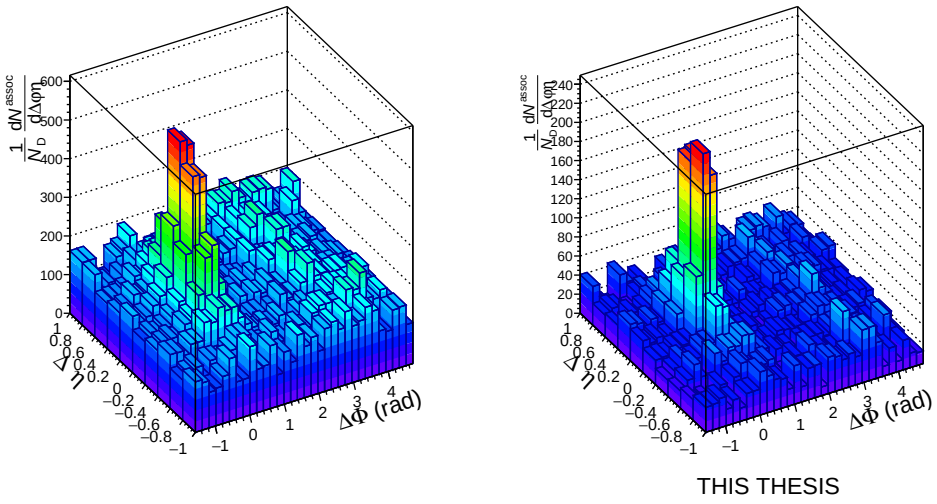

Figure 4.6 – D^{*+} *meson* $(\Delta\varphi, \Delta\eta)$ *correlation distribution for* $8 < p_{\mathrm{T}}(\mathrm{D}^{*+}) < 16$ *GeV/c with associated* $p_{\mathrm{T}}^{assoc} > 0.3$ *GeV/c. Left panel: mixed-event corrected distribution for inclusive* D^{*+} *candidates. Right panel: mixed-event corrected distribution for sideband candidates.*

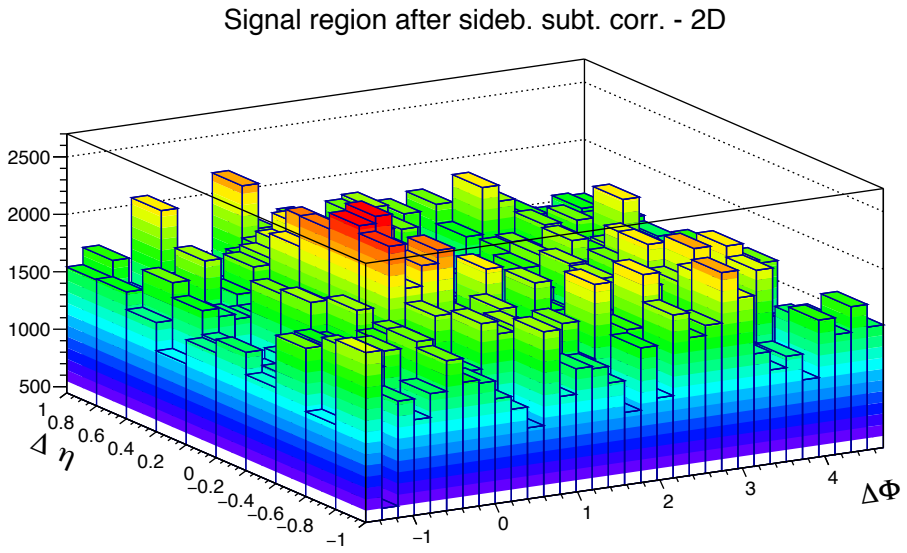

Figure 4.7 – *Mixed-event corrected correlation distribution of D^{*+}-h with $8 < p_{\mathrm{T}}(\mathrm{D}^{*+}) < 16$ GeV/c and associated track: $p_{\mathrm{T}}^{assoc} > 0.3$ GeV/c, after the background subtraction.*

Fig. 4.5 show the correlation distribution of the inclusive D^{*+} sample for the single event analysis on the left and the side-band candidates on the right. The second row illustrates the same, but for the mixed-event analysis. Both the inclusive and side-band distributions are corrected using the equation 4.1, and the distributions shown in Fig. 4.6 are obtained (left for the inclusive case and right for the side-bands). The outcome of the mixed-event correction after the background subtraction is provided in Fig. 4.7. The expected triangular shape in $\Delta\eta$, for the mixed-event distributions, addresses the effect of the limited detector pseudo-rapidity acceptance. In particular, it can be noticed that the mixed-event distribution is limited to the interval $|\Delta\eta| < 1$, even though this limit could be extended to $|\Delta\eta| < 1.6$ given the ALICE acceptance. The decision to limit the mixed-event correction, and thus the whole analysis, to the $|\Delta\eta| < 1$ range was taken in order to avoid the so-called "wing effect", i.e. the wing-like structures arising in the correlation distribution at large $\Delta\eta$ due to the limited filling of the correlation bins in that region which cause large statistical fluctuations. Such wings could bias the near- and away-side peaks, as well as would bias drastically the estimation of the baseline due to uncorrelated background from underlying events.

4.4.5 Correction for tracking and D-meson trigger efficiencies

(i) Tracking efficiency

The correlation distribution needs to be corrected for the amount of associated particles that are not reconstructed or are rejected by the track quality selection in each event.

The tracking efficiency was calculated by obtaining the ratio between the yield at the reconstructed level and generated level, for a defined "type" of particle (non-identified particle) and it was estimated differentially as a function of the charged track p_{T}, η and the position of the primary vertex along the beam axis z_{vtx}. Only primary pions, kaons, protons, electrons and muons were considered as charged particles. Hence, the efficiency maps were built by scaling the reconstructed spectra with the one generated using the PYTHIA event generator [148].
The single track efficiency extracted ($\epsilon(p_{\mathrm{T}}, \eta, z_{vtx})$) was used as weight of the two-dimensional correlation distribution. Fig. 4.8 shows the efficiency dependence on the transverse momentum of the charged track. The efficiency exhibits a steep raise at low-p_{T} and for $p_{\mathrm{T}}^{assoc} > 2$ GeV/c it decreases slightly before reaching a *plateau*.

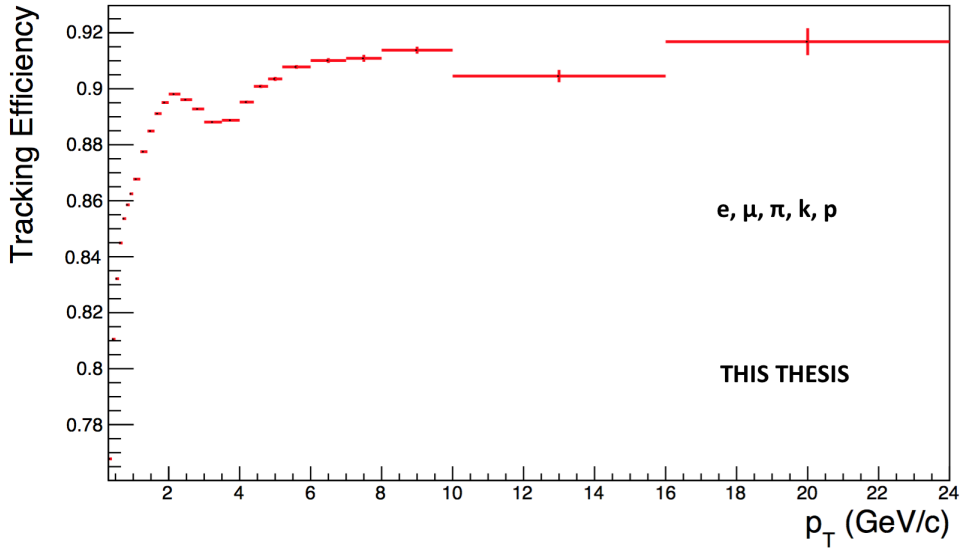

Figure 4.8 *– 1D tracking efficiency map as a function of the transverse momentum for standard track selection, evaluated for five species (electron, muon, pion, kaon and proton) and also different species using the minimum-bias Monte Carlo samples anchored to the analyzed data samples.*

(ii) D^{*+} meson efficiency

The azimuthal correlation distribution is affected by the reconstruction and selection efficiency of D^{*+} mesons. Indeed, the correlations are estimated in wide p_{T} bins of the D^{*+}, where the efficiency increases steeply as function of the p_{T} of the D^{*+}. The correction for the D^{*+} meson efficiency is necessary to properly take into account the p_{T}-dependence of the correlation distribution within the given D^{*+} meson p_{T} interval. In fact, only the shape of the p_{T} dependence of the D^{*+} meson efficiency is relevant while the average value in the p_{T} range is simplified due to the normalisation of the

correlation distribution to the number of trigger particles. The efficiency is estimated using a PYTHIA + GEANT3 Monte Carlo sample. Additionally, the obtained efficiency is corrected for the geometrical acceptance of the ALICE detectors. In Figs. 4.9 and 4.10, the prompt and feed-down D^{*+} reconstruction efficiency in pp collisions as function of the $D^{*+}(p_T)$ and of the multiplicity, quantified using the number of SPD tracklets, is reported on the left panel, while on the right panel the dependence on the transverse momentum is shown. The expected increase as function of both the variables is clearly visible. The correction is applied online, by using the two-dimensional map of D^{*+} meson efficiency to weight the correlation distribution with the inverse of the efficiency value for a given p_T and multiplicity yield.

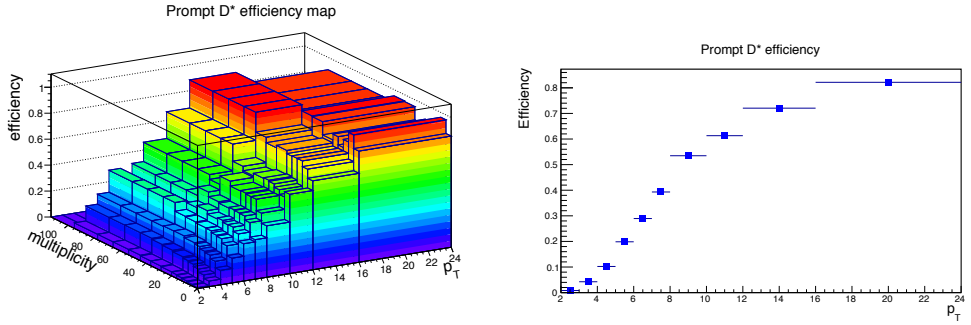

Figure 4.9 *– (p_T, multiplicity) dependence (left) and p_T dependence (right) of prompt D^{*+} meson efficiency.*

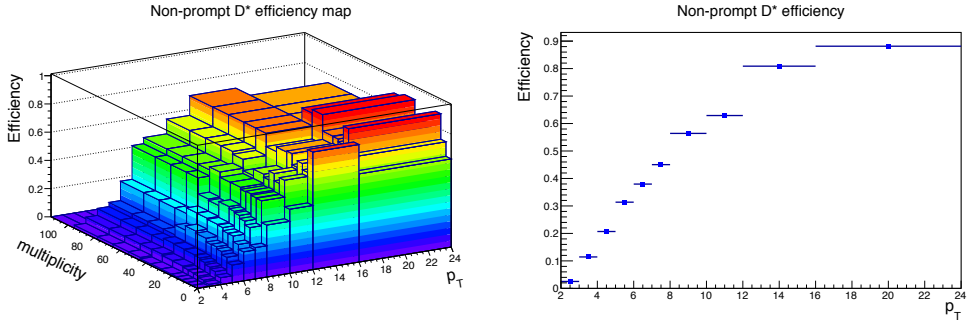

Figure 4.10 *– (p_T, multiplicity) dependence (left) and p_T dependence (right) of feed-down D^{*+} meson efficiency.*

4.4.6 Monte-Carlo closure test

To verify the consistency of the analysis chain and of the corrections applied to the correlation distributions extracted from data, an "ad-hoc" Monte-Carlo closure test was setup and performed for this purpose.

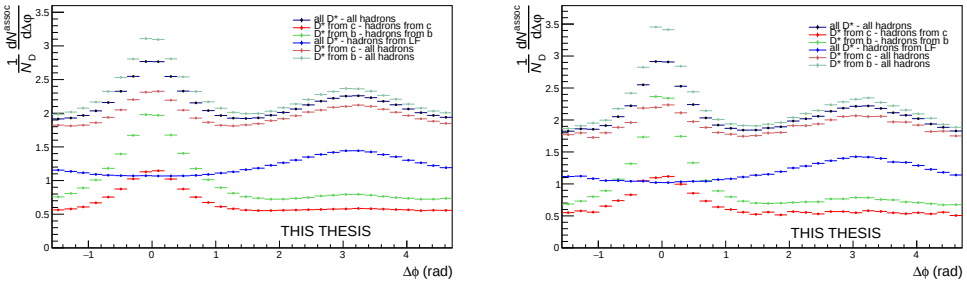

Figure 4.11 *– Azimuthal correlation distributions at kinematic level (left panel) and at kinematic level (right panel) for* $3 < p_{\mathrm{T}}(\mathrm{D}^{*+}) < 5\mathrm{GeV}/c$ *and associated* $p_T^{assoc} > 0.3\mathrm{GeV}/c$*. Black points: All* D^{*+}*-all hadrons, normalized by all* D^{*+} *triggers; light red points:* D^{*+} *from c-hadrons from c, normalized by c-*D^{*+} *triggers; dark red points:* D^{*+} *from c-all hadrons, normalized by c-*D^{*+} *triggers; light green points:* D^{*+} *from b-hadrons from b, normalized by b-*D^{*+} *triggers; dark green points:* D^{*+} *from b-all hadrons, normalized by b-*D^{*+} *triggers; blue points: all* D^{*+}*-hadrons from light quarks, normalized by all* D^{*+} *triggers.*

The correlation analysis was performed both at kinematic level and at reconstructed level on the Monte Carlo sample enriched with charm and beauty quarks content. At reconstructed the Monte Carlo simulations were combined with GEANT3 package [147] to simulate all the detector effects. At kinematic level, D^{*+} mesons were identified by their Monte Carlo identity and applying only acceptance cuts ($|\eta| < 0.9$). It was required that the D^{*+} decays into the hadronic decay channel. The associated tracks are selected as "all" possible primary charged particles in the final state and applying acceptance cuts as well.

At reconstruction level, the analysis was performed including the detector response. Therefore, all the corrections computed on data were applied at this level: starting from the event selection, then topological cuts on the D^{*+} and the particle identification selection were performed; only the true D^{*+} mesons, identified by matching with the Monte Carlo truth, were kept. Non-primary particles were rejected by means of a cut on the distance of closest approach to the primary vertex in the transverse plane (DCA_{xy}). Event mixing correction was applied both at reconstructed and at kinematic level, where it takes into account just the effects of the acceptance cuts. In addition, at reconstructed level, the efficiency corrections for D^{*+} mesons and associated tracks were also applied.

The origin of the D^{*+} and the charged particles has also been studied. For the purpose of this analysis, it is interesting to separate the particles depending on their origins, i.e. from the fragmentation of a charm or a beauty quark. For each D^{*+} and charged particle, the flavour of the mother (i.e. the particle that comes earlier in the production chain) is checked. If this arise from a beauty quark, then the particle is tagged as a "beauty-origin", while if it belongs from a charm quark, then it is tagged as "charm-

origin". Charged particles not originating from a beauty or charm quark are tagged as "non heavy-flavour particles". For the D^{*+}, if no charm or beauty quark is found, it is not considered for building the correlation distribution. The flavour-differential Monte Carlo analysis is performed for the main contributors to the correlation distribution, i.e. the correlations are studied for the following cases:

- correlations between all D^{*+} mesons (coming from the fragmentation of b or c quarks) with all hadrons;
- correlations between D^{*+} meson originating from c quarks and charged particles coming from c quarks as well;
- correlations among D^{*+} mesons coming from the charm fragmentation and all the hadrons;
- correlations between D^{*+} meson and hadrons, both coming from b quark fragmentation;
- correlations among D^{*+} mesons coming from the b fragmentation and hadrons, without any specific origin;
- correlations between all D^{*+} mesons and charged tracks coming from light quarks;

In each case the correlation distributions have been normalized by the number of D^{*+} mesons involved in the specific sample. The azimuthal correlation distributions at kinematic and reconstructed level are reported in Fig. 4.11. The black points represent the inclusive case for both the D^{*+} mesons and the associated tracks, the dark and light green are for beauty-originated D^{*+} mesons correlated with all hadrons and charmed tracks, respectively. The dark and light red distributions tags the charm-originated D^{*+} mesons correlated with all hadrons and charmed charged particles, respectively. The blue distribution represents the correlations of D^{*+} mesons with non-heavy flavour hadrons. The distributions show the expected pattern for near- and away-side peaks in all the cases, making exception only for the non-heavy flavoured distribution which is characterized by a rather flat behavior along $\Delta\varphi$, with an indication of an away-side correlation peak. Furthermore, both the beauty and the charm origin distributions have compatible have very similar properties with respect to the inclusive distribution, while when D^{*+} mesons are correlated with charged tracks originated from beauty or charm quarks, both the baseline and the away-side are suppressed.
The goal of this consistency check was to verify if, after having applied all the corrections to the azimuthal correlation plots at reconstructed level, the results were compatible with the ones at kinematic level. Hence, the ratios of fully corrected reconstructed plots over kinematic plots were evaluated in all the trigger p_{T} bins and for the various p_{T} thresholds for the associated tracks, separating the contributions for the different origins of particles and triggers.
The ratios of the average reconstructed over generated ratios are shown in Figure 4.12 for exemplary kinematic regions (covering anyway the full span of the measurement).

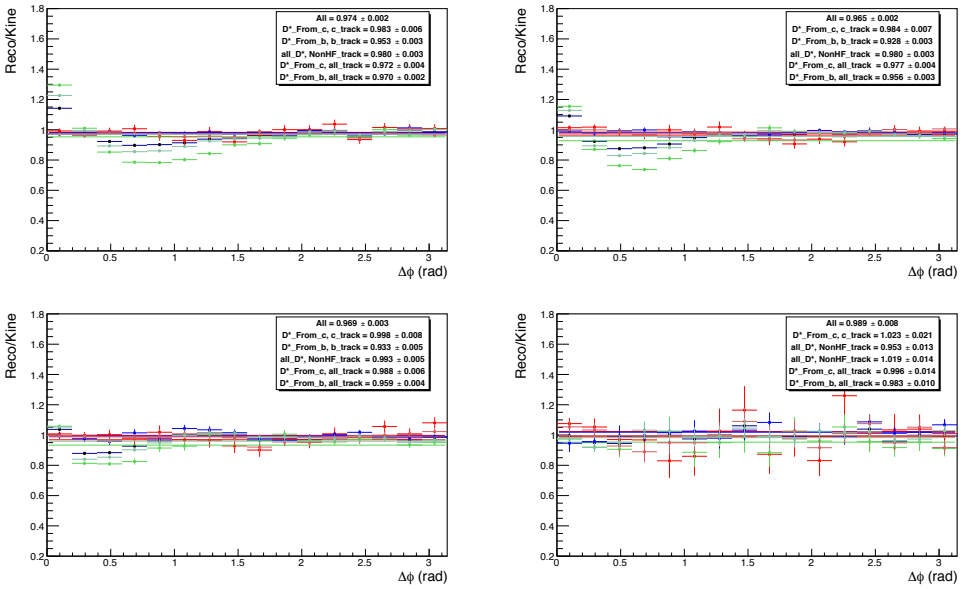

Figure 4.12 – *Ratios of fully corrected azimuthal correlation plots at reconstructed level over azimuthal correlation plots at kinematic level. for* D^{*+} p_T *bins, for the different associated* p_T *ranges. Black points: All* D^{*+}*-all hadrons, normalized by all* D^{*+} *triggers; light red points:* D^{*+} *from c-hadrons from c, normalized by c-*D^{*+} *triggers; dark red points:* D^{*+} *from c-all hadrons, normalized by c-*D^{*+} *triggers; light green points:* D^{*+} *from b-hadrons from b, normalized by b-*D^{*+} *triggers; dark green points:* D^{*+} *from b-all hadrons, normalized by b-*D^{*+} *triggers; blue points: All* D^{*+}*-hadrons from light quarks, normalized by all* D^{*+} *triggers. The panels show the ranges:* $3 < p_{\mathrm{T}}(\mathrm{D}^{*+}) < 5$ GeV/c *(top left);* $5 < p_{\mathrm{T}}(\mathrm{D}^{*+}) < 8$ GeV/c *(top right);* $8 < p_{\mathrm{T}}(\mathrm{D}^{*+}) < 16$ GeV/c *(bottom left) and* $16 < p_{\mathrm{T}}(\mathrm{D}^{*+}) < 24$ GeV/c *(bottom right) with* $p_{\mathrm{T}}^{assoc} > 1$ GeV/c *for the associated tracks.*

An overall good compatibility with 1, within the uncertainties, is obtained especially in the case of correlations of all D mesons with non heavy flavoured hadrons (blue curves). A small downward deviations at low p_{T} is present and will contribute with a 2-3% asymmetric systematic uncertainty.

The major exceptions to the previous conclusion are clearly the structures in the near side region for the beauty origin case. It was verified that these structures are induced by the topological selection for the D mesons. Indeed, in cases in which the D meson triggers come from the decay of beauty hadrons, the topological cuts applied (especially the cosine of the pointing angle) tends to favour cases with a small angular opening between the products of the B-hadron decay (i.e. the D meson trigger itself and other particles), with respect to cases where the B decay particles are less collinear.
In the Monte Carlo closure test, this situation is reflected in the correlation distributions at reconstructed level, where the topological selection is applied; while it does not occur at kinematic level. Hence, in the reconstructed/kinematic ratio, the distribution would show an excess for $\Delta\varphi = 0$ (due to the favoured decays with small opening angle), which is then compensated by a depletion for larger values of $\Delta\varphi$ (corresponding to B decays with larger angles, which are disfavoured). These structures are prominent at low p_{T} of D mesons, where the topological cuts are tighter, and tend to disappear at higher p_{T}, where the selections are released. They are also larger in the higher associated track p_{T} ranges, where the fraction of B-hadron decay tracks dominate the overall correlation distributions.
This bias and, in particular, the enhancement of beauty-origin correlation pairs at the centre of the near side region could influence the near-side peak features. In order to correct the data distributions for these effects, the amount of the b-origin excess is evaluated from the ratio of reconstructed and kinematic level, by considering the azimuthal correlations of D-mesons coming from beauty hadron decays and all the charged particles tracks case (dark green points in Fig 4.12). The excess at reconstructed level (affecting data) is quantified as a $\Delta\varphi$ modulation (denoted as **modul** in the Eq. 4.2) for the five points on each side of the $\Delta\varphi = 0$ value (or, equivalently, on the first five points of the reflected distributions, which start from $\Delta\varphi = 0$). This was done in each kinematic range analysed . Then, the correction is performed by applying this modulation to the data correlation distributions, but taking into account that only the correlation entries from B→D are affected, while the c→D correlations need to be left unaltered. In particular, it has to be considered that:

- on data, the B→D correlation pairs are only a fraction of the total: (1-f_{prompt}) and this fraction is evaluated via FONLL predictions [7];
- the amplitude of B→D$|_{\mathrm{amplit}}$ correlation pattern is different (greater) than the amplitude of the c→D$|_{\mathrm{amplit}}$ correlation pattern.

Thus, the following equation is applied to get the corrected $C(\Delta\varphi)_{\mathrm{corr}}$ data points starting from the raw ones, $C(\Delta\varphi)_{\mathrm{raw}}$:

$$C(\Delta\varphi)_{\mathrm{corr}} = C(\Delta\varphi)_{\mathrm{raw}} \cdot \left[\frac{\mathrm{c} \to \mathrm{D}|_{\mathrm{amplit}}}{(\mathrm{B}+\mathrm{c}) \to \mathrm{D}|_{\mathrm{amplit}}} \cdot f_{\mathrm{prompt}} + \frac{\mathrm{B} \to \mathrm{D}|_{\mathrm{amplit}}}{(\mathrm{B}+\mathrm{c}) \to \mathrm{D}|_{\mathrm{amplit}}} \cdot (1 - f_{\mathrm{prompt}}) \cdot \frac{1}{\mathbf{modul}} \right] \tag{4.2}$$

where $(\mathrm{B}+\mathrm{c}) \to \mathrm{D}|_{\mathrm{amplit}} = \mathrm{c} \to \mathrm{D}|_{\mathrm{amplit}} \cdot f_{\mathrm{prompt}} + \mathrm{B} \to \mathrm{D}|_{\mathrm{amplit}} \cdot (1 - f_{\mathrm{prompt}})$, and where the two amplitudes are evaluated from the Monte Carlo distributions at reconstructed level (so, including the bias), and f_{prompt} is the fraction of prompt D-mesons and is obtained with the procedure described in 4.4.8. Applying the **modul** factor to the beauty part of the data correlation distributions brings its value back to the generated level case, effectively removing the bias.
The effect of the correction is a shift of the data points in the near-side region: in general, downward in the first and second points, and upward in the others. The maximum value of the shift is of about 5%, at the centre of the near-side peak, for the lowest D-meson p_{T} range ($3 < p_{\mathrm{T}} < 5$ GeV/c) and the highest associated track p_{T} range ($p_{\mathrm{T}} > 3$ GeV/c). The typical values are instead of a couple of percentage points. The correction is zero in the highest D-meson p_{T} range. To take into account for possible inaccuracies in the definition of the modulations, or in their rescaling, a systematic uncertainty is applied on the corrected data points, with value $|C(\Delta\varphi)_{\mathrm{corr}} - C(\Delta\varphi)_{\mathrm{raw}}|/\sqrt{(12)}$, on each side of the data points affected by the bias (symmetric uncertainty).

4.4.7 Secondary track contamination

The contribution of secondary tracks inside the associated track sample, produced from the interaction of primary track with the detector material or coming from the decays of strange hadrons, is mostly removed by means of an upper cut on the distance of closest approach (DCA) cuts applied during the track selection phase (DCA(xy) < 1 cm, DCA(z) < 1 cm). However, a small fraction of secondary tracks survives this cut, and the data correlation distributions have to be corrected for this residual contamination.
The fraction of surviving secondary tracks is evaluated via a study on the enriched Monte Carlo sample, by counting the number of tracks accepted by the selection whose corresponding generated-level track doesn't satisfy the requirement of being a primary particle, and dividing this number by the total number of accepted tracks. From the check results that, on average, no more than about 4.5% secondary tracks pass the selection (6% in the lowest associated p_{T} range). Moreover, the fraction of residual secondary tracks is rather flat along the $\Delta\varphi$ axis, as shown, for exemplary p_{T} regions, in Figure 4.13, where the inhomogeneities are generally not larger than about 1%. The presence of these modulations, which vary from bin to bin, even if small, could be amplified after the subtraction of the baseline, when going to the yield evaluation. In order to take into account for them, the purity correction was estimated differentially though the azimuthal axis (i.e. applied bin-per-bin on the azimuthal correlation distributions).
In particular, three approaches were tried, by multiplying the data correlation distribution in each kinematic range by:

- the MC primary/inclusive histogram (blue histogram in Fig. 4.13)
- a polynomial fit applied to the Monte-Carlo primary/inclusive histogram (red curve in Fig. 4.13)

- a moving average, considering 3 points, of the MC primary/inclusive histogram (red histogram in Fig. 4.13)

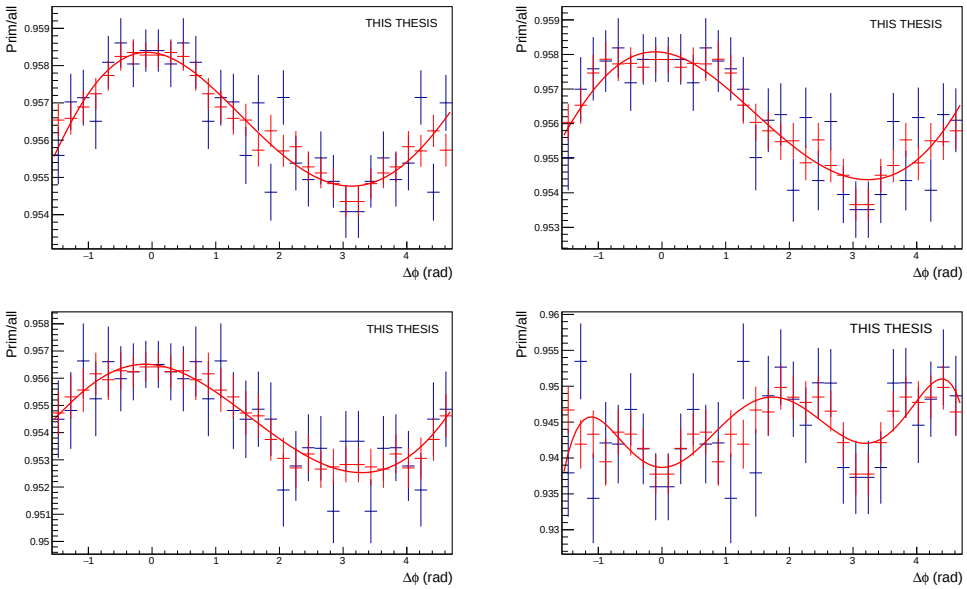

Figure 4.13 – *Fraction of primary tracks in the reconstructed associated track sample (blue histogram). The polynomial fit function (red curve) and the 3-point moving average (red histogram) are also superimposed. Top left:* $3 < p_{\mathrm{T}}(D) < 5$ GeV/c*; top right:* $5 < p_{\mathrm{T}}(D) < 8$ GeV/c*, bottom left:* $8 < p_{\mathrm{T}}(D) < 16$ GeV/c *and bottom right* $16 < p_{\mathrm{T}}(D) < 24$ GeV/c*, for* $p_{\mathrm{T}}(assoc) > 0.3$ *GeV/c.*

Each approach has pros and cons, since directly using the primary/inclusive histogram gives a correction strongly dependent on the statistical fluctuations, while using the fit or the moving average smoothen the fluctuation, but also the structures with a physical origin (and the fit misses a periodicity condition). For this reason, a comparison of the outcome of the correction after applying either of the approaches (adding also the "flat" correction approach used in the centrality integrated analysis in p–Pb collisions) was performed, which gave full compatibility (within less than 1%) of the correlation distributions corrected with either approach. The moving average approach was chosen as standard correction procedure.

It was also verified with the same Monte Carlo study that applying the DCA selection rejects less than 1% primary tracks (tagged as false positives) from the associated track sample, and less than 1% of heavy-flavour originated tracks, again with a flat azimuthal distribution, inducing hence a fully negligible bias on the data correlation distributions. This was also verified for specific charm-origin and beauty-origin tracks, due to their larger DCA with respect to primary tracks from light quarks. In this case, the fraction of rejected charm and beauty tracks stays below 1% in all the kinematic ranges apart

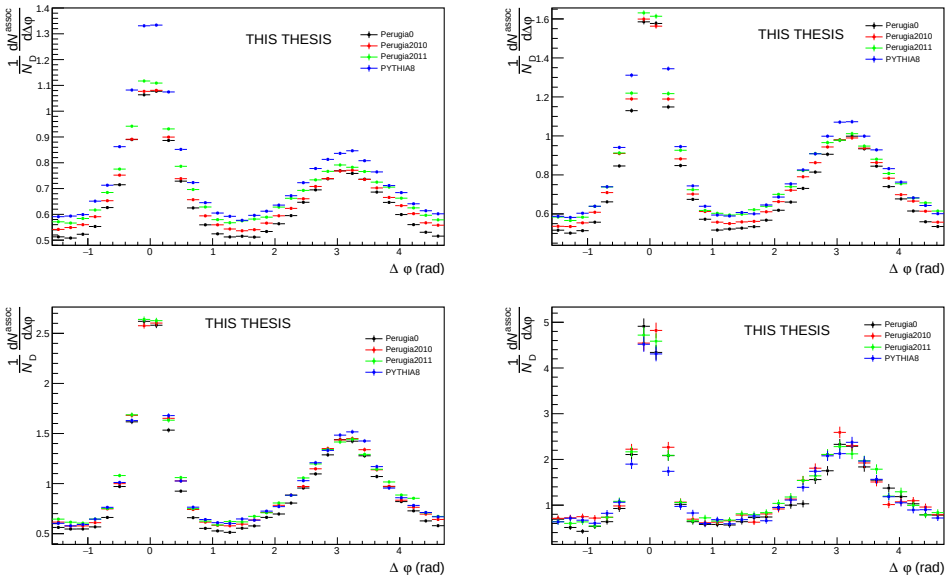

Figure 4.14 – *Top: Azimuthal correlation distribution between* D^{*+} *meson from b-hadron decay and charged particles obtained from Monte Carlo simulations based on PYTHIA-Perugia2010 tune (row1), PYTHIA-Perugia2011 tune (row2), PYTHIA8 tune 4C (row3) for associated track* $p_{\mathrm{T}} > 0.3$ GeV/c *and D-meson* p_{T} *ranges:* $3 < p_{\mathrm{T}}(D) < 5$ GeV/c*; top right:* $5 < p_{\mathrm{T}}(D) < 8$ GeV/c*, bottom left:* $8 < p_{\mathrm{T}}(D) < 16$ GeV/c *and bottom right* $16 < p_{\mathrm{T}}(D) < 24$ GeV/c.

from the associated track p_{T} regions $0.3 < p_{\mathrm{T}} < 1$ GeV/c and in the inclusive range $p_{\mathrm{T}} > 0.3$ GeV/c, where the rejection can be as high as 2%. In these kinematic ranges, though, the data correlation distributions are dominated by non-heavy-flavour tracks, as it was verified from the simulations, hence the overall bias is still contained below 1%, thus negligible. These studies were performed on an enriched Monte Carlo sample, which could not fully reproduce the relative abundances of the species. Anyway, for events with a reconstructed D-meson, this bias is expected to be minor, and only these events are used in the data analysis. However, the percentages obtained from the study were found to be consistent within 1%.

4.4.8 Beauty feed-down subtraction

A fraction of the reconstructed D^{*+} mesons is composed of secondary D^{*+} mesons coming from B-meson decays. The topological cuts applied preferentially select displaced vertices, leading to a larger efficiency for secondary D^{*+} meson than for prompt D^{*+} meson reconstruction. Therefore, the fraction f_{prompt} of reconstructed prompt D^{*+} mesons does not coincide simply with the natural fraction and depends on the analysis details. The different fragmentation, as well as the contribution of B-meson decay particles and a

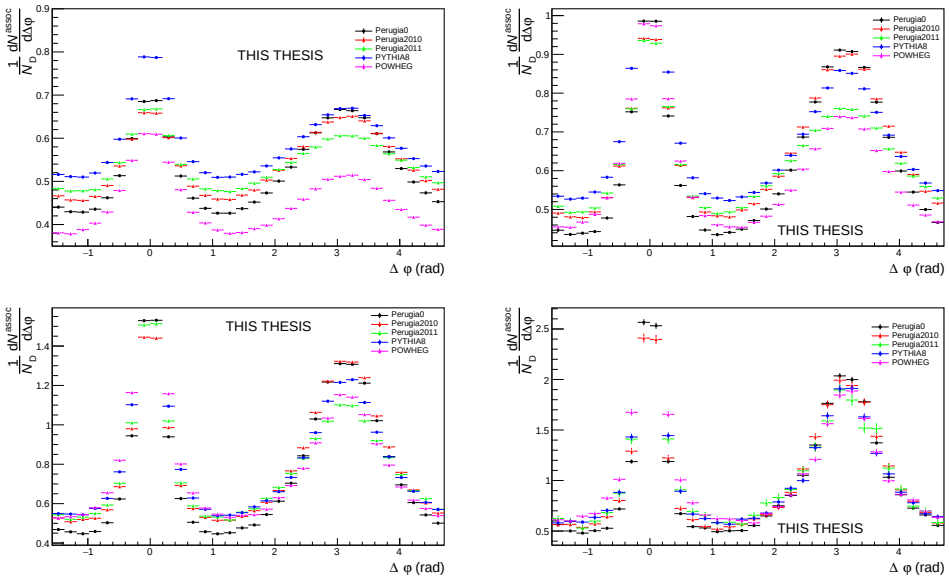

Figure 4.15 – *Azimuthal correlation distribution between prompt* D^{*+} *meson and charged particles obtained from Monte Carlo simulations based on PYTHIA-Perugia2010 tune (row1), PYTHIA-Perugia2011 tune (row2), PYTHIA8 tune 4C (row3) for associated track* $p_{\mathrm{T}} > 0.3$ GeV/c *and D-meson* p_{T} *ranges:* $3 < p_{\mathrm{T}}(D) < 5$ GeV/c*; top right:* $5 < p_{\mathrm{T}}(D) < 8$ GeV/c*, bottom left:* $8 < p_{\mathrm{T}}(D) < 16$ GeV/c *and bottom right* $16 < p_{\mathrm{T}}(D) < 24$ GeV/c*.* D^0 *in blue,* D^+ *in green,* D^{*+} *in red.*

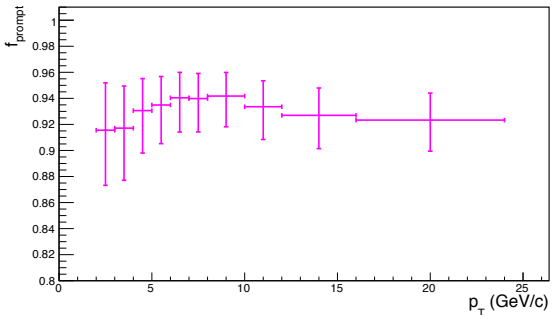

Figure 4.16 – $f_{\rm prompt}$ *as a function of the* $p_{\rm T}$ *for* $\rm D^{*+}$ *estimated on the basis of FONLL predictions*

possible different contribution of gluon splitting to charm- and beauty-quark production, imply a different angular-correlation distribution of prompt and secondary $\rm D^{*+}$ mesons with charged particles, as it was verified with the Monte-Carlo simulations, shown in Figs.4.14 and 4.15. The contribution of feed-down $\rm D^{*+}$ mesons to the measured angular correlation is subtracted as follows:

$$\tilde{C}_{\rm prompt\ D}(\Delta\varphi) = \frac{1}{f_{\rm prompt}}\left(\tilde{C}_{\rm inclusive}(\Delta\varphi) - (1-f_{\rm prompt})\tilde{C}^{\rm MC\ templ}_{\rm feed-down}(\Delta\varphi)\right). \qquad (4.3)$$

In the above equation, $\tilde{C}_{\rm inclusive}(\Delta\varphi)$ and $\tilde{C}_{\rm prompt\ D}(\Delta\varphi)$ are per-trigger azimuthal correlation distributions before and after the feed-down contribution subtraction, $f_{\rm prompt}$ is the fraction of prompt $\rm D^{*+}$ mesons and $\tilde{C}^{\rm MC\ templ}_{\rm feed-down}$ is a template of the azimuthal correlation distribution for the feed-down component obtained from "ad-hoc" Monte Carlo simulation at generated level, using PYTHIA6 with Perugia-2011 tune. $f_{\rm prompt}$ was evaluated on the basis of FONLL calculations of charm and beauty $p_{\rm T}$-differential production cross sections [7] and of the reconstruction efficiencies of prompt and secondary $\rm D^{*+}$ mesons, calculated using Monte-Carlo simulations. In order to avoid biases related to the different event multiplicity in real and simulated events, the correlation distribution were shifted to have the minimum coinciding with the baseline of the data azimuthal-correlation distribution before feed-down subtraction.
The value of $f_{\rm prompt}$ (Fig. 4.16), which depends on D-meson species and varies as a function of the $p_{\rm T}$, is estimated on the basis of FONLL predictions for the production of feed-down $\rm D^{*+}$ mesons at central rapidity, in pp collisions at $\sqrt{(s)} = 5$ TeV, and using the reconstruction efficiency of prompt and feed-down $\rm D^{*+}$ mesons, following the so-called $N_{\rm b}$ approach[2] described in [120]. Typical feed-down values for the $\rm D^{*+}$ are

[2]In this approach f_{prompt} is evaluated using the B production cross-section from the FONLL pQCD calculation and the B→D decay kinematics from the EvtGen package. The computed cross section for the feed-down component for each of the three D meson species was used,

about 5-8%, fully consistent with the value obtained for the p–Pb data sample, with rather similar cut selections.

4.5 Systematic uncertainty studies

4.5.1 Uncertainty on S and B extraction

The systematic uncertainty for the D^{*+} meson yield extraction was obtained by evaluating the raw yield of the signal candidates with the following alternative approaches of the invariant mass spectra with respect to the standard one:

- replacing the background fit function (convolution of an exponential with a threshold power function) of the invariant mass spectra with a second order polynomial function and a power function;
- fitting the invariant mass distribution in a smaller and larger range with respect to the standard one ($|M - \mu| < 2\sigma$);
- changing the range of invariant mass distribution in which the signal region is defined (and where signal and background are extracted);
- extracting signal and background via integral of the fit functions or by means of bin counting for the background and via integral of the Gaussian function for the signal.

Both the value of the yield and of the sidebands correlations normalization factor are influenced by the change of the yield extraction approach, while the rest of the procedure to extract the azimuthal correlation distribution is the same as in the standard analysis. The fully corrected azimuthal correlation plots were evaluated, for each of these approaches, in all D^{*+} meson p_{T} intervals and for each value of associated tracks p_{T} threshold. The ratios of the correlation distributions obtained with the standard yield extraction procedure and by differentiating the approach were evaluated. From the average of these ratios, which are found to be flat versus $\Delta\varphi$, a systematic uncertainty can be extracted, which was taken of about 1% for $3 < p_{\mathrm{T}}(D) < 16$ GeV/c and up to 3% in the highest p_{T} range ($16 < p_{\mathrm{T}}(D) < 24$ GeV/c). No dependence versus the associated track p_{T} was assumed, since from a physics point of view, it isn't expected any modification of the signal and sideband values to have a dependence of this kind.

---

together with the Monte Carlo acceptance times efficiency $(\mathrm{Acc}\times\epsilon)_{feed-down}$ for D mesons from B decays to compute the expected feed-down contribution:

$$f_{prompt} = 1 - (N^{\mathrm{D}^{*+}fromB}/N^{\mathrm{D}^{*+}raw}) \tag{4.4}$$

More details can be found in [120].

4.5.2 Uncertainty on background correlation shape

The systematic uncertainty for the subtraction of the background correlations includes the effects due to a potentially biased description of the background correlation shape, which is evaluated from the sidebands correlations. In particular, the background correlation shape could present some hidden invariant mass dependence. To estimate this uncertainty, the invariant mass range of the sidebands definitions was varied with respect to the default values. For the D^{*+} meson, the usual range of sideband in invariant mass spectra is 5 to 10 σ (only on the right side) from the centre of the peak of the Gaussian fit of the invariant mass spectra, and it was modified to:

- inner half (5 to 8 σ from the centre of the peak);
- outer half (8 to 13 σ from the centre of the peak);
- extended to 5 to 13 σ from the centre of the peak;
- extended to 5 to 16 σ from the centre of the peak.

The rest of the procedure for the azimuthal correlations distribution was unchanged, and the ratios of the fully corrected azimuthal correlation plots obtained with the standard sidebands range and the correlation plots extracted with different sidebands definitions, were evaluated for each D-meson p_{T} bin and associated tracks p_{T} threshold. From the values of the ratios extracted from the checks, which do not show any azimuthal dependence, a systematic uncertainty for the background subtraction can be evaluated. Also no dependence versus the associated track p_{T} was assumed also in this case. The uncertainty was hence taken of 1-2% for all the mesons in $3 < p_{\mathrm{T}}(D) < 16$ GeV/c and up to 3% in $16 < p_{\mathrm{T}}(D) < 24$ GeV/c.

4.5.3 Uncertainty on D-meson cut stability

To study the systematics due to the topological selections on the D^{*+} meson, the cut variation approach was used. Alternate sets of released and tightened selection cuts were applied to extract the correlation distribution, varying in particular the cosine of the pointing angle, the maximum distance of closest approach among the daughter tracks and the product of the daughter track impact parameters. For each set of cuts new D^{*+} meson efficiency map (as a function of p_{T} and multiplicity) was computed. To highlight how the different selections effectively varied the efficiency values, especially at low p_{T}, where cuts are more effective, the ratio of the different 1D efficiencies with the alternate cuts with respect to the default cut selection has been studied. The ratios are reasonably flat in $\Delta\varphi$, as a consequence that the correlation distribution are normalized by the total number of D^{*+} mesons. Hence a flat systematic was evaluated as systematic uncertainty for D^{*+}-meson cut variations. The uncertainty was evaluated to be from 1% to 2.5% depending on the D-meson specie and on the kinematic range.

4.5.4 Uncertainty on tracking efficiency evaluation

The systematic uncertainty assigned to cover a possible bias on the associated tracking efficiency is evaluated by varying the associated track selection. With respect to what done in subsection 4.4, additional variations were studied, for the D^{*+} mesons (as well for the other two mesons). In particular, the following alternative cut sets were considered:

- no request on the minimum number of clusters in the inner tracking system (ITS);
- minimum of 3 ITS clusters, among which at least one coming from the silicon pixel detector (SPD);
- minimum number hits in the time projection chamber (TPC) of 90;
- minimum ratio of hits and findable hits equal to 0.9 in the TPC;
- p_{T}-dependent cut on the minimum number of TPC clusters ($> 120 - (5/p_{\mathrm{T}})$).

For this uncertainty, to the values obtained from the above ratio an additional 2%, for a wrong evaluation of the ITS-TPC matching efficiency, was added in quadrature (being 1% for associated track p_{T} <1 GeV/c, 2% in $1 p_{\mathrm{T}} < 2$ GeV/c and 2.7% in 2< p_{T} <3 GeV/c). The assigned uncertainty varies from 2.5 to 5%, slightly increasing with the p_{T} of the associated tracks, mainly due to the increase of the ITS-TPC matching efficiency.

4.5.5 Uncertainty on secondary particle contamination

Secondary particles, i.e. particles coming from strange hadrons decays or particles produced in interactions with the material, are expected to be tagged and removed by means of a distance of closest approach (DCA) from primary vertex cut. The uncertainty arising from the residual contamination of secondary tracks can be estimated from a Monte Carlo study, at reconstructed level. The number of primary (secondary) tracks, accepted (rejected) from the DCA cut, was determined for different values of the DCA selection, and the correlation distributions for the various cases were evaluated. The variations were done in the xy direction, denoted by a better resolution on the DCA, and the following cases were tried (in addition to the default cut where the DCA_{xy} is set to 1 cm): 0.1 cm, 0.25 cm, 0.5 cm, filtering DCA cut (i.e. 2.4 cm).
Hence, this quantity represents the residual contamination of secondary tracks in the reconstructed track sample. From these values, the corresponding primary track purities (1-contamination) were extracted, in each of the momentum ranges. It was also verified that, for all the cut selections, the $\Delta\varphi$ distributions of the residual contaminations were rather flat (anyway, a bin-by-bin dependent purity correction value was evaluated, as for the standard analysis).
As a second step of the procedure to verify the DCA cut stability, the D-hadron analysis was performed with all the different DCA selection (each time with the proper tracking efficiency map). After having extracted the correlation distributions, these were rescaled

(bin-by-bin) for the corresponding purities and compared with the purity-corrected correlation distributions obtained with the standard DCA selection.
The ratios of the alternate selections over the standard selection show a flat trend along the $\Delta\varphi$ axis and, in general, a discrepancy from the value of 1 of no more than 3% (the worst case being the $0.3 < p_{\rm T} < 1$ GeV/c range for the associated track). Hence, a flat and symmetric 2% systematic uncertainty on the evaluation of the secondary contamination was assigned on the base of this check in $0.3 < p_{\rm T} <1$ GeV/c, reduced to 1% in $2 < p_{\rm T} <3$ GeV/c, $p_{\rm T} >0.3$ GeV/c and to 1.5% for the other ranges.

4.5.6 Uncertainty on feed-down subtraction

As described in Sect.4.4.8, the feed-down subtraction from the data distributions is performed by means of simulation templates of B→D-h correlation distributions from PYTHIA6 generator [148], with Perugia2011 tune, and considering the central value of $f_{\rm prompt}$ to extract the feed-down D-meson contribution. In order to evaluate a systematic uncertainty on this procedure, the feed-down subtraction procedure was repeated considering, together with PYTHIA6+Perugia2011 templates, also PYTHIA6+Perugia2010 and PYTHIA8 [34] simulations. In each case, not only the central value of the measured $f_{\rm prompt}$ was considered to rescale the distributions, but also the maximum and minimum values of its total uncertainty.
Then, the envelope of nine different cases obtained by varying the templates and the $f_{\rm prompt}$ assumption was considered, and a value of the systematics defined as the envelope spread divided by the squared root of the number of templates adopted (i.e. $\sqrt{3}$ in this analysis) was taken as systematic uncertainty. This uncertainty was assumed uncorrelated among the different $\Delta\varphi$ points and it contributes with $\sim$ 1% to the systematic uncertainty.

4.5.7 Uncertainty on correction for the bias on B to $\rm D^{*+}$ decay topologies

The evaluation of this systematic uncertainty was already explained in Section 4.4.6. For each of the five data points close to the center of the near-side peak, which are affected by the bias, a bilateral and symmetric uncertainty of amplitude $|C(\Delta\varphi)_{\rm corr} - C(\Delta\varphi)_{\rm raw}|/\sqrt{12}$ was assigned.
This because the uncorrected data points ($C(\Delta\phi)_{raw}$) are expected to be the extreme (with the current $\rm D^{*+}$-meson selection, the bias is always upwards at the centre of the peak, and always downwards on its sides). We then assume that, if the correction is properly evaluated, the corrected data points ($C(\Delta\phi)_{corr}$) are at the centre of the possible spread of the true unbiased results. In this case, the span of the possible true results (in case of underestimation/overestimation of the bias) goes from the uncorrected data points to its symmetric value, with respect to the corrected data point, on the other

direction. If this distribution is uniform, and constrained by these two values, the 1σ confidence region for the position of the true value of the unbiased points is in a bilateral $|C(\Delta\varphi)_{\mathrm{corr}} - C(\Delta\varphi)_{\mathrm{raw}}|/\sqrt{12}$ window, centered on the $C(\Delta\varphi)_{\mathrm{corr}}$ points.
This source of uncertainty was assumed uncorrelated among the $\Delta\varphi$ points.

4.6 Results

In this section, I will present the results of azimuthal correlations of D^{*+} mesons and charged particles in pp collisions at energies of $\sqrt{s}$= 5.02 TeV together with the averaged results from the D^{*+}, D^0 and D^+ meson analyses. The measurements are performed differentially as function of the transverse momentum of the D meson and associated particle, while the other kinematical and event topology variables are integrated over the whole range (i.e. they are not studied differentially). The results are obtained in four different intervals for the three D mesons: $3 < p_{\rm T}(D) < 5$ GeV/c, $5 < p_{\rm T}(D) < 8$ GeV/c, $8 < p_{\rm T}(D) < 16$ GeV/c and $16 < p_{\rm T}(D) < 24$ GeV/c with associated tracks transverse momentum: $p_{\rm T}^{assoc} > 0.3$ GeV/c and differentially in the following bins: $p_{\rm T}^{assoc} > 1$ GeV/c, $0.3 < p_{\rm T}^{assoc} < 1$ GeV/c, $1 < p_{\rm T}^{assoc} < 2$ GeV/c and $2 < p_{\rm T}^{assoc} < 3$ GeV/c.

4.6.1 Comparison and average of D^0, D^+ and D^{*+} meson correlation distributions

The ALICE collaboration measured also correlations of D^0 and D^+ mesons with charged particles. The D^0 and D^+ were fully reconstructed in the following hadronic channels: $D^0 \to K^-\pi^+$ (B.R. = 3.89% [152]) and $D^+ \to K^-\pi^+\pi^+$. The analysis follows the same strategy presented in this chapter, with the proper tunes for the D-meson reconstruction. To check the compatibility of three D meson analyses, the corrected azimuthal correlation distributions (except for the feed-down subtraction and the secondary contamination removal) for D^0-h, D^{*+}-h and D^+-h were compared. An overall agreement of the distributions from the three mesons within the uncertainties was found in all the kinematic ranges.

Given the compatibility within the uncertainties among the D^0, D^+ and D^{*+} azimuthal correlations, and since no large differences are visible in the correlation distributions observed in Monte Carlo simulations based on PYTHIA with Perugia0, 2010 and 2011 tunes[3], it was possible to perform a weighted average (eq. 4.5) of the azimuthal correlation distributions of D^0, D^+ and D^{*+}, in order to reduce the overall uncertainties. Although some correlation between the mesons could be present (about the 30% of the D^0, and also part of the D^+, come from D^{*+} decays), the three selected D-meson samples can be treated as uncorrelated. The sum of the statistical uncertainties, the systematics uncertainty on signal and background extraction and on background shape, are added in

[3]A slight near side hierarchy is present among the three meson results, with D^{*+} meson having a lower peak amplitude than D^0 and D^+. It was verified that this is induced by the presence of D^0 and D^+ mesons coming from D^{*+}, the latter having on average a larger p_T and coming, hence, on average, from a larger p_T quark parton, which fragments in slightly more tracks in the near-side.

quadrature and the inverse of this sum was used as weight, w_i.

$$\left\langle \frac{1}{N_{\rm D}} \frac{dN^{\rm assoc}}{dp_{\rm T}} \right\rangle_{Dmesons} = \frac{\sum_{\rm i=meson} w_i \frac{1}{N_{\rm D}} \frac{dN_i^{\rm assoc}}{d\Delta\varphi}}{\sum_{\rm i=meson} w_i} \quad , w_i = \frac{1}{\sigma^2_{i,\rm stat} + \sigma^2_{i,\rm uncorr.syst.}} \tag{4.5}$$

The statistical uncertainty and the uncertainties on signal and background extraction and on background shape (those used for the weights) on the average were then recalculated using the following formula:

$$\sigma^2 = \frac{1}{n_{\rm D}} \frac{\sum_{\rm i=meson} w_i \sigma_i^2}{\sum_{\rm i=meson} w_i} \tag{4.6}$$

where $n_{\rm D}$ is the number of mesons considered in the average. It can be observed that for $\sigma_i^2 = 1/w_i$ the formula coincides with the standard one giving the uncertainty on a weighted average. The contribution to the average systematic uncertainty for those uncertainty sources not included in the weight definition, was evaluated via error propagation on the formula of the weighted average (4.5), resulting in equation (4.7) and (4.8) for sources considered uncorrelated and correlated among the mesons. In particular, the uncertainties on the associated track reconstruction efficiency, on the contamination from secondary, on the feed-down subtraction, and that resulting from the Monte Carlo closure test were considered fully correlated among the mesons, while those deriving from the yield extraction (included in the weight definition) and on the D meson reconstruction and selection efficiency were treated as uncorrelated.

$$\sigma^2 = \frac{\sum_{\rm i=meson} w_i^2 \sigma_i^2}{\left(\sum_{\rm i=meson} w_i\right)^2} \tag{4.7}$$

$$\sigma = \frac{\sum_{\rm i=meson} w_i \sigma_i}{\sum_{\rm i=meson} w_i} \tag{4.8}$$

As an example, the Fig. 4.17 and Fig. 4.18 shows the superimposed azimuthal correlation distributions of $\rm D^0$, $\rm D^+$ and $\rm D^{*+}$ in all the kinematic regions analyzed for the D-mesons and in charged particles $p_{\rm T}$ intervals of $0.3< p_{\rm T} < 1$ GeV/c and $p_{\rm T} > 1$ GeV/c, respectively.

As expected, a rising trend of the height of the near- and away-side peak with increasing D-meson $p_{\rm T}$ is observed, the peaks are more significant for higher $p_{\rm T}$ of the associated tracks; a decrease of the baseline level with increasing $p_{\rm T}$ of the associated tracks is also observed.
Given the symmetry of the correlation distributions around $\Delta\varphi = 0$ and $\Delta\varphi = \pi$, the azimuthal distributions are reported in the range $0 < \Delta\varphi < \pi$ to reduce statistical fluctuations. This allowed to reduce the impact of statistical fluctuations on the data points. Indeed, supposing equal statistics for a pair of symmetric bins, after the reflection the relative statistical uncertainty for the resulting bin is reduced by a factor $1/\sqrt{2}$.
The usage of weighted average requires, as an underlying assumption, identical results

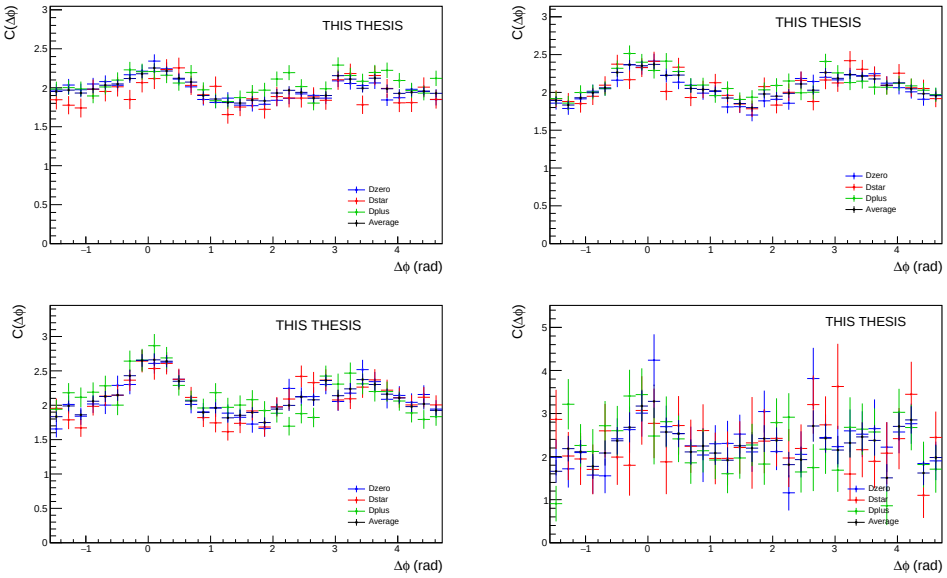

Figure 4.17 – *Superimposed azimuthal correlation distributions of* D^0 *(blue),* D^+ *(green) and* D^{*+} *(red) with charged particles, in the D meson* p_T *intervals* $3 < p_\mathrm{T} < 5$ GeV/c, $5 < p_\mathrm{T} < 8$ GeV/c, $8 < p_\mathrm{T} < 16$ GeV/c *and* $16 < p_\mathrm{T} < 24$ GeV/c *with associated tracks with* $0.3 < p_\mathrm{T} < 1$ GeV/c. *Also the* D^0, D^{*+} *and* D^+ *average (black) distribution is superimposed to the others.*

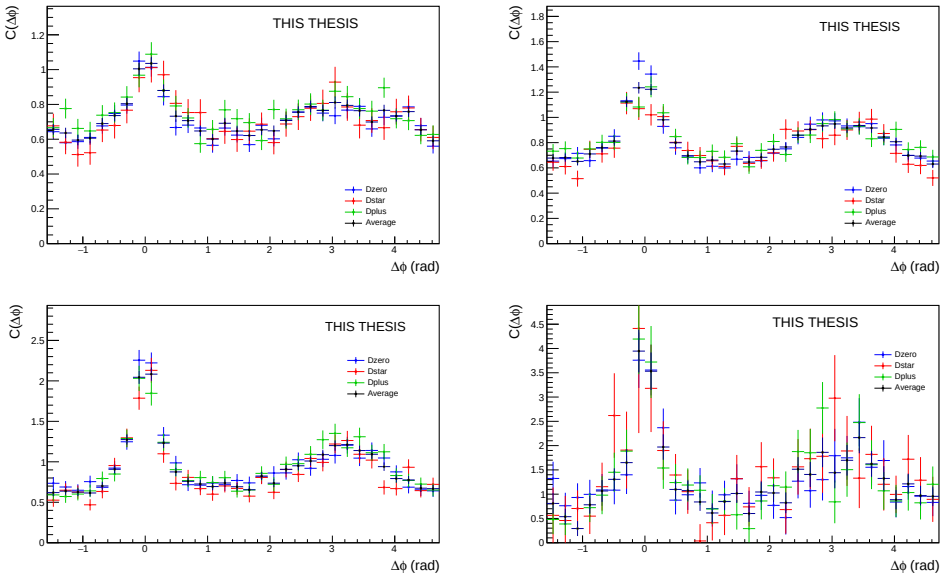

Figure 4.18 – *Superimposed azimuthal correlation distributions of* D^0 *(blue),* D^+ *(green) and* D^{*+} *(red) with charged particles, in the D meson* p_{T} *intervals* $3 < p_{\mathrm{T}} < 5$ GeV/c, $5 < p_{\mathrm{T}} < 8$ GeV/c, $8 < p_{\mathrm{T}} < 16$ GeV/c *and* $16 < p_{\mathrm{T}} < 24$ GeV/c *with associated tracks with* $p_{\mathrm{T}} > 1$ GeV/c. *Also the* D^0, D^{*+} *and* D^+ *average (black) distribution is superimposed to the others.*

expected for different species (or, at least, compatible within the uncertainties). Anyway, it was also verified that the usage of the arithmetic average instead of the weighted average increases the uncertainties on the points, but produces a negligible shift of their central values.

4.6.2 Fit of correlation distributions and observables

In order to extract quantitative and physical information from the data correlation patterns, the averaged D-h correlation distributions are fitted with two Gaussian functions describing the near- ($\Delta\varphi$=0) and away-side peaks ($\Delta\varphi$=π), plus a constant term (baseline) modeling the so-called "transverse region" ($\frac{\pi}{4} < |\Delta\varphi| < \frac{\pi}{2}$). A periodicity condition ($f(0) = f(\pi)$) is also applied to the fit function to obtain the same value at the bounds of 2π range. The expression of the fit function is reported below (equation 5.3):

$$f\left(\Delta\varphi\right) = c + \frac{A_{NS}}{\sqrt{2\pi}\sigma_{NS}} e^{-\frac{(\Delta\varphi-\mu_{NS})^2}{2\sigma_{NS}^2}} + \frac{A_{AS}}{\sqrt{2\pi}\sigma_{AS}} e^{-\frac{(\Delta\varphi-\mu_{AS})^2}{2\sigma_{AS}^2}} \tag{4.9}$$

where the baseline is calculated as the weighted average of the points lying transverse region. Hence, the physical observables are encoded with the yields and the widths of

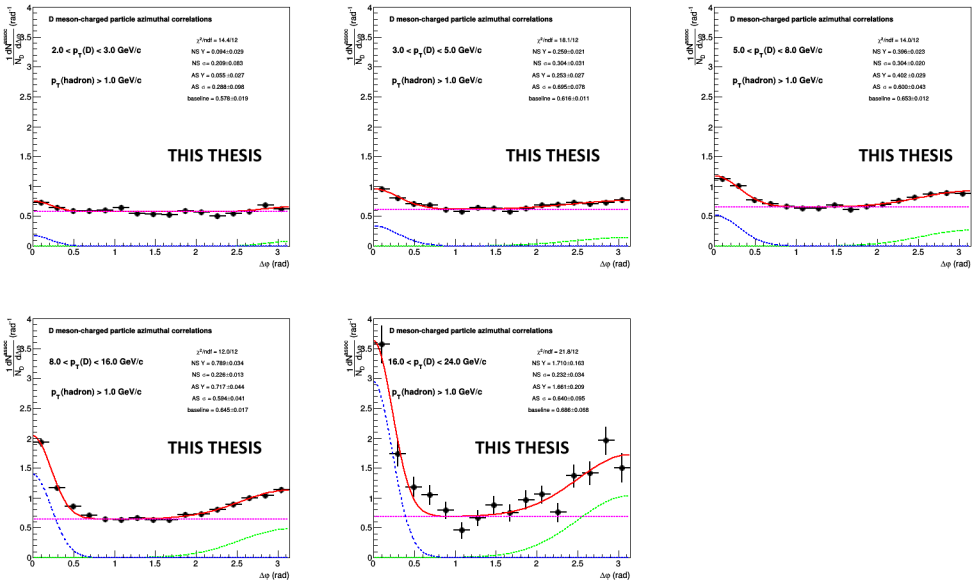

Figure 4.19 *– Fits to azimuthal correlation distributions and baseline estimation. The set of five panels is for $p_{\mathrm{T}} > 1$ GeV/c. The corresponding p_{T} ranges of D-mesons are reported in each panel.*

the two Gaussians as well as with the baseline values. In particular, the integrals of the Gaussian terms, A_{NS} and A_{AS}, correspond to the associated-particle yields for the near (NS)- and away (AS)-side peaks, respectively, while σ_{NS} and σ_{AS} quantify the widths of the correlation peaks. The baseline b represents the physical minimum of the $\Delta\phi$ distribution. To limit the effect of statistical fluctuations on the estimate of the associated yields, b is fixed to the weighted average of the points in the transverse region, using the inverse of the square of the point statistical uncertainty as weights. An example

of the resulting fit for the studied kinematical regions is shown in Figure 4.19, displaying also the values of near-side and away-side peak yields (the Gaussian integrals) and widths (the σ of the two Gaussians).
From the fit outcome, it is possible to retrieve the near-side and away-side yield and widths (integral and sigma of the Gaussian functions, respectively), as well as the baseline height of the correlation distribution. The near-side observables give information on the multiplicity and angular spread of the tracks from the fragmentation of the charm jet which gave birth to the D-meson trigger. At first order, instead, the away-side observables are related to the hadronization of the charm parton produced in the opposite direction (though the presence of NLO processes for charm production breaks the full validity of this assumption). The baseline value is a rough indicator of the underlying event multiplicity, though below the baseline level also charm and beauty-related pairs are contained (especially in cases of NLO production for the heavy quarks).

Baseline estimation

The azimuthal correlation distribution contains also the contribution of tracks originating from the so called underlying events. As in first approximation, the underlying event is not correlated with the hard-scattering process, the azimuthal distribution of those tracks is expected to be uniform with respect the D meson direction. This statement holds in pp collisions, where collective phenomena (flow) do not take place. On the other hand, the tracks that originate from the heavy-flavour hadronisation process show a correlation on the near side and away side due to the effects of different heavy-flavour pair production mechanisms. In order to study the properties of the jets originating from heavy-flavours, the baseline has been calculated and the value has been used to subtract a flat contribution from the correlation distribution (in order to compare the near-side and away-side correlation structure among different collision systems and the Monte Carlo predictions) and to constrain the baseline value in the fitting procedure. As a general feature, two-particle correlation analyses uses the ZYAM (Zero Yield At Minimum) approach [138] to determine the baseline. According to this method, the minimum of the $\Delta\varphi$ distribution is the baseline value, the yield of associated pairs can be computed using this value as reference zero. However, this approach is reliable in case of large statistics. In the study presented in this thesis, the limited statistics of the datasets does not allow for the use of the ZYAM method, as a statistical fluctuation is very likely to represent the minimum of the distribution, leading to a wrong estimation of the baseline, and of the physics results. In order to limit the sensitivity to statistical fluctuations, a $\Delta\varphi$ interval (denoted as "transverse region") has been used to estimate the baseline, rather than single points. Therefore, the weighted average of the points in the region $\pi/4 < \Delta\varphi < \pi/2$ has been used. The weight is defined as the inverse of the statistical uncertainty of the single point. As it can be noticed, the width of the away-side peak represents a physical boundary to the baseline region definition. Since in the fitting

procedure the baseline value is constrained, in order to take into account of the statistic uncertainty on the baseline definition, it enters at least as a systematic uncertainty, evaluated by studying the variation of the baseline value estimated in different regions of $\Delta\varphi$ as described later.

Generalized Gaussian for near-side peak

At high transverse momentum of the D-meson and of the associated track the tails of the near-side peak are underestimated by the fitting function, if a standard Gaussian is employed for fitting the near-side (and, in general, the shape of the peak seems not well described by a Gaussian).
To dig into this issue, an alternate fitting function was adopted for the near-side peak fitting, i.e. the generalized Gaussian function with the typical shape shown in Fig. 4.20 and parametrized with the following distribution function:

$$f(\Delta\varphi) = \frac{\beta}{2\alpha\Gamma(1/\beta)} \cdot e^{-(|x-\mu|/\alpha)^{\beta}} \tag{4.10}$$

and having as variance $\frac{\alpha\Gamma(3/\beta)}{\Gamma(1/\beta)}$. The square root of the variance was used as near-side width fit observable instead of the Gaussian σ, together with the integral of the fitting function, which defines the near-side yield.

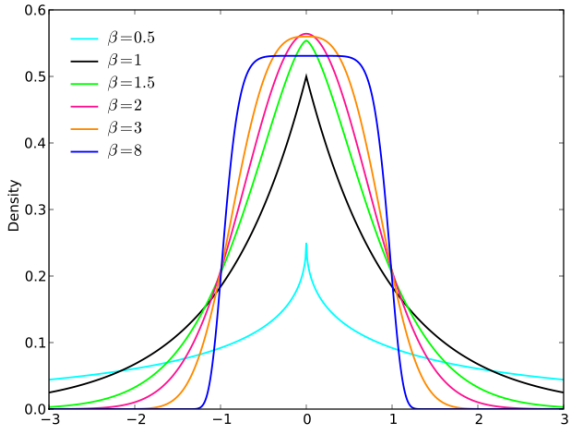

Figure 4.20 – *Generalized Gaussian function for different β parameter values.*

The near-side yields remain very similar in the two approaches, apart from an increase of the yields up to 10% in 16-24 GeV/c. The widths are generally comparable at low p_{T} of the D-meson, then increase in the generalized Gaussian case from 8 GeV/c onwards, up to about a 20% difference. In any case, the width has not the same interpretation for the two fitting functions (there's no probabilistic meaning for the width in the case of

generalized Gaussian).
Further information can be obtained comparing the fits with the two function for Monte Carlo templates, where the statistical precision is much better than on data, allowing us to check which function has effectively the compatibility with the points - by visually comparing the fit and the distribution, looking at the χ^2/ndf and comparing the values of the yields with the bin-counting extracted yields.
This comparison has been performed for two low and two high p_{T} ranges and are reported in Figs. 4.21, 4.22, 4.23, 4.24. While at low p_{T} the two fit outcomes are rather similar, as the β parameter is quite close to 2 (the standard Gaussian value), at high p_{T} the two fit results are much more differentiated, β is sensibly smaller than 2, the shape of the generalized Gaussian has much thinner core and higher tails, and catches much better the peak tails (having also a better χ^2 and a better agreement with bin-counting yields).

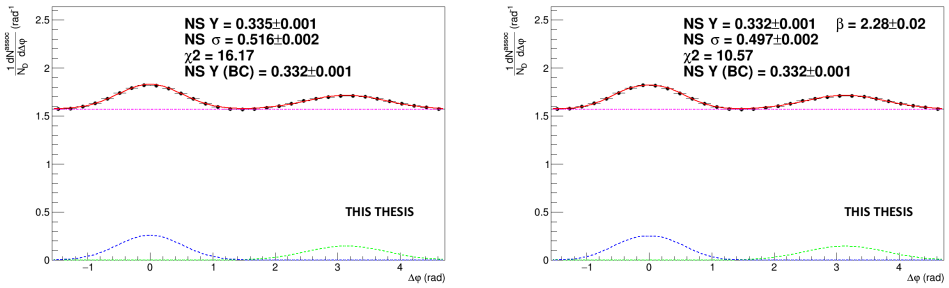

Figure 4.21 *– Comparison of fit outcome for POWHEG+PYTHIA templates for standard (left) and generalized Gaussian (right) for the near-side, for* $3 < p_{\mathrm{T}}(D) < 5$ GeV/c *and* $0.3 < p_{\mathrm{T}}(assoc) < 1$ GeV/c.

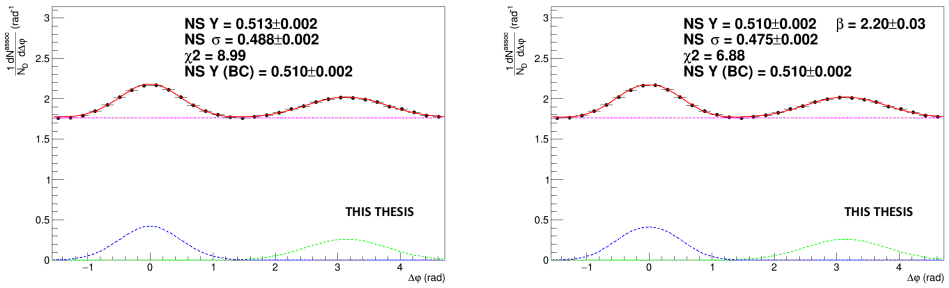

Figure 4.22 *– Comparison of fit outcome for POWHEG+PYTHIA templates for standard (left) and generalized Gaussian (right) for the near-side, for* $5 < p_{\mathrm{T}}(D) < 8$ GeV/c *and* $0.3 < p_{\mathrm{T}}(assoc) < 1$ GeV/c.

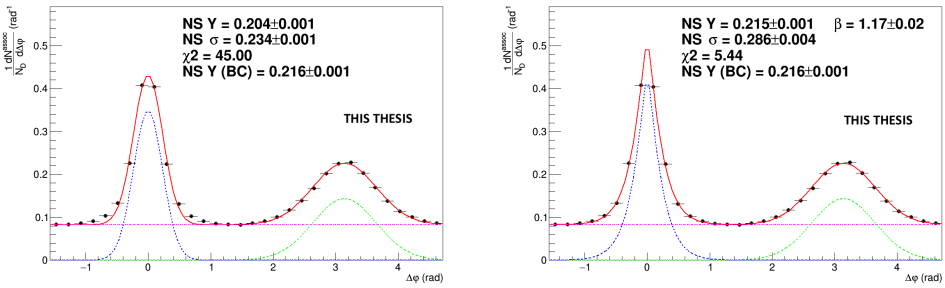

Figure 4.23 – *Comparison of fit outcome for POWHEG+PYTHIA templates for standard (left) and generalized Gaussian (right) for the near-side, for* $8 < p_{\mathrm{T}}(D) < 16$ GeV/c *and* $2 < p_{\mathrm{T}}(assoc) < 3$ GeV/c.

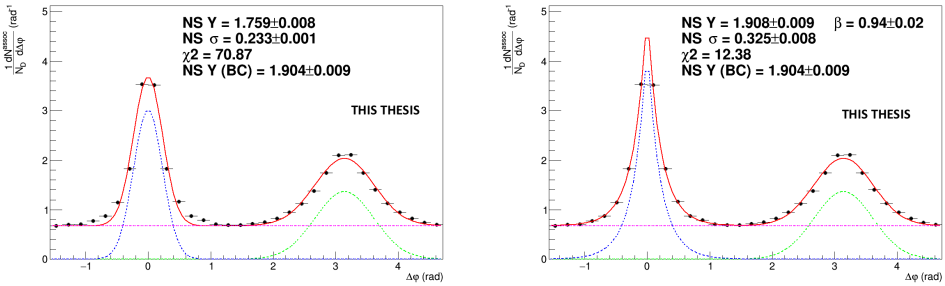

Figure 4.24 – *Comparison of fit outcome for POWHEG+PYTHIA templates for standard (left) and generalized Gaussian (right) for the near-side, for* $16 < p_{\mathrm{T}}(D) < 24$ GeV/c *and* $p_{\mathrm{T}}(assoc) > 1$ GeV/c.

4.6.3 Systematic uncertainties on the fit observables

The evaluation of the systematic uncertainties on the observables obtained from the fits was performed as follows:

1. The fits were repeated by changing the range of the transverse region in which the baseline is evaluated. Alternate definitions are: $\frac{\pi}{4} < |\Delta\varphi| < \frac{3\pi}{8}$, $\frac{3\pi}{8} < |\Delta\varphi| < \frac{\pi}{2}$ and $\frac{\pi}{4} < |\Delta\varphi| < \frac{5\pi}{8}$ are considered.
2. The alternative definition of the transverse region were performed with the two possible fitting procedure of the near-side peak description: the standard Gaussian function and the generalized Gaussian function. Hence, four total variations for each fitting function were considered.
3. $\Delta\varphi$ correlation points are shifted to the upper and lower bounds of their uncorrelated systematic boxes, and refitted (with the standard Gaussian).
4. The fits were also repeated by moving the baseline value from its default value (i.e. with the default transverse region) on top and on bottom of its statistic

uncertainty before fitting with the default function. Including it in a systematic uncertainty helps to account for the statistical uncertainty on the baseline position (since in the fit the baseline is constrained, and its error is not propagated to the other observables).

The envelope between the RMS of the relative variations of the parameters between the fit outcomes defined in the first three points, and the relative variations of the parameters from the fit outcomes defined in the fourth point, is considered as systematic uncertainty for the near-side and away-side widths. For the estimation of the baseline and of the near-side and away-side yields, instead, the previous value is added in quadrature with the $\Delta\varphi$-correlated systematics in the correlation distributions, since these values are affected by a change in the global normalization of the distributions.

$$\sigma^{syst} = \sqrt{\left(Max\left(\Delta par^{ped.mode, fit funct.}, \Delta par^{\Delta\varphi point}\right)\right)^2 + (\sigma^{corr}_{Syst})^2}. \tag{4.11}$$

The width of the distribution on the near side does not depend on the rescaling of the distribution: in this case only the uncertainty from the baseline definition has been considered as systematic uncertainty.

4.6.4 Comparisons of D-h correlations in pp collisions at $\sqrt{s}$ = 5, 7 and 13 TeV

The averages of the fully corrected and baseline subtracted D^0, D^+ and D^{*+} azimuthal correlation distributions are shown, in Fig. 4.25 for pp collisions at $\sqrt{s}$= 5 TeV compared with pp at $\sqrt{s}$= 7 TeV and 13 TeV, for all the common kinematic ranges analyzed. A rising trend of the height of the near-side peak with increasing D-meson $p_{\rm T}$ is observed for all the center-of-mass energy. An increase of hadron multiplicity in jets with increasing energy of the jet is expected from the evolution of parton cascade with the parton energy for light and heavy quarks. The comparison among the different collisions energy confirms the energy scaling expected. Indeed, it can be qualitatively observed a larger yield values for $\sqrt{s}$ =13 TeV than yields at $\sqrt{s}$ = 5 TeV. The data distribution of pp at $\sqrt{s}$= 5 TeV are affected by much lower uncertainties with respect to 7 TeV dataset. Better statistical and systematic uncertainties with respect to the pp data sample at $\sqrt{s}$=13 TeV are shown (the analysis with this data sample was performed only for two D-mesons). However, a good compatibility between the three energy systems is found, within uncertainties, for all the common kinematic ranges analyzed.
A further comparison of the results from pp at three different collision energies is done by quantifying the integrals and the widths of the near-side correlation peaks by fitting the measured distributions as described in the Sec. 4.6.2. The fit results are reported only for the near-side peak parameters because of the poor statistical precision on the fit parameters for the away-side peaks. On the top of the Fig. 4.26, the comparison of the evolution of the near-side associated yield among the three systems is shown. In

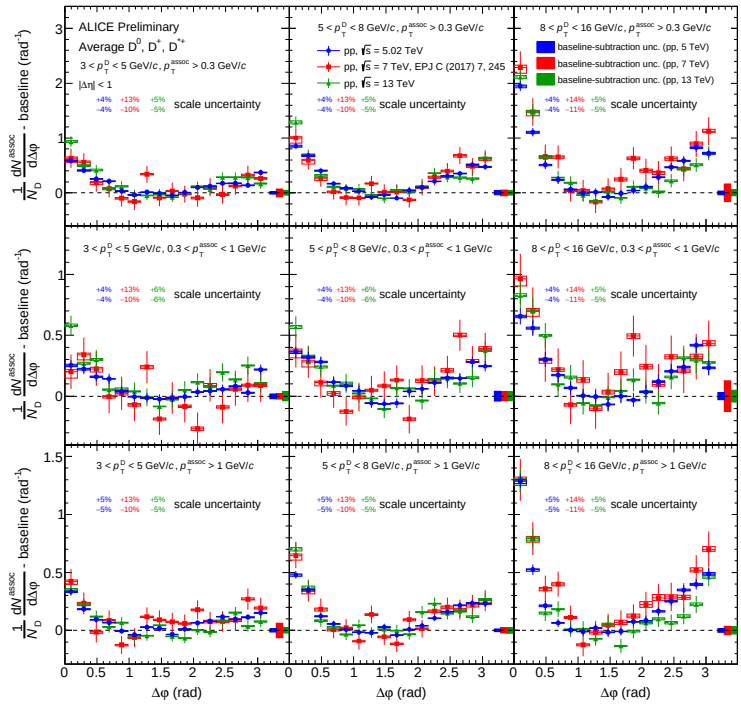

Figure 4.25 – *Average of* D^0, D^+ *and* D^{*+} *azimuthal correlations in pp collisions at* $\sqrt{s}$ *= 5 (blue), 7 (red) and 13 (green) TeV in all the common kinematic ranges of trigger and associated particles.*

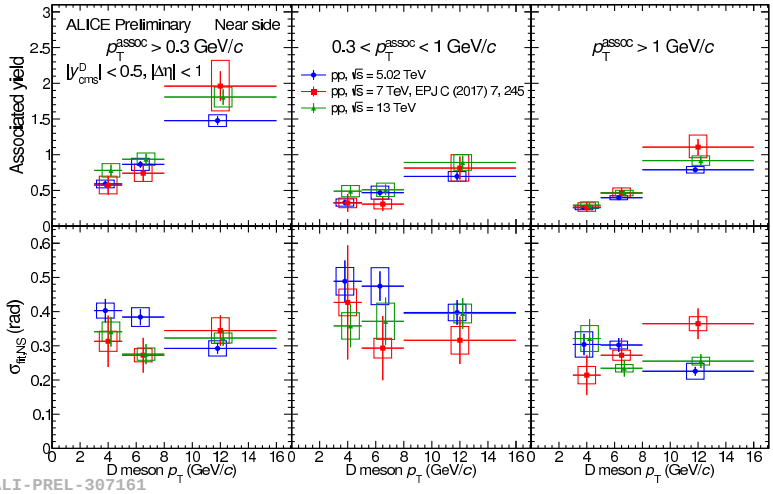

Figure 4.26 – *Near-side yield and width for the average of* D^0, D^+ *and* D^{*+} *azimuthal correlations in pp collisions at* $\sqrt{s}$ *= 5 (blue), 7 (red) and 13 (green) TeV in all the common kinematic regions of trigger and associated track.*

the bottom row of the same figure, the width of the near-side Gaussian term (σ_{NS}) is reported. The near-side observables do not spot any difference above the uncertainties, which are large (especially for past results). Therefore, the current level of precision doesn't allow for any quantification of the energy dependence of the yields. From Monte-Carlo simulations (with PYTHIA8 and POWHEG+PYTHIA), it is expected a difference of the order of 5-6% for pp collisions at $\sqrt{s} = 5$ with respect to $\sqrt{s} = 7$ TeV and of 10-12% when comparing $\sqrt{s}$= 5 TeV with respect to 13 TeV results.

4.6.5 Comparisons of D-h correlations in pp collisions with model predictions

The structure of the near and away side correlations has been compared with predictions from PYTHIA6 [148] using different PerugiaTunes [149], PYTHIA 8 [34] and from POWHEG [46] + PYTHIA6. Figs. 4.27 and 4.28 shows the average of D^0, D^+ and D^{*+} azimuthal correlations for pp for several ranges of trigger and associated p_T, compared to different PYTHIA6 tunes (Perugia 0, 2010, 2011), PYTHIA 8 (tune 4C) and POWHEG+PYTHIA at the same collision energy. In order to focus on the structure of the correlation peaks, the baseline has been subtracted from the plots in both the distributions from data and simulations, using the strategy described in the previous section.

A substantial agreement in the overall momentum evolution of the correlation pattern is observed within uncertainties for what concerns the near-side region, apart from very high p_T of the D-meson, where the peak seems to be slightly underestimated, at least by PYTHIA predictions. For the away-side region, the models themselves differentiate in predicting the height of the peak, and generally the strength of the peak overestimate the data measurements, especially for the older Perugia tunes (PYTHIA6-Perugia0 and PYTHIA6-Perugia2010). When looking more differentially, it is interesting to observe that the peaks are much more suppressed in closer kinematic regions of the trigger and the associated tracks. Indeed, on the bottom left panel of the Fig. 4.28, where low-p_T D mesons ($3 < p_T^D < 5$ GeV/c) are correlated with harder tracks ($2 < p_T^{assoc} < 3$ GeV/c), a lower near-side peak is visible and no away-side peak is emerges. This behavior is also well reproduced by the models. The finer p_T bins of the associated tracks are affected by large statistical uncertainties for the very high p_T range of the D mesons.

The near- and away-side physical observables have been extracted and studied as a function of the p_T of the D meson for different associated track p_T intervals. In Figs. 4.29 and 4.30 the comparison of the yield, width and baseline height of near-side and away-side is presented. In the same plots the comparison with PYTHIA6, PYTHIA8 and POWHEG+PYTHIA simulations is reported as well.

Concerning the near-side yields, shown in the upper row of the figures, POWHEG tends to predict larger values than PYTHIA6 and PYTHIA8, in all associated track p_T regions. Data results seem to behave in-between of the two predictions, apart from $16 < p_T(D) <$

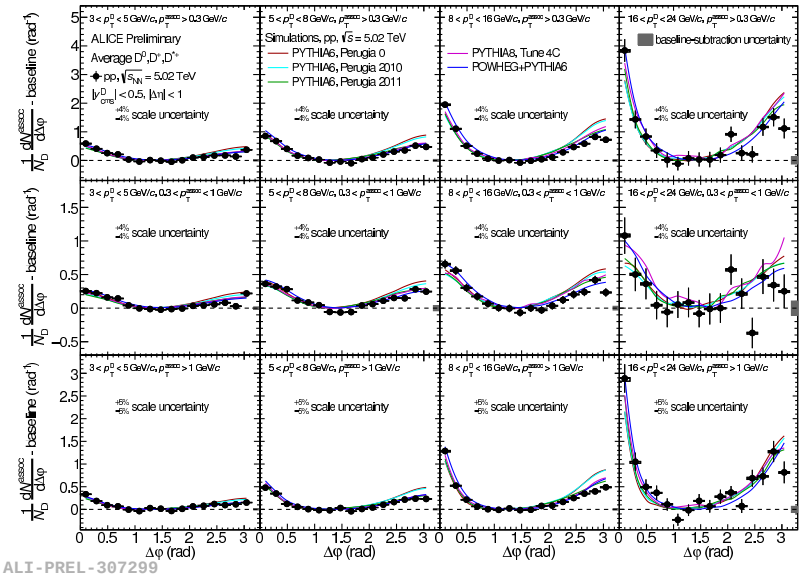

Figure 4.27 – *Comparison of $\Delta\varphi$ azimuthal distribution for D-meson averages, obtained from data and simulations different event generators (PYTHIA, with three tunes, and POWHEG+PYTHIA), in the different kinematic ranges analyzed.*

24GeV/c range, where excluding the lowest associated p_{T} range, data are better described by POWHEG. For the near-side width, POWHEG also tends to predict wider peaks, in this case generally overpredicting the observed values, which are better matched by PYTHIA predictions (though no model can be ruled out with current uncertainties).
Focusing on the away-side region, POWHEG expectation foresees smaller peaks, with respect to all PYTHIA6 predictions, which is confirmed by data, especially for the yields, and in the intermediate D-meson p_{T} region (while PYTHIA6 predictions overestimate the data especially at mid-high p_{T}). PYTHIA8 predictions are in-between POWHEG and PYTHIA6. The values of the widths show a reversed model hierarchy with respect to the near-side predictions, but with small differences, and all models can generally reproduce data. All the models tend to underestimate the value of the baseline, although considering the systematic uncertainty, they result compatible with the measured values. PYTHIA6-Perugia0 (which is the oldest) shows larger discrepancies with respect to the measurements.
An alternative way of studying the correlation distributions has been introduced: instead of the "standard" dependence of the physical observables with respect to the p_{T} of D mesons, another option is to look at the distribution of the associated particles in fixed interval of D meson transverse momentum. In Figs. 4.31 and 4.32 the results of these alternative study is shown together with the comparison with Monte-Carlo predictions (PYTHIA6 with several Perugia tunes [148], PYTHIA8 [34] and POWHEG +

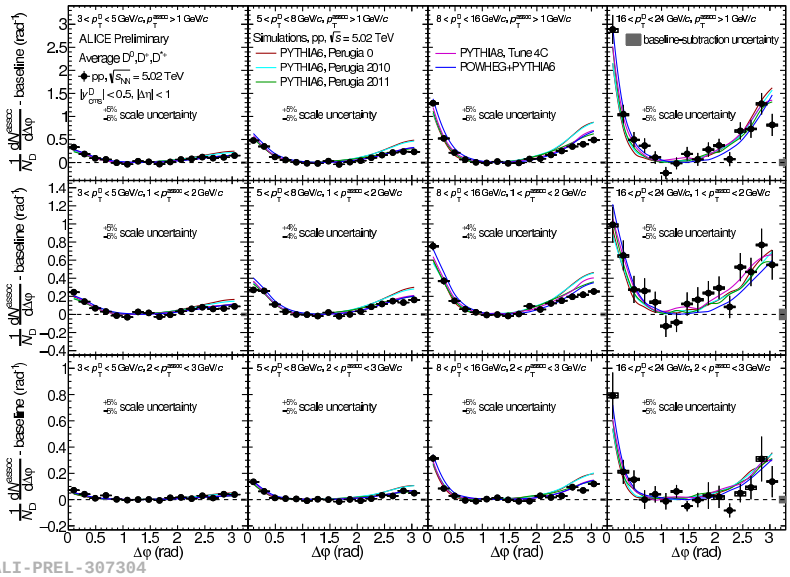

Figure 4.28 – *Comparison of $\Delta\varphi$ azimuthal distribution for D-meson averages, obtained from data and simulations different event generators (PYTHIA, with three tunes, and POWHEG+PYTHIA), in the different kinematic ranges analyzed.*

PYTHIA [46]) for the near- and away-side observables, respectively. A decreasing trend of the height of the near- and away-side peak with increasing associated particle transverse momentum is observed. This confirms the expectation of how the original parton momentum is distributed within a jet: more particles characterized by a lower transverse momentum and few particle carrying higher transverse momentum fraction. The compatibility observed between the near- and away-side yields is in agreement with the correlation pattern expected for proton proton collisions, leading to a common physical origin of the two peaks. In addition, a decreasing trend of the sigma of the associated particle in the near-side peak is also visible independently to the p_{T} of the trigger particle. This confirms that more energetic particles are more collimated to the trigger particle direction. On the away side, the sigma follows a flat trend as a function both of the associated particle p_{T} and of the trigger p_{T}.
The near-side observables (both yields and widths) are well reproduced in all the kinematic regions by all the Monte-Carlo simulations. Data are better described by POWHEG, excepting the lowest p_{T} range of D mesons. Also for the away-side observables, where the simulations predict physical observables with more pronounced differences among the models (especially in the lowest p_{T} of the associated particles), the better match with data is reached with POWHEG.

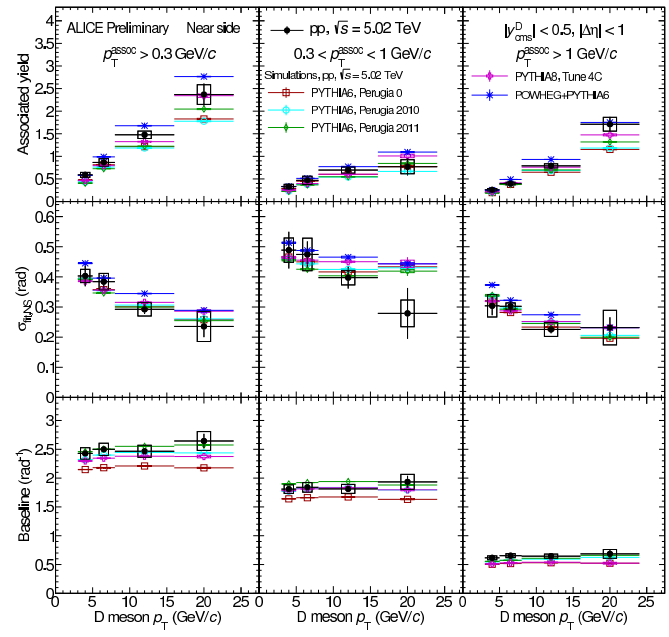

ALI-PREL-307362

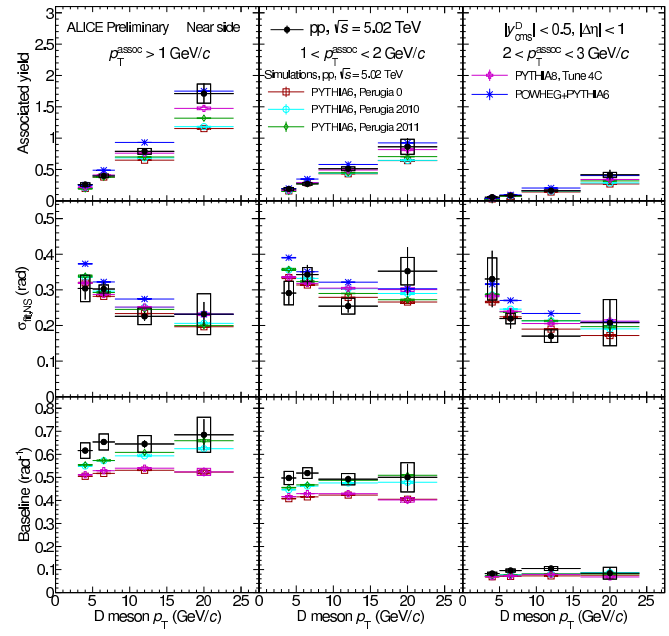

ALI-PREL-307371

Figure 4.29 – *Near-side fit parameters (yield on top, width in the middle and baseline height in the bottom panels) obtained for D-meson averages as a function of the transverse momentum of D mesons, extracted from data and compared with different predictions (PYTHIA6 with three tunes, PYTHIA8 and POWHEG+PYTHIA), in all the kinematic ranges of the associated tracks analyzed.*

.

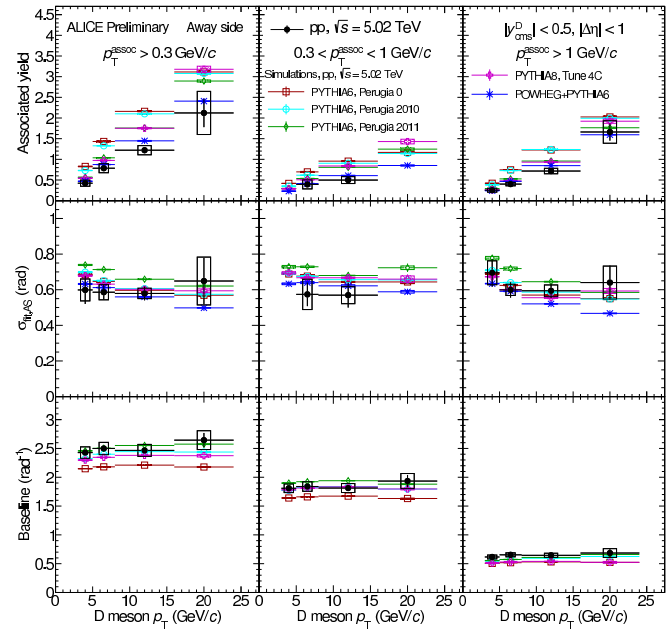

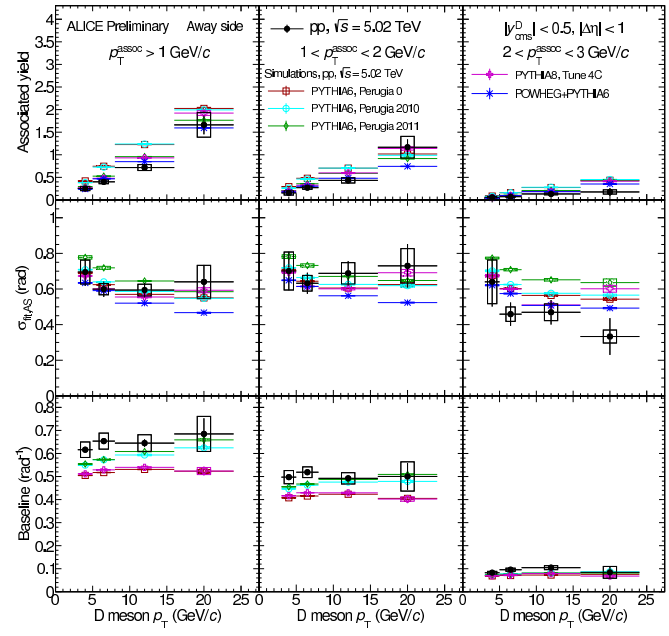

Figure 4.30 – *Away-side fit parameters (yield on top, width in the middle and baseline height in the bottom panels) obtained for D-meson averages as a function of the transverse momentum of D mesons, extracted from data and compared with different predictions(PYTHIA6, with three tunes, PYTHIA8 and POWHEG+PYTHIA), in all the kinematic ranges of the associated tracks analyzed.*

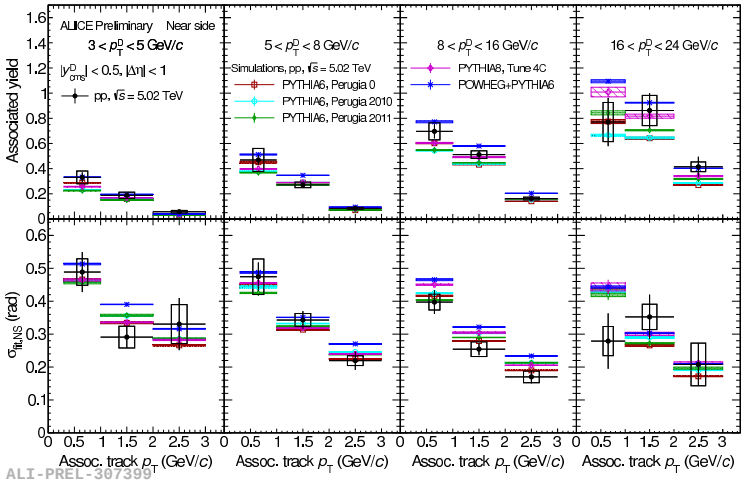

Figure 4.31 – *Near-side fit parameters obtained for D-meson averages as a function of the* p_T *of the associated tracks, extracted from data and simulations different event generators (PYTHIA6, with three tunes, PYTHIA8 and POWHEG+PYTHIA), in all the different kinematic ranges analyzed for the D mesons.*

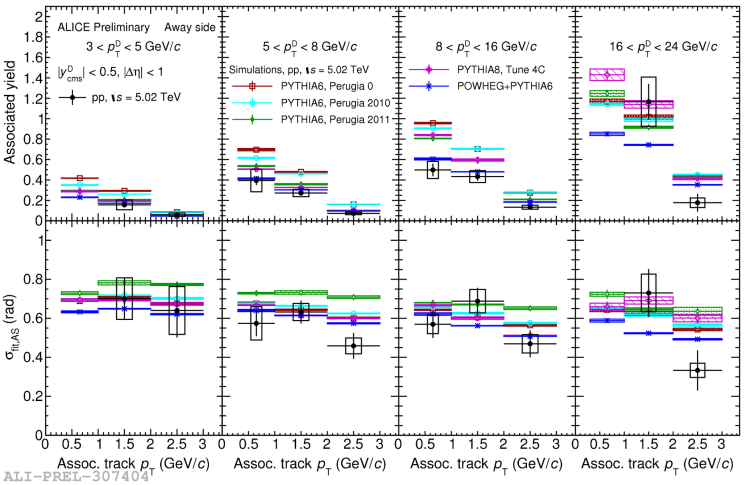

Figure 4.32 – *Away-side fit parameters obtained for D-meson averages as a function of the* p_T *of the associated tracks, extracted from data and simulations different event generators (PYTHIA6, with three tunes, PYTHIA8 and POWHEG+PYTHIA), i in all the different kinematic ranges analyzed for the D mesons.*

5

D-h correlations in p-Pb collisions at $\sqrt{s_{\rm NN}} = 5.02$ TeV

In more complex systems, the angular distribution of particles produced in an event is sensitive to collective effects that correlate particle production over a wide phase-space region. This is observed, for example, in non central Pb–Pb collisions, where the azimuthal asymmetry of the overlapping region of the colliding nuclei is translated into an anisotropy in the azimuthal distribution of the particle momenta. This physical phenomenon is described in terms of a non-zero second order term (elliptic flow, v_2) modeling the $\Delta\phi$ distribution of two particle correlations. Similar collective motions (positive v_2) were observed also in high-multiplicity pp and p-A collisions at LHC and RHIC, as widely discussed in the second chapter. Therefore, a modification of the azimuthal correlations of D mesons with charged particles in p–Pb with respect to pp collisions could occur at the LHC as a consequence of the presence of initial state or final state effects and there could be a signal of the presence of long-range v_2-like correlations for particles originating from hard-scattering process, leading to additional information to that obtained from correlations in the light-flavour sector, which at low-$p_{\rm T}$ are primarily produced in soft processes. The former aspect can be investigated exploiting the angular distributions in centrality integrated p–Pb collisions, while the latter motivates the analysis in p–Pb collisions as a function of multiplicity. Thanks to the high statistics and precision available for this data sample, it was possible to explore new kinematic regions, allowing to investigate more differentially the charm quark fragmentation properties aimed to place better constraints on the description of charm fragmentation and charm jet properties provided by models.

In this chapter, I will present the measurements of azimuthal correlations of prompt $\rm D^{*+}$ mesons and primary charged π, K, p, e, μ performed in the ALICE central barrel in p–Pb collisions at $\sqrt{\rm s_{NN}} = 5.02$ TeV.Two different analysis have been carried out on this data sample: a centrality integrated analysis and a centrality dependent one. The latter

was performed in three centrality classes defined by the energy deposited in the ZNA detector (Zero-Degree Neutron Calorimeter) [157]: 0-20%, 20-60%, 60-100%.
The centrality dependent analysis aimes to investigate for possible modifications of the correlation peak features (in terms of associated yield and width) among the various centrality classes, which could point toward a different fragmentation and hadronization of the charm quark at different collision centralities. The possibility of studying the D-meson v_2 by subtracting low-multiplicity form high-multiplicity events was also checked, but the available statistics resulted to be too small for such a study. Therefore, this latter study will not be shown here.

Since the analysis steps are very similar to the ones described for the azimuthal correlations in pp collision system, in this chapter I will give a faster description of the procedure (i.e. analysis strategy, corrections applied and systematic uncertainties) pointing out especially the differences for which the analysis in p–Pb collisions has been specialized. Finally, the results of both analyses will be presented.

5.1 Data sample

The data used for the analyses were the AOD samples of the following four datasets: LHC16q_FAST, LHC16q_CENT_woSDD, LHC16t_FAST, LHC16t_CENT_woSDD. The reason for choosing these data samples (in particular, those without the drifts for the CENT cluster) is explained later on, in this section. It was verified, by looking at D-meson and associated charged track η and φ distributions, and at the mixed-event correlation distributions for each subsamples, that no visible differences is present for the four periods, hence it was possible to perform the analysis directly on the merged samples without any bias.
The Monte Carlo productions adopted for this study were:

1. LHC17d2a_fast_new: p–Pb collisions are simulated using the HIJING [153] event generator on top of PYTHIA6 [148] with Perugia2011 tune event. In each event a $c\bar{c}$ and $b\bar{b}$ pair is present (enriched Monte-Carlo sample) and with forced hadronic decays of the charmed hadrons. This production was used for D-meson efficiency evaluation, purity estimation and the Monte Carlo closure test.

2. LHC17f2b_cent_woSDD and LHC17f2b_fast: Monte-Carlo minimum-bias samples produced with DPMJET generator. They used for the evaluation of the tracking efficiencies.

In both the Monte-Carlo samples, the generated particles are transported through the ALICE apparatus using the GEANT3 package [147].
As described in 4.3, the measured angular-correlation distributions are compared to simulation results obtained with the event generators PYTHIA 6.4.25 [148] (tunes Perugia-0,

Perugia-2010, and Perugia-2011sets [149]), PYTHIA 8.2 (tune 4C) [34], POWHEG [46] coupled to PYTHIA6 (Perugia-2011 tune). The same considerations made in the previous chapter, still hold for these models. Furthermore, dealing with p–Pb collision system, in the simulations presented in this chapter, the centre-of-mass frame is boosted in rapidity by $\Delta y_{\rm NN}$= 0.465 in order to reproduce the rapidity shift of the reference frame of the nucleon-nucleon collision in the p–Pb collision system both in PYTHIA and in POWHEG.
The event selection and the general settings applied are the same reported in the Section 4.2, taking into account for specific features of the p–Pb collisions. One of the most important is to consider also in the data (as done for the Monte Carlo simulations) the shift in rapidity of the center-of-mass reference frame of the nucleon-nucleon collision in the proton direction with respect to the laboratory frame, due to the different per-nucleon energies of the proton and the lead beams.
In the analysis performed as a function of the centrality, an additional requirement related to the centrality slicing on the event selection was introduced with respect to the centrality integrated analysis: the ZNA estimator is employed to slice the data sample in three complementary centrality classes (0-20%, 20-60%, 60-100%). The chosen slicing grants substantial differences, in terms of average centrality, between the first and the third class, and also allows to fairly equalize the number of D-mesons in each class (since the second and third classes are wider, but also have a lower N_{coll} value with respect to the first).
The number of analyzed events for the three centrality classes is approximately:

- 123M for 0-20% centrality
- 247M for 20-60% centrality
- 246M for 60-100% centrality

The possibility of using the V0A estimator was also explored - and fully-corrected results for V0A estimator are also available - but the final choice of the centrality estimator fell on the ZNA. Indeed, this estimator is more directly related to the collision geometry than the V0A, which is instead more related to the event multiplicity.
Since data collected during p-Pb 2016 data taking are distinguished into two categories - one including SDD detector (CENT_wSDD sample) and the second one without the SDD in the reconstruction, or in the acquisition (CENT_woSDD and FAST samples, respectively), a study of performance of the D-hadron correlation analysis with respect to the data samples employed has been carried out for D^{*+} and D^{+} mesons (more sensitive to the presence of the SDD with respect to the D^0, due to their reconstruction from three decay tracks).
For this reason, a comparison of the D-hadron correlation distribution was performed between the data sample with the SDD information (denoted as wSDD, hereafter) and the one without them (denoted as woSDD, hereafter) on the LHC16q period. Such a comparison was carried out by estimating the relative statistical uncertainty in the two cases.

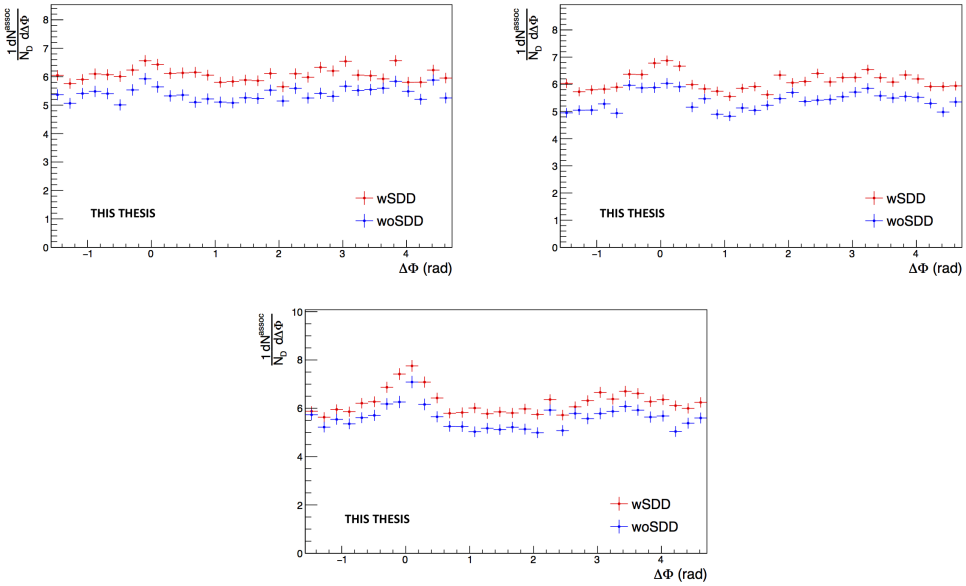

Figure 5.1 – *Normalized azimuthal correlation distribution of* D^{*+} *for low* p_{T} *(*$3 < p_{\mathrm{T}}(\mathrm{D}^{*+}) < 5$ GeV/c*) on the top panel, mid* p_{T} *(*$5 < p_{\mathrm{T}}(\mathrm{D}^{*+}) < 8$ GeV/c*) on the middle panel and high* p_{T} *(*$8 < p_{\mathrm{T}}(\mathrm{D}^{*+}) < 16$ GeV/c*) on the bottom panel with a* p_{T} *threshold for associated tracks of* $p_{\mathrm{T}}(assoc) > 0.3$ GeV/c*. Blue points are referred to the woSDD sample while red points represent wSDD data.*

The goal was to understand if it was better to use the choose FAST and CENT_woSDD samples, as it was ultimately done (which have the same detector conditions, and can be simply merged and considered, in the analysis chain, as a unique sample), of instead to use FAST and CENT_wSDD samples (with different detector conditions, and hence requiring to perform the analysis separately on the two data sample, applying different corrections). In particular, this study was crucial for the correlation analysis involving the D^{*+} meson, because the track reconstruction efficiency of the soft pion is $\approx 10\%$ higher employing also the SDD information. Figure 5.1 shows the normalized azimuthal correlation distribution for low, mid and high p_{T} for D^{*+} meson. Blue points are referred to the woSDD sample while the red points represents wSDD data. Figure 5.2 shows the relative statistical uncentainty extracted from the azimuthal correlation distributions for the D^{*+} in different kinematic ranges.

It can be observed that the data sample that includes the SDD information is characterized by $\approx 10-15\%$ more statistics in each p_{T} ranges analyzed. This difference is related to the larger efficiency in track reconstruction with the wSDD sample - a larger number of tracks survives to the selection request of 3 points in the ITS, which is part of the selection requests applied on the previous D-h analysis.

As a result, the wSDD sample is also affected by a slightly lower relative statistical

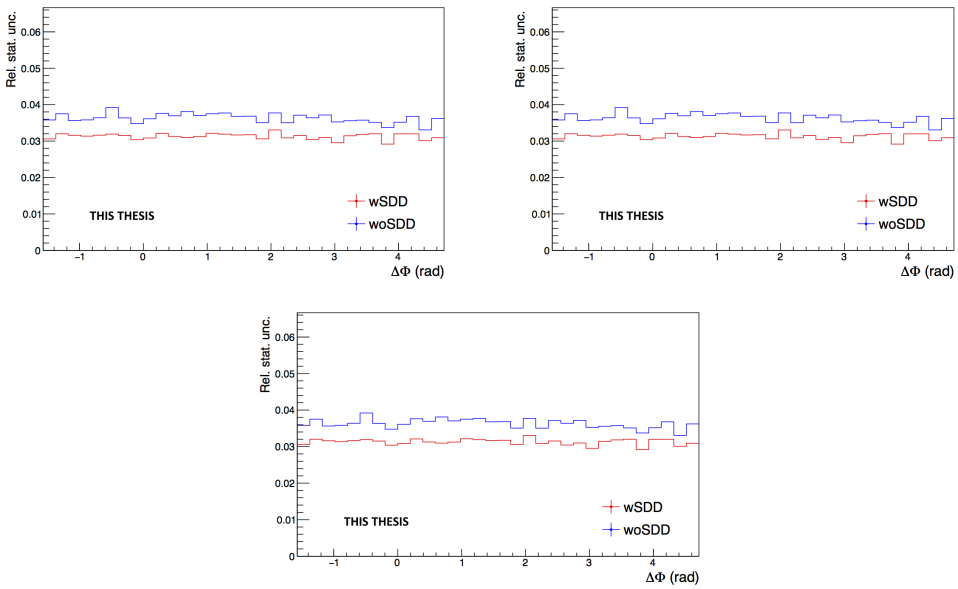

Figure 5.2 – *Statistical uncertainty extracted from the azimuthal correlation distribution of* D^{*+} *with associated charged particles. Top panel:* $3 < p_{\mathrm{T}}(\mathrm{D}^{*+}) < 5$ GeV/c. *Mid panel:* $5 < p_{\mathrm{T}}(\mathrm{D}^{*+}) < 8$ GeV/c. *Bottom panel:* $8 < p_{\mathrm{T}}(\mathrm{D}^{*+}) < 16$ GeV/c. *Blue line is referred to the woSDD sample while the red line represents wSDD data.*

uncertainty (about 12-15%) due to several reasons: the larger tracking efficiency, the larger number of signal entries in the invariant mass distributions (again an effect of the larger tracking efficiency) and a slight increase of S/B, which reflects in a slight decrease of uncertainty from the sideband subtraction. It has also to be considered that, on the full sample including also the FAST cluster, the increase in performance would be further reduced. The overall statistical uncertainty difference resulting from the comparison is not enough to justify the implementation of two different analysis and two subsequent different corrections either for D^{*+} and D^{+}.

In order to cope with the lower tracking efficiency, after this study, it was decided to reduce the ITS request for the associated tracks from 3 to 2 ITS clusters as a default selection criterion.

5.2 Analysis Strategy

The analysis follows the same strategy used in pp data sample, described in the Sec. 4.4. Correlation pairs are formed by trigger particles (D^{*+} mesons) reconstructed and selected in the following p_T^{trig} ranges: $3 < p_T^{trig} < 5$ GeV/c, $5 < p_T^{trig} < 8$ GeV/c, $8 < p_T^{trig} < 16$ GeV/c, $16 < p_T^{trig} < 24$ GeV/c, and associated particles (charged tracks) for the p_T >0.3 GeV/c with following p_T^{assoc} differential intervals: $0.3 < p_T^{assoc} < 1$ GeV/c, $1 < p_T^{assoc} < 2$ GeV/c, $2 < p_T^{assoc} < 3$ GeV/c, $p_T^{assoc} > 1$ GeV/c, and $p_T^{assoc} > 3$ GeV/c for the centrality-integrated analysis (where more statistics is avalable). When performing the analysis as a function of the multiplicity, due to the lower statistics available for each centrality class, only the following p_T regions of the associated tracks were exploited in addition to the inclusive interval: $0.3 < p_T^{assoc} < 1$ GeV/c and $p_T^{assoc} > 1$ GeV/c. In this analysis, the particle identification defines the trigger particle rather than a momentum cut and therefore the momentum range of the associated particles is not constrained by that of the trigger particle. The associated particles include primary particles of the following species: pion, kaon, proton, electron, muon. The primary particle definition comprises particle coming from the primary vertex of interaction, including those coming from strong and electromagnetic decay of unstable particles, and particles deriving from the decay of hadrons with charm or beauty. Therefore, any charged π, K, p, e, μ except those coming from weak decays of strange particles and particles produced in the interaction with the detector material are included in the analysis. All associated particles surviving the selection cuts and not matching the adopted criterion are considered as a contamination whose contribution has to be corrected for.

5.2.1 D^{*+} meson selection and signal extraction

For each single event, "trigger" particles are defined as the selected D^{*+} meson candidates (D^0, D^+ and D^{*+}) within a given p_T^{trig} range. The detection strategy for D^{*+} mesons at central rapidity is the same performed for the analyses of the D-meson production at central rapidity [120]. It is based on the reconstruction of decay vertices displayed from the primary vertex by a few hundred μm and on the identification of the decay-particle species. The identification of the charged kaon and pion in the TPC and TOF detectors is also used, to further reduce the background at low p_T. An invariant-mass analysis is then used to extract the raw signal yield, using the same fit functions described in [121]. D^{*+} mesons are selected in the rapidity range varying from $|y| < 0.5$ at low p_T to $|y| < 0.8$ for $p_T > 5$ GeV/c. Figs. 5.3 and 5.4 show the invariant mass distributions in fine $p_T(D^{*+})$ bins ranging from 3 GeV/c to 24 GeV/c.

Analogously, the topological selection of the centrality-dependent analysis is largely based on the cut values used for the centrality-integrated analysis. For the D^{*+} reconstruction, a cut optimization in each centrality class was performed trying to tighten the cosine of

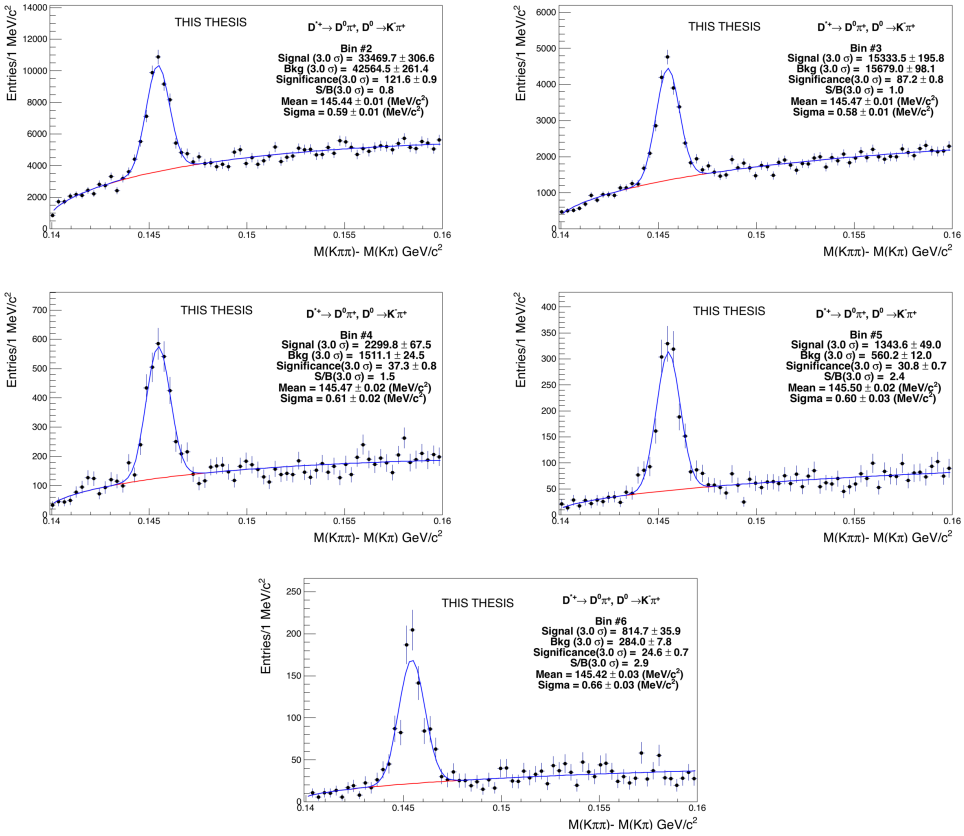

Figure 5.3 – *$M(K\pi\pi) - M(K\pi)$ invariant mass distribution for the fine $p_{\rm T}$-bins in p–Pb collisions at $\sqrt{s_{\rm NN}}$=5.02 TeV. Upper panels: 3 < $p_{\rm T}$(D^{*+}) < 4 GeV/c (left) and 4 < $p_{\rm T}$(D^{*+}) <5 GeV/c (right) in 20-60% centrality class. Mid panels: 5 < $p_{\rm T}$(D^{*+}) <6 GeV/c (left) and 6 < $p_{\rm T}$(D^{*+}) <7 GeV/c (right) in 60-100% centrality class. Bottom panel: 7< $p_{\rm T}$(D^{*+}) <8 GeV/c in 60-100% centrality class.*

pointing angle cut for the high multiplicity centrality class (0-20%); slightly loosening the cosine of pointing angle and tightening at the same time the normalized L_{xy} for the semi-central centrality class (20-60%) and, finally, releasing the cosine of pointing angle cut for the peripheral centrality class (60-100%). This procedure improved the performance of about 2-3%; hence, since no significant improvement was obtained, the centrality-integrated selection were kept and applied in each centrality class.

5.2.2 Correlation of D^{*+} candidates with associated tracks

Particle pairs are formed by correlating each trigger particle with the charged primary particles passing the track selection (excluding those coming from the decay of the D^{*+}-meson candidate) in a specified p_T^{assoc} interval (which can overlap with the $p_{\rm T}^{\rm trig}$ range)

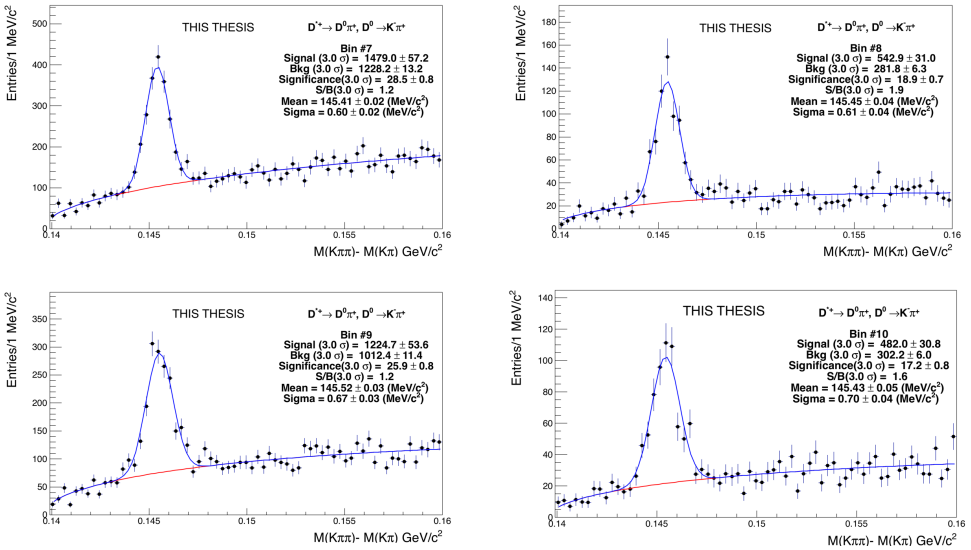

Figure 5.4 *– $M(K\pi\pi) - M(K\pi)$ invariant mass distribution for the fine $p_{\rm T}$-bins in p–Pb collisions at $\sqrt{s_{\rm NN}}$=5.02 TeV. Upper panels: 8 < $p_{\rm T}(\rm D^{*+})$ < 10 GeV/c (left) and 10 < $p_{\rm T}(\rm D^{*+})$ <12 GeV/c (right) in 0-20% centrality class. Mid panels: 12 < $p_{\rm T}(\rm D^{*+})$ <16 GeV/c (left) and 16 < $p_{\rm T}(\rm D^{*+})$ <24 GeV/c (right) centrality integrated (0-100%).*

and in the pseudo-rapidity range $|\eta| < 0.8$. For the $\rm D^0$ meson, also the low-momentum pion tracks from feed-down of $\rm D^{*+}$ mesons are removed via 3σ invariant mass cut on the $M(K\pi\pi) - M(K\pi)$ difference. This is because these soft pions are not related to the charm quark fragmentation chain. For $\rm D^{*+}$ meson candidates in the invariant mass signal region, defined by a $\pm\ 2\sigma$ interval around the $M(K\pi\pi) - M(K\pi)$ mass peak, the azimuthal angle difference $\varphi^{\rm assoc} - \varphi^{\rm trigg} \equiv \Delta\varphi$ and the pseudorapidity difference $\eta^{\rm assoc} - \eta^{\rm trig} \equiv \Delta\eta$ are evaluated and stored to build two-dimensional correlation distributions.

5.2.3 Correction for limited acceptance and detector inhomogeneities with Event Mixing

The angular correlation distribution may be affected, even for uncorrelated pair of particles, by structures not due to physical effects, but originating from the limited detector acceptance, as well as from angular inhomogeneities in the trigger and track reconstruction efficiencies as a function of $\Delta\varphi$ and $\Delta\eta$. Effects of this kind are removed using the Event Mixing technique. In this technique, the analysis is executed on the same data sample of the standard one (called "same event" analysis, SE), but the trigger particles found in each event are correlated to charged particles reconstructed in different events ("Mixed Events" analysis, ME) with similar characteristic, in particular concerning the event multiplicity and z position of the primary vertex (see Section 4.4.4).

The differential yield of associated particles per trigger particle is obtained by

$$\frac{1}{N_{\rm trig}}\frac{{\rm d}^2N^{\rm pair}}{{\rm d}\Delta\eta\,{\rm d}\Delta\varphi} = B_{ME}(0,0)\times\frac{S(\Delta\eta,\Delta\varphi)}{B_{ME}(\Delta\eta,\Delta\varphi)}, \tag{5.1}$$

where $N^{\rm pair}$ is the total number of correlated D-hadron pairs. The functions $S(\Delta\eta,\Delta\varphi)$ and $B_{ME}(\Delta\eta,\Delta\varphi)$ are the signal and the mixed event background distributions, respectively. The latter is normalized to its value in $(\Delta\eta,\Delta\varphi)=(0,0)$, i.e. $(B(0,0))$.
In order to take into account for the rapidity shift of the center-of-mass frame of the nucleon-nucleon collision in the p–Pb system and for the higher charged particle production in p–Pb events, the pools used in the event mixing are modified with respect to the pp analysis as follows:

- Multiplicity bins: $(0,35)\,;(35,55)\,;(55,+\infty)$
- Vertex z (cm) $=(-10,-1.5)\,;(-1.5,3.5)\,;(3.5,10)$

In the centrality dependent analysis, the pools were tuned in order to take into account for the different SPD tracklet multiplicity distributions in the three centrality classes. Therefore, the only small difference with respect to the centrality integrated analysis deals with the definition of the multiplicity ranges of the mixed events pool. The following modification was applied on the multiplicity bins in order to balance the number of events entering in each mixed event pool:

- Multiplicity bins for high multiplicity class (0-20%): $(0,55)\,;(55,80)\,;(80,+\infty)$;
- Multiplicity bins for central multiplicity class (20-60%): $(0,35)\,;(35,55)\,;(55,+\infty)$;
- Multiplicity bins for low multiplicity class (60-100%): $(0,20)\,;(20,30)\,;(30,+\infty)$;

5.2.4 Subtraction of background correlation from signal distribution

The invariant mass signal region also includes background D-meson candidates. Their contribution to the raw correlation distribution is subtracted as follows. For each $p_{\rm T}$ bin, the mean and the sigma of the invariant mass spectrum are extracted. For $\rm D^0$ and $\rm D^+$, a "background" region is defined in the sidebands of the mass distribution as the interval 4 GeV/c^2 $<|m-m^{\rm pdg}|<$ 8 GeV/c^2, while for the $\rm D^{*+}$ meson the background is defined in the region 5 GeV/c^2 $<|m-m^{\rm pdg}|<$ 10 GeV/c^2 (only on the right sideband). The angular correlation distribution for background candidates in this region is extracted and normalized with respect to the background in the signal region estimated from the mass fit. This normalized background correlation distribution is then subtracted from the raw signal one to obtain the signal correlation distribution. The normalization factor is the ratio of the number of background candidates under the signal peak (obtained by integrating the background of the fit function within the signal region) over the

number of background candidates in the sidebands (obtained via bin-counting in the sideband region). An example of the signal region, sideband and sideband-subtracted 1D correlation distributions (along $\Delta\varphi$) is shown in Fig. 5.5, together with the comparison of the three distributions after the normalization to the number of triggers.

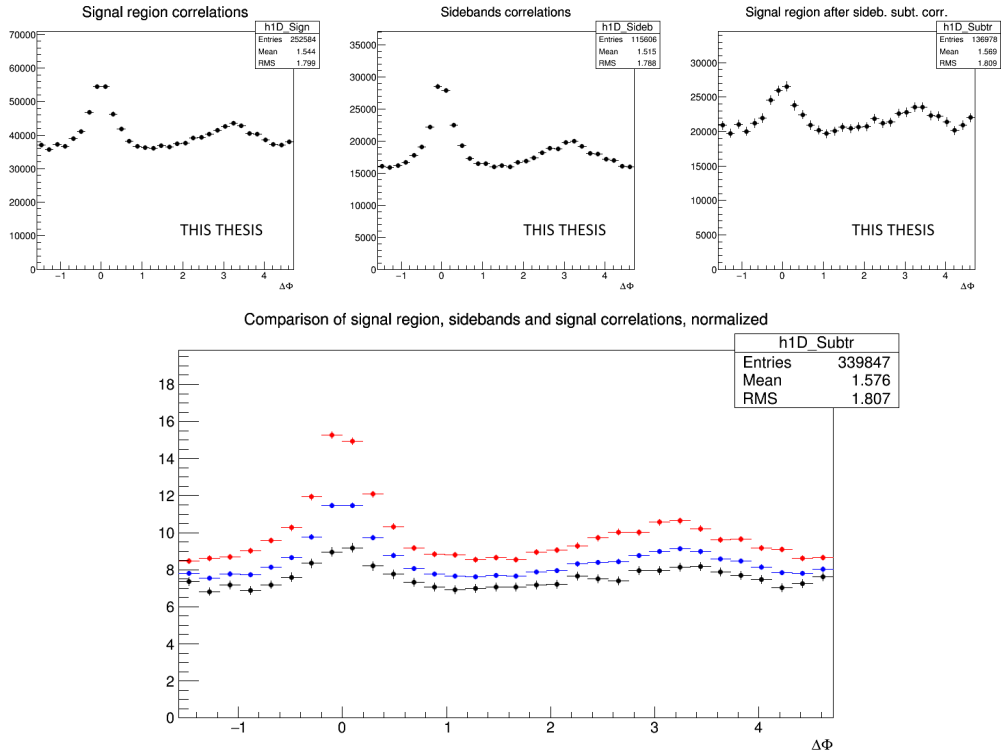

Figure 5.5 *– Top: Example of* D^{*+}*-h signal region (left), sideband (middle), and signal minus sideband (right) correlation distributions. Bottom: signal region per-trigger normalized correlation distribution (blue), sideband region per-trigger normalized correlation distribution (red), background-subtracted per-trigger normalized correlation distribution (black).*

5.2.5 Correction for D^{*+} meson efficiency and associated track efficiency

After filling the signal and background (sidebands) correlation distributions, it is necessary to take into account also for the correlations with not reconstructed tracks or not passing the quality selection due to poor reconstruction. In the same way, the loss of D^{*+}-mesons which are not reconstructed, or do not pass the selection, impacts the correlation distribution shape. Hence, each pair is weighted by the inverse of the product of the associated track and D meson reconstruction efficiencies, ϵ_{trk} and ϵ_{trig}. In the centrality integrated analysis, the same procedure applied in pp collisions holds. The

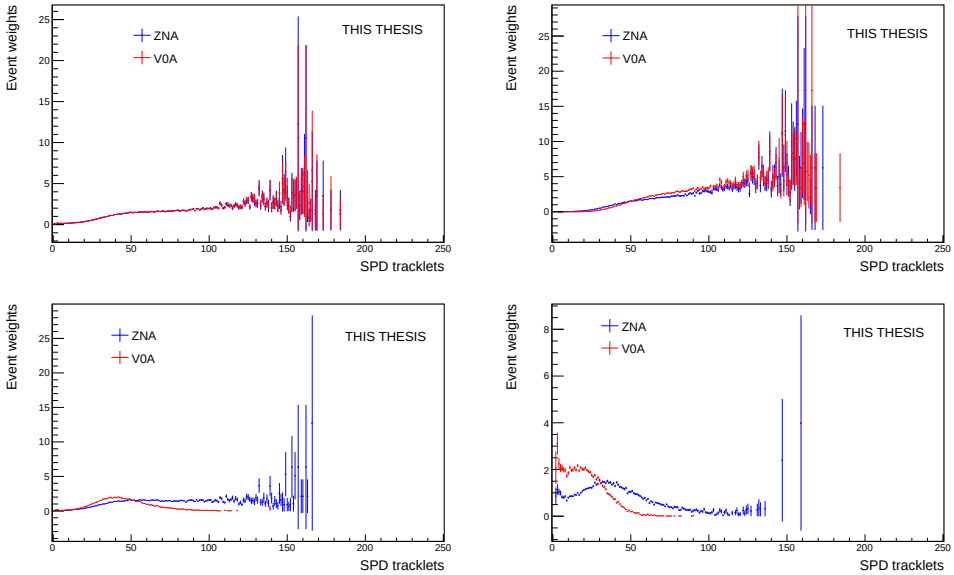

Figure 5.6 – *Event weights applied to Monte Carlo sample, to mimic the multiplicity distribution for centralities: 0-100% (centrality-integrated), 0-20%, 20-60%, 60-100%. Blue points are for ZNA, red points for V0A estimator.*

centrality dependent analysis, instead, required a peculiar treatment for the efficiencies. In the following the specific choices adopted for this analysis are discussed.

Tracking efficiency

The associated track efficiency is based on an online weighting of the D-meson and associated track correlation pairs, by means of a three-dimensional efficiency map, as described in details in subsection 4.4.5. The same efficiency of the centrality integrated analysis has been used. This choice was based on the fact that no variations on the associated track cuts was performed between the two analyses, so the efficiency is not varied, and that there is a negligible dependence of the tracking efficiency on the event centrality/multiplicity. The latter assumption was checked by evaluating tracking efficiency maps for each centrality slice, i.e. running the tracking efficiency task on a sample of Monte Carlo reproducing the same event multiplicity distributions (in terms of SPD tracklets) observed on data for each slice.
The event weights applied to the Monte Carlo events to mimic each centrality slice (as well as those to reproduce the same multiplicity also for the centrality-integrated sample) are shown in Fig. 5.6. They are presented for both ZNA and V0A estimator. As it is evident, the V0A tends to favour more high-multiplicity events for the 0-20% centrality class, and low-multiplicity events for the 60-100%; the ZNA estimator instead equalizes more the event multiplicity distribution in the three centrality slices.

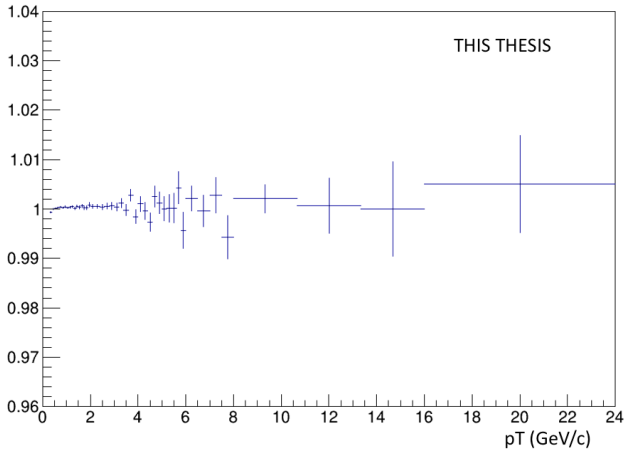

Figure 5.7 *– Ratio of 1D track efficiency map vs p_{T} with and without event weights (example for 0-20%) applied on the Monte Carlo sample.*

After comparing the tracking efficiency maps evaluated applying the event weights on the monte Carlo events, with those obtained running on the unweighted Monte Carlo sample, differences of the order of few per mille were found, confirming the possibility of using the same tracking efficiency map for the various centrality slices. As an example, the ratio of p_{T}-projection of the tracking efficiency maps when 0-20% weights are applied and where no weights are applied on the events is shown in Fig. 5.7, and it results to be fully compatible with 1.

Trigger efficiency

Differently from the tracking efficiency, the D-meson reconstruction and selection efficiency can have a dependence on the event multiplicity that has to be taken into account. This mainly depends on the lower efficiency on the reconstruction of the primary vertex (included in the overall D-meson reconstruction efficiency) for very low multiplicity events. Indeed, the efficiency is rather flat above 20-30 tracklets, and starts to drop below that SPD tracklet multiplicity. To consider this dependence, separate trigger efficiency maps were built for each centrality slice, by running the trigger efficiency task on the reweighted Monte Carlo enriched sample (using the same event weights described above). Then, the trigger efficiency correction follows the same procedure, based on an online-weighting of the correlation pairs. In Fig. 5.8 the trigger efficiency as a function of the transverse momentum for prompt (left panel) and feed-down (right panel) D^{*+} is reported in the three centrality classes (0-20%, 20-60% and 60-100%) and for the centrality integrated case. In Fig. 5.9 the same trigger efficiency is shown as a function of the multiplicity. It can be noticed that the efficiency has a rather flat trend above 20-30

tracklets.

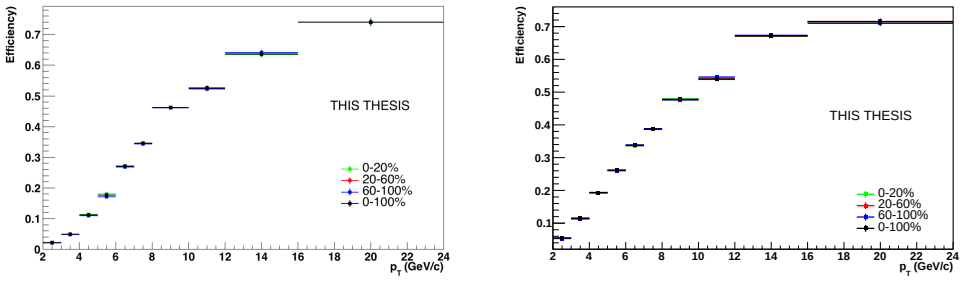

Figure 5.8 *– Superimposed efficiency of prompt (left) and feed-down (right)* D^{*+} *as a function of the transverse momentum, for the three centrality class (0-20%, 20-60%, 60-100%) and the centrality integrated case (0-100%).*

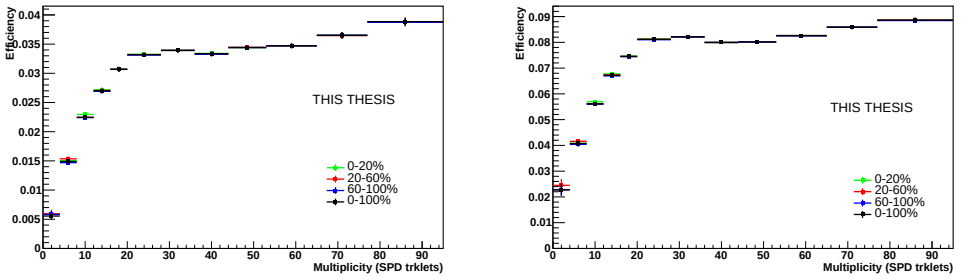

Figure 5.9 *– Superimposed efficiency of prompt (left) and feed-down (right)* D^{*+} *as a function of the multiplicity of SPD tracklets, for the three centrality class (0-20%, 20-60%, 60-100%) and the centrality integrated case (0-100%).*

5.2.6 Correction for the contamination of secondary particles

The contribution of secondary tracks in the sample was removed via an upper cut on the distance of closest approach to the primary vertex in the transverse plane (DCA_{xy}), applied during the track selection. Secondary particles are, indeed, produced either from long-lived strange hadrons or from interaction of particles with the detector material. The standard selection cut was set to $\mathrm{DCA}_{xy} < 0.25$. However, a residual contamination from secondary tracks is expected in the correlation distributions. This contamination is estimated from Monte Carlo simulation based on PYTHIA and GEANT3 particle transport package which provides a detailed description of the geometry of the apparatus and of the detector response. In the centrality integrated analysis, the fully corrected correlation distributions were multiplied by a purity factor to account for this contribution, while in the centrality dependent analysis a more sophisticated method was adopted in

order to consider some modulation structures along $\Delta\varphi$. The presence of these modulations, which vary from bin to bin, even if small, could be amplified after the subtraction of the baseline, when going to the yield evaluation. In order to take into account for them, the purity correction was estimated differentially though the azimuthal axis (i.e. applied bin-per-bin on the azimuthal correlation distributions) as was done for the proton-proton sample in section 4.4.7.

5.2.7 Monte-Carlo closure test

In order to check the whole procedure, the analysis was performed with Monte Carlo simulations both at generated and reconstructed level. The latter includes the detector response and, its comparison with the simulations at generated level, allow to test the correction procedure. As observed in subsection 4.4.6 for the pp collision analysis, performing a Monte Carlo closure test allows to spot the presence of structures in the near-side region for B$\rightarrow$ D^{*+}-h correlations, induced by the topological selection on the D. Indeed, the presence of the topological cuts for the D^{*+}-meson selection indirectly induce a bias on D^{*+} coming from the decay of beauty hadrons, favouring cases with a small opening angle between the D^{*+}-meson and the other tracks from the beauty hadron decay. This affects the feed-down component of the data correlation distributions. After the projection of the correlation distributions on $\Delta\varphi$, the resulting one-dimensional angular correlations are corrected for this effect with the same procedure described in the subsection 4.4.6.
When performing the analysis in bins of centrality class, the procedure for the evaluation of the correction to apply on data was repeated for each class. The outcome of the MC closure test, highlights larger B$\rightarrow$D^{*+} structures in 0-20% than in 60-100% if only the associated tracks coming from beauty were considered. The situation was reversed when considering all the associated tracks, i.e. also the uncorrelated pairs - which was the case to be considered to evaluate the correction. This is understandable, due to the lower presence of uncorrelated pairs in 60-100%, which enhanced the peak/baseline ratio with respect to 0-20%. This was also reflected in a (slightly) larger correction for 60-100% centrality class rather than for 20-60% and 0-20%. In any case, the overall correction applied on data is always lower than 3%, even for the worst case, being the lowest D^{*+}-meson p_{T} bin ($3 < p_{\mathrm{T}} < 5$ GeV/c) and the highest associated track p_{T} bin ($p_{\mathrm{T}} > 1$ GeV/c). Furthermore, the difference of the correction values among the different centrality classes is never larger than 1.5%.

5.2.8 Correction for feed-down of D^{*+} meson from b-hadron decay

The selected sample of D^{*+} mesons contain also the contributions of those coming from the decay of beauty hadrons, known as "feed-down" contribution. The correlation dis-

tribution of these secondary D^{*+} mesons is sensitive to the properties of beauty jets and beauty hadron decay, which in general differ from those relative to charm jets and hadrons. For instance, it should be observed that the selection strategy employed for the D^{*+} meson candidate selection tends to enhance the fraction of reconstructed feed-down D^{*+} mesons. Since, with the available statistics, it was not possible to measure the correlation of $B \to D^{*+}$ and charged particles, the beauty feed-down contribution was subtracted using templates of Monte-Carlo simulations, in a similar way as was done for the pp analysis (described in Sec.4.4.8). However, in the case of p-Pb analysis, it was appropriate to make an assumption on the nuclear modification factor of the feed-down D^{*+} ($R_{pPb}^{\mathrm{feed-down}D^{*+}}$). In particular, it was assumed that the ratio $R_{pPb}^{\mathrm{feed-down}D^{*+}}/R_{pPb}^{\mathrm{prompt}D^{*+}}$ could vary into an interval of [0.9-1.3] and this variation was also introduced in the systematic uncertainty evaluation. In p–Pb analysis an additional hypothesis due to a v_2 of beauty hadrons was done and added to the templates. This modulation plays a role in the evaluation of systematic errors due to the feed-down correction. In particular, the baseline of the templates was modulated with a v_2-like shape, given by:

$$f_{v_2} \propto (1 + 2v_2^{B\to D^{*+}} v_2^{had} \cos\Delta\varphi) \tag{5.2}$$

where for $v_2^{B\to D^{*+}}$ and v_2^{had}, the ALICE measurements were adopted. The modulated template is then plugged in the extrapolation of the final template of prompt D^{*+} mesons. This contribution was also considered as a source of systematic uncertainty.
In the analysis of correlations of D^{*+} correlations with charged particle as a function of the centrality, the procedure fully coincides to the one used for the centrality-integrated case.The only modification consists in a possible dependence of the feed-down correction on the centrality of the event, for the following reasons:

- the D-meson efficiency varies as a function of the centrality, due to the lower primary vertex reconstruction efficiency at low multiplicity and, for D^0, to centrality-dependent topological cut values. This, in turn, impacts on f_{prompt} because of its dependence on the D-meson efficiency.
- Possible variation of $R_{\mathrm{pPb}}(B \to D)/R_{\mathrm{pPb}}(\mathrm{D})$, on which f_{prompt} depends, on the centrality of the event.
- Dependence of the B→D-hadron correlation peaks on the event centrality. This would require modifying the MC templates for B→D-hadron correlations used for each centrality class. This effect was neglected, since no evidences exist, at the moment, on a possible modification of the heavy-flavour quark fragmentation versus the event multiplicity.

To consider the above effects, an independent evaluation of f_{prompt} was performed in each centrality class, using the specific trigger efficiency maps and possible ranges of $R_{\mathrm{pPb}}(B \to D)/R_{\mathrm{pPb}}(D)$ (entering in the f_{prompt} uncertainty), from [0.9,1.1] in 60-100% to [0.9,1.3] in 0-20%. The resulting f_{prompt} values for the D^{*+} is reported in Fig. 5.10 for

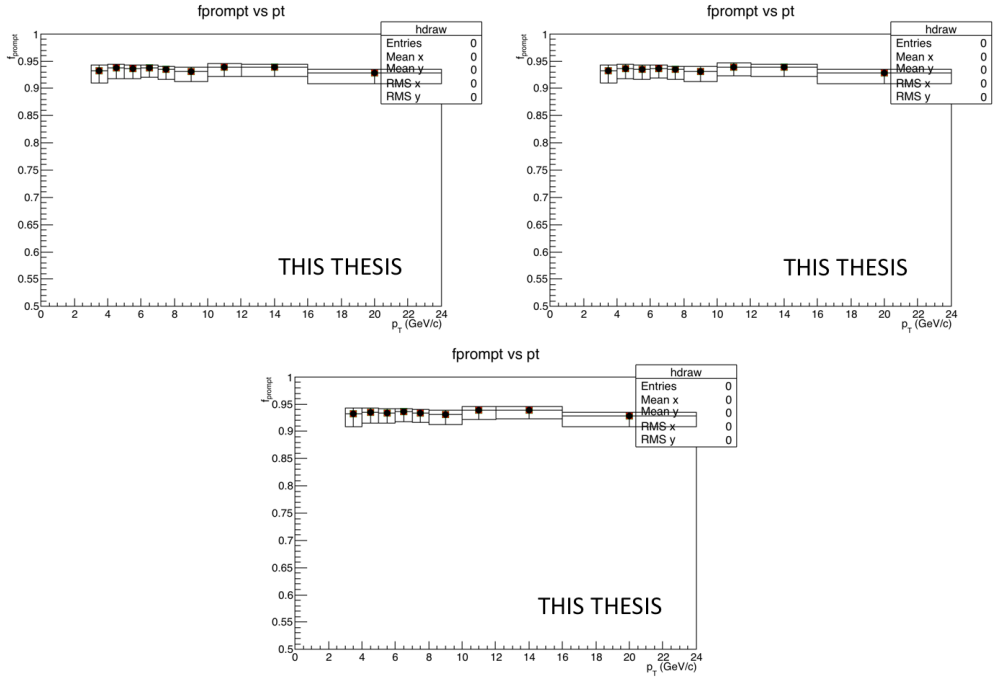

Figure 5.10 – f_{prompt} *as a function of the* p_{T} *for* D^{*+} *in 0-20%(top), 20-60% (mid) and 60-100% (bottom) estimated on the basis of FONLL predictions.*

the three centrality classes studied. Feed-down D^{*+} are typically about 5-8%, in both the analysis.

5.2.9 Study of correlation properties

The limited statistics available does not allow to study the two dimensional $(\Delta\eta, \Delta\varphi)$ distribution, which is therefore projected to the $\Delta\varphi$ axis by integrating on $|\Delta\eta|$. Despite the maximum $\Delta\eta$ acceptance is of $|\Delta\eta| < 1.6$, the distribution are integrated in $|\Delta\eta| < 1$. The choice to remove the large $|\Delta\eta|$ regions relies in the necessity of avoid the so-called "wings" effect. Indeed, those angular regions are affected by very low statistics and, for this reason, a large mixed-event correction would amplify the statistical fluctuations. As the difference in the azimuthal angle is periodic ($\Delta\varphi = 0 = 2\pi$), the $\Delta\varphi$-range is limited to the essential range of 2π. The $\Delta\varphi$-limits are chosen to be $[-\pi/2, 3\pi/2]$ in order to provide a good visibility of the correlation pattern, which peaks around $\Delta\varphi = 0$ and $\Delta\varphi = \pi$.

The properties of the azimuthal correlation distribution are quantified by fitting the distribution with a function composed of two Gaussian, modelling the near- and the away-side peaks, and a constant term describing the baseline. The mean of the Gaussian are fixed at $\Delta\varphi = 0$ and $\Delta\varphi = \pi$. To accomplish the 2π periodicity of the $\Delta\varphi$ variable,

the Gaussian functions are "duplicated" with mean at $\Delta\varphi = 2\pi$ and $\Delta\varphi = -\pi$. The fitting procedure was described in details in Section 4.6.

5.3 Systematic uncertainties

The evaluation of the systematic uncertainty on the $\Delta\varphi$ correlation distributions and on the fit observables is exactly the same as that described in subsections 4.5 and 4.6.3. Hence, the $\Delta\varphi$ correlated and uncorrelated systematic uncertainties were estimated for the azimuthal correlation distributions. The $\Delta\varphi$-correlated systematic uncertainties on the correlation distributions account for the following contributions:

- uncertainty on the extraction of signal and background;
- uncertainty on the background correlation shape;
- uncertainty on the tracking efficiency;
- uncertainty on the D-meson cut stability;
- uncertainty on the cut stability of the distance of closest approach (for the secondaries discrimination);

The following $\Delta\varphi$-uncorrelated systematic uncertainty were computed:

- uncertainty on the feed-down subtraction;
- uncertainty on the correction for bias on B to D decay topologies.

These systematic uncertainties have been evaluated looking at the ratio of the correlation distributions retrieved with the alternate approaches over those with the standard approach. The total systematic uncertainty was estimated combining the $\Delta\varphi$ correlated and uncorrelated uncertainties with the systematic uncertainty on the fit observables (in particular on the baseline definition). The approaches used are the same described for the analysis in pp collisions. The only modification that involves the systematic uncertainty evaluation on the fit observables deals with the values chosen for the v_2 hypothesis, in the analysis as a function of multiplicity. Here the v_2 assumption has been tuned on the basis of the centrality class. The hypotheses on the charged particle v_2 versus centrality were guessed on the bases of the results obtained on charged hadron v_2 in p–Pb collisions (2016 sample) in different V0A multiplicity classes, after the subtraction of the non-flow contribution (which, in our fits, we account with the Gaussian functions). However, a different centrality estimator (V0A) was used. The ZNA estimator, employed in this thesis work, tends to equalize more the different event multiplicities among the various centrality classes, hence shall give slightly lower (higher) v_2 values in 0-20% (60-100%) with respect to V0A estimator. For this reason, despite the V0A v_2 values for hadrons are compatible with zero, a very small modulation was assigned also in this class. The

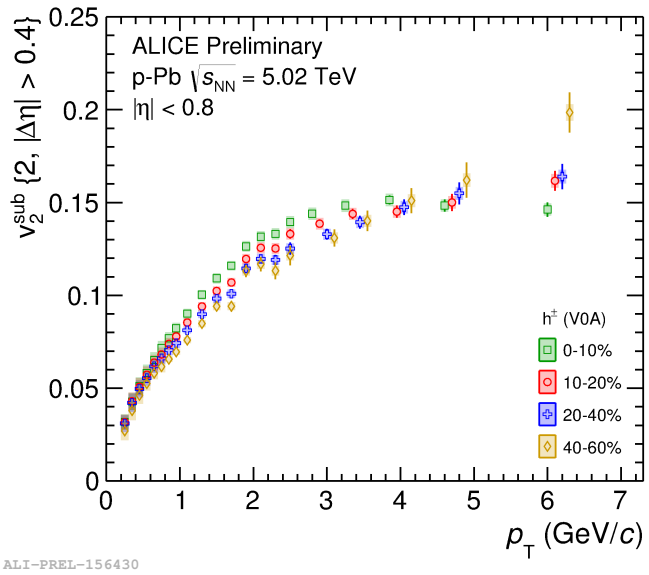

Figure 5.11 *– Reference plots for estimation of $v_2(h)$ hypotheses in the three centrality classes.*

V0A v_2 values, extracted from Fig.5.11, wasn't decreased for the high-multiplicity class to stay safe with our assumptions.

The hypotheses on D-meson v_2 were guessed starting from ALICE preliminary results of heavy-flavour decay electron v_2 in the same collision system, using the ZNA estimator (left panel of Fig. 5.12). The measurement was performed in lower $p_{\rm T}$(e) ranges, but which by chance are fairly similar to the average $p_{\rm T}$ of out D-meson correlation ranges, if the $p_{\rm T}$ of the parent D-hadron is considered for charm-origin heavy-flavour decay electrons - as shown in the right panel of Fig. 5.12. The drawback of this choice relies in the fact that these v_2 values were obtained after the subtraction of the low-multiplicity angular correlation distributions from the high-multiplicity ones [154], while in this analysis a hypotheses for v_2 in each centrality class was needed. Hence, as done for heavy-flavour decay electron v_2, a negligible (though not completely null) elliptic flow was assumed for the peripheral centrality class (60-100%), and the values extracted from Fig. 5.12 for the high multiplicity centrality class (0-20%) [154] were used. The 20-60% centrality class was assumed to follow the same centrality trend observed for the hadron v_2. Another potential drawback relies in the fact that heavy-flavour electron v_2 includes the contribution from beauty-hadron decay electrons, while the B-feed-down is instead subtracted in our D-meson analysis. In any case, the beauty contribution of electrons should be small for $p_{\rm T} < 3$ GeV/c, where the heavy-flavour electron v_2 has its largest value.

In the following, thus, the v_2 hypotheses adopted for the evaluation of the systematic on the fit observables due to a possible presence of flow:

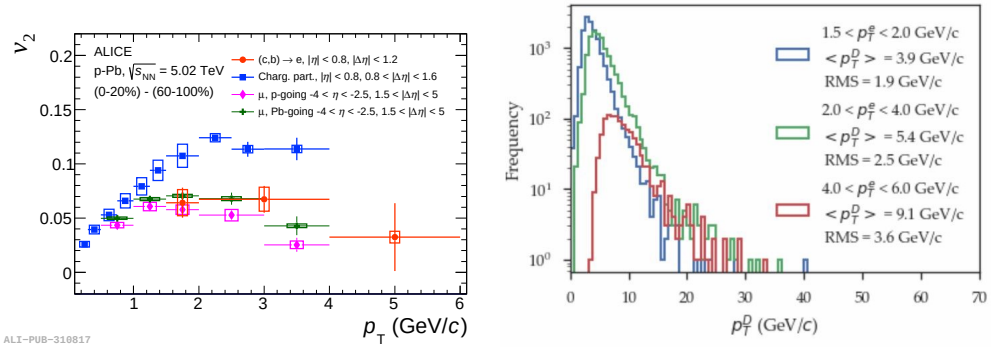

Figure 5.12 *– Left: v_2 of heavy-flavour decay electrons in p–Pb, after the subtraction of the low multiplicity angular correlation distributions from the high-multiplicity ones. Right: corrispondence of $p_T(e)$ and p_T of the parent D-meson (for charm-origin electrons).*

- For 0-20%: 0.08, 0.08, 0.04, 0.02 (for p_T(D) 3-5, 5-8, 8-16, 16-24 GeV/c); 0.06, 0.05, 0.08 (for p_T(assoc) $>$ 0.3, 0.3-1, $>$ 1 GeV/c)
- For 20-60%: 0.04, 0.04, 0.02, 0.01 (for p_T(D) 3-5, 5-8, 8-16, 16-24 GeV/c); 0.03, 0.02, 0.05 (for p_T(assoc) $>$ 0.3, 0.3-1, $>$ 1 GeV/c)
- For 60-100%: 0.02, 0.02, 0.01, 0.00 (for p_T(D) 3-5, 5-8, 8-16, 16-24 GeV/c); 0.01, 0.005, 0.015 (for p_T(assoc) $>$ 0.3, 0.3-1, $>$ 1 GeV/c)

In Fig. 5.13, and in Fig. 5.14 the associated yield, width (together with their statistical and systematic uncertainties) and the correspondent plot showing the systematic uncertainty of the considered observable deriving from the variation of the fit approaches (which is the full systematic uncertainty for the widths) as well as the full systematic uncertainty are reported for the near-side and away-side. In Fig. 5.15 the baseline height, the systematic related to the variation of the fit approach and the total systematic uncertainty on the baseline is shown. As an example, they are reported only in the inclusive momentum interval of the associated tracks.

5.4 Results

5.4.1 Centrality-integrated results

To check the compatibility of two-particle angular correlation analysis performed independently on the three D mesons, their fully corrected distributions -except for the feed-down subtraction and the secondary contamination removal- were compared. Figure 5.16 shows the superimposed corrected azimuthal correlation distributions from D^0-h, D^{*+}-h and D^+-h on the p–Pb data sample used in the analysis. An overall agreement among the different D-meson species emerged in all the kinematic ranges studied.

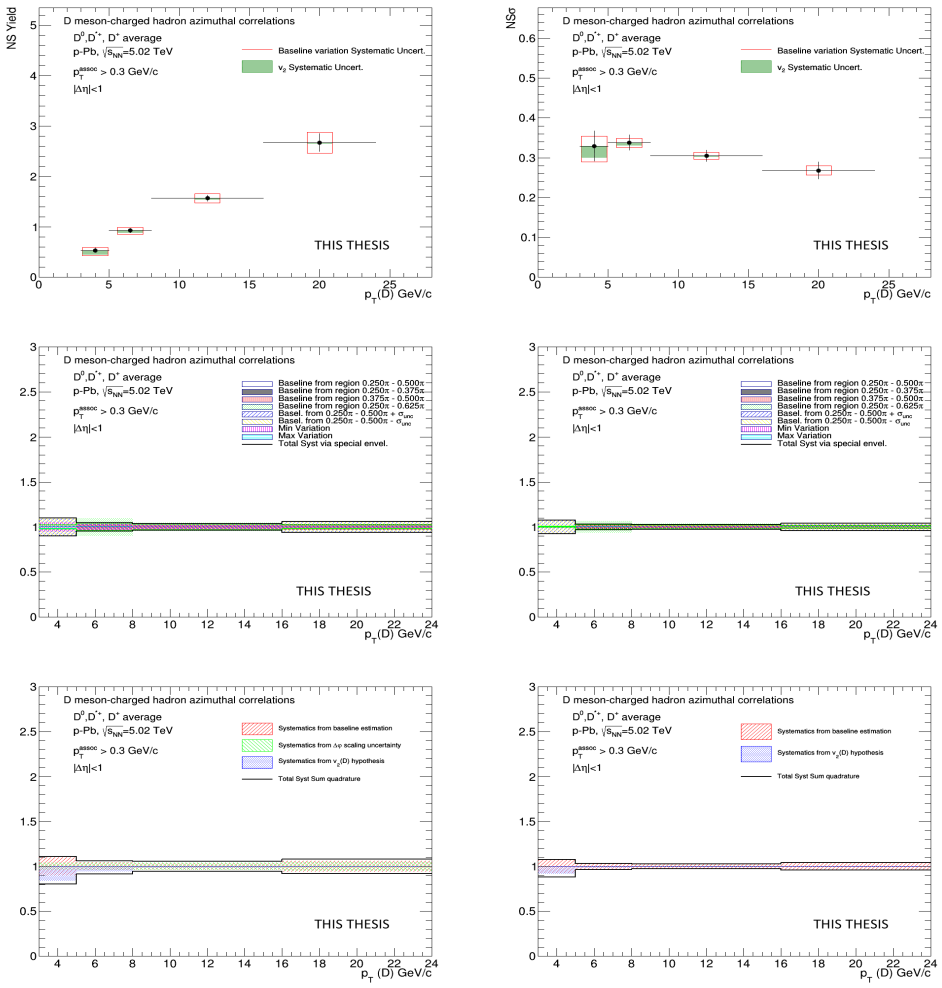

Figure 5.13 – *Near-side associated yield (top left) and width (top right). The vertical bars represent the statistical uncertainty while the red empty boxes are related to the systematic uncertainty (the green shaded area inside the boxes represents the uncertainty on the v_2 hypotheses). The correspondent systematic uncertainties deriving from the variation of the fit approaches (which is the full systematic uncertainty for the widths) are reported in the second row for the near-side yield (left) and width (right). In the legend the different contribution of the fit variations are reported. On the bottom the full systematic uncertainty for the near-side yield (left) and width (right) is shown.*

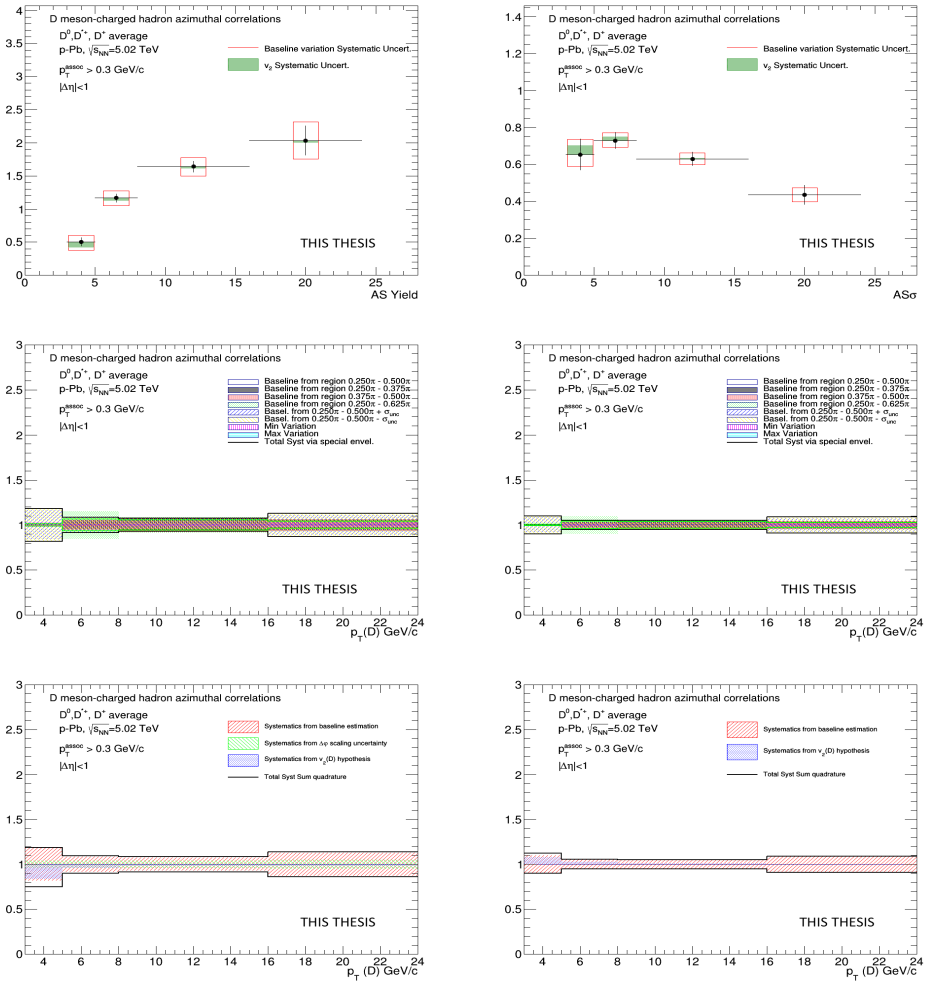

Figure 5.14 – *Away-side associated yield (top left) and width (top right). The vertical bars represent the statistical uncertainty while the red empty boxes are related to the systematic uncertainty (the green shaded area inside the boxes represents the uncertainty on the v_2 hypotheses). The correspondent systematic uncertainties deriving from the variation of the fit approaches (which is the full systematic uncertainty for the widths) are reported in the second row for the away-side yield (left) and width (right). In the legend the different contribution of the fit variations are reported. On the bottom the full systematic uncertainty for the away-side yield (left) and width (right) is shown.*

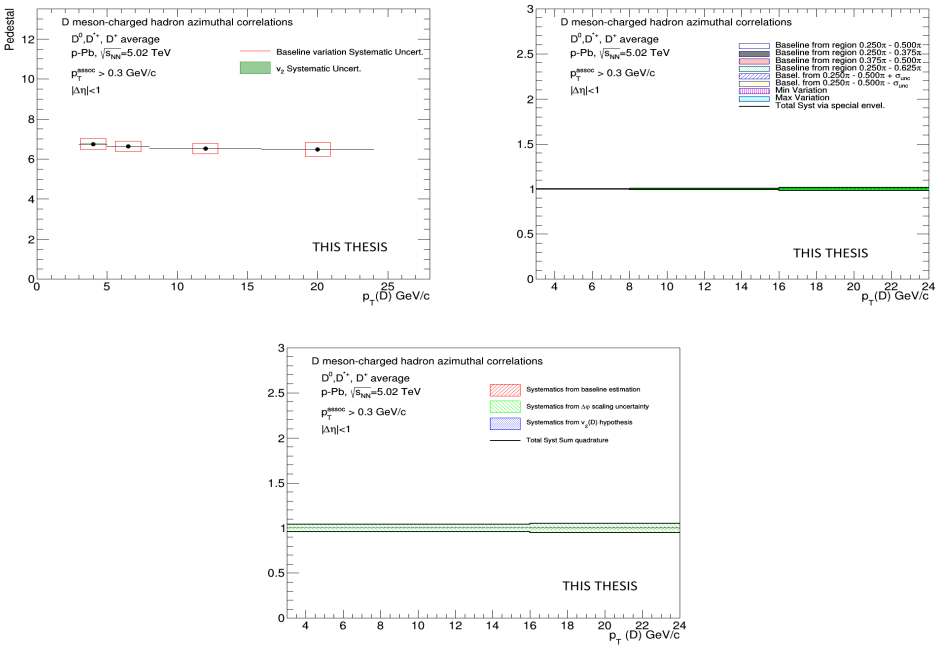

Figure 5.15 – *On the top left plot the baseline height is shown. The vertical bars represent the statistical uncertainty while the red empty boxes are related to the systematic uncertainty (the green shaded area inside the boxes represents the uncertainty on the v_2 hypotheses). The correspondent systematic uncertainty deriving from the variation of the fit approaches (which is the full systematic uncertainty for the widths) is reported in the top right. In the legend the different contribution of the fit variations are reported. On the bottom the full systematic uncertainty on the baseline height is shown.*

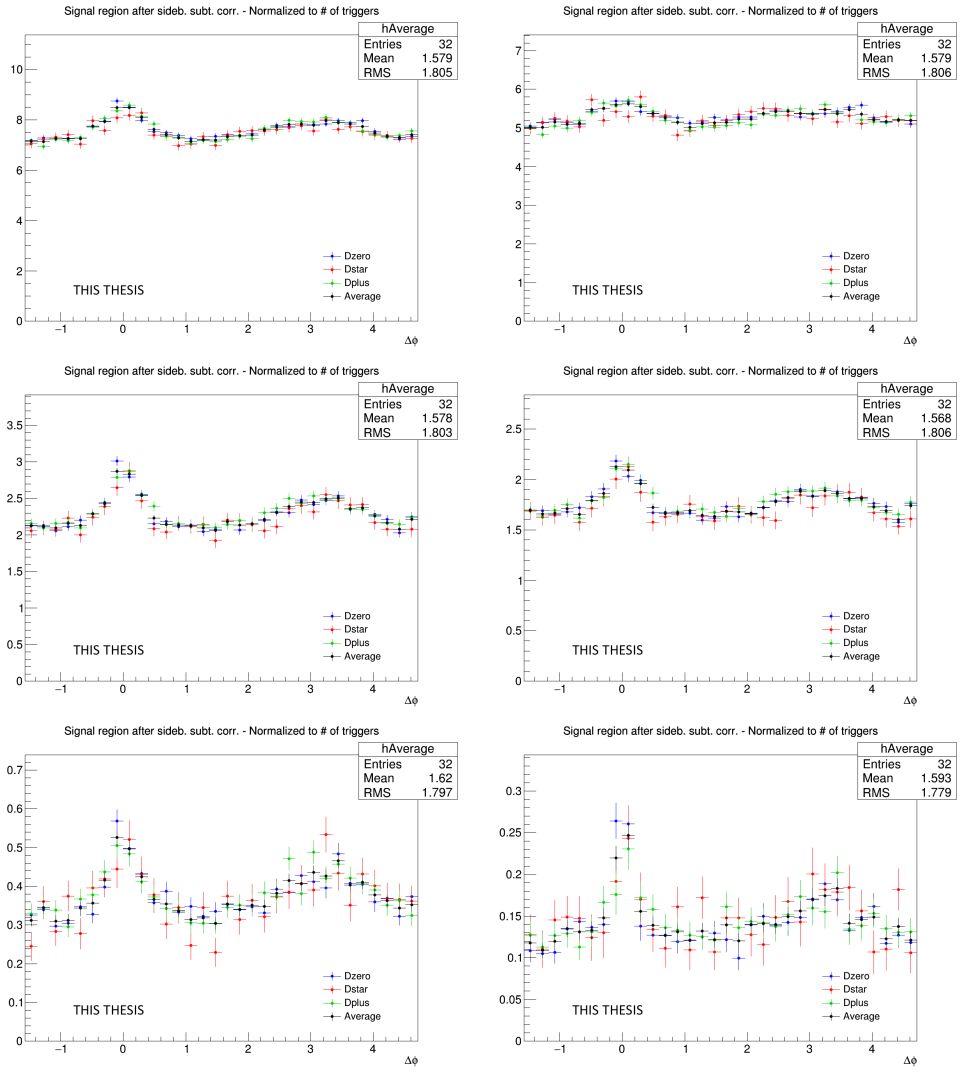

Figure 5.16 – *Superimposition of the corrected (apart from feed-down and purity) distribution of D-hadrons azimuthal correlations for the three species of the analyzed D-meson. and different associated track p_T ranges, and D-meson p_T 5< p_T <8 GeV/c. In these plots, the distributions for $5 < D\ p_T < 8$ GeV/c with associated tracks (from the top left onward) $p_T > 0.3$, $p_T > 1$, $0.3 < p_T < 1$ GeV/c, $1 < p_T < 2$ GeV/c, $2 < p_T < 3$ GeV/c and $p_T > 3$ GeV/c.*

As for the proton-proton analysis, despite being evaluated in the full 2π range, the range of final results was then reduced to $[0, \pi]$ radians, reflecting the points outside that range over the value of $\Delta\varphi = 0$ and $\Delta\varphi = \pi$ under the assumption that symmetric bins have equal statistics. This allowed to reduce the impact of statistical fluctuations on the data points; after the reflection the relative statistical uncertainty for the resulting bin is reduced by a factor $1/\sqrt{2}$.
Thanks to the proven compatibility within the uncertainties among the D^0, D^+ and D^{*+} azimuthal correlations, and since no large differences are visible in the correlation distributions observed in Monte Carlo simulations based on PYTHIA with Perugia0, 2010 and 2011 tunes, in order to reduce the overall uncertainties, the weighted average (eq. 4.5) of the azimuthal correlation distributions of D^0, D^+ and D^{*+} was extracted.
Quantitative and physical informations from the data correlation patterns were extracted fitting the averaged D-h correlation distributions with two Gaussian functions (with means fixed at $\Delta\varphi$=0 and $\Delta\varphi$=π values), plus a constant term (baseline). A periodicity condition is also applied to the fit function to obtain the same value at the bounds of 2π range. The expression of the fit function is reported below:

$$f(\Delta\varphi) = c + \frac{Y_{NS}}{\sqrt{2\pi}\sigma_{NS}} e^{-\frac{(\Delta\varphi-\mu_{NS})^2}{2\sigma_{NS}^2}} + \frac{Y_{AS}}{\sqrt{2\pi}\sigma_{AS}} e^{-\frac{(\Delta\varphi-\mu_{AS})^2}{2\sigma_{AS}^2}} \tag{5.3}$$

where baseline is calculated as the weighted average of the points lying in the so-called "transverse region", i.e. the interval $\frac{\pi}{4} < |\Delta\varphi| < \frac{\pi}{2}$.
An example of the results from the fit for D-meson p_{T} in the interval $5 < p_{\mathrm{T}} < 8$ GeV/c and for $p_{\mathrm{T}}^{ass} > 1 GeV/c$ is shown in Fig. 5.17.
From the fit outcome, it is possible to retrieve the near-side and away-side yield and widths (integral and sigma of the Gaussian functions, respectively), as well as the baseline height of the correlation distribution. The near-side observables give information on the multiplicity and angular spread of the tracks from the fragmentation of the charm jet which gave birth to the D-meson trigger. At first order, instead, the away-side observables are related to the hadronization of the charm parton produced in the opposite direction (though the presence of NLO processes for charm production breaks the full validity of this assumption). The baseline value is a rough indicator of the underlying event multiplicity, though below the baseline level also charm and beauty-related pairs are contained (especially in cases of NLO production for the heavy quarks).
The evaluation of the systematic uncertainties on the fit observables follows the same strategy adopted in the proton-proton analysis.

Comparison of pp and p–Pb results

The pp and p–Pb collision analyses discussed in this thesis, performed at the same center-of-mass energy were compared. Figs 5.18 and 5.19 show the average of D^0, D^+ and D^{*+} azimuthal correlations for pp and p–Pb at the same collision energy, for the overlapping

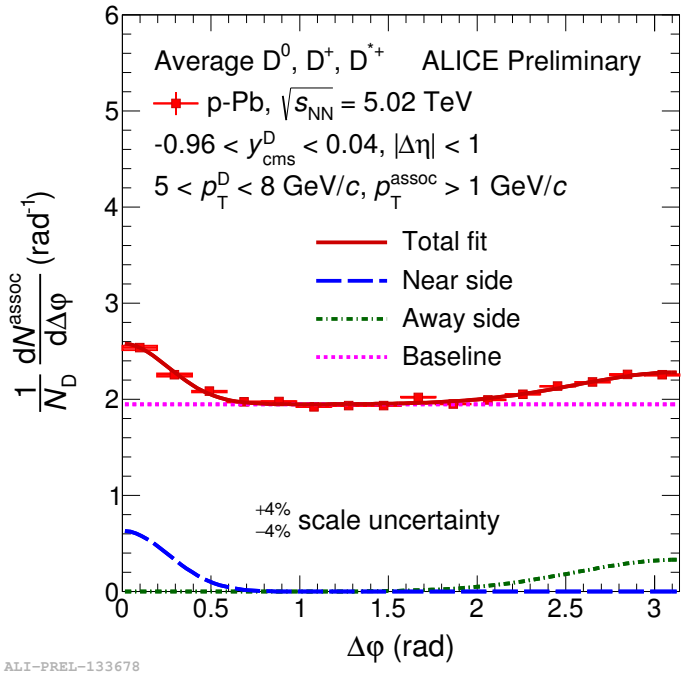

Figure 5.17 – *Example of fit to azimuthal correlation distributions and baseline estimation.*

kinematic ranges of trigger and associated particles p_{T} studied. The measurements are multiplicity-integrated. The baseline has been subtracted in both the collision systems. An overall compatibility within uncertainties between the two collision systems is found for all the common kinematic ranges analyzed, and a similar evolution of the correlation pattern with transverse momentum holds for the two systems: narrower an higher correlation distributions for increasing p_{T} of the D meson.

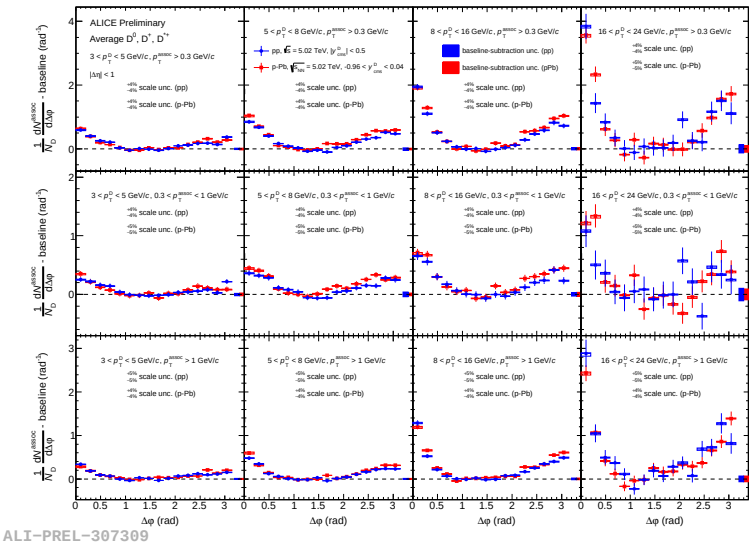

Figure 5.18 – *Average of* D^0, D^+ *and* D^{*+} *azimuthal correlations in pp (red) and p-Pb (blue) with D meson* p_{T} *in the range* $5 < p_{\mathrm{T}} < 8$ GeV/c *and* $8 < p_{\mathrm{T}} < 16$ GeV/c, *for the three regions of associated track transverse momentum.*

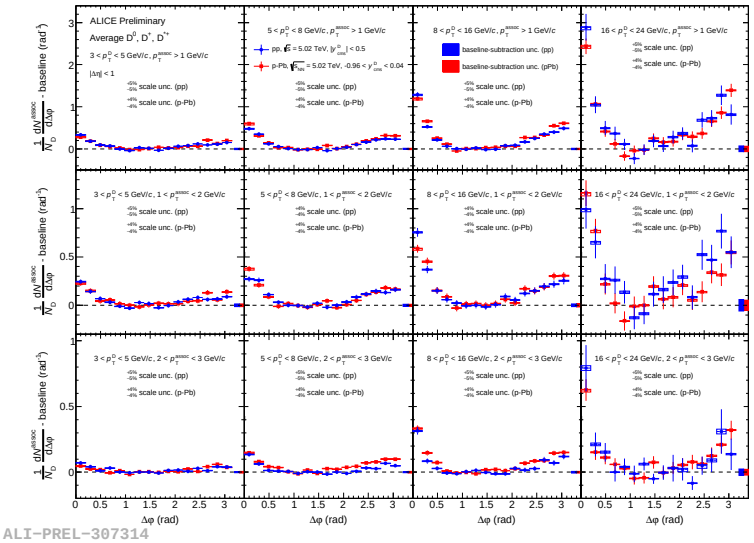

Figure 5.19 – *Average of* D^0, D^+ *and* D^{*+} *azimuthal correlations in pp (red) and p-Pb (blue) with D meson* p_{T} *in the range* $5 < p_{\mathrm{T}} < 8$ GeV/c *and* $8 < p_{\mathrm{T}} < 16$ GeV/c, *for the three regions of associated track transverse momentum.*

Focusing on the peak regions, while one can appreciate a full near-side compatibility, for some kinematic regions the away-side region seems to be enhanced in p–Pb with respect to pp. As it could be already noticed from the comparison of the distributions, near-side observables are fully consistent. For the away-side region, instead, the peak widths are roughly compatible (within rather large uncertainties), while a hint of larger yields in p–Pb can be observed, especially for the D-meson $p_{\rm T}$ included in the interval from 5 to 16 GeV/c, generally in all the associated track $p_{\rm T}$ regions. In Figs. 5.20, 5.21 the comparison of the observables extracted from the fits (near-side yield and width) is also presented.
To quantify the possible hint of enhanced away side, observed when comparing p-Pb with respect to pp collisions for 5< $p_{\rm T}$ < 8 and 8< $p_{\rm T}$ <16 GeV/c in several associated $p_{\rm T}$ ranges, the ratio of the correlation distributions was computed. Here, all the uncertainties have been propagated [1] and the away-side points were fitted with a constant function (red line in the Fig. 5.22).
In Fig. 5.22, the resulting ratios from the performed check are reported. The outcome fit gives an excess ranging from 1 to 2.5σ, so nothing can be firmly concluded on the away-side yield enhancement for $5 < p_{\rm T} < 16$GeV/c.

Comparison of p–Pb results and models

A comparison of the average D-h correlation distributions on the new p-Pb data samples with expectations from Monte Carlo simulations (currently PYTHIA6-Perugia2011, PYTHIA6-Perugia2010, PYTHIA6-Perugia0, PYTHIA8 and POWHEG+PYTHIA with EPS09 nPDF) is shown in Fig. 5.23, after the baseline subtraction (which differs strongly between data and simulations, due to the very different underlying event). Despite using simulations for pp collisions, in order to reproduce the p–Pb collision events, the boost of the center-of-mass along the beam axis present in p-Pb collisions and nuclear PDF have been included in the simulations. The shape of the correlation distributions is well reproduced by all the models, together with their $p_{\rm T}$ trend and with the evolution of the correlation peaks. Thanks to the high statistics and to the good precision of the p–Pb data sample, it was possible to investigate more differentially the correlation distributions with respect to the kinematic intervals. Indeed, it was possible to access to $p_{\rm T}$ intervals of associated tracks very close to the $p_{\rm T}$ of D-mesons ($p_{\rm T}^{assoc} \approx p_{\rm T}^{D}$), as for example in the bottom left panel of Fig. 5.23 where $3 < p_{\rm T}^{D} < 5$GeV/c and $p_{\rm T}^{assoc} > 3$GeV/c. This opens the possibility to explore kinematical regions closer to the kinematics of the original parton, allowing to enhance the sensitivity to the charm production processes. Indeed, for production mechanism at the leading order it is not expected any near side peak since the D meson carries the larger fraction (z) of the total jet momentum. The presence of a peak in the near-side region could arise from next-to-leading-order mecha-

[1] the propagation of each error box is independent among the two systems, so the uncertainty box for each $\Delta\varphi$ bin can be evaluated with standard error propagation.

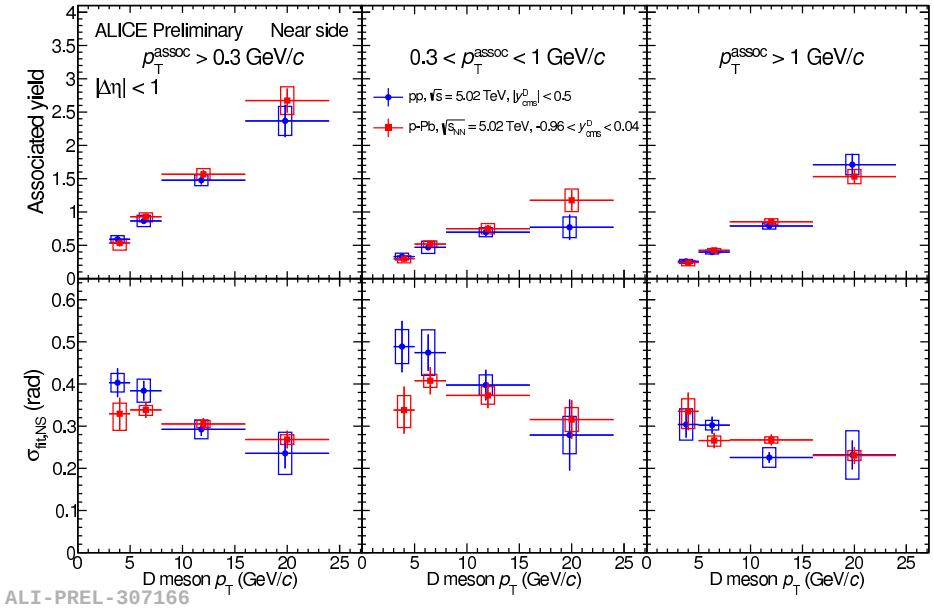

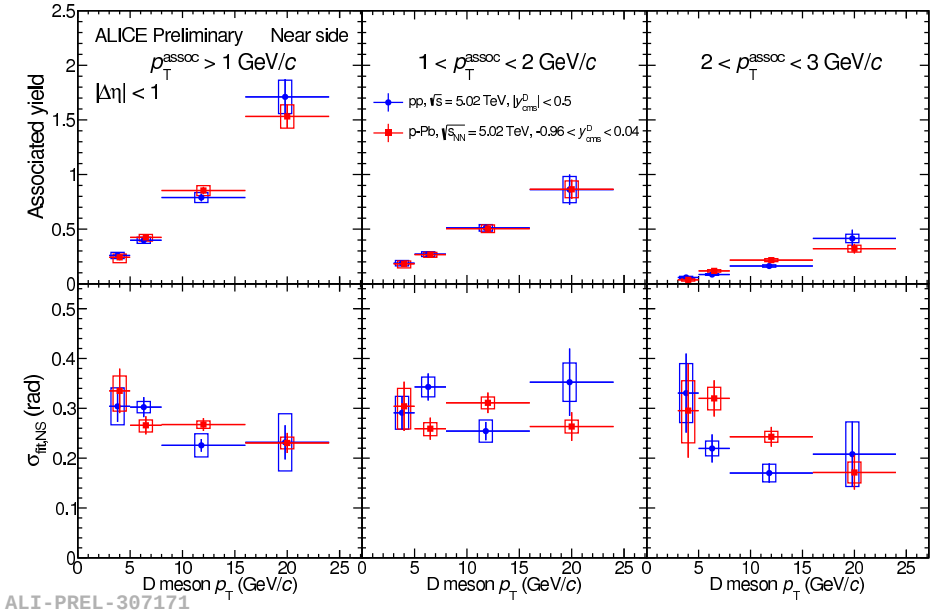

Figure 5.20 – *Near-side yield and sigmas for the average of* D^0, D^+ *and* D^{*+} *azimuthal correlations in pp (blue) and p-Pb (red) in all the kinematic regions of trigger and associated track.*

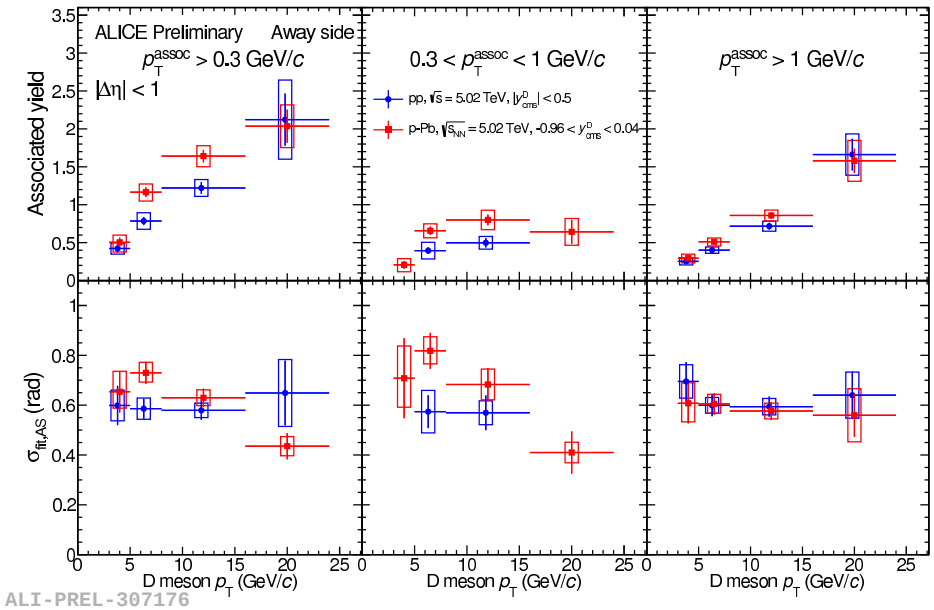

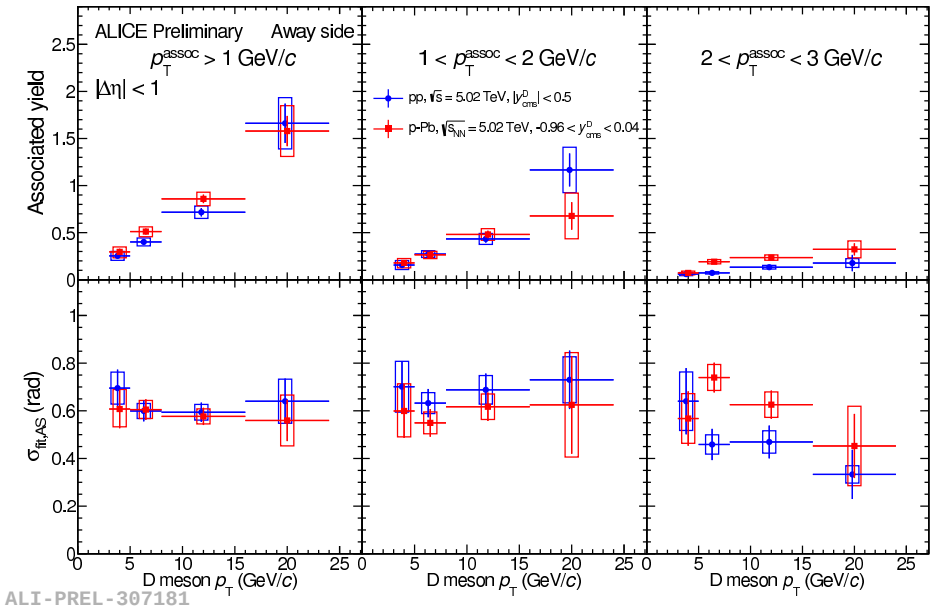

Figure 5.21 – *Away-side yield and sigmas for the average of* D^0, D^+ *and* D^{*+} *azimuthal correlations in pp (blue) and p-Pb (red) in all the kinematic regions of trigger and associated track.*

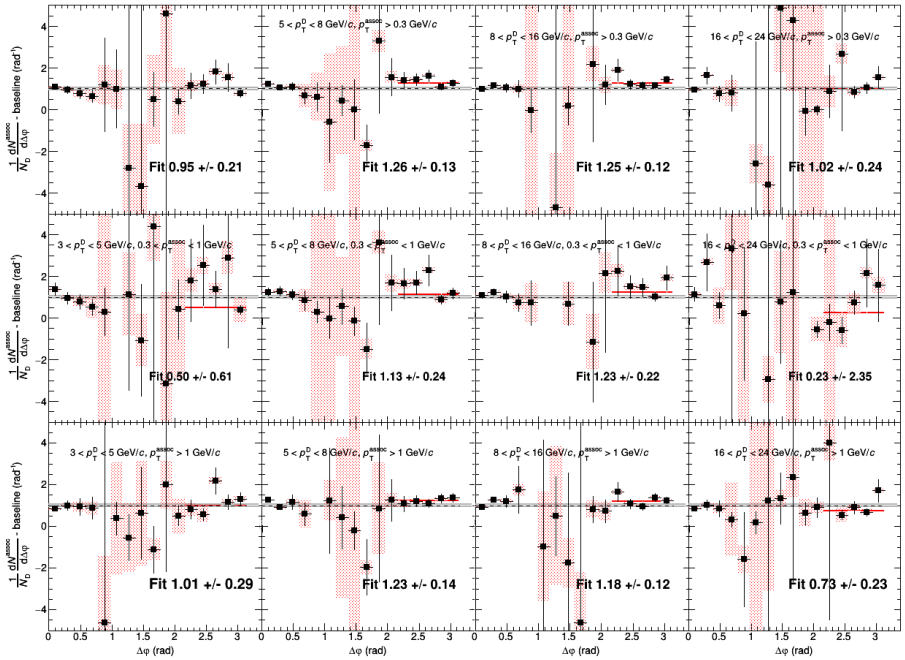

Figure 5.22 – *Ratio of the $\Delta\phi$ correlation distributions in pp and in p-Pb collisions for lower (top) and higher (bottom) p_{T} of the associated tracks. The red line represents the fit on the away-side points. The grey band represent the correlated uncertainty while the red box describe the fully-correlated uncertainty on the baseline.The fit outcome is reported in each box.*

nisms. However, looking at the bottom left panel of the Fig. 5.23 no peak is present in both the near and away-side regions.

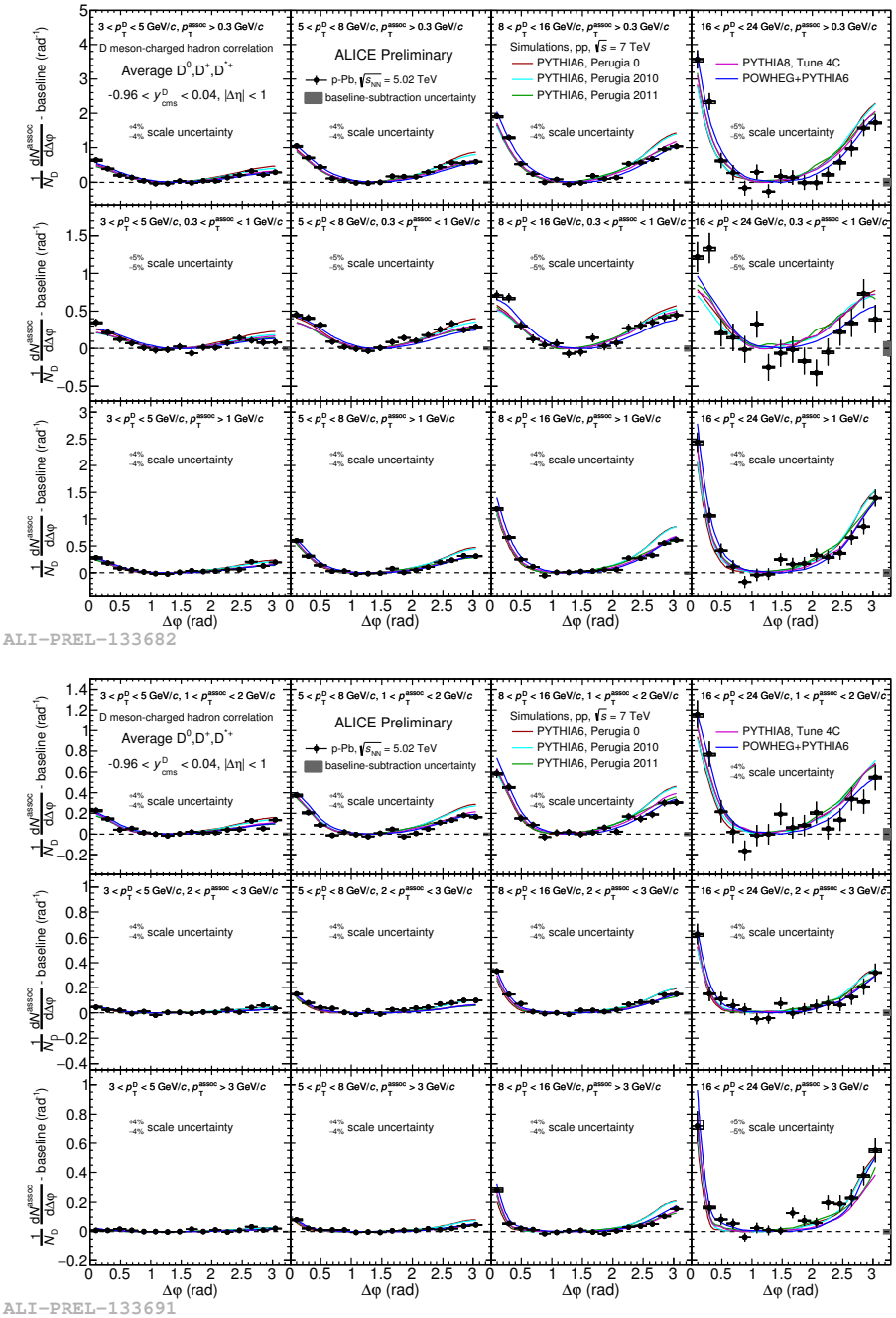

Figure 5.23 – *Comparison of p-Pb 2016 average D-h correlation distributions and model expectations, for all the studied kinematic ranges.*

Figures 5.24 and 5.25 show the same comparison for the fit observables (peak yields and widths for near-side and away-side, respectively), for all the addressed p_{T} ranges. Here, the compatibility of the physics observables with models is confirmed in both the near- and away-side regions. Some tensions are present on the description of the near-side yields for high p_{T} of the D and softer tracks with respect to PYTHIA6 and PYTHIA8 predictions. A rather good descriptions of the near-side width is obtained for most of the kinematic regions, making exception just for the low-p_{T} of the associated tracks, especially when compared with POWHEG predictions. The away-side observables in Fig. 5.25 are well described by the model predictions in all the kinematic regions, even if it could be noticed that the PYTHIA simulations match always the data on the lower side, while POWHEG is rather closer to data and gives, in general, lower away-side yields with respect to PYTHIA6 and PYTHIA8. It should be observed that the main uncertainty comes from the assumption used for the baseline subtraction (described in the subsection 4.6.2) and it can be reduced only with a larger statistics sample.

5.4.2 Centrality dependent results

The procedure for the extraction of the results, after having evaluated all the needed correction, is totally equivalent to the one described for the centrality integrated as well as for the proton-proton azimuthal correlation analysis: the weighted average of the azimuthal correlation distributions for the three D-meson species was evaluated for each kinematic range under study, and the fit function (composed of a double Gaussian for the near- and away-side peak and a constant baseline) in Eq. 5.3 was applied to the average distribution, in order to extract the near- and away-side associated yield and widths. The procedure was performed independently on each of the three centrality classes. A comparison of the baseline subtracted correlation distributions among the three multiplicity classes is reported in Fig. 5.26. In particular, the blue distributions represent the high multiplicity class (0-20%), the red the mid-centrality class (20-60%) while in green the low-multiplicity class (60-100%).
Each panel represents a different kinematic range. In all the three centrality classes, the correlation distributions show very similar shapes of the correlation peaks, and a consistent evolution with respect to the p_{T} of the triggers.
In Fig. 5.27 the comparison of the near-side fit observables (yields and width) among the three centrality classes is shown. The same legend of the superimposed correlation distributions (Fig. 5.26) still holds. In addition, in Fig. 5.27 the error bars encode the statistical uncertainty while the empty boxes represent the total correlated systematic uncertainty (the uncorrelated systematic error is shown as scale uncertainty) and the shaded boxes represent the v_2 related uncertainty. The systematic error on the baseline subtraction is shown in the boxes on the top of the x-axis. Within the current uncertainties, no clear modifications of the near-side peak properties appear for the different centrality classes. The usual increasing trend with p_{T}(D) is observed, due to the

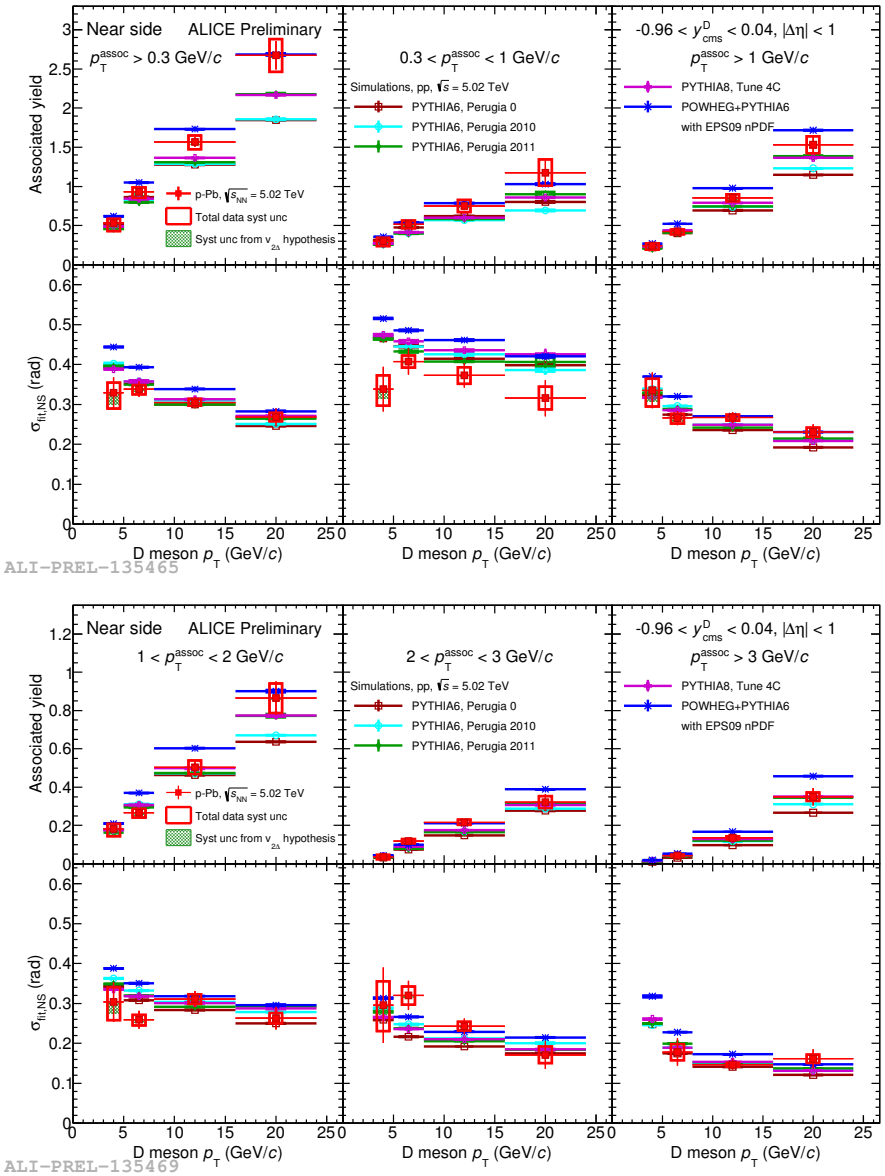

Figure 5.24 – *Comparison of near-side peak yields and widths from p-Pb 2016 results and model expectations, for all the studied kinematic ranges.*

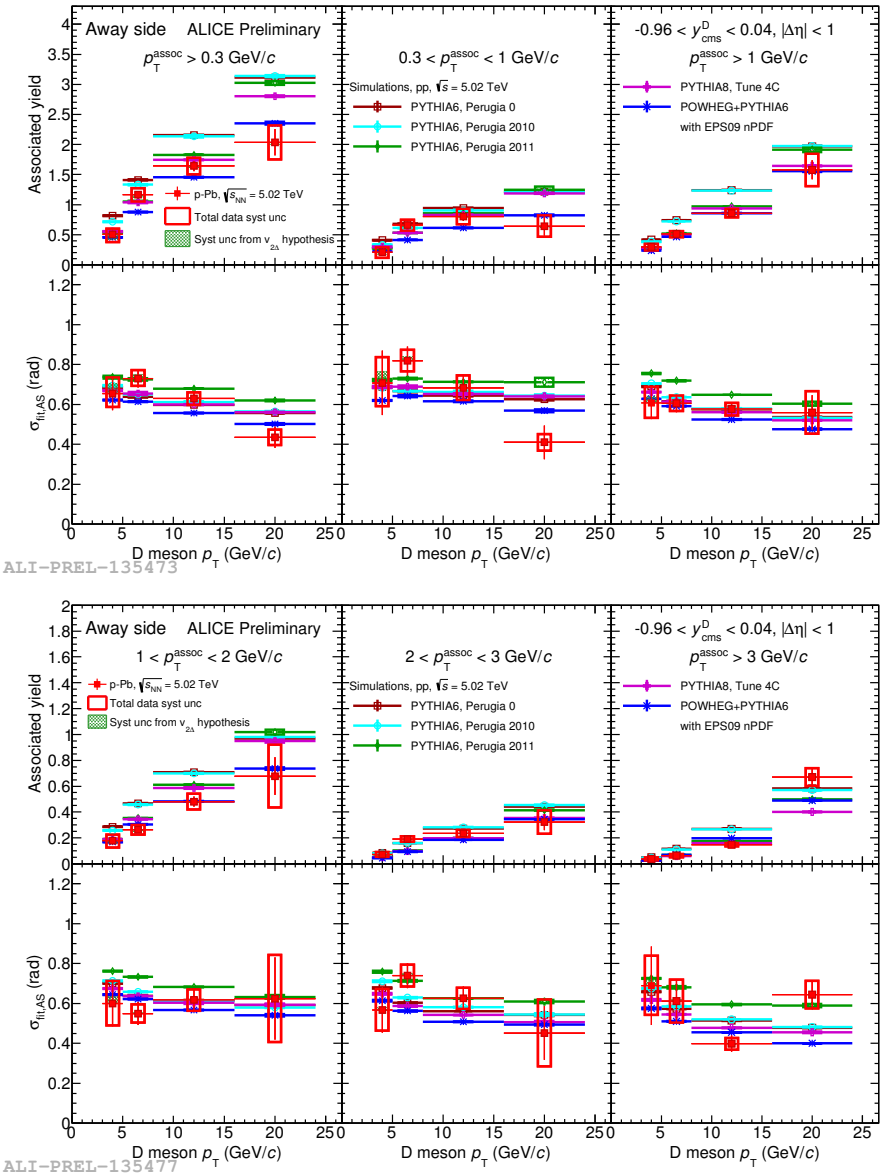

Figure 5.25 – *Comparison of away-side peak yields and widths from p-Pb 2016 results and model expectations, for all the studied kinematic ranges.*

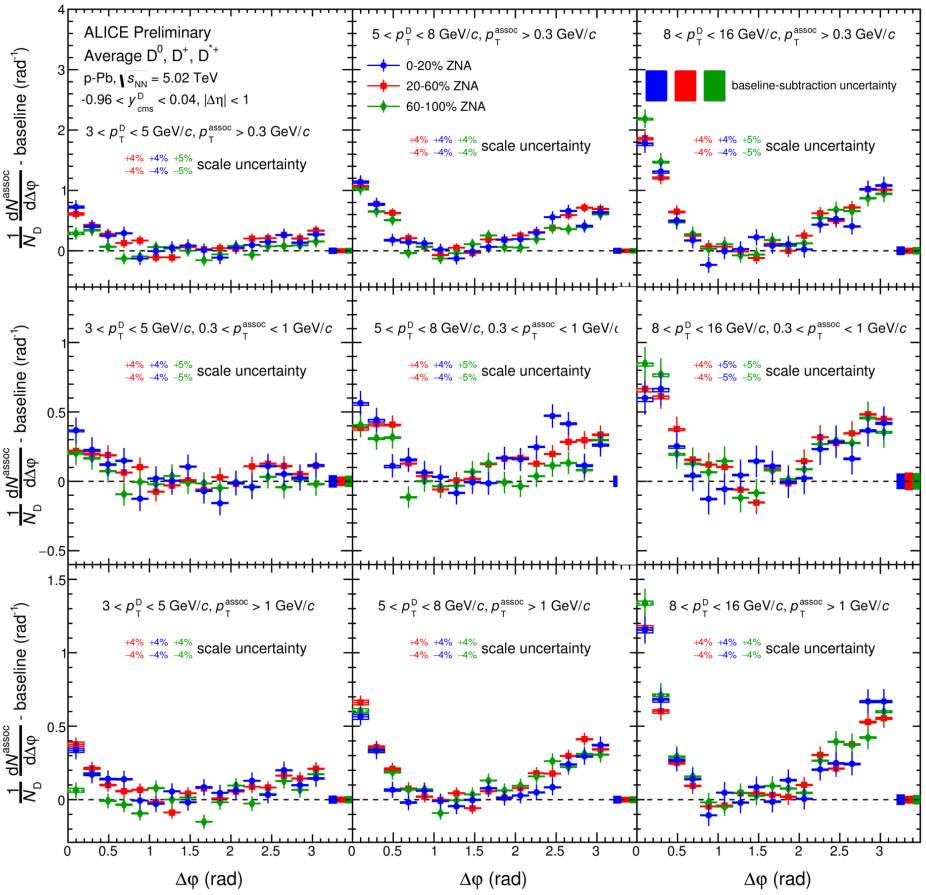

Figure 5.26 – *Comparison of baseline-subtracted correlation distributions in the different centrality classes. Each color is a different centrality class, as described in the legend. The error bars represent the statistical uncertainty, the empty boxes represent the overall systematic uncertainties, the shaded boxes represent the v_2 related uncertainties.*

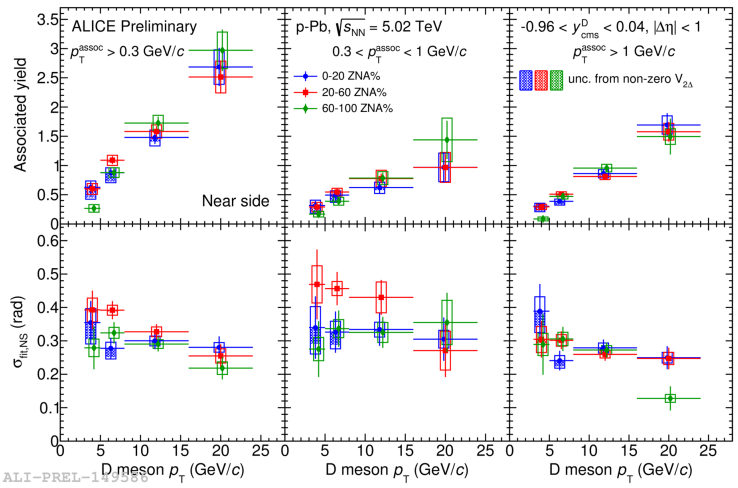

Figure 5.27 – *Comparison of near-side observables in the different centrality classes. Each color is a different centrality class, as described in the legend. The error bars represent the statistical uncertainty, the empty boxes represent the overall systematic uncertainties, the shaded boxed represent the v_2 related uncertainties.*

increased energy of the originally parton which results in more production of fragmentation tracks, as a similar slight decrease of the peak angular spread when going to higher p_{T}(D), due to the stronger collimation of the fragmentation tracks of the charm quark caused by the harder p_{T} spectra of the produced tracks. In particular, one can notice small values of the yield for the lowest p_{T} interval of D mesons (3< p_{T} <5 GeV/c) in the low-multiplicity class, especially for higher p_{T} of the associated tracks. Most probably, this is not a physical feature, but comes from an unlucky positioning of the points at $\Delta\varphi \approx 0$ of the azimuthal correlation (mainly due to fluctuations), especially for the first point, as it can be seen from the superimposed correlation distributions (Fig. 5.26).
The overall compatibility observed with respect to the centrality of the collision does not make the analysis sensitive to the elliptic flow of the D-meson. Indeed, a similar analysis performed with the azimuthal correlation of heavy flavoured electrons and charged particles revealed an excess on the high multiplicity distributions with respect to the low-multiplicity. This excess was well described by a Fourier expansion with a dominant elliptic flow component, as reported in the second chapter of this thesis.
For completeness, the comparison of the away-side fit observables are also shown in Fig. 5.28 even if not approved by the ALICE collaboration due to the large uncertainties present. Indeed, some of the fits even fail in reproducing the away-side peak, while this doesn't happen for the near-side peak region. On top of the uncertainties, an increase of the yields with p_{T}(D), though probably slightly milder than for the near-side, can be observed, as well as a very similar sligthly decreasing trend for the away-side width - though the values are approximately twofold with respect to the near-side width.

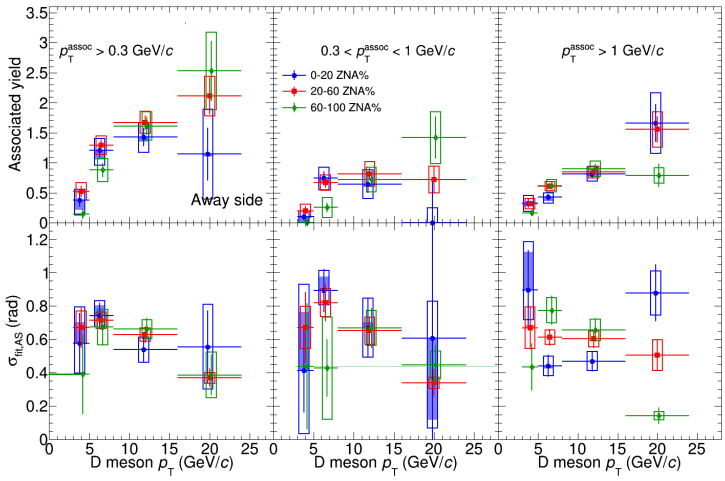

Figure 5.28 – *Comparison of away-side observables in the different centrality classes. Each color is a different centrality class, as described in the legend. The error bars represent the statistical uncertainty, the empty boxes represent the overall systematic uncertainties, the shaded boxed represent the v_2 related uncertainties.*

6

Conclusions

In this thesis I presented the measurement of angular correlations between D mesons and unidentified charged particles in proton-proton collisions and in p–Pb collisions at the same center-of-mass collision energy of 5.02 TeV. The analysis was performed using the ALICE detector at the LHC. This study in pp collisions aimed to test perturbative QCD calculations and to provide a reference for the study in heavy-ion collisions. Measurements in p–Pb collisions help to characterize the effects due to the presence of a nucleus in the collision (cold nuclear matter effects), in order to disentangle them from effects due to the interaction with the Quark-Gluon Plasma in Pb–Pb collisions. Moreover, the analysis of angular correlations between heavy-flavour particles and charged hadrons is a tool to characterize the heavy-quark fragmentation process since it is sensitive to their production mechanism. Indeed, differences between pp and p–Pb collisions give an insight into the cold nuclear matter effects on heavy-quark production and hadronization in p–Pb collisions as well as for the possible presence of collective behavior, which motivates the choose to perform the analysis not only in centrality integrated p–Pb collisions but also as a function of the centrality.

Thanks to the high statistics available for both the data samples, the analysis was performed in extended p_{T} range for the trigger particles and more differentially with respect to the transverse momentum interval of the associated particles, allowing to test perturbative QCD predictions in more interesting kinematic regions (i.e. regions with $p_{\mathrm{T}}(D) \approx p_{\mathrm{T}}(assoc)$ or $p_{\mathrm{T}}(D) < p_{\mathrm{T}}(assoc)$) for which the interplay of LO and NLO mechanisms could be highlighted. The analysis was performed independently for three D mesons (D^0, D^{*+} and D^+) and, finally, the one-dimensional weighted averages of the D^0, D^{*+} and D^+ azimuthal correlation distributions were computed. By fitting the data using a proper function, it was possible to extract physical quantities, like the baseline height of the D-hadron azimuthal correlation distributions, the yield and the width of the near-side and, for the first time, of the away-side peaks. The dependence of these quantities on the D meson p_{T} was evaluated. The values of the physical quantities extracted from the fit to the distributions can be used as benchmarks for the comparison with

future Pb-Pb measurements. A comparison of the azimuthal correlation distributions to expectations from the PYTHIA6, PYTHIA8 and POWHEG+PYTHIA event generators was performed for both the collision systems. Different tunes of PYTHIA parameters were considered for this study. The comparison showed a substantial agreement within the uncertainties between data and models both for pp and for p–Pb collisions in all the kinematic regions studied. Comparing the angular correlation distributions among the two collision systems, no difference was found for the near-side region while an hint of enhancement on the away-side in p–Pb data with respect to pp was observed, also when looking at the near- and away-side physical observables. However, the available statistics and the current performance of ALICE detector did not allow to extract any firm conclusion on it.

A full compatibility of the azimuthal correlation distributions as well as of the near-side observables was found among the three centrality classes (0-20%, 20-60% and 60-100%) in p–Pb collisions. This result did not give the sensitivity to test the presence of a collective behavior of the D mesons (non-zero elliptic flow v_2).

Finally, all the results presented in this thesis are a very good reference for the upcoming measurements in Pb–Pb collisions, with the impending data collection (indeed, the current statistics available did not make the measurement feasible in heavy-ion collisions). This will enable a comparison of the $\Delta\phi$ correlation distributions from all the three collision systems.

Appendices

Appendix A

Color Glass Condensate Theory

A.1 Introduction

A traditional approach of QCD on high energy scattering is to divide them into "hard" and "soft" scattering, corresponding to large and small momentum exchanges in the scattering. In the former, it can be treated in a perturbative framework due to the "asymptotic" freedom of QCD. In the latter case, since the momentum transfer is small, the coupling is large and the scattering behaves in a non-perturbative way. Moreover, in the Bjorken limit of QCD and according to the parton model, the hadron is viewed, in the infinite momentum frame (IMF) as a dilute collection of valence quarks, small-x gluons and sea quark pairs. For $Q^2 \to \infty$, the phase space density is very small despite the high number of gluons and sea quarks and thus the hadron is dilute, as shown in Fig. A.1. In this limit, to leading order in the coupling constant, the interaction of a probe with the hadron, on the characteristic time scale 1/Q, can be expressed as a hard interaction with an individual parton. In this approximation, the interaction of the struck parton in the hadron with co–moving partons is suppressed due to time dilation. The separation of hard and soft scattering is valid in this context. Powerful tools such as the Operator Product Expansion (OPE) and factorization theorems extend, to high orders in the coupling constant expansion, the hard-soft separation between process-dependent physics at the scale 1/Q and universal, long distance, non-perturbative Parton Distribution Functions (PDFs). The evolution of the separation of hard and soft scales is given by renormalization group (RG) equations called the DGLAP (Dokshitzer-Gribov-Lipatov-Altarelli-Parisi) equations [22].
With the advent of high energy colliders, hadron structure in the Regge-Gribov limit can be explored with $Q^2 \geq 1\ GeV^2$. As strikingly demonstrated by the HERA DIS data shown in Fig. A.1, the gluon distribution $xG(x, Q^2)$ in a proton rises very fast with

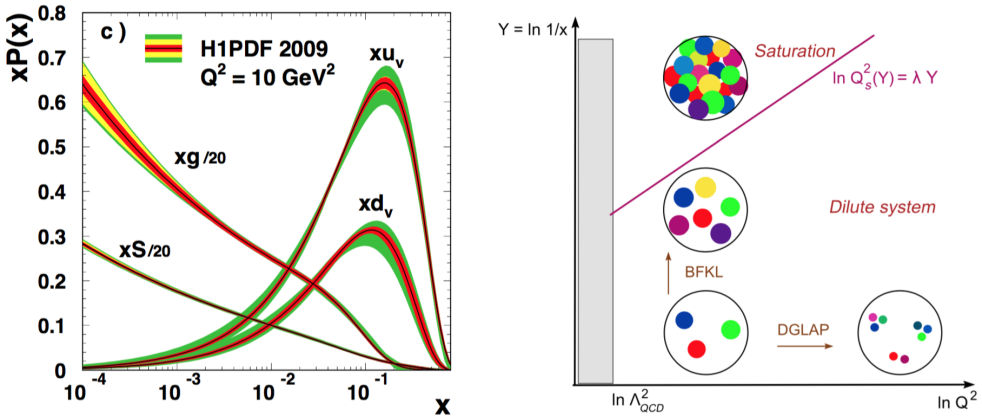

Figure A.1 – *Left: the x-evolution of the gluon, sea quark, and valence quark distributions for $Q^2 = 10\ GeV^2$ measured at HERA [159]. Right: the ?phase–diagram? for QCD evolution; each colored dot represents a parton with transverse area $\delta S_\perp \sim 1/Q^2$ and longitudinal momentum $k^+ = xP^+$.*

decreasing x at large, fixed Q^2 – roughly, as a power $x^{-\lambda}$ with $\lambda \simeq 0.3$. In the IMF frame of the parton model, $xG(x, Q^2)$ is the number of gluons with a transverse area $\delta S_\perp \geq 1/Q^2$ and a fraction $k^+/P^+ \sim x$ of the proton longitudinal momentum. In the Regge-Gribov limit, the rapid rise of the gluon distribution at small x is given by the BFKL (Balitsky-Fadin-Kuraev-Lipatov) equation. The stability of the theory formulated in the IMF requires that gluons have a maximal occupation number of order $1/\alpha_s$. This bound is saturated for gluon modes with transverse momenta $k_\perp \leq Q_s$, where $Q_s(x)$ is a semi-hard scale, the "saturation scale", that grows as x decreases. In this novel "saturation" regime of QCD, illustrated in Fig. A.1 (right panel), the proton becomes a dense many body system of gluons. In addition to the strong x dependence, the saturation scale Q_s has an A dependence because of the Lorentz contraction of the nuclear parton density in the probe rest frame. The dynamics of gluons in the saturation regime is non-perturbative as it is typical of strongly correlated systems. The Color Glass Condensate (CGC) is the description of the properties of saturated gluons in the IMF in the Regge-Gribov limit. The effective degrees of freedom in this framework are color sources ρ at large x and gauge fields A^μ at small x. At high energies, because of time dilation, the former are frozen color configurations on the natural time scales of the strong interactions and are distributed randomly from event to event. The latter are dynamical fields coupled to the static color sources. It is the stochastic nature of the sources, combined with the separation of time scales, that justify the "glass" appellation. The "condensate" designation comes from the fact that in the IMF, saturated gluons have large occupation numbers $O(1/\alpha_s)$, with typical momenta peaked about a characteristic value $k_\perp \sim Q_s$. The dynamical features of the CGC are captured by the JIMWLK3 renormalization group

(RG) equation that describes how the statistical distribution $W[\rho]$ of the fast sources at a given x scale evolves with decreasing x. In nuclear collisions, CGC dynamics produces "Glasma" field configurations at early times: strong longitudinal chromo-electric and chromo-magnetic fields color screened on transverse distance scales $1/Q_s$. These generate long range rapidity correlations and instabilities analogous to those seen in QED plasmas. The CGC framework is applicable to a wide variety of processes in e+p/A, p+A and A+A collisions. It provides an *ab initio* approach to study thermalization in heavy ion collisions and the initial conditions for the evolution of a thermalized Quark Gluon Plasma (QGP). The interaction of hard probes with the Glasma is little understood and is important for quantifying the transport properties of the QGP precursor.

A.2 CGC effective field theory

The CGC is an effective field theory based on the separation of the degrees of freedom into fast frozen color sources and slow dynamical color fields [160]. A renormalization group equation (the JIMWLK equation [163, 164]) ensures the independence of physical quantities with respect to the cutoff that separates the two kinds of degrees of freedom. The fast gluons with longitudinal momentum $k^+ > \Lambda^+$ are frozen by Lorentz time dilation in configurations specified by a color current $J_a\mu = \delta^{\mu+}\rho^a$, where ρ^a is the corresponding color charge density. On the other hand, slow gluons with $k^+ < \Lambda^+$ are described by the usual gauge fields A^μ of QCD. The fast gluons thus act as sources for the fields that represent the slow gluons. Although it is frozen for the duration of a given collision, the color source density ρ^a varies randomly event by event. The CGC provides a gauge invariant distribution $W_{\Lambda^+}[\rho]$, which gives the probability of a configuration ρ. This functional encodes all the correlations of the color charge density at the cutoff scale Λ^+ separating the fast and slow degrees of freedom. The power counting of the CGC EFT is such that in the saturated regime the sources ρ are of order g^{-1}. Attaching an additional source to a given Feynman graph does not alter its order in g; the vertex where this new source attaches to the graph is compensated by the g^{-1} of the source. Thus, computing an observable at a certain order in g^2 requires the resummation of all the contributions obtained by adding extra sources to the relevant graphs. The leading order in g^2 is given by a sum of tree diagrams, which can be expressed in terms of classical solutions of the Yang-Mills equations. Next-to-leading order (NLO) computations in the CGC EFT involve a sum of one-loop diagrams embedded in the above classical field. To prevent double counting, momenta in loops are required to be below the cutoff Λ^+. This leads to a logarithmic dependence in Λ^+ of these loop corrections. These logarithms are large if Λ^+ is well above the typical longitudinal momentum scale of the observable considered, and must be resummed. For gluon correlations inside the the hadron wavefunction and also for sufficiently inclusive observables in a collision, the leading logarithms are universal and can be absorbed into a redefinition of the distribution $\mathrm{W}_{\Lambda^+}[\rho]$ of the hard sources. The

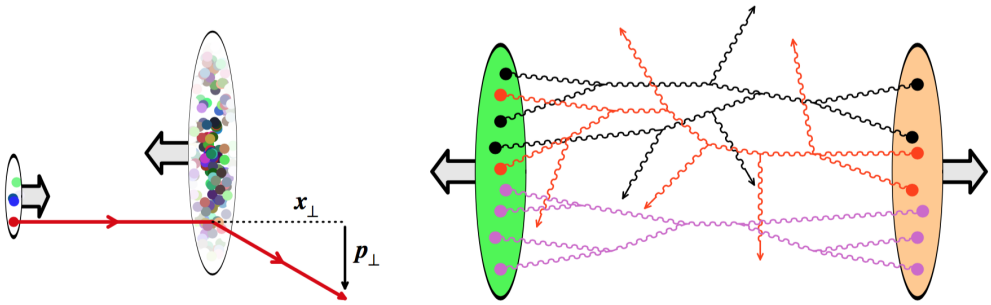

Figure A.2 *– Left: sketch of a proton-nucleus collision. Right: example of leading order contribution in a nucleus-nucleus collision*

evolution of $W_{\Lambda^+}[\rho]$ with Λ^+ is governed by the JIMWLK Hamiltonian. This operator contains up to two derivatives $\delta/\delta\rho$, and arbitrary powers in ρ.

A.3 The CGC in p–A collisions

Because the gluon densities scale as $A^{1/3}$, these phenomena are enhanced when the target is changed from a proton to a heavy nucleus. In this case, the probe ?sees? a large number of color charges, proportional to $A^{1/3}$. These charges add up to form a higher dimensional representation of the gauge group, and can therefore be treated as classical color distributions [161,162]. Further, the color charge distribution $W_{\Lambda_0^+}[\rho]$ is a Gaussian distribution in ρ (assumption valid according to the MV model). The variance of this distribution -the color charge squared per unit area- is proportional to $A^{1/3}$ and provides a semi-hard scale that makes weak coupling computations feasible. In addition to its role in motivating the EFT and serving as the initial condition in JIMWLK evolution, the MV model allows for direct phenomenological studies in p+A and A+A collisions in regimes where the values of x are not so small as to require evolution. Collisions between a dilute hadron projectile and a dense hadron target can be studied semi-analytically in the CGC framework. The archetype of such collisions is a proton-nucleus collision. However, the dilute-dense treatment also applies to proton-proton collisions for measurements at forward rapidities where the wave-function of one of the projectiles is probed at large x and that of the other at small x. These asymmetrical collisions can be treated using conventional parton distributions for the proton and the CGC for the nucleus. The simplest quantity to compute in this context is the single particle inclusive spectrum. In the CGC framework, this process is due to the scattering of a parton from the proton off the color field of the target nucleus, as illustrated in Fig. A.2 (left). When the parton is a quark, the amplitude of the scattering is proportional to the Fourier transform M_{LO} and the squared amplitude is proportional to the dipole scattering amplitude. Therefore,

in the CGC framework, the cross-section for this process is simply the Fourier transform of the dipole cross-section σ_{dipole}. An additional contribution to the single inclusive particle spectrum in a p+A collision is due to an incoming gluon instead of a quark. The treatment is nearly identical to the incoming quark case.
The CGC theoretical formalism is employed to analyze and predict a wide range of phenomena ranging from DIS in e+p and e+A collisions to the scattering of hadronic projectiles ranging from p+p to p+A to A+A collisions or to particle multiplicities in d+A and A+A collisions as well as for two-hadron correlations in d+A and A+A collisions.

Bibliography

[1] K. Aamodt et al. "The ALICE experiment at the CERN LHC". In: JINST 3 (2008), S08002. doi: 10.1088/1748-0221/3/08/S08002.

[2] M. Bedjidian, D. Blaschke, G. T. Bodwin, N. Carrer, B. Cole, P. Crochet, A. Dainese and A. Deandrea *et al.*, "Hard probes in heavy ion collisions at the LHC: Heavy flavor physics," hep-ph/0311048.

[3] E. Iancu, "QCD in heavy ion collisions," doi:10.5170/CERN-2014-003.197 arXiv:1205.0579 [hep-ph].

[4] H. Abramowicz *et al.* [H1 and ZEUS Collaborations], "Combination of measurements of inclusive deep inelastic $e^{\pm}p$ scattering cross sections and QCD analysis of HERA data," Eur. Phys. J. C **75** (2015) no.12, 580 doi:10.1140/epjc/s10052-015-3710-4 [arXiv:1506.06042 [hep-ex]].

[5] [Yuri L. Dokshitzer, Valery A. Khoze, and S. I. Troian. "On specific QCD properties of heavy quark fragmentation ('dead cone')" J. Phys. G17 (1991), pp. 1602-1604 doi: 10.1088/0954-3899/17/10/023.

[6] E. Norrbin and T. Sjostrand, "Production and hadronization of heavy quarks", Eur. Phys. J. C **17** (2000) 137 doi:10.1007/s100520000460 [hep-ph/0005110].

[7] Matteo Cacciari, Stefano Frixione, and Paolo Nason. "The p(T) spectrum in heavy flavor photoproduction". JHEP 03 (2001), p. 006 doi: 10.1088/1126-6708/2001/03/006 arXiv: hep-ph/0102134 [hep-ph]

[8] Matteo Cacciari, Mario Greco, and Paolo Nason. "The P(T) spectrum in heavy flavor hadroproduction". JHEP 05 (1998), p. 007 doi: 10.1088/1126-6708/1998/05/007 arXiv: hep-ph/9803400 [hep-ph].

[9] B. A. Kniehl et al. "Inclusive D^{*+-} production in p anti-p collisions with massive charm quarks". Phys. Rev. D71 (2005), p. 014018 doi: 10.1103/PhysRevD.71.014018 arXiv: hep-ph/0410289 [hep-ph].

[10] M. Cacciari, S. Frixione, N. Houdeau, M. L. Mangano, P. Nason and G. Ridolfi, "Theoretical predictions for charm and bottom production at the LHC," JHEP **1210** (2012) 137 doi:10.1007/JHEP10(2012)137 [arXiv:1205.6344 [hep-ph]].

[11] M. Cacciari, M. L. Mangano and P. Nason, 'Gluon PDF constraints from the ratio of forward heavy quark production at the LHC at $\sqrt{s}$=7 and 13 TeV," arXiv:1507.06197 [hep-ph].

[12] B. Abelev *et al.* [ALICE Collaboration], "Measurement of charm production at central rapidity in proton-proton collisions at $\sqrt{s} = 7$ TeV," JHEP **1201** (2012) 128 doi:10.1007/JHEP01(2012)128 [arXiv:1111.1553 [hep-ex]].

[13] V. Khachatryan *et al.* [CMS Collaboration], "Measurement of the B^+ Production Cross Section in pp Collisions at $\sqrt{s} = 7$ TeV," Phys. Rev. Lett. **106** (2011) 112001 doi:10.1103/PhysRevLett.106.112001 [arXiv:1101.0131 [hep-ex]].

[14] S. Chatrchyan *et al.* [CMS Collaboration], "Measurement of the B^0 production cross section in *pp* Collisions at $\sqrt{s} = 7$ TeV," Phys. Rev. Lett. **106** (2011) 252001 doi:10.1103/PhysRevLett.106.252001 [arXiv:1104.2892 [hep-ex]].

[15] K. Fukushima and K. Kashiwa, "Polyakov loop and QCD thermodynamics from the gluon and ghost propagators," Phys. Lett. B **723** (2013) 360 doi:10.1016/j.physletb.2013.05.037 [arXiv:1206.0685 [hep-ph]].

[16] B. A. Kniehl, G. Kramer, I. Schienbein and H. Spiesberger, "Collinear subtractions in hadroproduction of heavy quarks," Eur. Phys. J. C **41** (2005) 199 doi:10.1140/epjc/s2005-02200-7 [hep-ph/0502194].

[17] T. Sjostrand, S. Mrenna and P. Z. Skands, "A Brief Introduction to PYTHIA 8.1," Comput. Phys. Commun. **178** (2008) 852 doi:10.1016/j.cpc.2008.01.036 [arXiv:0710.3820 [hep-ph]].

[18] G. Corcella, I. G. Knowles, G. Marchesini, S. Moretti, K. Odagiri, P. Richardson, M. H. Seymour and B. R. Webber, "HERWIG 6: An Event generator for hadron emission reactions with interfering gluons (including supersymmetric processes)," JHEP **0101** (2001) 010 doi:10.1088/1126-6708/2001/01/010 [hep-ph/0011363].

[19] S. Frixione, P. Nason and B. R. Webber, "Matching NLO QCD and parton showers in heavy flavor production," JHEP **0308** (2003) 007 doi:10.1088/1126-6708/2003/08/007 [hep-ph/0305252].

[20] Shreyasi Acharya et al. "Measurement of D-meson production at mid-rapidity in pp collisions at $\sqrt{s}$ =7 TeV". Eur. Phys. J. C77.8 (2017), p. 550 doi: 10.1140/epjc/s10052-017-5090-4 arXiv: 1702.00766 [hep-ex].

[21] N. Armesto. "Nuclear shadowing". J. Phys., G32:R367-R394, 2006.

[22] Altarelli G and Parisi "Asymptotic freedom in parton language" G 1977, Nucl. Phys. B **126** 298

[23] Alan D. Martin "Proton structure, Partons, QCD, DGLAP and beyond" Acta Phys.Polon. B39: 2025-2062, 2008 arXiv:0802.0161 [hep-ph]

[24] M. Hirai, S. Kumano and T.-H. Nagai, "Determination of nuclear parton distribution functions and their uncertainties in next-to-leading order," Phys. Rev. C **76** (2007) 065207 doi:10.1103/PhysRevC.76.065207 [arXiv:0709.3038 [hep-ph]].

[25] Zheng Huang, Hung Jung Lu, Ina Sarcevic "Partonic Picture of Nuclear Shadowing at Small x" Nucl. Phys. A **637** (1998) 79-106

[26] K. J. Eskola, P. Paakkinen, V. J. Kolhinen and C. A. Salgado, "The scale dependent nuclear effects in parton distributions for practical applications" Eur. Phys. J. C **9** 61 hep-ph/9807297

[27] Frankfurt L L, Guzey V, McDermott M and Strikman M I 2002 "Nuclear shadowing in deep inelastic scattering on nuclei: leading twist versus eikonal approaches" JHEP **0202** 027

[28] Armesto N 2002 "A simple model for nuclear structure functions at small x in the dipole picture" Eur. Phys. J. C **26** p.35

[29] Shi-yuan Li, Xin-Nian Wang "Gluon shadowing and hadron production at RHIC" Phys. Lett. B **527** 2002 p. 85

[30] Accardi A. et al. "Hard probes in heavy ion collisions at the LHC: PDFs, shadowing and pA collisions" CERN Yellow Report on Hard probes in Heavy-Ion Collisions at the LHC (CERN-2004-009) arXiv:hep-ph/0308248

[31] J.W. Cronin, Henry J. Frisch, M.J. Shochet, J.P. Boymond, R. Mermod, et al. "Production of Hadrons with Large Transverse Momentum at 200 GeV, 300 GeV and 400 GeV." Phys. Rev. D, 11:3105, 1975.

[32] F. Arleo, S. Peigne and T. Sami, "Revisiting scaling properties of medium-induced gluon radiation," Phys. Rev. D **83** (2011) 114036 doi:10.1103/PhysRevD.83.114036 [arXiv:1006.0818 [hep-ph]].

[33] ALICE Collaboration, "Production of muons from heavy-flavour hadron decays in p-Pb collisions at $\sqrt{s_{NN}}$=5.02 TeV Phys. Lett. B770 (2017), pp. 459-472. doi: 10.1016/j.physletb.2017.03.049. arXiv: 1702.01479[nucl-ex].

[34] T. Sjostrand, S. Ask, J.R. Christiansen, R. Corke, N. Desai, P. Ilten, S. Mrenna, S. Prestel, C.O. Rasmussen, P.Z. Skands, "An introduction to PYTHIA 8.2", Comput. Phys. Commun. 191 (2015) 159-177, arXiv:1410.3012 [hep-ph].

[35] ALICE Collaboration, B. Abelev, et al., "Production of muons from heavy flavour decays at forward rapidity in pp and Pb–Pb collisions at $\sqrt{s}_{\rm NN}$=2.76TeV", Phys. Rev. Lett. 109 (2012) 112301, arXiv:1205.6443 [hep-ex].

[36] PHENIX Collaboration, A. Adare, et al., "Cold-nuclear-matter effects on heavy-quark production at forward and backward rapidity in d+Au collisions at $\sqrt{s}_{\rm NN}$ = 200GeV", Phys. Rev. Lett. 112(25) (2014) 252301, arXiv:1310.1005 [nucl-ex].

[37] M.L. Mangano, P. Nason, G. Ridolfi, "Heavy quark correlations in hadron collisions at next-to-leading order", Nucl. Phys. B 373 (1992) 295-345.

[38] K. J. Eskola, H. Paukkunen and C. A. Salgado, "EPS09: A New Generation of NLO and LO Nuclear Parton Distribution Functions," JHEP **0904** (2009) 065 doi:10.1088/1126-6708/2009/04/065 [arXiv:0902.4154 [hep-ph]].

[39] D. Stump, J. Huston, J. Pumplin, W.-K. Tung, H.L. Lai, S. Kuhlmann, J.F. Owens, "Inclusive jet production, parton distributions, and the search for new physics," JHEP 10 (2003) 046, arXiv:hep-ph/0303013

[40] R. Sharma, I. Vitev, B.-W. Zhang, "Light-cone wave function approach to open heavy flavor dynamics in QCD matter", Phys. Rev. C 80 (2009) 054902, arXiv:0904.0032 [hep-ph].

[41] ALICE Collaboration, J. Adam, et al., "Measurement of electrons from heavy-flavour hadron decays in p-Pb collisions at $\sqrt{s}_{\rm NN}$ = 5.02TeV", Phys. Lett. B 754 (2016) 81-93, arXiv:1509.07491 [nucl-ex]

[42] Z.-B. Kang, I. Vitev, E. Wang, H. Xing, and C. Zhang, "Multiple scattering effects on heavy meson production in p+A collisions at backward rapidity", Phys. Lett. B740 (2015) 23-29, arXiv:1409.2494 [hep-ph]

[43] A. M. Sickles, "Possible Evidence for Radial Flow of Heavy Mesons in d+Au Collisions" Phys. Lett. B731 (2014) 51-56, arXiv:1309.6924 [nucl-th].

[44] ALICE Collaboration, B. B. Abelev et al. "Multiplicity dependence of pion. kaon, proton and lambda production in p-Pb collisions at $\sqrt{s_{\rm NN}}$= 5.02 TeV", Phys. Lett. B728 (2014) 25-38, arXiv:1307.6796 [nucl-ex].

[45] ALICE Collaboration, J. Adam et al., "D-meson production in p–Pb collisions at $\sqrt{s_{\rm NN}}$= 5.02 TeV and in pp collisions at $\sqrt{s_{\rm NN}}$ = 7 TeV", Phys. Rev. C94 no. 5, (2016) 054908, arXiv:1605.07569 [nucl-ex].

[46] S. Frixione, P. Nason, and G. Ridolfi, "A Positive-weight next-to-leading-order Monte Carlo for heavy flavour hadroproduction", JHEP 09 (2007) 126, arXiv:0707.3088 [hep-ph].

[47] A. Beraudo, A. De Pace, M. Monteno, M. Nardi, and F. Prino, "Heavy-flavour production in high-energy d-Au and p-Pb collisions", JHEP 03 (2016) 123, arXiv:1512.05186 [hep-ph]

[48] M. Alford, K. Rajagopal, T. Schafer, A. Schmitt. "Color superconductivity in dense quark matter", Reviews of Modern Phys., 80:1455-1515, 2008.

[49] R.A. Maloney, W.A. Fowler. "On Nuclear Reactions and ^{9}Be Production in Inhomogeneous Cosmologies". Ap. J., 345:L5, 1989.

[50] R.N. Boyd, T. Kajino. "Can ^{9}Be Provide a Test of Cosmological Theories?" Ap. J., 336:L55, 1989.

[51] F. Karsch and E. Laermann, "Thermodynamics and in medium hadron properties from lattice QCD," In *Hwa, R.C. (ed.) et al.: Quark gluon plasma* 1-59 [hep-lat/0305025].

[52] F. Karsch. "Lattice QCD at High Temperature and Density". Lect. Notes Phys., 583: 209-249, 2002.

[53] H. T. Ding, F. Karsch and S. Mukherjee, "Thermodynamics of strong-interaction matter from Lattice QCD," Int. J. Mod. Phys. E **24** (2015) no.10, 1530007 doi:10.1142/S0218301315300076 [arXiv:1504.05274 [hep-lat]].

[54] A. Andronic, "An overview of the experimental study of quark-gluon matter in high-energy nucleus-nucleus collisions," Int. J. Mod. Phys. A **29** (2014) 1430047 doi:10.1142/S0217751X14300476 [arXiv:1407.5003 [nucl-ex]].

[55] R. Baier, Y.L. Dokshitzer, A.H. Mueller, S. Peign, D. Schiff " Radiative energy loss and p_T-broadening of high energy partons in nuclei". Nucl. Phys., B484: 265-282, 1997.

[56] M. Gyulassy and M. Plumer. "Jet Quenching in Dense Matter." Phys. Lett., B 243:432-438, 1990.

[57] R. Baier, Y.L. Dokshitzer, A.H. Mueller, S. Peign, D. Schi. "Radiative energy loss of high energy quarks and gluons in a finite volume quark-gluon plasma." Nucl. Phys., B483:291–320, 1997.

[58] R. Baier, Y.L. Dokshitzer, A.H. Mueller, S. Peign, D. Schi. "Radiative energy loss and $p_\perp$ broadening of high energy partons in nuclei". Nucl. Phys., B484:265–282, 1997.

[59] Y.L. Dokshitzer, V.A. Khoze and S.I. Troian. "Particle spectra in light and heavy quark jets". J. Phys., G17:1602, 1991.

[60] M. Gyulassy, P. Levai and I. Vitev. "Non-Abelian Energy Loss at Finite Opacity." Phys. Rev. Lett., 85:5535, 2000.

[61] M. L. Miller, K. Reygers, S. J. Sanders and P. Steinberg. "Glauber Modeling in High-Energy Nuclear Collisions." Ann. Rev. Nucl. Part. Sci., 57:205, 2007.

[62] ALICE Collaboration. "Charm and beauty production at LHC". ALICE-INT-2003-019.

[63] Shanshan Cao, Guang-You Qin, and Steffen A. Bass. "Heavy-quark dynamics and hadronization in ultrarelativistic heavy-ion collisions: Collisional versus radiative energy loss". Phys. Rev. C88 (2013), p. 044907. doi: 10.1103/ PhysRevC.88.044907. arXiv: 1308.0617 [nucl-th].

[64] Y. L. Dokshitzer and D. E. Kharzeev, "Heavy quark colorimetry of QCD matter," Phys. Lett. B 519 (2001) 199 doi:10.1016/S0370-2693(01)01130-3 [hep-ph/0106202].

[65] M. C. Abreu et al. "Evidence for deconfinement of quarks and gluons from the J/ψ suppression pattern measured in Pb–Pb collisions at the CERN SPS". Phys. Lett. B477 (2000), pp. 28-36. doi: 10.1016/S0370-2693(00)002379.

[66] H. Satz, "Quarkonium Binding and Dissociation: The Spectral Analysis of the QGP" Nucl. Phys.A 783: 249-260, 2007 doi: 10.1016/j.nuclphysa.2006.11.026

[67] ALICE Collaboration, S. Acharya et al., "Transverse momentum spectra and nuclear modification factors of charged particles in pp, p-Pb and Pb–Pb collisions at the LHC," arXiv:1802.09145 [nucl-ex].

[68] L. Adamczyk et al. "Observation of D^0 Meson Nuclear Modifications in Au–Au Collisions at $\sqrt{s_{\rm NN}}$ = 200 GeV". Phys. Rev. Lett. 113.14 (2014), p. 142301. doi: 10.1103/PhysRevLett.113.142301. arXiv: 1404.6185 [nucl-ex].

[69] ALICE Collaboration, S. Acharya et al., "Measurement of $\rm D^0$, $\rm D^+$, $\rm D^{*+}$ and D_s^+ production in Pb–Pb collisions at $\sqrt{s_{\rm NN}}$ = 5.02 TeV", JHEP 1810 (2018) 174 DOI: 10.1007/JHEP10(2018)174

[70] STAR Collaboration, B. Abelev et al., "Transverse momentum and centrality dependence of high-$p_{\rm T}$ non-photonic electron suppression in Au–Au collisions at $\sqrt{s_{\rm NN}}$ = 200 GeV," Phys. Rev. Lett. 98 (2007) 192301, arXiv:nucl-ex/0607012 [nucl-ex].

[71] Hard Probe Collaboration, R. Vogt, "The A dependence of open charm and bottom production," Int. J. Mod. Phys. E12 (2003) 211-270, arXiv:hep-ph/0111271 [hep-ph].

[72] A. Andronic *et al.*, "Heavy-flavour and quarkonium production in the LHC era: from proton-proton to heavy-ion collisions," Eur. Phys. J. C **76** (2016) no.3, 107 doi:10.1140/epjc/s10052-015-3819-5 [arXiv:1506.03981 [nucl-ex]].

[73] E. Norrbin and T. Sjostrand, "Production and hadronization of heavy quarks", Eur. Phys. J. C**17** (2000) 137-161, arXiv:hep-ph/0005110 [hep-ph].

[74] ALICE Collaboration, B. Abelev et al. "Beauty production in pp collisions at $\sqrt{s}$ = 2.76 TeV measured via semi-electronic decays", Phys.Lett. B738 (2014) 97-108, DOI: 10.1016/j.physletb.2014.09.026

[75] M. Djordjevic and M. Djordjevic, "Predictions of heavy-flavor suppression at 5.1 TeV Pb-Pb collisions at the CERN Large Hadron Collider", Phys. Rev. C92 no. 2, (2015) 024918, arXiv:1505.04316 [nucl-th].

[76] S. Batsouli, S. Kelly, M. Gyulassy, and J. L. Nagle, "Does the charm flow at RHIC?," Phys. Lett. B557 (2003) 26, arXiv:nucl-th/0212068 [nucl-th].

[77] M. Gyulassy, I. Vitev, and X. N. Wang, "High p(T) azimuthal asymmetry in non-central A+A at RHIC," Phys. Rev. Lett. 86 (2001) 2537, arXiv:nucl-th/0012092 [nucl-th].

[78] D. Molnar, "Charm elliptic flow from quark coalescence dynamics," J. Phys. G31 (2005) S421, arXiv:nucl-th/0410041 [nucl-th].

[79] A. Andronic, P. Braun-Munzinger, K. Redlich, and J. Stachel, "Statistical hadronization of charm in heavy ion collisions at SPS, RHIC and LHC," Phys. Lett. B571 (2003) 36, arXiv:nucl-th/0303036 [nucl-th].

[80] PHENIX Collaboration, A. Adare et al., "Heavy Quark Production in p + p and Energy Loss and Flow of Heavy Quarks in Au+Au Collisions at $\sqrt{s_{\rm NN}} = 200$ GeV," Phys. Rev. C84 (2011) 044905, arXiv:1005.1627 [nucl-ex].

[81] PHENIX Collaboration, "High pT measurements from PHENIX," Nucl. Phys., A715:199c-208c, 2003.

[82] STAR Collaboration, L. Adamczyk et al., "Measurement of D^0 azimuthal anisotropy at midrapidity in Au+Au Collisions at $\sqrt{s_{\rm NN}} = 200$ GeV," Phys. Rev. Lett. 118 no. 21, (2017) 212301, arXiv:1701.06060 [nucl-ex].

[83] CMS Collaboration, V. Khachatryan et al., "Suppression and azimuthal anisotropy of prompt and non-prompt J/ψ production in Pb-Pb collisions at $\sqrt{s_{\rm NN}} = 2.76$ TeV," Eur. Phys. J. C (2016) , arXiv:1610.00613 [nucl-ex].

[84] ALICE Collaboration, B. Abelev et al., "D meson elliptic flow in non-central Pb-Pb collisions at $\sqrt{s_{\rm NN}} = 2.76$ TeV," Phys. Rev. Lett. 111 (2013) 102301, arXiv:1305.2707 [nucl-ex].

[85] ALICE Collaboration, Shreyasi Acharya et al. "D-meson azimuthal anisotropy in mid-central Pb–Pb collisions at $\sqrt{s_{\rm NN}} = 5.02$ TeV" Phys.Rev.Lett. 120 (2018) no.10, 102301 doi: 10.1103/PhysRevLett.120.102301

[86] ALICE Collaboration, J. Adam et al., "Anisotropic flow of charged particles in Pb-Pb collisions at $\sqrt{s_{\rm NN}}$= 5.02 TeV," Phys. Rev. Lett. 116 (2016) 132302, arXiv:1602.01119 [nucl-ex].

[87] ALICE Collaboration, B. Abelev et al., "Anisotropic flow of charged hadrons, pions and (anti-)protons measured at high transverse momentum in Pb-Pb collisions at $\sqrt{s_{\rm NN}} = 2.76$ TeV," Phys. Lett. B719 (2013) 18, arXiv:1205.5761 [nucl-ex].

[88] ALICE Collaboration, B. Abelev et al., "Elliptic flow of identified hadrons in Pb-Pb collisions at $\sqrt{s_{\rm NN}} = 2.76$ TeV," JHEP 06 (2015) 190, arXiv:1405.4632 [nucl-ex].

[89] J. Uphoff, O. Fochler, Z. Xu, and C. Greiner, "Elastic and radiative heavy quark interactions in ultra-relativistic heavy-ion collisions," J. Phys. G42 (2015) 115106, arXiv:1408.2964[hep-ph].

[90] M. He, R. J. Fries, and R. Rapp, "Heavy Flavor at the Large Hadron Collider in a Strong Coupling Approach," Phys. Lett. B735 (2014) 445, arXiv:1401.3817 [nucl-th].

[91] S. Cao, T. Luo, G.-Y. Qin, and X.-N. Wang, "Heavy and light flavor jet quenching at RHIC and LHC energies," arXiv:1703.00822 [nucl-th].

[92] M. Nahrgang, J. Aichelin, P. B. Gossiaux, and K. Werner, "Influence of hadronic bound states above T_c on heavy-quark observables in Pb + Pb collisions at at the CERN Large Hadron Collider," Phys. Rev. C89 (2014) 014905, arXiv:1305.6544 [hep-ph].

[93] T. Song, H. Berrehrah, D. Cabrera, W. Cassing, and E. Bratkovskaya, "Charm production in Pb + Pb collisions at energies available at the CERN Large Hadron Collider," Phys. Rev. C93 (2016)034906, arXiv:1512.00891 [nucl-th].

[94] X.-N. Wang, "Studying mini-jets via the p_T dependence of the two particle correlation in azimuthal angle ϕ," Phys. Rev. D47 (1993) 2754-2760, arXiv:hep-ph/9306215 [hep-ph].

[95] STAR Collaboration, B. I. Abelev et al., "Long range rapidity correlations and jet production in high energy nuclear collisions," Phys. Rev. C80 (2009) 064912, arXiv:0909.0191 [nucl-ex].

[96] ALICE Collaboration, K. Aamodt et al., "Harmonic decomposition of two-particle angular correlations in Pb–Pb collisions at $\sqrt{s_{\rm NN}} = 2.76$ TeV," Phys. Lett. B708 (2012) 249-264, arXiv:1109.2501 [nucl-ex].

[97] ALICE Collaboration, B. Abelev et al., "Long-range angular correlations on the near and away side in p-Pb collisions at $\sqrt{s_{\rm NN}} = 5.02$ TeV," Phys. Lett. B719 (2013) 29-41, arXiv:1212.2001 [nucl-ex].

[98] ATLAS Collaboration, M. Aaboud et al., "Measurements of long-range azimuthal anisotropies and associated Fourier coefficients for pp collisions at $\sqrt{s_{\rm NN}} = 5.02$ and 13 TeV and p+Pb collisions at $\sqrt{s_{\rm NN}} = 5.02$ TeV with the ATLAS detector," Phys. Rev. C96 no. 2, (2017) 024908, arXiv:1609.06213 [nucl-ex].

[99] CMS Collaboration, S. Chatrchyan et al., "Multiplicity and transverse momentum dependence of two- and four-particle correlations in pPb and PbPb collisions," Phys. Lett. B724 (2013) 213-240, arXiv:1305.0609 [nucl-ex].

[100] CMS Collaboration, V. Khachatryan et al., "Long-range two-particle correlations of strange hadrons with charged particles in pPb and PbPb collisions at LHC energies," Phys. Lett. B742 (2015) 200-224, arXiv:1409.3392 [nucl-ex].

[101] PHENIX Collaboration, A. Adare et al., "Quadrupole Anisotropy in Dihadron Azimuthal Correlations in Central d+Au Collisions at $\sqrt{s_{\rm NN}} = 200$ GeV," Phys. Rev. Lett. 111 no. 21, (2016) 212301, arXiv:1303.1794 [nucl-ex].

[102] STAR Collaboration, L. Adamczyk et al., "Long-range pseudorapidity dihadron correlations in d+Au collisions at $\sqrt{s_{\rm NN}}$ = 200 GeV," Phys. Lett. B747 (2015) 265-271, arXiv:1502.07652 [nucl-ex].

[103] CMS Collaboration, V. Khachatryan et al., "Observation of Long-Range Near-Side Angular Correlations in Proton-Proton Collisions at the LHC," JHEP 09 (2010) 091, arXiv:1009.4122 [hep-ex].

[104] K. Werner, I. Karpenko, and T. Pierog, "The 'Ridge' in Proton-Proton Scattering at 7 TeV," Phys. Rev. Lett. 106 (2011) 122004, arXiv:1011.0375 [hep-ph].

[105] W.-T. Deng, Z. Xu, and C. Greiner, "Elliptic and Triangular Flow and their Correlation in Ultrarelativistic High Multiplicity Proton Proton Collisions at 14 TeV," Phys. Lett. B711 (2012) 301- 306, arXiv:1112.0470 [hep-ph].

[106] K. Dusling and R. Venugopalan, "Comparison of the color glass condensate to dihadron correlations in proton-proton and proton-nucleus collisions," Phys. Rev. D87 no. 9, (2013) 094034, arXiv:1302.7018 [hep-ph].

[107] A. Bzdak, B. Schenke, P. Tribedy, and R. Venugopalan, "Initial state geometry and the role of hydrodynamics in proton-proton, proton-nucleus and deuteron-nucleus collisions," Phys. Rev. C87 no. 6, (2013) 064906, arXiv:1304.3403 [nucl-th].

[108] M Bedjidian et al. "Hard Probes in Heavy Ion Collisions at the LHC: Heavy Flavour Physics," arXiv:0311048 [hep-ph].

[109] M. Nahrgang, J. Aichelin, P.B. Gossiaux, K. Werner, "Heavy-flavor azimuthal correlations of D-mesons" Nuclear Physics A 00 (2014) 1-5, doi: 10.1016/j.nuclphysa.2014.08.094 arXiv:1409.1464 [hep-ph]

[110] M. Nahrgang, J. Aichelin, P.B. Gossiaux, K. Werner, "Azimuthal correlations of heavy quarks in Pb+Pb collisions at $\sqrt{s_{\rm NN}}$ = 2.76 TeV at the CERN Large Hadron Collider", Phys. Rev. C 90, 024907 (2014) arXiv:1305.3823 [hep-ph]

[111] STAR Collaboration, "Measurement of the Bottom Quark Contribution to Non-photonic Electron Production in p+p Collisions at $\sqrt{s} = 200$ GeV," Phys. Rev. Lett. 105, 202301 (2010)

[112] "Charm (and Beauty) Production at the Tevatron," J. Rademacker for the CDF Collaboration, FERMILAB-CONF-07-634-E

[113] LHCb Collaboration "Observation of double charm production involving open charm in pp collisions at $\sqrt{s}$ = 7 TeV," JHEP, 06:141, 2012

[114] K. Eggert et al., "Angular Correlations Between the Charged Particles Produced in pp Collisions at ISR Energies," Nucl.Phys. B86 (1975) 201

[115] PHOBOS Collaboration, B. Alver et al., "Cluster properties from two-particle angular correlations in p + p collisions at s**(1/2) = 200-GeV and 410-GeV", Phys.Rev. C75 (2007) 054913, arXiv:0704.0966

[116] K. Dudling, R. Venugopalan, "Comparison of the color glass condensate to di-hadron correlations in proton-proton and proton-nucleus collisions" Phys. Rev. D 87, 094034 (2013)

[117] STAR Collaboration, C. Adler et al., "Disappearance of Back-To-Back High-p_{T} Hadron Correlations in Central Au+Au Collisions at $\sqrt{s_{\mathrm{NN}}}$=200 GeV Phys. Rev. Lett. 90, 082302

[118] STAR Collaboration, "Evidence from d+Au measurements for final-state suppression of high p_{T} hadrons in Au+Au collisions at RHIC," Phys. Rev. Lett. 91:072304, 2003 arXiv:nucl-ex/0306024

[119] STAR Collaboration "Direct Observation of Dijets in Central Au+Au Collisions at $\sqrt{s_{\mathrm{NN}}}$ = 200 GeV," Phys. Rev. Lett., 97:162301, 2006.

[120] B. Abelev *et al.* [ALICE Collaboration], "Measurement of charm production at central rapidity in proton-proton collisions at $\sqrt{s} = 7$ TeV," JHEP **1201** (2012) 128 doi:10.1007/JHEP01(2012)128 [arXiv:1111.1553 [hep-ex]].

[121] B. Abelev et al. [ALICE Collaboration], Eur. Phys. J. C (2017) 77:245

[122] B. Abelev et al. [ALICE Collaboration], Phys.Lett. B719 (2013) 29-41

[123] B. Abelev et al. [ALICE Collaboration], Phys.Lett. B726 (2013) 164-177

[124] https://aliceinfo.cern.ch/Figure/node/12130 (ALI-PREL-138003)

[125] ALICE Collaboration, arXiv:1609.06643 [nucl-ex]

[126] https://aliceinfo.cern.ch/Notes/node/785

[127] https://aliceinfo.cern.ch/Notes/node/238

[128] https://aliceinfo.cern.ch/Notes/node/201

[129] P. Bozek and W. Broniowski, "Correlations from hydrodynamic flow in p–Pb collisions," arXiv:1211.0845 [nucl-th].

[130] K. Dusling and R. Venugopalan, "Explanation of systematics of CMS p–Pb high multiplicity di-hadron data at $\sqrt{s_{\mathrm{NN}}} = 5.02$ TeV," arXiv:1211.3701 [hep-ph].

[131] M. Luzum, "Collective flow and long-range correlations in relativistic heavy ion collisions," Phys. Lett. B 696, 499-504 (2011)

[132] ATLAS Collaboration, "Observation of Associated Near-Side and Away-Side Long-Range Correlations in $\sqrt{s_{\mathrm{NN}}}$ Proton-Lead Collisions with the ATLAS Detector," Phys. Rev. Lett. 110, 182302 doi: https://doi.org/10.1103/PhysRevLett.110.182302

[133] Piotr Bozek, "Collective flow in p-Pb and d-Pb collisions at TeV energies," Phys. Rev. C 85, 014911

[134] Adam Bzdak, Bjorn Schenke, Prithwish Tribedy, and Raju Venugopalan "Initial-state geometry and the role of hydrodynamics in proton-proton, proton-nucleus, and deuteron-nucleus collisions" Phys. Rev. C 87, 064906

[135] CMS Collaboration, "Elliptic flow of charm and strange hadrons in high-multiplicity pPb collisions at $\sqrt{s_{\rm NN}}$= 8.16TeV" Phys. Rev. Lett. doi:10.1103/PhysRevLett.121.082301.

[136] ALICE Collaboration, S. Acharya et al., "Search for collectivity with azimuthal J/ψ-hadron correlations in high multiplicity p-Pb collisions at $\sqrt{s_{\rm NN}}$ = 5.02 and 8.16 TeV," Phys. Lett. B780 (2018) 7-20, arXiv:1709.06807 [nucl-ex].

[137] ALICE Collaboration, J. Adam et al., "Forward-central two-particle correlations in p-Pb collisions at $\sqrt{s_{\rm NN}}$ = 5.02 TeV, Phys. Lett. B753 (2016) 126–139, arXiv:1506.08032 [nucl-ex].

[138] PHENIX Collaboration, S. S. Adler et al., "Dense-Medium Modifications to Jet-Induced Hadron Pair Distributions in Au+Au Collisions at $\sqrt{s_{\rm NN}}$ = 200 GeV," Phys. Rev. Lett. 97 (2006) 052301, arXiv:nucl-ex/0507004 [nucl-ex].

[139] ALICE Collaboration, B. B. Abelev et al., "Long-range angular correlations of π, K and p in p-Pb collisions at $\sqrt{s_{\rm NN}}$ = 5.02 TeV," Phys. Lett. B726 (2013) 164-177, arXiv:1307.3237[nucl-ex].

[140] ALICE Collaboration, K. Aamodt et al., "Particle-yield modification in jet-like azimuthal di-hadron correlations in Pb-Pb collisions at $\sqrt{s_{\rm NN}}$= 2.76 TeV", Phys. Rev. Lett. 108 (2012) 092301 doi: 10.1103/PhysRevLett.108.092301.

[141] ALICE Collaboration, J. Adam et al., "Forward-central two-particle correlations in p-Pb collisions at $\sqrt{s_{\rm NN}}$ = 5.02 TeV," Phys. Lett. B753 (2016) 126 -139, arXiv:1506.08032 [nucl-ex].

[142] G. Aglieri Rinella et al. "The pixel trigger system for the ALICE experiment", PoS (RD09) 005, 2009.

[143] R. Fruhwirth, "Application of Kalman fitering to track and vertex fitting". Nucl. Instrum. Meth. A262 (1987), pp. 444-450. doi: 10 . 1016 / 0168 -9002(87)90887-4.

[144] B. Abelev et al. ALICE Collaboration, "Performance of the ALICE Experiment at the CERN LHC," Int. J. Mod. Phys. A 29 (2014) 1430044 doi:10.1142/S0217751X14300440 [arXiv:1402.4476 [nucl-ex]].

[145] B. Abelev et al. "Centrality determination of Pb–Pb collisions at $\sqrt{s_{\rm NN}}$= 2.76 TeV with ALICE". Phys. Rev. C88.4 (2013), p. 044909. doi: 10.1103/PhysRevC.88.044909. arXiv: 1301.4361 [nucl-ex].

[146] R. J. Glauber and G. Matthiae, "High-energy scattering of protons by nuclei," Nucl. Phys. B **21** (1970) 135. doi:10.1016/0550-3213(70)90511-0

[147] R. Brun, F. Bruyant, F. Carminati, S. Giani, M. Maire, A. McPherson, G. Patrick and L. Urban, "GEANT Detector Description and Simulation Tool," doi:10.17181/CERN.MUHF.DMJ1

[148] T. Sjostrand, S. Mrenna, and P. Z. Skands, "PYTHIA 6.4 Physics and Manual," JHEP 05 (2006) 026, arXiv:hep-ph/0603175 [hep-ph].

[149] P. Z. Skands, "Tuning Monte Carlo Generators: The Perugia Tunes," Phys. Rev. D82 (2010) 074018, arXiv:1005.3457 [hep-ph].

[150] S. Alioli, P. Nason, C. Oleari, and E. Re, "A general framework for implementing NLO calculations in shower Monte Carlo programs: the POWHEG BOX," JHEP 06 (2010) 043, arXiv:1002.2581 [hep-ph].

[151] H.-L. Lai, M. Guzzi, J. Huston, Z. Li, P. M. Nadolsky, J. Pumplin, and C. P. Yuan, "New parton distributions for collider physics," Phys. Rev. D82 (2010) 074024, arXiv:1007.2241 [hep-ph].

[152] S. Bethke, G. Dissertori and G. Salam, *Quantum Chromodynamics*, in: C. Patrignani *et al.* [Particle Data Group], "Review of Particle Physics," Chin. Phys. C **40** (2016) no.10, 100001. doi:10.1088/1674-1137/40/10/100001

[153] X.-N. Wang and M. Gyulassy, "HIJING: A Monte Carlo model for multiple jet production in pp, pA and AA collisions," Phys. Rev. D44 (1991) 3501-3516.

[154] ALICE Collaboration, " Azimuthal anisotropy of heavy-flavour decay electrons in p-Pb collisions at $\sqrt{s_{\rm NN}}$= 5.02 TeV," arXiv:1805.04367 [nucl-ex]

[155] G. Corcella, I.G. Knowles, G. Marchesini, S. Moretti, K. Odagiri, P. Richardson, M.H. Seymour, and B.R. Webber, "HERWIG 6: an event generator for hadron emission reactions with interfering gluons (including supersymmetric processes)," JHEP 0101 (2001) 010.

[156] K. Werner, B. Guiot, I. Karpenko, and T. Pierog, "Analysing radial flow features in p-Pb and p-p collisions at several TeV by studying identified particle production in EPOS3," Phys. Rev. C89 no. 6, (2014) 064903, arXiv:1312.1233 [nucl-th].

[157] ALICE Collaboration, J. Adam, et al, "Centrality dependence of particle production in p–Pb collisions at $\sqrt{s_{\rm NN}}$= 5.02 TeV", *Phys. Rev. C 91 (6)* (2015) 064905, doi:10.1103/PhysRevC.91.064905.

[158] W. Florkowski, "Phenomenology of Ultra-Relativistic Heavy-Ion Collisions," Singapore, Singapore: World Scientific (2010) 416 p

[159] F.D. Aaron, et al, [H1 Collaboration] "A precision measurement of the inclusive ep scattering cross section at HERA" Eur. Phys. J. C 64, 561 (2009).

[160] L.D. McLerran, R. Venugopalan, "Computing quark and gluon distribution functions for very large nuclei" Phys. Rev. D 49, 2233 (1994);

[161] E. Ferreiro, E. Iancu, A. Leonidov, L.D. McLerran, "How Pomerons meet in coloured glass" Nucl. Phys. A 703, 489 (2002)

[162] Sangyong Jeon and Raju Venugopalan "Random walks of partons in SU(N_c) and classical representations of color charges in QCD at small x" Phys. Rev. D 70, 105012 (2004)

[163] Kovner, Alex and Lublinsky, Michael and Mulian, Yair "Jalilian-Marian, Iancu, McLerran, Weigert, Leonidov, Kovner evolution at next to leading order" Phys. B 504, 415 (1997)

[164] E. Iancu, A. Leonidov, L.D. McLerran, "The Color Glass Condensate to the Strongly Interacting Quark Gluon Plasma: Theoretical Developments" Nucl. Phys. A 692, 583 (2001)

Ringraziamenti

Ringrazio il mio supervisor, prof. Domenico Di Bari, che mi ha trasmesso più di ogni altro la passione per la ricerca in fisica delle particelle e mi ha dato l'opportunità di entrare in questo affascinante mondo. A lui devo lo spirito critico con il quale approcciare ogni genere di problematica e /o risultato.
Un ringraziamento speciale va al dott. Fabio Colamaria che mi ha seguito per tutto il lavoro di analisi con pazienza e professionalità, insegnandomi il "rigore" scientifico. Un ringraziamento per aver condiviso anche momenti gioviali e non, cercando di incoraggiarmi in ogni momento.
Desidero ringraziare anche tutti gli altri membri del gruppo ALICE della sezione di INFN di Bari. Un ringraziamento particolare va a Giuseppe Bruno e Vito Manzari che mi hanno spronato a vivere un anno del mio percorso di dottorato al CERN.
Una menzione speciale va ai miei amici-colleghi GT, Adriano e Lucianna con cui abbiamo condiviso mesi pazzi al CERN, diventando una piccola famiglia sulla quale poter sempre fare affidamento.
Ringrazio la mia famiglia per essermi sempre stata di supporto nelle mie scelte.
L'ultimo ringraziamento è generale e va a tutte le persone che hanno arricchito a vario titolo la mia formazione durante questi tre anni. Penso che ci sia un minimo comun denominatore a tutte loro ed è il prodotto dell'entusiasmo che contraddistingue il mondo della ricerca scientifica per un pizzico di follia!